Modelling Tides in the Persian Gulf using Dynamic Nesting

Hashem Saberi Najafi, B.Sc (Hons, Mashhad-Iran), M.Sc (Brunel-UK)

Thesis submitted for the degree of
Doctor of Philosophy
in
Applied Mathematics
at
The University of Adelaide
(Faculty of Mathematical and Computer Sciences)

Department of Applied Mathematics

February 14, 1997

Acknowledgements

I wish to use this opportunity to express my sincere thanks to my supervisor, Assoc. Professor. John Noye, for his support, encouragement and criticism throughout the development and writing up of this thesis. The thesis would not have been possible without his help and continuing guidance.

I wish to sincerely thank my co-supervisor Dr. Michael Teubner for his continual interest, inspiring discussions and enthusiasm throughout the work. I also would like to thank him for his final reading of my thesis and providing me with many valuable suggestions and comments.

I also wish to thank Dr. Peter Bills my first co-supervisor during the first year of my studies. I appreciate very much the encouragement and expert guidance that I received from him during my studies.

I would like to thank all members of the tidal modelling group in the Department of Applied Mathematics, for their assistance and friendship.

I also would like to thank the Head of the Applied Mathematics Department, Dr. Peter Gill for his help and friendship.

I wish to express my gratitude to my wife, and to my two daughters for their company, encouragement and assistance during the period of my studies.

Finally I would like to acknowledge the financial assistance of the Iranian Ministry of Culture and Higher Education during the period of my studies in the form of a Guilan University Scholarship.

Signed Statement

This work contains no material which has been accepted for the award of any other degree or diploma in any university or other tertiary institution and, to the best of my knowledge and belief, contains no material previously published or written by another person, except where due reference has been made in the text.

I consent to this copy of my thesis, when deposited in the University Library, being available for loan and photocopying.

SIGNED: DATE: ...14./2./97.....

Contents

ERRATA

- The references Bills (1991) and Bills (1992) are the same; they indicate different years of publication of the same document.
- p. 7: references to Figure 1 should read Figure 2.1.
- p.50: reference to Mitchell (1985) should be changed to Bills (1992).
- p.52: the definition of ε_c should read "is the absolute difference in amplitude (cm) and phase (in degrees) between the observed ...."
- p.88, 2nd paragraph: change "do not contaminated" to "do not contaminate".
- p.88: delete equation and following sentence after "..... in which case C_c/C_f would be $\frac{1}{3}$
- p.97, 2nd paragraph: change "do not contaminated" to "do not contaminate".
- p.114, caption for Figure 7.18: should read "..... of the fifth hour of a five hour period".
- p.128, 2nd paragraph: change "do not contaminated" to "do not contaminate".
- p.130, 3nd to last line: delete "is developed".

Abstract

The Persian Gulf is a centre for world oil production, both on-shore and off-shore. The coastal regions of Iran and the Arabian countries on the Gulf support industrial activities and produce petroleum products which are shipped out through the Gulf. As a result of oil transport activities and consequential occasional oil spill events, the hydrodynamics of the Gulf waters is of great importance.

The tides of the Persian Gulf are very complex and while vast areas are very shallow and populated by tiny islands and mangroves, a third of the Gulf is more than $40\,m$ deep. What is needed is a modeling approach that can incorporate the disparate bathymetry of the different regions more appropriately.

The aim of this thesis is to develop and apply mathematical models to examine tidal movement in the Gulf, especially around the Iranian coast which has largely been neglected in the past. To do this a new technique for improving numerical models of tides in coastal regions has been developed and applied to the Persian Gulf.

In this approach a fine grid has been superimposed over important regions of a coarse grid model in order to improve the accuracy of the model predictions in these areas. Having completed one sweep of the coarse model with a large time step, the information from that model is used as a boundary condition to solve the tidal equations with a number of smaller time steps within the fine-grid regions. These time steps are an integral fraction of the coarse time step, and are chosen to maintain the same average Courant number of both coarse and fine-grid models at their interface. Because of this, there is no abrupt change in phase-speed of modelled tidal waves, with associated refraction and reflection, at the junction of the coarse and fine grids.

The thesis discusses the development of and application to the Gulf of three different numerical tidal models, namely a uniform grid Cartesian model, a uniform grid spherical model and a spherical model containing dynamically nested regions with finer spatial and temporal grids. The following are used in this approach:

- The depth-averaged Cartesian and spherical equations of tidal motions.
- An explicit finite-difference scheme based on the "Arakawa C" spatial grid.
- Calibration against measurements at forty observational stations, in the Persian Gulf.

- Dynamical nesting in space and time in shallow waters and other regions of interest such as areas containing large numbers of oil wells.

The results from the three models have been compared with the Admiralty chart, 5081, and tidal constants computed from records from tidal stations. There is good agreement between computed and observed values. In particular, results from the dynamically nested model match recorded values better than those obtained from both the Cartesian and spherical models.

Chapter 1

Introduction

1.1 Description of the Persian Gulf

The Persian Gulf has the following specifications:

- Latitude: 24° to 30° north latitude.
- Longitude: 48° to 57° east longitude.
- Surface: 239000 km^2.
- Length: 1000 km.
- Depth: the Gulf basin lies on a shallow continental platform with a mean depth of about $32m$.
- Width: the width varies from a maximum of $340km$ to a minimum of $60km$.

Figure 1.1 shows the position of the Gulf with the countries that surround it. It is a semienclosed marginal sea oriented in the north-west and south-east direction. It is connected to the Gulf of Oman in the Indian ocean through the Strait of Hormuz at its eastern end. The maximum depth in the Strait of Hormuz is almost $90m$ which is much smaller than the typical depth of the Gulf of Oman ($1000m$).

The Gulf is relatively young, having been formed 3–4 million years ago (see Lehr, 1984). A wide area of mud bottom is found in the northern and eastern parts of the Gulf, with sand bottom predominant in the southern and western part. The bottom of the Strait of Hormuz is essentially rocky. The land south of the Gulf consists of arid, flat desert stretching hundreds of miles.

The Tigris-Euphrates-Karun delta at the head of the Gulf provides a modest amount of freshwater discharge, known as the Shatt-al-Arab/Arvand river, into the basin (see Chao et al., 1992).

Figure 1.1: *A map of the Persian Gulf and neighbouring countries.*

1.2 Importance of this study

This study intends to provide an analysis of the water movement in the Persian Gulf due to astronomical tides, especially in shallow, complicated coastal areas. This information will help oil companies, oceanographers, meteorologists and engineers as well as assisting mariners to navigate in these waters. Few numerical models for the Gulf are available in Iran and the Iranian government is interested to have more work performed on the Gulf. These studies are of great importance for the country in terms of economic, scientific and environmental factors. For example, oil pollution represents a serious threat to the total marine environment in the Gulf. Research work in this respect should be developed in order to eliminate or to minimize the environmental damage caused by oil pollution and chemical discharge. Since pollutants are usually most concentrated in the shallow coastal areas, priority should be given to study these regions. Another economic importance of the study is fisheries. There are three main fisheries of current economic value in the Gulf, pelagic or midwater fisheries, demersal fisheries and the shrimp or prawn fishery (see Crisp, 1976).

The aim of this thesis is to develop and apply mathematical models to examine tidal movement in the Gulf, especially around the Iranian coast which has largely been neglected in the past. This may help the marine science division in Iran, which is interested in gaining comprehensive knowledge about all natural phenomena within the Persian Gulf. Furthermore, it may provide necessary basic information for engineers to solve the problems of the coastal areas. Developing a suitable numerical hydrodynamic model for the Gulf will help the country and the interested researchers to carry on more works in the coastal areas.

1.3 Summary of the thesis

This thesis deals with three numerical tidal models, namely a Cartesian, a spherical and a dynamically nested tidal model of the Persian Gulf. The main reason for developing the Cartesian numerical model is to compare the results with that from the spherical-coordinate model, to determine the effect of considering the earth's curvature in the computations.

To improve the predictions obtained from the application of a depth-averaged spherical-coordinate model of the Persian Gulf, a new model is developed in Chapter 6, with the advantage of having a fine grid in areas where high resolution is required, without using the fine grid everywhere with very small time steps. Results of using this model for the Persian Gulf are presented.

From the application of a depth-averaged spherical coordinate model of the Persian Gulf, close agreement between observed and computed tides was obtained, but to solve coastal engineering problems and to provide relevant answers for the other questions in the shallow and complicated coastal areas, it seems to be necessary to refine the grid to improve the predictions there.

In this approach the aim is to dynamically superimpose a fine grid over certain regions of a coarse grid model in order to improve the accuracy of model predictions in areas of particular importance. Having completed one sweep of the coarse model with a large time step, the information from that model is used as a boundary condition to solve the tidal equations with a number of smaller time steps within the fine-grid regions. These time steps are an integral fraction of the coarse time step, and are chosen small enough to maintain the same average Courant number of both coarse and fine-grid models. Because the Courant number is approximately the same each side of the interface of the coarse and fine grid, there is no abrupt change in phase-speed of modelled tidal waves, with associated refraction and reflection.

Chapter 2

Mathematical Formulation

In this chapter the equations describing barotropic tidal motion are presented for depth-averaged flows in Cartesian and spherical coordinates. In order to explain the characteristics of tidal dynamics in shallow seas, the physical parameters of each equation along with the physical meanings of various terms are given.

2.1 Tides and tidal prediction

The periodic rise and fall of the sea level is known as "*the tide*". Most of the earth's oceans have tides with average period of 12.4 h, but some places have tides with a period of 24.8 h, for example, the southern coast of Western Australia and the Persian Gulf. Tide heights vary significantly; for example, on the Mediterranean coast the tides are almost unnoticeable, whereas at the head of the Bay of Fundy a tidal range of over 12 m has been reported, which is one of the largest tidal ranges in the world (Greenberg, 1982).

2.1.1 Tidal prediction

For prediction of tidal heights at a particular location, the rise and fall of the water needs to be recorded as a function of time. The observed tide-height consists of the sum of a number of simple harmonic or partial tides of different periods, phases and amplitudes. The period of each of the partial tides corresponds to the period of the relative astronomical motions between the earth, the sun and the moon. These constituents are usually classified into three categories; with periods of approximately a half day (semi-diurnal), one day (diurnal) and longer. However, the observed tide-height must be analyze, to obtain its simple harmonic constituents, which may then be used for predicting future tides. The usual and most useful method, which resolves the observed tide into its simple harmonic constituents, is the harmonic method. Each constituent can be represented by a sinusoidal function. The amplitude and phase describes the contribution of the constituent to the total tide. For any future time the predicted tidal height can be obtained by adding all the constituents for that place.

The basic equation of tidal heights (see Pugh, 1987, pp.19 and 112) is

$$\zeta(t) = \sum_{j=1}^{k} f_j a_j \cos(\omega_j t + V_{oj} + \mu_j - \gamma_j) \tag{2.1}$$

where

a_j, γ_j	are the amplitude and phase for constituent j, respectively,
ω_j	is the angular frequency of the constituent,
f_j, μ_j	are the correction factors for the amplitude and phase, respectively, and
V_{oj}	is the phase of the constituent j at Greenwich at the start of the epoch.

In this formula, the k major astronomical constituents are used.

The four major constituents are O_1, K_1, M_2 and S_2. Table 2.1 (Pond and Pickard, 1993) lists the important constituents, and gives the Darwinian symbols and period in solar hours.

Species and name	Symbol	Period (solar hours)
Semi-diurnal:		
Principal lunar	M_2	12.42
Principal solar	S_2	12.00
Larger lunar elliptic	N_2	12.66
Luni-solar semi-diurnal	K_2	11.97
Diurnal:		
Luni-solar diurnal	K_1	23.93
Principal lunar diurnal	O_1	25.82
Principal solar diurnal	P_1	24.07
Larger lunar elliptic	Q_1	26.87
Long period:		
Lunar fortnightly	M_f	327.9
Lunar monthly	M_m	661.3
Solar semi-annual	S_{sa}	4383

Table 2.1: *Showing the characteristics of the principal tide constituents. (Source: Pond and Pickard ,1993, p.260)*

2.2 Tidal dynamics in shallow seas

The shape and configuration of coastal basins influence the tidal motion which occurs in them. As the tide moves in the deep ocean a series of waves is produced. These waves enter a partially enclosed basin, like a gulf, at its mouth and propagate

through the basin. As a consequence, the water level rises and falls as the water enters or leaves.

The most common type of tide is the *semi-diurnal*, in which two high waters and two low waters occur each day, Figure 1 (b,c). The times of occurrence of high or low water are not the same each day; they occur with about 50 minutes delay from one day to the next. Another type of tide is the *diurnal tide*, in which there is one high water and one low water in each lunar day (24.8 h), Figure 1 (a). The third type of tide is the *mixed tide* which is a combination of the diurnal and semi-diurnal tides; essentially, they appear as semi-diurnal tides in which successive high waters have different heights, and consecutive low waters have different depths as in Figure 1 (c). For these reasons, mixed tides are sometimes called *semi-diurnal unequal tides.* It should be pointed out that the magnitude of each type depends on the topography of the basin and the location of the region with respect to the earth's surface.

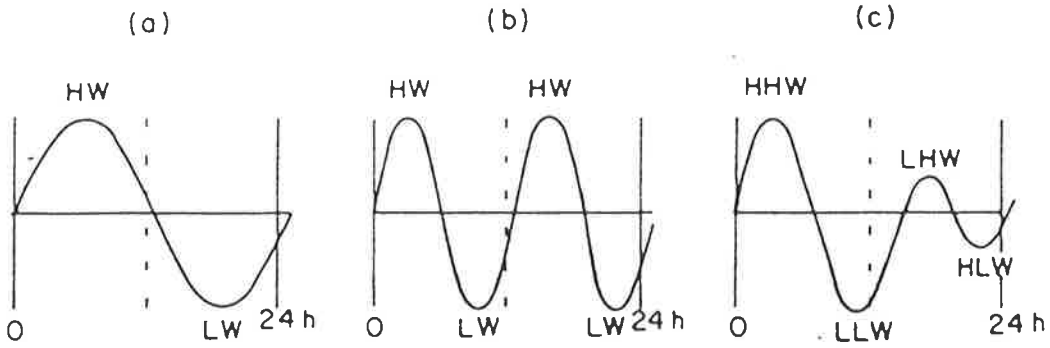

Figure 2.1: *Showing: (a) diurnal, (b) semi-diurnal, (c) semi-diurnal unequal tides* HW = *high water*, LW = *low water*, HHW = *higher high water*, LLW = *lower low water*, LHW = *lower high water*, HLW = higher low water. *(Source: Pond and Pickard, 1993, p.266)*

2.3 Forces

Dynamical oceanography is concerned with the forces acting on the ocean waters and investigates the resultant motions. The important forces are:

- **Gravity:** In Section 2.1 the gravitational effects on the production of tides have been described. This is the main force exerted on a body of water.

- **Wind stress:** This force is generated by the wind over the surface of the water.
- **Atmospheric pressure:** In some cases the effect of atmospheric pressure can be ignored because it has a negligible effect, whereas in some other cases, like storm-surge predictions, it is one of the main parameters.
- **Coriolis force:** This occurs as a result of the rotation of the earth around its axis and gives clockwise rotation to flows in large water bodies in the Northern Hemisphere and anti-clockwise rotation in the Southern Hemisphere.
- **Bottom friction:** This frictional force has the effect of retarding the flow.
- **Viscosity:** Viscosity is basically due to adhesion and molecular mobility of a fluid. It opposes the motion of the fluid.

2.4 Depth-averaged Cartesian tidal equations

The depth-averaged partial differential equations for tidal flow in shallow water can be obtained by integrating the three-dimensional equations over the water depth, from the sea bottom to the sea surface. These equations are based on the general hydrodynamic continuity and momentum equations (Kowalik and Murty, 1993, and Weiyan, 1992). They are presented in this section, along with the physical meaning of each term.

The equations of motion used in depth-averaged hydrodynamic models are obtained from the two fundamental laws of physics:

(1) Mass conservation law

In a control volume V with closed surface S of a fluid, if mass is not generated or destroyed in V, then mass is conserved. In other words:
The time rate of increase of total mass inside the control volume V = The net amount of mass flowing out of the control volume V across S. For an incompressible fluid this law mathematically can be written as

$$\nabla \cdot \boldsymbol{q} = 0 \tag{2.2}$$

where

∇ is the gradient operator,
$\boldsymbol{q}$ is the vector velocity field (ms^{-1}).

(2) Momentum conservation law

The conservation of momentum law is based on Newton's second law, which states

that: if a resultant force $\mathbf{F}$ acts on a body of mass m then, *the rate of increase of linear momentum is equal to the force* $\mathbf{F}$. For a viscous incompressible fluid the mathematical equation representing this law is

$$\frac{D\boldsymbol{q}}{Dt} = -\frac{1}{\rho}\boldsymbol{\nabla} p + \nu\nabla^2\boldsymbol{q} + \boldsymbol{F} \tag{2.3}$$

where

- ρ is the fluid density (kgm^{-3}),
- t is time (s),
- ∇^2 is the Laplacian operator,
- p is the pressure (Nm^{-2}),
- ν is the coefficient of viscosity (ms^{-2}).

2.4.1 The continuity equation

The equation that results from applying the mass conservation law to tidal motions is often called the continuity equation. The depth-averaged form of this equation (Bills, 1991, p.15) is:

$$\frac{\partial\zeta}{\partial t} + \frac{\partial(Hu)}{\partial x} + \frac{\partial(Hv)}{\partial y} = 0. \tag{2.4}$$

where

- t is the time (s),
- x, y are the horizontal Cartesian spatial coordinates (m),
- ζ is the elevation of the sea surface above mean sea level (m),
- u, v are components of vertically averaged velocity in the x and y directions, respectively (ms^{-1}),
- H is the total depth $(h + \zeta)$, where h is the mean sea depth (m).

2.4.2 Physical meaning of each term

The terms in the continuity equation have the following meanings:

(a) $\frac{\partial\zeta}{\partial t}$ is the rate of change of the surface elevation,

(b) $\frac{\partial(Hu)}{\partial x}$ is the gradient of x component of volumetric flow between surface and seafloor,

(c) $\frac{\partial(Hv)}{\partial y}$ is the gradient of y component of above.

2.4.3 The momentum equation

For non-stratified well mixed coastal flows involving tides, winds and atmospheric the depth-averaged momentum equation along the x-direction (Bills, 1991, p.15) is:

$$\begin{aligned}\frac{\partial u}{\partial t} &+ u\frac{\partial u}{\partial x} + v\frac{\partial u}{\partial y} - fv = -g\frac{\partial \zeta}{\partial x} - \frac{1}{\rho}\frac{\partial p_a}{\partial x} \\ &+ N_x\frac{\partial^2 u}{\partial x^2} + N_y\frac{\partial^2 u}{\partial y^2} + \frac{\rho_a}{\rho H}c_{10}u_{10}\sqrt{(u_{10})^2 + (v_{10})^2} - C_b\frac{1}{H}u\sqrt{u^2+v^2},\end{aligned} \tag{2.5}$$

and along the y-direction (ibid., p.15) is:

$$\begin{aligned}\frac{\partial v}{\partial t} &+ u\frac{\partial v}{\partial x} + v\frac{\partial v}{\partial y} + fu = -g\frac{\partial \zeta}{\partial y} - \frac{1}{\rho}\frac{\partial p_a}{\partial y} \\ &+ N_x\frac{\partial^2 v}{\partial x^2} + N_y\frac{\partial^2 v}{\partial y^2} + \frac{\rho_a}{\rho H}c_{10}v_{10}\sqrt{(u_{10})^2 + (v_{10})^2} - C_b\frac{1}{H}v\sqrt{u^2+v^2}.\end{aligned} \tag{2.6}$$

The symbols used in these equations are:

t, x,y, ζ, H,u, v	have the same meaning as in the continuity equation,
f	is the Coriolis parameter, and equals $2\Omega\sin\phi$ where Ω is the earth's angular velocity, (s^{-1}), and ϕ is north latitude (positive northward),
g	is the acceleration due to gravity (ms^{-2}),
ρ	is the density of sea water, assumed uniform $(= 1027\,kgm^{-3})$,
p_a	is the atmospheric pressure (Nm^{-2}),
N_x, N_y	are the eddy viscosity coefficients in the x-direction and y-direction, respectively (ms^{-2})
ρ_a	is the density of air, assumed uniform $(= 1.225\,kgm^{-3})$,
c_{10}	is a dimensionless drag coefficient which depends on the wind speed according to an empirical formula (Bills, 1991, p.13),
u_{10}, v_{10}	are the vertically averaged air velocities at a distance of $10\,m$ above the sea surface (ms^{-1}), and
C_b	is the dimensionless coefficient of quadratic friction.

2.4.4 Physical meaning of each term

The physical meaning of each term in the x-momentum equation is described below; the terms in the y-momentum equation are similar.

(1) $\frac{\partial u}{\partial t}$	the time rate of change of x component of velocity at a point, also called the local variation of momentum with time,
(2) $u\frac{\partial u}{\partial x} + v\frac{\partial u}{\partial y}$	the advective terms. The terms are nonlinear and are sometimes called spatial acceleration terms,
(3) fv	the Coriolis term, a function of the rotation of the earth,
(4) $g\frac{\partial \zeta}{\partial x}$	the gravity term, which involves the force due to the gradient of the surface elevation in the x-direction,
(5) $\frac{1}{\rho}\frac{\partial p_a}{\partial x}$	the atmospheric pressure gradient, in the x-direction,
(6) $N_x\frac{\partial^2 u}{\partial x^2} + N_y\frac{\partial^2 u}{\partial y^2}$	horizontal eddy viscosity terms,
(7) $\frac{\rho_a}{\rho H}c_{10}u_{10}\sqrt{(u_{10})^2 + (v_{10})^2}$	the x component of wind stress, acting on the surface of the sea,
(8) $C_b\frac{1}{H}u\sqrt{u^2+v^2}$	the x component of friction, acting on the bottom surface.

2.4.5 Boundary and initial conditions

The solution of the partial differential equations (2.7)-(2.9) requires the definition of boundary conditions, one condition per highest degree of derivative; for example, a first order derivative in time requires one initial condition; a second order derivative in space needs two boundary conditions.

Assumptions

1. When solving the continuity and momentum equations in coastal regions, two types of boundary conditions usually appear:
   (a) If the entire **coastal boundary** consists of a shoreline with no river inflows, velocities normal to the boundary are set at zero; in other words, it is assumed that the model coastline is impermeable so there can be no flow through the boundaries.
   (b) If the boundary is an interface between two water bodies, it is called an **open boundary**; the water level elevation ζ is defined at all points on the open boundary.

2. A no-slip condition is applied at the bottom of the sea.

3. The total depth is initially set to be the depth below mean sea level and the sea is considered stationary.

2.5 Depth-averaged spherical tidal equations

When fluid motion is considered over a sufficiently large region, the earth's curvature is important and should be taken into account. In this case, the equations of continuity and momentum should be written in spherical polar coordinates. The spherical polar coordinates, which will be referred to as **spherical coordinates** for simplicity, are λ (latitude) and ϕ (longitude) and the radial coordinate, which has direction opposite that of gravity.

2.6 Equations of continuity and momentum

The differential equations which describe depth-averaged tidal motion are presented below. These equations have been derived from the full three-dimensional spherical tidal equations (Semtner, 1986, p.188) and are the same as those used by Matthews (1995, pp.37-39).

Continuity equation

$$\frac{\partial \zeta}{\partial t} + \frac{1}{R\cos\phi}\frac{\partial (Hu)}{\partial \lambda} + \frac{1}{R\cos\phi}\frac{\partial (Hv\cos\phi)}{\partial \phi} = 0, \tag{2.7}$$

Latitudinal momentum equation

$$\begin{aligned}
\frac{\partial u}{\partial t} &+ \frac{u}{R\cos\phi}\frac{\partial u}{\partial \lambda} + \frac{v}{R}\frac{\partial u}{\partial \phi} - \frac{uv\tan\phi}{R} - 2v\Omega\sin\phi = \\
&- \frac{g}{R\cos\phi}\frac{\partial \zeta}{\partial \lambda} - \frac{1}{\rho R\cos\phi}\frac{\partial p_a}{\partial \lambda} + \frac{a_h}{R^2\cos^2\phi}\frac{\partial^2 u}{\partial \lambda^2} + \frac{a_h}{R^2\cos\phi}\frac{\partial}{\partial \phi}(\cos\phi\frac{\partial u}{\partial \phi}) \\
&+ \frac{(1-\tan^2\phi)u}{R^2} - \frac{2\tan\phi}{R^2\cos\phi}\frac{\partial v}{\partial \lambda} \\
&+ \frac{\rho_a}{\rho H}c_{10}u_{10}\sqrt{(u_{10})^2+(v_{10})^2} - \frac{C_b}{H}u\sqrt{u^2+v^2},
\end{aligned} \tag{2.8}$$

Longitudinal momentum equation

$$\begin{aligned}
\frac{\partial v}{\partial t} &+ \frac{u}{R\cos\phi}\frac{\partial v}{\partial \lambda} + \frac{v}{R}\frac{\partial v}{\partial \phi} + \frac{u^2\tan\phi}{R} + 2u\Omega\sin\phi = \\
&- \frac{g}{R}\frac{\partial \zeta}{\partial \phi} - \frac{1}{\rho R}\frac{\partial p_a}{\partial \phi} + \frac{a_h}{R^2\cos^2\phi}\frac{\partial^2 v}{\partial \lambda^2} + \frac{a_h}{R^2\cos\phi}\frac{\partial}{\partial \phi}(\cos\phi\frac{\partial v}{\partial \phi}) \\
&+ \frac{(1-\tan^2\phi)v}{R^2} + \frac{2\tan\phi}{R^2\cos\phi}\frac{\partial u}{\partial \lambda} \\
&+ \frac{\rho_a}{\rho H}c_{10}v_{10}\sqrt{(u_{10})^2+(v_{10})^2} - \frac{C_b}{H}v\sqrt{u^2+v^2},
\end{aligned} \tag{2.9}$$

where

λ, ϕ are longitude (positive eastward) and latitude (positive northward), respectively (deg),

R is the radius of the Earth, assumed uniform ($= 6.37\times10^6\ m$),

a_h is the coefficient of horizontal eddy viscosity (ms^{-2}).

The relationship between a_h, N_x and N_y is discussed in detail below.

2.6.1 Viscosity coefficients

The horizontal eddy viscosity coefficients in the x-direction, N_x, and in the y-direction, N_y, are formulated as in Greenberg (1983), namely

$$N_x = \frac{a}{2}H\Delta x \quad and \quad N_y = \frac{a}{2}H\Delta y \tag{2.10}$$

where Δx and Δy are the element sizes (m) and a is the depth-averaged reduced horizontal eddy viscosity coefficient (s^{-1}). The formula that Greenberg (1983) provides for eddy viscosity coefficients, is a simplification of Schwiderski's (1980a) general formula in spherical coordinates. This formula has also been used by Bills (1991, p.164) and Matthews (1995, p.35).

In this thesis, the horizontal eddy viscosity coefficient in spherical coordinates is denoted as a_h. It is formulated as

$$(a_h)_\lambda = \frac{a}{2}L_\lambda H(1+\mu\cos\phi), \quad latitudinal \tag{2.11}$$

and

$$(a_h)_\phi = \frac{a}{2}L_\phi H(1+\mu\cos\phi), \quad longitudinal \tag{2.12}$$

where $L_\lambda = R\Delta\lambda$ and $L_\phi = R\Delta\phi$, $\Delta\lambda$ and $\Delta\phi$ are the element sizes (rad), a is the reduced eddy viscosity coefficient, and μ is a longitudinal grading parameter. This parameter varies by latitude; Schwiderski(1980, p.184) uses a value of $\mu = 1$ for $\phi = 60°$ to $\phi = -60°$, which includes the region covered by the Persian Gulf.

Chapter 3

Finite Difference Techniques

3.1 Introduction

The finite difference technique is the most commonly used method in depth-averaged numerical tidal models, for example, Heaps (1969, 1973), Blumberg and Mellor (1977), Leendertse (1967, 1970), Bills (1992), Bills and Noye (1984, 1986, 1987, 1992) and Casulli and Cheng (1992).

The basic idea of the finite difference scheme is to replace derivatives by finite difference approximations. In this section the most commonly used **forward**, **centred** and **backward** difference approximations for derivatives of a function of one variable are described. These types of approximations are used in discrete formulation of the-depth-averaged tidal equations in Section 3.3.2.

Assume u is a function of one variable x, and suppose its derivatives are single-valued, and continuous functions of x. Using a Taylor's series expansion for $u(x_i + \Delta x)$, about the point x_i, where $x_i = x_0 + i\Delta x$, $i = 1, 2, 3, \cdots$, gives:

$$u(x_i + \Delta x) = u(x_i) + (\Delta x)(\frac{du}{dx})_{x_i} + \frac{1}{2!}(\Delta x)^2(\frac{d^2u}{dx^2})_{x_i} + \frac{1}{3!}(\Delta x)^3(\frac{d^3u}{dx^3})_{x_i} + \cdots, \quad (3.1)$$

If $u(x_i)$ is denoted u_i then $u(x_i + \Delta x) = u_{i+1}$, where Δx is the grid spacing in the x-direction. Using this notation in Equation (3.1) leads to

$$u_{i+1} = u_i + (\Delta x)(\frac{du}{dx})_i + \frac{1}{2!}(\Delta x)^2(\frac{d^2u}{dx^2})_i + \frac{1}{3!}(\Delta x)^3(\frac{d^3u}{dx^3})_i + \cdots \quad (3.2)$$

Also consider the similar expansion for u_{i-1}, that is,

$$u_{i-1} = u_i - (\Delta x)(\frac{du}{dx})_i + \frac{1}{2!}(\Delta x)^2(\frac{d^2u}{dx^2})_i - \frac{1}{3!}(\Delta x)^3(\frac{d^3u}{dx^3})_i + \cdots \quad (3.3)$$

Using the above equations the required approximations for the first derivative can be found as follows:

(1) **Forward difference**

Rearranging Equation (3.2) gives

$$(\frac{du}{dx})_i = \frac{u_{i+1} - u_i}{\Delta x} - \frac{1}{2!}(\Delta x)(\frac{d^2u}{dx^2})_i - \cdots, \tag{3.4}$$

and from this equation the most commonly used **forward difference** approximation is found, namely

$$(\frac{du}{dx})_i \simeq \frac{u_{i+1} - u_i}{\Delta x}. \tag{3.5}$$

The remaining terms on the right hand side of Equation (3.4) represent the truncation error. Using the usual mathematical notation for truncation error, that is, $O(\Delta x)$, in Equation (3.4) leads to

$$(\frac{du}{dx})_i = \frac{u_{i+1} - u_i}{\Delta x} + O(\Delta x). \tag{3.6}$$

The term $(\Delta x)(d^2u/dx^2)_i/(2!)$ in Equation (3.4), which is proportional to Δx, is the largest term in the truncation error. That is, the error in the approximation depends on Δx to the first power, so this **forward difference** approximation for $(du/dx)_i$ is said to be **first-order** convergent.

(2) **Centred difference**

If Equation (3.3) is subtracted from (3.2) and the result rearranged,

$$(\frac{du}{dx})_i = \frac{u_{i+1} - u_{i-1}}{2\Delta x} + O(\Delta x)^2 \tag{3.7}$$

is obtained. This yields the commonly used **centred difference** approximation

$$(\frac{du}{dx})_i \simeq \frac{u_{i+1} - u_{i-1}}{2\Delta x}. \tag{3.8}$$

Equation (3.7) shows that the error in the approximation (3.8) depends on Δx to the second power, so this **centred difference** approximation for $(du/dx)_i$ is **second-order** convergent.

(3) **Backward difference**

Rearranging Equation (3.3) and using the notation for the truncation error yields the expression

$$(\frac{du}{dx})_i = \frac{u_i - u_{i-1}}{\Delta x} + O(\Delta x). \tag{3.9}$$

This equation gives the most commonly used **backward difference** approximation

$$(\frac{du}{dx})_i \simeq \frac{u_i - u_{i-1}}{\Delta x}. \tag{3.10}$$

As Equation (3.9) suggests, the error in this approximation depends on Δx to the first power, so this **backward difference** approximation for $(du/dx)_i$ is **first-order** convergent.

The commonly used approximation for the second derivative is one which involves central-differencing, and is obtained as follows:
Adding equations (3.2) and (3.3), rearranging and using the notation for truncation error to obtain the expression

$$(\frac{d^2u}{dx^2})_i = \frac{u_{i+1} - 2u_i + u_{i-1}}{(\Delta x)^2} + O(\Delta x)^2, \tag{3.11}$$

so this **centred difference** approximation to the second derivative is

$$(\frac{d^2u}{dx^2})_i \simeq \frac{u_{i+1} - 2u_i + u_{i-1}}{(\Delta x)^2}. \tag{3.12}$$

3.1.1 Explicit and implicit schemes

A finite difference scheme which expresses a single unknown value at the new time level directly in terms of known values at the present time level, is called an **explicit** scheme. A scheme which calculates the unknown values at the new time level by solving a set of simultaneous equations is known as a **implicit** scheme. In the latter scheme the values at a new time level depend also on the unknown values at the new time level. The former method is computationally simple, and needs less storage than the latter. However, the explicit technique must satisfy a stability condition, whereas the implicit technique may not. Implicit methods are generally very computationally stable and therefore may use large time steps. However, it must be kept in mind that making the time steps very large may cause the loss of accuracy of the approximate solution.

3.1.2 Arakawa C spatial grid

The finite difference representation of horizontal space derivatives depends on the distribution of the dependent variables on a grid. Various types of grids have been developed and used by different authors for different purposes. Arakawa and Lamb (1977) investigate four different spatially staggered grids which are used to difference the shallow water equations. They consider the space discretisation error for different distributions of the dependent variables on a grid, and suggest the use of the layout shown in Figure 3.1. This layout is known as the "Arakawa C" grid or the "Richardson lattice". It has been used by many authors, for example, Leendertse (1967, 1970), Flather and Heaps (1975), Blumberg (1977), Davies and Flather (1977, 1978), Greenberg (1981), Stevens and Noye (1984), Bills and Noye (1984, 1987, 1992), Noye and Bills (1990,1992), and Bills (1992). Some of the advantages of using the "Arakawa C" grid are:

- It allows spatial derivatives to be conveniently approximated in second-order central difference form.
- Land boundaries can be simply represented, by means of straight-line segments parallel to the coordinate axes.

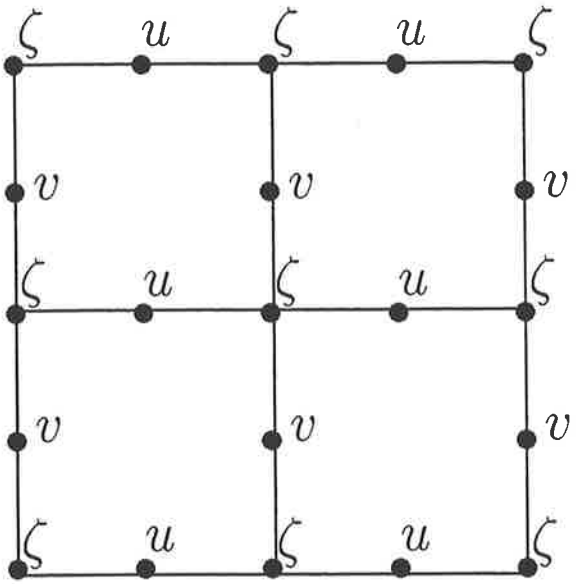

Figure 3.1: *The Arakawa C grid or the Richardson lattice.*

3.1.3 The temporal grid

In the following a grid staggered in time as well as in space is used (see Figure 3.2). The general finite difference scheme used is three-level in time (see Noye and Bills, 1990, 1992, and Bills, 1992), that is, each time step involves three time levels: the entry level, the half time step level and the full time step level (see, Bills, 1992, p.22). Figure 3.2 shows the time levels included in a computational time step. As this figure shows, in each time step one calculation of ζ is carried out for each set of calculations of u and v. This calculation uses $\zeta^{n-1/2}$, u^n and v^n to provide a time centred $\zeta^{n+1/2}$. To obtain ζ^{n+1} the values ζ^n, u^{n+1} and v^{n+1} are used.

3.1.4 The finite difference code

A number of finite difference codes exist for solving the depth-averaged tidal equations, for example:

1. In Cartesian coordinates: Blumberg and Mellor (1980), Lardner et al. (1982), Murty and El-Sabh (1984), Casulli (1990), Bills (1992), Casulli and Cheng (1992), and the Proudman Oceanographic Laboratory model (Proctor et al. 1992)

2. In spherical coordinates: Davies and Flather (1977, 1978), Evans-Roberts (1979), Chilicka et al. (1983), Mitchell and Noye (1983), Verboom et al. (1992).

The finite difference code described in Bills (1992) has been chosen because it has been thoroughly tested and has been used for some years by the tidal modelling group of the Department of Applied Mathematics at the University of Adelaide.

The programs, written in Fortran 77, have been converted, by the author, from the original Cartesian coordinates to spherical coordinates. The code has also been modified to produce the nested spherical model of Chapter 6. The basic idea of the code along with some necessary definitions will be given here, to allow an explanation of the development of the nested spherical model later. The original idea and definitions come from Bills (1992, pp.17-70).

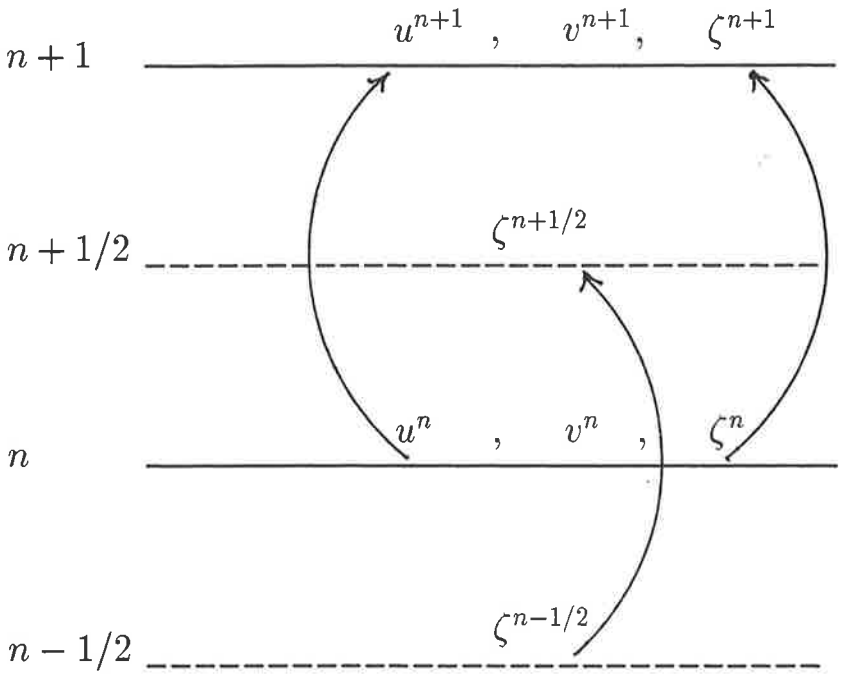

Figure 3.2: *The time levels in each time step.*

3.2 Discrete formulation in Cartesian coordinates

In this section, the governing equations are discretised on the "Arakawa C" space grid and the time-staggered grid.

The grid element, the basic unit of the grid, consists of three grid points, which are the free surface elevation ζ, and horizontal velocity components u and v, as shown in Figure 3.3.

This figure shows that the spacing between different grid points in the x-direction and y-direction are Δx and Δy respectively, and between similar grid points it is $2\Delta x$ and $2\Delta y$. Therefore the area of the element is $4\Delta x \Delta y$.

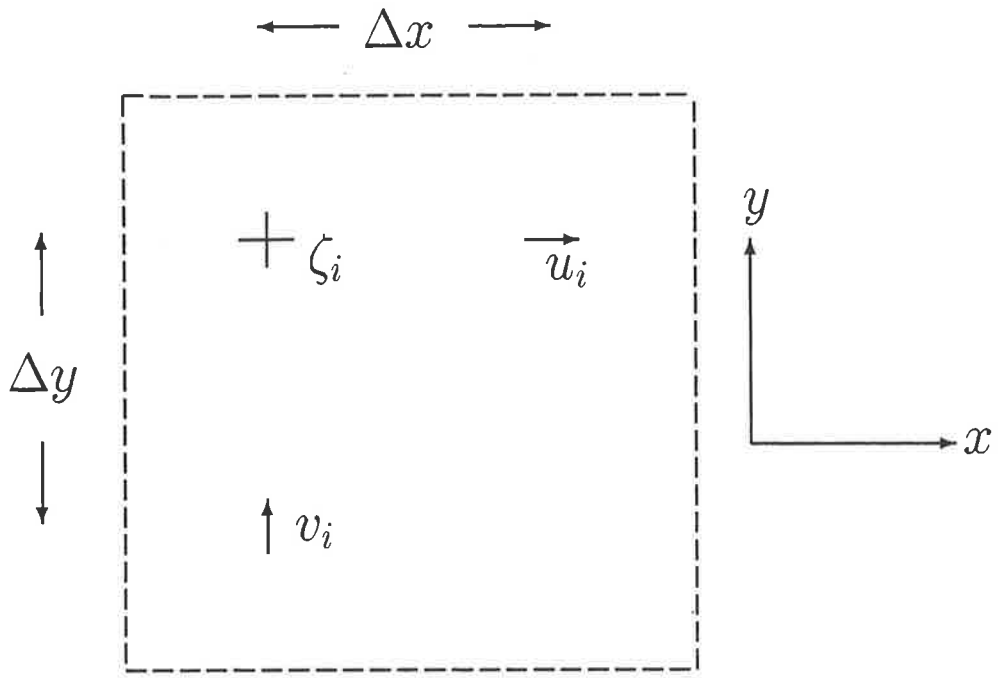

Figure 3.3: *The ith grid element showing locations of grid points ζ_i, u_i and v_i. Δx and Δy are the grid step size. The dashed lines show the boundaries of the element.*

Figure 3.4 shows the numbering system of the ith computational element and its eight neighbours, used in the code. The elements above and below the ith are indexed as i_1th and i_2th elements, respectively. The immediate elements to the right and left side of the ith, are specified $i+1$ and $i-1$, respectively. If the model needs to refer to the next neighbours, other than the first eight neighbours of the ith element, this indexing system can be generalized to a 25-element block by using indices i_{11}, i_{22}, etc. The i_{11}th element is located above the i_1th element and i_{22}th is below the i_2th element, and so on. This 25-element indexing system is used in Chapter 6. It should be noted that the calculations in each time step are carried out by passing from one element of each model row to the next from left to right, and proceeds down the rows from top to bottom.

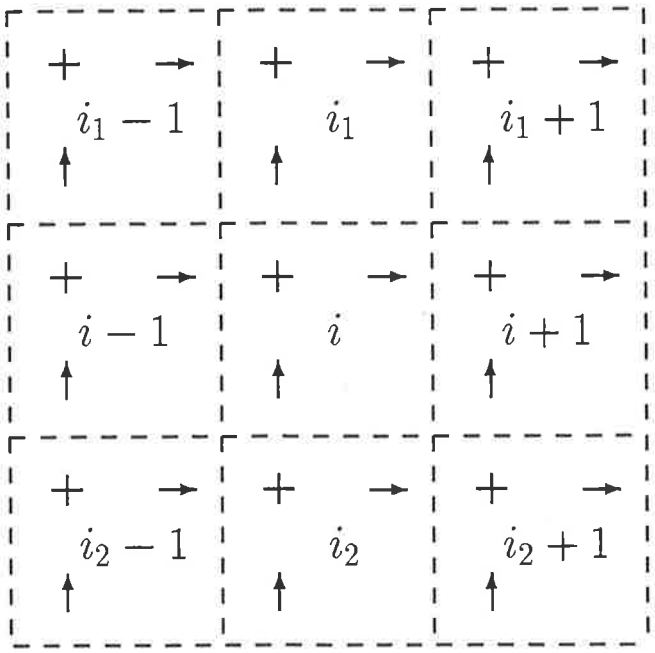

Figure 3.4: *The ith computational element and its eight immediate neighbours, showing the indexing system used to lable the elements. The dashed lines represent element boundaries (see Bills, 1992, p.20)*

3.2.1 Discrete formulation of the governing equations

The finite difference equations which approximate the depth-averaged tidal equations in Cartesian coordinates, that is, equations (2.4), (2.5) and (2.6), are presented in this section. These equations are similar to those used by Bills (1992, pp.24-70) for three-dimensional tidal equations, but the complete form of the approximations to the depth-averaged equations is given in this thesis.

The depth-averaged continuity equation (2.4) is written as

$$\frac{\partial \zeta}{\partial t} = -\frac{\partial (Hu)}{\partial x} - \frac{\partial (Hv)}{\partial y}. \tag{3.13}$$

Consider the finite difference expression of the above equation; centring it about the time level n, in discrete time, and the ζ grid point, in discrete (horizontal plane) space (see Figure 3.3), gives

$$\left\{\frac{\partial \zeta}{\partial t}\right\}_{\zeta_i}^{n} = -\left\{\frac{\partial (Hu)}{\partial x}\right\}_{\zeta_i}^{n} - \left\{\frac{\partial (Hv)}{\partial y}\right\}_{\zeta_i}^{n}. \tag{3.14}$$

The difference approximations of the terms in this equation are:
(i)

$$\left\{\frac{\partial \zeta}{\partial t}\right\}_{\zeta_i}^{n} \simeq \frac{1}{\Delta t}\left({\zeta_i}^{n+1/2} - {\zeta_i}^{n-1/2}\right), \tag{3.15}$$

(ii)

$$\left\{\frac{\partial (Hu)}{\partial x}\right\}_{\zeta_i}^{n} \simeq \frac{1}{4\Delta x}\left[\left(H_i^n + H_{i+1}^n\right) u_i^n - \left(H_{i-1}^n + H_i^n\right) u_{i-1}^n\right], \tag{3.16}$$

(iii)

$$\left\{\frac{\partial (Hv)}{\partial y}\right\}_{\zeta_i}^{n} \simeq \frac{1}{4\Delta y}\left[\left(H_i^n + H_{i1}^n\right) v_{i1}^n - \left(H_{i2}^n + H_i^n\right) v_i^n\right]. \tag{3.17}$$

Expression (3.15) is second order convergent, because it is a centred difference in time, and (3.16) and (3.17) are second order convergent in space, because the difference $u_i^n - u_{i-1}^n$ is centred about ζ_i.

By substituting equations (3.15), (3.16) and (3.17) into equation (3.14), we obtain the explicit expression for the sea surface elevation at time level $(n + 1/2)$, namely

$$\begin{aligned} {\zeta_i}^{n+1/2} = {\zeta_i}^{n-1/2} &- \frac{\Delta t}{4\Delta x}\left[\left(H_i^n + H_{i+1}^n\right) u_i^n - \left(H_{i-1}^n + H_i^n\right) u_{i-1}^n\right] \\ &- \frac{\Delta t}{4\Delta y}\left[\left(H_i^n + H_{i_1}^n\right) v_{i_1}^n - \left(H_{i2}^n + H_i^n\right) v_i^n\right], \end{aligned} \tag{3.18}$$

which is second order convergent in space and time.

The total depth $H = \zeta + h$, at time $(n + 1/2)\Delta t$, is approximated as

$$H_i^{n+1/2} = {\zeta_i}^{n+1/2} + h_i, \tag{3.19}$$

where H_i is computed at the same position in the horizontal plane as ζ_i.

The finite difference expression for the x-momentum equation (2.5), using centred differences about u_i in space and about the $(n + 1/2)$ level in time, is based on the equation

$$\begin{aligned} \left\{\frac{\partial u}{\partial t}\right\}_{u_i}^{n+1/2} &+ \left\{u\frac{\partial u}{\partial x}\right\}_{u_i}^{n+1/2} + \left\{v\frac{\partial u}{\partial y}\right\}_{u_i}^{n+1/2} - \{fv\}_{u_i}^{n} \\ &= -g\left\{\frac{\partial \zeta}{\partial x}\right\}_{u_i}^{n+1/2} + \left\{N_x\frac{\partial^2 u}{\partial x^2}\right\}_{u_i}^{n+1/2} + \left\{N_y\frac{\partial^2 u}{\partial y^2}\right\}_{u_i}^{n+1/2} \\ &- C_b\left\{\frac{1}{H}u\sqrt{u^2+v^2}\right\}_{u_i}^{n+1/2}. \end{aligned} \tag{3.20}$$

Note that the wind stress and the atmospheric pressure are ignored.

The terms of this are differenced as follows:

(i)

$$\left\{\frac{\partial u}{\partial t}\right\}_{u_i}^{n+1/2} \simeq \frac{1}{\Delta t}\left(u_i^{n+1} - u_i^n\right), \tag{3.21}$$

which is second order in time, because this is a centred-difference in time.
(ii)

$$\left\{u\frac{\partial u}{\partial x}\right\}_{u_i}^{n+1/2} \simeq {u_i}^{n+1}\left\{\frac{\partial u}{\partial x}\right\}_{u_i}^{n} \simeq \frac{1}{4\Delta x}u_i^{n+1}\left(u_{i+1}^n - u_{i-1}^n\right), \tag{3.22}$$

which is approximately second order in space.
(iii)

$$\left\{v\frac{\partial u}{\partial y}\right\}_{u_i}^{n+1/2} \simeq \{v\}_{u_i}^n\left\{\frac{\partial u}{\partial y}\right\}_{u_i}^{n} \simeq \frac{1}{16\Delta y}\left(v_{i_1}^n + v_{i_1+1}^n + v_i^n + v_{i+1}^n\right)\left(u_{i_1}^n - u_{i_2}^n\right), \tag{3.23}$$

which is quasi second order in space.
(iv)

$$\{fv\}_{u_i}^n \simeq \frac{1}{8}\left(f_i + f_{i+1}\right)\left(v_{i_1}^n + v_{i_1+1}^n + v_i^n + v_{i+1}^n\right), \tag{3.24}$$

in which the Coriolis coefficient f_i is given by $f_i = 2\Omega\sin\phi_i$.
(v)

$$\left\{\frac{\partial \zeta}{\partial x}\right\}_{u_i}^{n+1/2} \simeq \frac{1}{2\Delta x}\left({\zeta_{i+1}}^{n+1/2} - {\zeta_i}^{n+1/2}\right), \tag{3.25}$$

which has a second order spatial discretisation error.

The depth-averaged horizontal eddy viscosity coefficients are given in equation (2.10). They are approximated as follows:
At the u_i grid point and the $(n+1/2)$ time level

$$\begin{aligned}\{N_x\}_{u_i}^{n+1/2} &= (\frac{a}{2})(2\Delta x)\{H\}_{u_i}^{n+1/2} \\ &\simeq (a)(\Delta x)\frac{\left(H_i^{n+1/2} + H_{i+1}^{n+1/2}\right)}{2},\end{aligned} \tag{3.26}$$

and

$$\begin{aligned}\{N_y\}_{u_i}^{n+1/2} &= (\frac{a}{2})(2\Delta y)\{H\}_{u_i}^{n+1/2} \\ &\simeq (a)(\Delta y)\frac{\left(H_i^{n+1/2} + H_{i+1}^{n+1/2}\right)}{2}.\end{aligned} \tag{3.27}$$

The approximations (3.26) and (3.27) are used in the terms (vi) and (vii), respectively.
(vi)

$$\begin{aligned}\left\{N_x\frac{\partial^2 u}{\partial x^2}\right\}_{u_i}^{n+1/2} &\simeq \{N_x\}_{u_i}^{n+1/2}\left\{\frac{\partial^2 u}{\partial x^2}\right\}_{u_i}^{n} \\ &\simeq \frac{a}{8\Delta x}\left(H_i^{n+1/2} + H_{i+1}^{n+1/2}\right)\left(u_{i+1}^n - 2u_i^n + u_{i-1}^n\right),\end{aligned} \tag{3.28}$$

which is approximately second order in space.
(vii)

$$\left\{N_y \frac{\partial^2 u}{\partial y^2}\right\}_{u_i}^{n+1/2} \simeq \{N_y\}_{u_i}^{n+1/2} \left\{\frac{\partial^2 u}{\partial y^2}\right\}_{u_i}^{n} \simeq \frac{a}{8\Delta y}\left(H_i^{n+1/2} + H_{i+1}^{n+1/2}\right)\left(u_{i_1}^n - 2u_i^n + u_{i_2}^n\right), \tag{3.29}$$

which is approximately second order in space.
(viii)

$$C_b\left\{\frac{1}{H}u\sqrt{u^2+v^2}\right\}_{u_i}^{n+1/2} \simeq \frac{2C_b}{\left(H_i^{n+1/2} + H_{i+1}^{n+1/2}\right)} u_i^{n+1} \times\sqrt{(u_i^n)^2 + \frac{1}{16}\left(v_{i_1}^n + v_{i_1+1}^n + v_i^n + v_{i+1}^n\right)^2}. \tag{3.30}$$

Substituting all the approximations (3.22)–(3.29) into (3.21), gives the corresponding finite difference approximation

$$\begin{aligned}
\frac{1}{\Delta t}\left(u_i^{n+1} - u_i^n\right) &+ \frac{1}{4\Delta x} u_i^{n+1}\left(u_{i+1}^n - u_{i-1}^n\right) \\
&+ \frac{1}{16\Delta y}\left(v_{i_1}^n + v_{i_1+1}^n + v_i^n + v_{i+1}^n\right)\left(u_{i_1}^n - u_{i_2}^n\right) \\
&- \frac{1}{8}(f_i + f_{i+1})\left(v_{i_1}^n + v_{i_1+1}^n + v_i^n + v_{i+1}^n\right) \\
&= -g\frac{1}{\Delta x}\left({\zeta_{i+1}}^{n+1/2} - {\zeta_i}^{n+1/2}\right) \\
&+ \frac{a}{8\Delta x}\left(H_i^{n+1/2} + H_{i+1}^{n+1/2}\right)\left(u_{i+1}^n - 2u_i^n + u_{i-1}^n\right) \\
&+ \frac{a}{8\Delta y}\left(H_i^{n+1/2} + H_{i+1}^{n+1/2}\right)\left(u_{i_1}^n - 2u_i^n + u_{i_2}^n\right) \\
&- \frac{2C_b}{\left(H_i^{n+1/2} + H_{i+1}^{n+1/2}\right)} u_i^{n+1}\sqrt{(u_i^n)^2 + \frac{1}{16}\left(v_{i_1}^n + v_{i_1+1}^n + v_i^n + v_{i+1}^n\right)^2}.
\end{aligned} \tag{3.31}$$

Values of u at the new time level $(n+1)$ are given by making u_i^{n+1} the subject of the formula (3.31), yielding

$$\begin{aligned}
u_i^{n+1} = D_x^{-1}\Bigg[&u_i^n - \frac{\Delta t}{16\Delta y}\left(v_{i-1}^n + v_{i_1+1}^n + v_i^n + v_{i+1}^n\right)\left(u_{i_1}^n - u_{i_2}^n\right) \\
&+ \frac{\Delta t}{8}(f_i + f_{i+1})\left(v_{i_1}^n + v_{i_1+1}^n + v_i^n + v_{i+1}^n\right) - g\frac{\Delta t}{2\Delta x}\left({\zeta_{i+1}}^{n+1/2} - {\zeta_i}^{n+1/2}\right) \\
&+ \frac{a\Delta t}{8\Delta x}\left(H_i^{n+1/2} + H_{i+1}^{n+1/2}\right)\left(u_{i+1}^n - 2u_i^n + u_{i-1}^n\right) \\
&+ \frac{a\Delta t}{8\Delta y}\left(H_i^{n+1/2} + H_{i+1}^{n+1/2}\right)\left(u_{i_1}^n - 2u_i^n + u_{i_2}^n\right)\Bigg],
\end{aligned} \tag{3.32}$$

where

$$D_x = \left[1 + \frac{\Delta t}{4\Delta x}\left(u_{i+1}^n - u_{i-1}^n\right)\right. \tag{3.33}$$
$$\left. + \frac{2C_b\Delta t}{\left(H_i^{n+1/2} + H_{i+1}^{n+1/2}\right)} \sqrt{\left(u_i^n\right)^2 + \frac{1}{16}\left(v_{i_1}^n + v_{i_1+1}^n + v_i^n + v_{i+1}^n\right)^2}\right].$$

This is second order in space, and is approximately second order in time.

At the v_i point and the $(n + 1/2)$ time level, the depth-averaged y-momentum equation (2.9), namely

$$\left\{\frac{\partial v}{\partial t}\right\}_{v_i}^{n+1/2} + \left\{u\frac{\partial v}{\partial x}\right\}_{v_i}^{n+1/2} + \left\{v\frac{\partial v}{\partial y}\right\}_{v_i}^{n+1/2} + \{fu\}_{v_i}^{n+1/2} \tag{3.34}$$
$$= -g\left\{\frac{\partial \zeta}{\partial y}\right\}_{v_i}^{n+1/2} + \left\{N_x\frac{\partial^2 v}{\partial x^2}\right\}_{v_i}^{n+1/2} + \left\{N_y\frac{\partial^2 v}{\partial y^2}\right\}_{v_i}^{n+1/2}$$
$$- C_b\left\{\frac{1}{H}v\sqrt{u^2+v^2}\right\}_{v_i}^{n+1/2}.$$

is differenced in the same way as the x-momentum equation. To make it easier for the other users of this model, the finite difference expression for the y-momentum equation (2.6) given in detail, because indices are different since the list runs in the x-direction and not in the y-direction. The averaging is different so, the values of f are obtained differently, and updated values of u^{n+1} are used in place of u^n.

The approximations for the terms of (3.34) follow:

(i)

$$\left\{\frac{\partial v}{\partial t}\right\}_{v_i}^{n+1/2} \simeq \frac{1}{\Delta t}\left(v_i^{n+1} - v_i^n\right), \tag{3.35}$$

which is second order in time, because this is a centred difference in time.

(ii)

$$\left\{u\frac{\partial v}{\partial x}\right\}_{v_i}^{n+1/2} \simeq v_i{}^{n+1/12}\left\{\frac{\partial v}{\partial x}\right\}_{v_i}^{n} \simeq \frac{1}{16\Delta x}\left(u_i^{n+1} + u_{i-1}^{n+1} + u_{i_2}^{n+1} + u_{i_2-1}^{n+1}\right)\left(v_{i+1}^n - v_{i-1}^n\right), \tag{3.36}$$

which is approximately second order in space. Note that the values of u at the level $(n + 1)$ are now available (the x-momentum equation is solved first).

(iii)

$$\left\{v\frac{\partial v}{\partial y}\right\}_{v_i}^{n+1/2} \simeq v_i^{n+1}\left\{\frac{\partial v}{\partial y}\right\} \simeq \frac{1}{4\Delta y}v_i^{n+1}\left(v_{i_1}^n - v_{i_2}^n\right), \tag{3.37}$$

which is approximately second order in space.

(iv)

$$\{fu\}_{v_i}^{n+1/2} \simeq \frac{1}{8}(f_i + f_{i2})\left(u_i^{n+1} + u_{i-1}^{n+1} + u_{i2}^{n+1} + u_{i2-1}^{n+1}\right). \tag{3.38}$$

Once again the values of u at the level $n+1$ are now available. In this expression $f_i = 2\Omega \sin\phi_i$.

(v)

$$\left\{\frac{\partial \zeta}{\partial y}\right\}_{v_i}^{n+1/2} \simeq \frac{1}{\Delta y}\left({\zeta_i}^{n+1/2} - {\zeta_{i2}}^{n+1/2}\right), \tag{3.39}$$

which has a second order spatial discretisation error.

(vi)

$$\begin{aligned}\left\{N_x \frac{\partial^2 v}{\partial x^2}\right\}_{v_i}^{n+1/2} &\simeq \{N_x\}_{v_i}^{n+1/2}\left\{\frac{\partial^2 v}{\partial x^2}\right\}_{v_i}^{n} \\ &\simeq \frac{a}{8\Delta x}\left(H_i^{n+1/2} + H_{i2}^{n+1/2}\right)\left(v_{i+1}^n - 2v_i^n + v_{i-1}^n\right),\end{aligned} \tag{3.40}$$

which is approximately second order in space.

(vii)

$$\begin{aligned}\left\{N_y \frac{\partial^2 v}{\partial y^2}\right\}_{v_i}^{n+1/2} &\simeq \{N_y\}_{v_i}^{n+1/2}\left\{\frac{\partial^2 v}{\partial y^2}\right\}_{v_i}^{n} \\ &\simeq \frac{a}{8\Delta y}\left(H_i^{n+1/2} + H_i^{n+1/2}\right)\left(v_{i1}^n - 2v_i^n + v_{i2}^n\right),\end{aligned} \tag{3.41}$$

which is approximately second order in space.

(viii)

$$\begin{aligned}C_b\left\{\frac{1}{H} v\sqrt{u^2+v^2}\right\}_{v_i}^{n+1/2} &\simeq \frac{2C_b}{\left(H_i^{n+1/2} + H_{i2}^{n+1/2}\right)} v_i^{n+1} \\ &\times \sqrt{(v_i^n)^2 + \frac{1}{16}\left(u_i^{n+1} + u_{i-1}^{n+1} + u_{i2}^{n+1} + u_{i2-1}^{n+1}\right)^2}.\end{aligned} \tag{3.42}$$

Note that updated values of u^{n+1} are used in (3.42), which is different from the use of v^n in (3.31), used in the x-momentum equation.

Substituting approximations(3.35)–(3.42) into (3.34) yields the approximation

$$\begin{aligned}\frac{1}{\Delta t}\left(v_i^{n+1} - v_i^n\right) &+ \frac{1}{16\Delta x}\left(u_i^{n+1} + u_{i-1}^{n+1} + u_{i2}^n + u_{i2-1}^n\right)\left(v_{i+1}^n - v_{i-1}^n\right) \\ &+ \frac{1}{4\Delta y} v_i^{n+1}\left(v_{i1}^n - v_{i2}^n\right) \\ &- \frac{1}{8}(f_i + f_{i2})\left(u_i^{n+1} + u_{i-1}^{n+1} + u_{i2}^{n+1} + v_{i2-1}^{n+1}\right) \\ &= -g\frac{1}{2\Delta y}\left({\zeta_i}^{n+1/2} - {\zeta_{i2}}^{n+1/2}\right)\end{aligned} \tag{3.43}$$

$$+ \quad \frac{a}{8\Delta y}\left(H_i^{n+1/2}+H_{i2}^{n+1/2}\right)\left(v_{i1}^n-2v_i^n+v_{i2}^n\right)$$
$$+ \quad \frac{a}{8\Delta x}\left(H_i^{n+1/2}+H_{i2}^{n+1/2}\right)\left(v_{i+1}^n-2v_i^n+v_{i-1}^n\right)$$
$$- \quad \frac{2C_b}{\left(H_i^{n+1/2}+H_{i2}^{n+1/2}\right)}v_i^{n+1}\sqrt{(v_i^n)^2+\frac{1}{16}\left(u_i^{n+1}+u_{i-1}^{n+1}+u_{i2}^{n+1}+u_{i2-1}^{n+1}\right)^2}.$$

Values of v at the new time level $(n+1)$ are therefore given by making v_i^{n+1} the subject of the formula (3.43), giving

$$\begin{aligned} v_i^{n+1} &= D_y^{-1}\left[v_i^n-\frac{\Delta t}{16\Delta y}\left(u_i^{n+1}+u_{i-1}^{n+1}+u_{i2}^n+u_{i2-1}^n\right)\left(v_{i+1}^n-v_{i-1}^n\right)\right. \qquad (3.44)\\ &- \frac{\Delta t}{8}\left(f_i+f_{i2}\right)\left(u_i^{n+1}+u_{i-1}^{n+1}+u_{i2}^{n+1}+u_{i2-1}^{n+1}\right)-g\frac{\Delta t}{2\Delta y}\left(\zeta_i{}^{n+1/2}-\zeta_{i2}{}^{n+1/2}\right)\\ &+ \frac{a\Delta t}{8\Delta y}\left(H_i^{n+1/2}+H_{i2}^{n+1/2}\right)\left(v_{i1}^n-2v_i^n+v_{i2}^n\right)\\ &+ \left.\frac{a\Delta t}{8\Delta x}\left(H_i^{n+1/2}+H_{i2}^{n+1/2}\right)\left(v_{i+1}^n-2v_i^n+v_{i-1}^n\right)\right]. \end{aligned}$$

where

$$\begin{aligned} D_y &= \left[1+\frac{\Delta t}{4\Delta y}\left(v_{i1}^n-v_{i2}^n\right)\right. \qquad (3.45)\\ &+ \left.\frac{2C_b\Delta t}{\left(H_i^{n+1/2}+H_{i2}^{n+1/2}\right)}\sqrt{(v_i^n)^2+\frac{1}{16}\left(u_i^{n+1}+u_{i-1}^{n+1}+u_{i2}^{n+1}+u_{i2-1}^{n+1}\right)^2}\right]. \end{aligned}$$

This is second order in space, and is approximately second order in time.

It should be pointed out that in equation (3.18) the value of H^n, which is as the full time level, is required. Values at the full time level are found using

$$\begin{aligned} \zeta_i{}^{n+1} = \zeta_i{}^n &- \frac{\Delta t}{8\Delta x}\left[\left(H_i^{n+1/2}+H_{i+1}^{n+1/2}\right)\left(u_i^{n+1}+u_i^n\right)\right. \qquad (3.46)\\ &- \left.\left(H_{i-1}^{n+1/2}+H_i^{n+1/2}\right)\left(u_{i-1}^{n+1}+u_{i-1}^n\right)\right]\\ &- \frac{\Delta t}{8\Delta y}\left[\left(H_i^{n+1/2}+H_{i_1}^{n+1/2}\right)\left(v_{i_1}^{n+1}+v_{i_1}^n\right)\right.\\ &- \left.\left(H_{i2}^{n+1/2}+H_i^{n+1/2}\right)\left(v_i^{n+1}+v_i^n\right)\right]. \end{aligned}$$

which is second order convergent in space and time.

The total depth $H=\zeta+h$, at time $(n+1)\Delta t$, is approximated as

$$H_i^{n+1}=\zeta_i{}^{n+1}+h_i, \qquad (3.47)$$

Note that, in the above $\zeta_i{}^{n+1/2}$ are calculated for all i, then the pair $u_i{}^{n+1}$, $v_i{}^{n+1}$ are calculated for all i, and finally $\zeta_i{}^{n+1}$ calculated for all i.

3.2.2 Boundary conditions

In finite-difference models the land-water boundaries of any shape are approximated by grid line segments, parallel to the x and y axes. The boundary conditions used for the depth-averaged Cartesian tidal equations are similar to those commonly used in the literature, for example, Flather and Heaps (1975), Greenberg (1983), Noye et al. (1982), and Noye and Bills (1992). These conditions are:

1. Assuming the model coastline is "solid", that is, there is no flow across the coastal boundary, the following condition of impermeability is set:

$$(u, v) \cdot \boldsymbol{n} = 0 \quad \text{on the coastline,} \tag{3.48}$$

   where $\boldsymbol{n}$ is the normal vector to the coastline.
   The coastal line segments pass through the velocity grid points u or v on the staggered grid (see Figure 3.2), therefore

   (i) if the coast is parallel to the x-axis,

$$v = 0 \text{ at } v \text{ grid points;}$$

   (ii) if the coast is parallel to the y-axis,

$$u = 0 \text{ at } u \text{ grid points.}$$

2. The open boundaries of the model pass through elevation points and gridpoints at which the velocity is tangential to these boundaries. At the position b on the open boundary of the model, the sea surface elevation ζ_b is specified for all time by means of ten major tidal constituents, using

$$\zeta_b = \sum_{j=1}^{10} f_j a_j \cos(\omega_j t + V_{oj} + \mu_j - \gamma_j). \tag{3.49}$$

   Parameters in this formula are defined in Section 2.1.1. The ten tidal components provided by Proctor et al. (1992), see Section 4.4.

3. There is some discharge from the Arvandrood/Shatt-al-Arab, at the head of the Persian Gulf (Figure 1.1), into the basin. This may require a boundary condition, other than $v = 0$, but data was not available and the discharge was assumed to be negligible compared with other effects. It should be noted that in recent years, reservoirs and dams in Iraq, Syria, and Turkey have reduced the river discharge (Chao, et al. 1992) so that assuming a zero velocity in this region is considered to be a reasonable approximation.

3.2.3 Initial conditions

The initial conditions for the depth-averaged tidal equations are similar to those used by Flather and Heaps (1975), Greenberg (1983), Noye and Bills (1992), Bills (1991), and Matthews (1995).
A common method for setting up initial conditions is to start from a zero condition. That is, for all points in the interior of the model, set

$$\zeta = u = v = 0 \quad \text{at time } t = 0. \tag{3.50}$$

which means that the fluid is initially at rest. This assumes that the dependence of the solution on the initial conditions will rapidly decay with time (Kowalik and Murty, 1993, p.112).

Using zero initial conditions (sometimes referred to as a "cold" start) produces starting transients. The model must run until appropriate flow conditions are simulated everywhere within the model area, and so a few tide cycles are required in order for the transients to die out. In this way an acceptable "steady" periodic solution, is obtained (see Figure 3.5.)

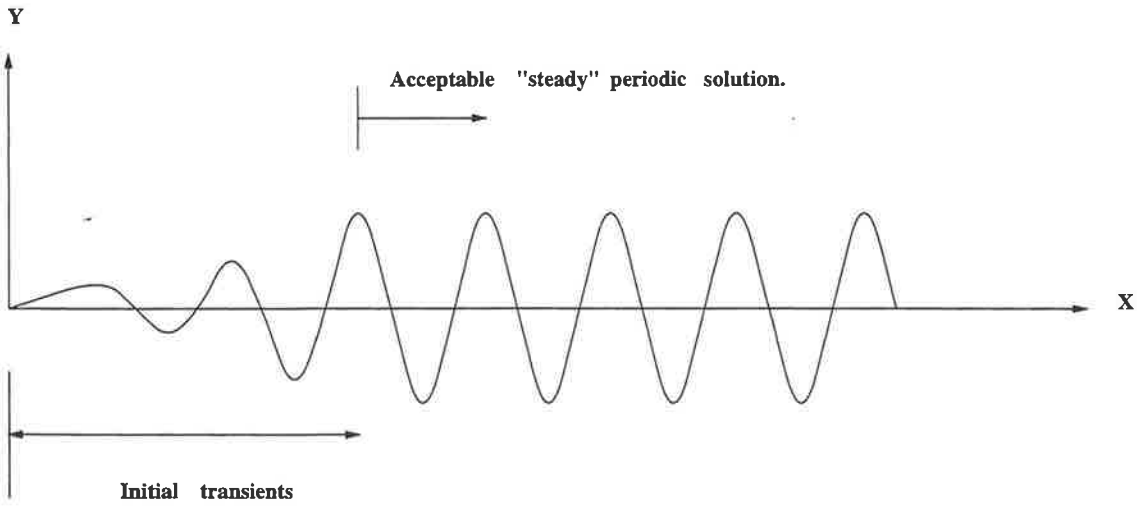

Figure 3.5: *The initial transients and periodic response of the waves.*

3.3 Discrete formulation in spherical coordinates

The spherical coordinate grid has been widely used in the computational oceanography field, for example, Mitchell and Noye (1983), Hunter (1984), Fang and Yang (1988), Verboom et al. (1992) and Davies and Lawrence (1994).

The explicit finite difference technique used to discretize the spherical tidal equations of (2.7), (2.8) and (2.9) on the "Arakawa C" grid in space. is analogous to that used in Section 3.2.3 to discretize the Cartesian tidal equations. This is now presented.

3.3.1 Computational grid

Figure 3.6 shows the discretised locations of ζ_i, u_i and v_i in the ith spherical grid element. Here $\Delta\lambda$ and $\Delta\phi$ are the grid step sizes between grid points in the ϕ and λ directions, respectively.

The elements are indexed in a manner analogous to that described for the Cartesian model in Section 3.3. Figure 3.7 shows the type indexing system of the ith computational element and the eight neighbours.

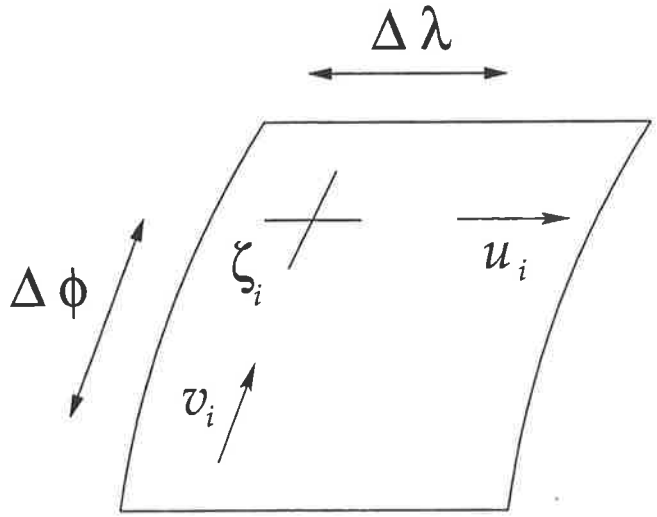

Figure 3.6: *The ith spherical grid element showing discretised locations of ζ_i, u_i and v_i, where $\Delta\lambda$ and $\Delta\phi$ are grid sizes(degrees).*

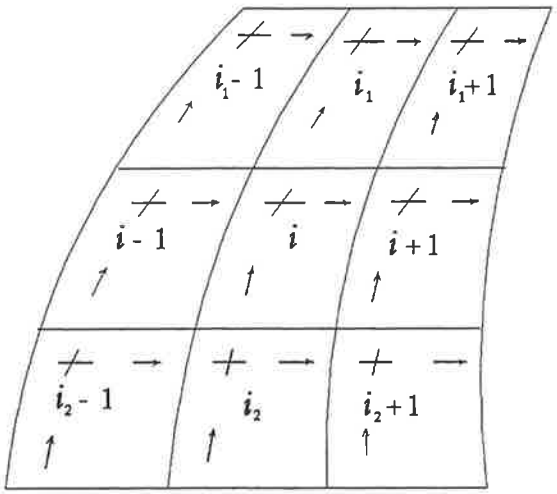

Figure 3.7: *The ith spherical computational element and its eight immediate neighbours, showing the index system used to label the elements. The solid lines represent element boundaries.*

3.3.2 Discrete formulation

The finite difference equations used to approximate the depth-averaged spherical tidal equations, (2.7)–(2.9), are presented in this section. They are approximated in a similar manner as depth-averaged Cartesian equations (see Section 3.2.1), for this reason the approximations are not presented in detail.

The depth-averaged continuity equation (2.7) is written as

$$\frac{\partial \zeta}{\partial t} = -\frac{1}{R\cos\phi}\frac{\partial (Hu)}{\partial \lambda} - \frac{1}{R\cos\phi}\frac{\partial (Hv)}{\partial \phi}. \tag{3.51}$$

The latitude ϕ is evaluated at grid points ζ_i, u_i, and v_i. These values will be denoted as ϕ_{ζ_i}, ϕ_{u_i} and ϕ_{v_i}, respectively. The latitude at the ζ_i grid point is the same as the latitude of the u_i grid point, since both are horizontal grid points located in a plane parallel to the equatorial plane.

It should be pointed out that in spherical coordinates the arc lengths are $2R(\Delta\lambda)\cos\phi$ and $2R\Delta\phi$, which correspond to the horizontal grid spacings $2\Delta x$ and $2\Delta y$ respectively in Cartesian coordinates.

The finite difference approximation of equation (3.51), centred about the time level n in discrete time and the ζ grid point in discrete (horizontal plane) space, is:

$$\left\{\frac{\partial \zeta}{\partial t}\right\}_{\zeta_i}^{n} = -\left\{\frac{1}{R\cos\phi}\frac{\partial (Hu)}{\partial \lambda}\right\}_{\zeta_i}^{n} - \left\{\frac{1}{R\cos\phi}\frac{\partial (Hv\cos\phi)}{\partial \phi}\right\}_{\zeta_i}^{n}. \tag{3.52}$$

By substituting the required approximations into equation (3.51) the explicit expression for the sea surface elevation at time level $(n+1/2)$ is obtained as follows:

$$\begin{aligned} \zeta_i^{n+1/2} &= \zeta_i^{n-1/2} \\ &- \frac{\Delta t}{4R\Delta\lambda\cos\phi_{\zeta_i}}\left[\left(H_i^n + H_{i+1}^n\right)u_i^n - \left(H_{i-1}^n + H_i^n\right)u_{i-1}^n\right] \\ &- \frac{\Delta t}{4R\Delta\phi}\left[\left(H_i^n + H_{i_1}^n\right)v_{i_1}^n - \left(H_{i2}^n + H_i^n\right)v_i^n\right] \\ &+ \frac{\Delta t\tan\phi_{\zeta_i}}{2R}\left(v_i^n + v_{i_1}^n\right)H_i^n, \end{aligned} \tag{3.53}$$

which is second order convergent in both space and time.

The total depth, $H = \zeta + h$, at time $(n+1/2)\Delta t$ is approximated as explained in Section 3.2.1.

The finite difference approximation for the latitudinal momentum equation (2.8), using centred differences about u_i in space and $(n+1/2)$ in time, is obtained by

$$\begin{aligned} \left\{\frac{\partial u}{\partial t}\right\}_{u_i}^{n+1/2} &+ \frac{1}{R}\left\{\frac{u}{\cos\phi}\frac{\partial u}{\partial x}\right\}_{u_i}^{n+1/2} + \frac{1}{R}\left\{v\frac{\partial u}{\partial \phi}\right\}_{u_i}^{n+1/2} - \frac{1}{R}\left\{uv\tan\phi\right\}_{u_i}^{n+1/2} \\ &- \left\{fv\right\}_{u_i}^{n+1/2} = -\frac{g}{R}\left\{\frac{1}{\cos\phi}\frac{\partial \zeta}{\partial \lambda}\right\}_{u_i}^{n+1/2} \end{aligned} \tag{3.54}$$

$$+ \quad \frac{1}{R^2}\left\{\frac{(a_h)_\lambda}{\cos^2\phi}\frac{\partial^2 u}{\partial\lambda^2}\right\}_{u_i}^{n+1/2} + \frac{1}{R^2}\left\{\frac{(a_h)_\phi}{\cos\phi}\frac{\partial}{\partial\phi}(\cos\phi\frac{\partial u}{\partial\phi})\right\}_{u_i}^{n+1/2}$$

$$+ \quad \frac{1}{R^2}\left\{(a_h)_\phi(1-\tan^2\phi)u\right\}_{u_i}^{n+1/2} - \frac{2}{R^2}\left\{\frac{(a_h)_\lambda\tan\phi}{\cos\phi}\frac{\partial v}{\partial\lambda}\right\}_{u_i}^{n+1/2}$$

$$- \quad C_b\left\{\frac{1}{H}u\sqrt{u^2+v^2}\right\}_{u_i}^{n+1/2}.$$

Substituting all required approximations into equation (3.54) gives the following formula for calculating the values of u at the new time level $(n+1)$, that is,

$$\begin{aligned} u_i^{n+1} &= D_\phi^{-1}\left[u_i^n - \frac{\Delta t}{16R\Delta\phi}\left(v_{i_1}^n + v_{i_1+1}^n + v_i^n + v_{i+1}^n\right)\left(u_{i_1}^n - u_{i_2}^n\right)\right. \\ &+ \frac{\Delta t}{8R}u_i^n\left(v_{i_1}^n + v_{i_1+1}^n + v_i^n + v_{i+1}^n\right)\tan\phi_{u_i} \\ &+ \frac{\Delta t}{8}\left(f_i + f_{i+1}\right)\left(v_{i_1}^n + v_{i_1+1}^n + v_i^n + v_{i+1}^n\right) - \frac{g\Delta t}{2R\Delta\lambda\cos\phi_{u_i}}\left(\zeta_{i+1}^{n+1/2} - \zeta_i^{n+1/2}\right) \\ &+ \{(a_h)_\lambda\}_{u_i}^{n+1/2}\frac{\Delta t}{4R^2(\Delta\lambda)^2\cos^2\phi_{u_i}}\left(u_{i+1}^n - 2u_i^n + u_{i-1}^n\right) \\ &+ \{(a_h)_\phi\}_{u_i}^{n+1/2}\frac{\Delta t}{4R^2}(u_{i_1}^n - 2u_i^n + u_{i_2}^n) + \{(a_h)_\phi\}_{u_i}^{n+1/2}\Delta t(1-\tan^2\phi_{u_i})u_i^n \\ &- \left.\{(a_h)_\lambda\}_{u_i}^{n+1/2}\frac{2\Delta t}{4R^2\Delta\lambda}\frac{\tan\phi_{u_i}}{\cos\phi_{u_i}}(v_{i+1}^n - v_{i-1}^n)\right], \end{aligned} \tag{3.55}$$

where

$$\begin{aligned} D_\phi &= \left[1 + \frac{\Delta t}{4R\Delta\lambda\cos\phi_{u_i}}\left(u_{i+1}^n - u_{i-1}^n\right)\right. \\ &- \frac{\Delta t}{8R}\left(v_{i_1}^n + v_{i_1+1}^n + v_i^n + v_{i+1}^n\right)\tan\phi_{u_i} \\ &+ \left.\frac{2C_b\Delta t}{\left(H_i^{n+1/2} + H_{i+1}^{n+1/2}\right)}\sqrt{(u_i^n)^2 + \frac{1}{16}\left(v_{i_1}^n + v_{i_1+1}^n + v_i^n + v_{i+1}^n\right)^2}\right]. \end{aligned} \tag{3.56}$$

The formula for u_i^{n+1} is second order in space and is approximately second order in time.

At the v_i point and the $(n+1/2)$ time level, the longitudinal momentum equation (2.9), namely

$$\left\{\frac{\partial v}{\partial t}\right\}_{v_i}^{n+1/2} + \frac{1}{R}\left\{\frac{u}{\cos\phi}\frac{\partial v}{\partial\lambda}\right\}_{v_i}^{n+1/2} + \frac{1}{R}\left\{v\frac{\partial v}{\partial\phi}\right\}_{v_i}^{n+1/2} + \frac{1}{R}\left\{u^2\tan\phi\right\}_{v_i}^{n+1/2} \tag{3.57}$$

$$+ \{fv\}_{v_i}^{n+1/2} = -\frac{g}{R}\left\{\frac{\partial\zeta}{\partial\phi}\right\}_{v_i}^{n+1/2} -$$

$$
\begin{aligned}
&+ \frac{1}{R^2}\left\{\frac{(a_h)_\lambda}{\cos^2\phi}\frac{\partial^2 v}{\partial\lambda^2}\right\}_{v_i}^{n+1/2} + \frac{1}{R^2}\left\{\frac{(a_h)_\phi}{\cos\phi}\frac{\partial}{\partial\phi}(\cos\phi\frac{\partial v}{\partial\phi})\right\}_{v_i}^{n+1/2} \\
&+ \frac{1}{R^2}\left\{(a_h)_\phi(1-\tan^2\phi)v\right\}_{v_i}^{n+1/2} + \frac{2}{R^2}\left\{\frac{(a_h)_\lambda\tan\phi}{\cos\phi}\frac{\partial u}{\partial\lambda}\right\}_{v_i}^{n+1/2} \\
&- C_b\left\{\frac{1}{H}v\sqrt{u^2+v^2}\right\}_{v_i}^{n+1/2\}} ,
\end{aligned}
$$

is differenced in the same way as the latitudinal momentum equation (2.8), that is, values of v at the new time level $(n+1)$ are given by the following formula , which is

$$
\begin{aligned}
v_i^{n+1} &= D_\lambda^{-1}\left[v_i^n - -\frac{\Delta t}{16R\Delta\lambda\cos\phi_{v_i}}\left(u_i^{n+1}+u_{i_1}^{n+1}+u_{i2}^{n+1}+u_{i2-1}^{n+1}\right)\left(v_{i+1}^n - v_{i_1}^n\right)\right. \quad (3.58)\\
&- \frac{\Delta t}{16R}\left(u_i^{n+1}+u_{i_1}^{n+1}+u_{i2}^{n+1}+u_{i2-1}^{n+1}\right)\tan\phi_{v_i} \\
&- \frac{\Delta t}{8}(f_i+f_{i2})\left(u_i^{n+1}+u_{i_1}^{n+1}+u_{i2}^{n+1}+u_{i2-1}^{n+1}\right) - \frac{g\Delta t}{2R\Delta\phi\cos\phi_{u_i}}\left(\zeta_i^{n+1/2}-\zeta_{i2}^{n+1/2}\right) \\
&+ \{(a_h)_\lambda\}_{v_i}^{n+1/2}\frac{\Delta t}{4R^2(\Delta\lambda)^2\cos^2\phi_{v_i}}\left(v_{i+1}^n - 2v_i^n + v_{i-1}^n\right) \\
&+ \{(a_h)_\phi\}_{v_i}^{n+1/2}\Delta t\left(\frac{v_{i_1}^n - 2v_i^n + v_{i_2}^n}{4R^2(\Delta\phi)^2} - \frac{v_{i_1}^n - v_{i_2}^n}{4R^2\Delta\phi}\tan\phi_{v_i}\right) \\
&+ \{(a_h)_\phi\}_{v_i}^{n+1/2}\frac{\Delta t}{R^2}(1-\tan^2\phi_{v_i})v_i^n \\
&+ \left.\{(a_h)_\lambda\}_{v_i}^{n+1/2}\frac{2\Delta t}{4R^2\Delta\lambda}\frac{\tan\phi_{v_i}}{\cos\phi_{v_i}}(u_{i+1}^n - u_{i-1}^n)\right] .
\end{aligned}
$$

in which

$$
\begin{aligned}
D_\lambda = &\left[1 + \frac{\Delta t}{4R\Delta\phi}\left(v_{i_1}^n - v_{i_2}^n\right)\right. \quad (3.59)\\
&+ \left.\frac{2C_b\Delta t}{\left(H_i^{n+1/2}+H_{i2}^{n+1/2}\right)}\sqrt{(v_i^n)^2 + \frac{1}{16}\left(u_i^{n+1}+u_{i_1}^{n+1}+u_{i2}^{n+1}+u_{i2-1}^{n+1}\right)^2}\right] .
\end{aligned}
$$

This is second order in space and is approximately second order in time.

3.3.3 Computational algorithm

The governing equations are solved on the basis of the following algorithm:

1. Input model data and set initial data. Time $t = 0$ (that is, $n = 0$, and $t = n\Delta t$, also $\zeta_i^{-\frac{1}{2}} = \zeta_i^0 = u_i^0 = v_i^0 = 0, H_i^0 = h_i$ and on the open boundary $H_i^0 = h_i + \zeta_i^0$).

2. Update model time to level $(n + 1/2)$, so $t = (n + 1/2)\Delta t$.
   Update open boundary elevation to time level $(n + 1/2)$.
   Solve the continuity equation (2.4) in Cartesian or (2.7) in spherical coordinates to find $\zeta^{n+1/2}$ using $H^{n+1/2}$.

3. Update model time to level $(n + 1)$. Time $t = (n + 1)\Delta t$.
   Solve the momentum equations (2.5) in Cartesian or (2.8) in spherical coordinates and (2.6) or (2.9) for u^{n+1} and v^{n+1}, using $\zeta^{n+1/2}$.

4. Update open boundary elevation to time level $(n + 1)$.
   Solve equation (2.4) or (2.7) for ζ^{n+1}; using u^{n+1}, v^{n+1} and H^{n+1}.

5. Return to step 2 and continue until the period of the simulation is completed.

3.4 Programming scheme

In this section some important features of the programming scheme for solving the finite difference equations are described, based on the schemes developed by Bills (1992). This procedure will be modified for the development of the nesting model of the Persian Gulf, in Chapter 6, so it is necessary to present the basic definitions of the scheme here. These are:

1. The element classification:
   Regarding the elevation gridpoint of each grid element the following definitions (Bills, 1992, p.36) are given:

   - If the elevation point lies on land, the grid element is called "type 0" and coded as '0';

   - If the elevation point lies on water within the model, the grid element is called "type 1" and coded as '1';

   - If the grid elevation point lies on an open boundary, the grid element is called "type 2" and coded as '2;

   - If the elevation point lies on water outside the model region, the grid element is called "type 4" and coded as '4'.

2. Labelling convention
   The immediate family of eight neighbour codes of the central computational element is labelled as in Figure 3.8.

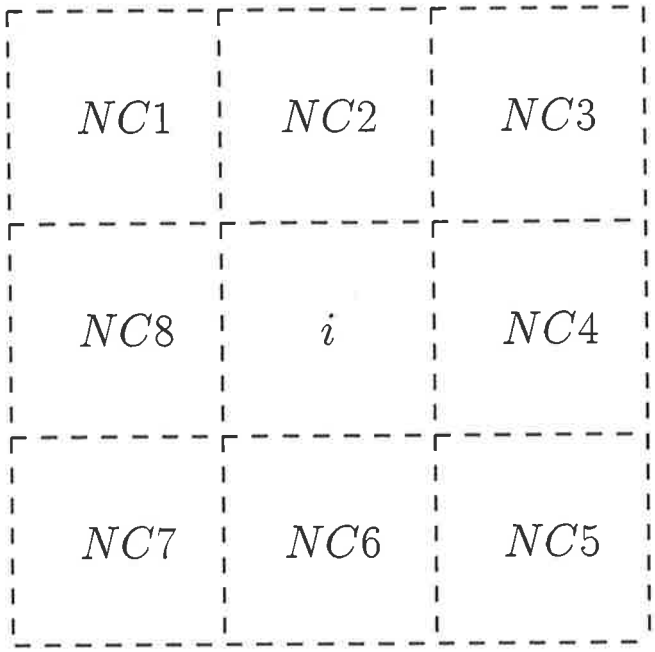

Figure 3.8: *The labelling convention for the eight immediate neighbours of the central element i. (Source: Bills, 1991, p.37)*

As Figure 3.8 shows, the neighbours are labelled clockwise from the top-left element of the 9-element block. It should be noted that, at each computation the finite difference equations use a selection of neighbours. For example, for the finite difference approximation of the continuity equation, the elements labelled, NC_2, NC_4, NC_6 and NC_8 will be used.

3. One-dimensional arrays
   For the purpose of computation, several permanent one-dimensional arrays are created. A simple example of a study region is presented below in Figure 3.9, to illustrate how the codes are stored and retrieved, and how the arrays are constructed from the neighbourhood. A similar process may be used where the elevation point of the computational element lies on an open boundary.

   By using the definitions of the four types of elements, the array corresponding to Figure 3.9 is shown in Figure 3.10. This array is called the type matrix of the model region.

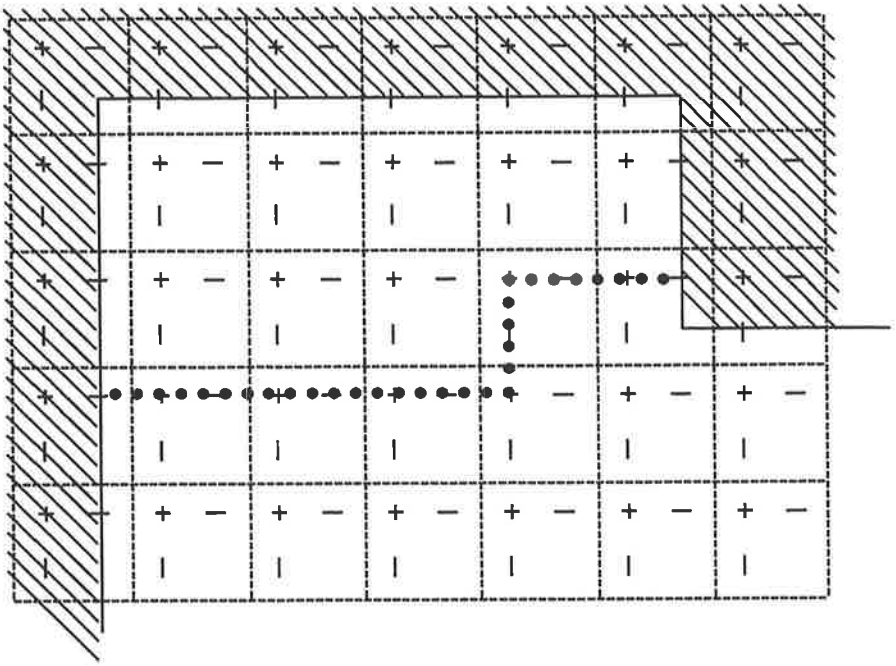

Figure 3.9: *Showing a model region. Solid line segments are coastal boundaries and the dotted line segments are the open boundaries of the model (through the + signs). The velocities are shown by −,|. The hatched regions are land areas.*

0	0	0	0	0	0	0
0	1	1	1	1	1	0
0	1	1	1	2	2	0
0	2	2	2	2	4	4
0	4	4	4	4	4	4

Figure 3.10: *The array of the neighbourhood codes of the region, using Figure 3.9.*

Chapter 4

A Depth-averaged Cartesian Model of the Persian Gulf

4.1 Introduction

In this chapter the development of a Cartesian depth-averaged model of the Persian Gulf is described. The main reason for developing this model is to compare the results from it with those from some other works who used Cartesian coordinates, and also with the spherical coordinate model in chapter 5, to find out the effect of considering the earth's curvature.

Figure 4.1 shows the locations of some places inside the Gulf which will be referred to later.

Figure 4.1: *The location of some places in the Persian Gulf.*

4.2 Tides in the Persian Gulf

Existing information on tides in the Persian Gulf is based primarily on the Admiralty chart, which has been constructed from observations available at a number of sites along the coast and a limited number of points within the Gulf. By their very nature, the Admiralty chart only provides approximations to the true tidal conditions within the Gulf. However, they form an initial basis for understanding tidal movement in the Persian Gulf and for comparison with mathematical models developed within this thesis and by other researchers whose work is reviewed in Section 4.3.

In Figure 4.2 the locations of 84 tidal observation stations in the Gulf are given, along with four stations in the Gulf of Oman. The density of observation stations is high along the coasts of Saudi Arabia, Qatar and the United Arab Emirates. This map, together with corresponding sets of harmonic constituents for O_1, K_1, M_2 and S_2, was supplied by the National Tidal Facility at the Flinders University of South Australia, based on an electronic record of constants originally produced by the British Admiralty. From the analysis of the tidal heights of the stations in the Gulf, the Hydrographic Department of the British Admiralty published comprehensive charts of co-amplitudes and co-phase lines for the principal constituents O_1, K_1, M_2 and S_2. Figures 4.3–4.6 show the Admiralty chart, 5081, reproduced by the Danish Hydraulic Institute.

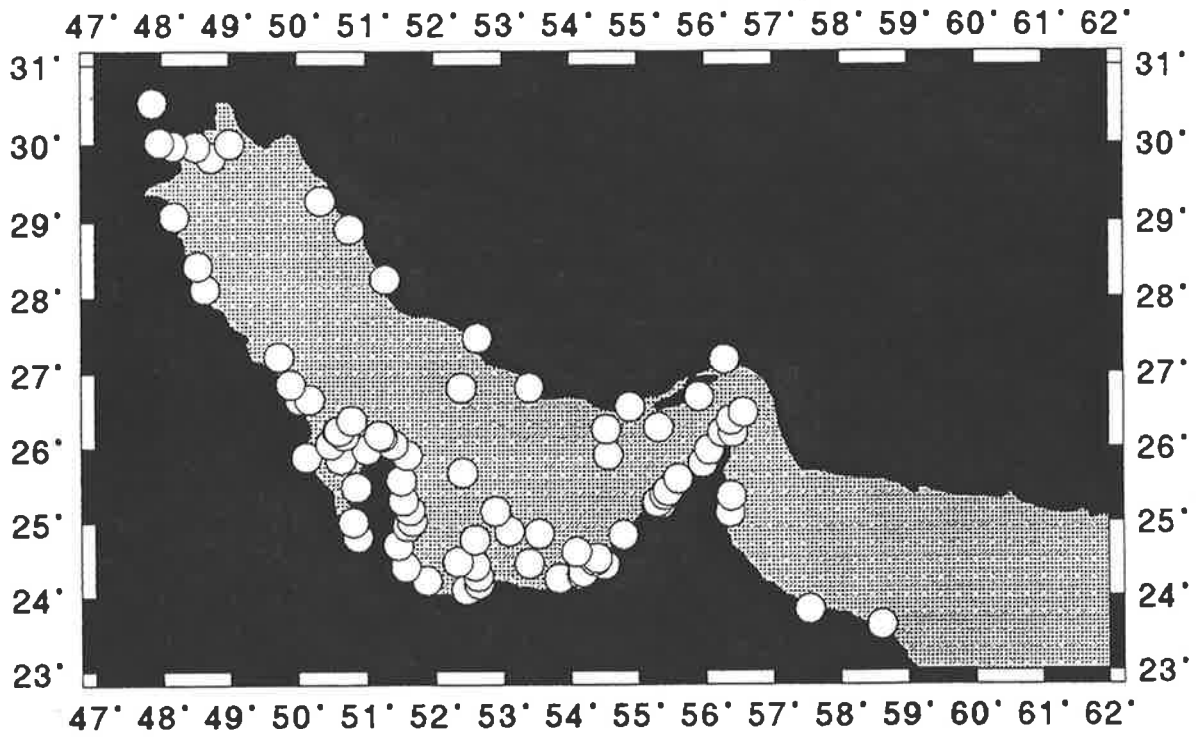

Figure 4.2: *The locations of the 84 tidal observation stations in the Persian Gulf (Source: National Tidal Facility at the Flinders University of South Australia.)*

The tides in the Persian Gulf are complex and consist of different types as was shown in Figure 2.2. The tidal ranges are large throughout: over three meters at Shatt Al-Arab/Arvand Rood at the head of the Gulf, and over a meter everywhere else (Lehr, 1984, p.4). Tidal energy enters the Gulf through the Strait of Hormuz and progresses up the Iranian coast and down the Arabian side as a Kelvin wave. The resultant of these two opposite Kelvin waves forms a set of amphidromic points (see Figures 4.3–4.6). The O_1 and K_1 components have a single amphidromic point, which is set at the centre of the Gulf (see Figures 4.3 and 4.4, respectively). The M_2 and S_2 constituents have two amphidromic points, located at almost a quarter and three-quarters up the Gulf from the Strait of Hormuz (see Figures 4.5 and 4.6, respectively). It should be noted that if the incident and reflected waves have the same amplitude, then the amphidromic points will be situated at the points equidistant from both coasts. However, as Figures 4.3-4.6 show, they are closer to the Arabian side, because the reflected wave is weaker, and because the speed of the wave is a function of depth, and the Arabian side is shallower than Iranian coast. The principal semi-diurnal M_2 and S_2 and diurnal K_1 and O_1 constituents are the dominant tidal motions in the Gulf.

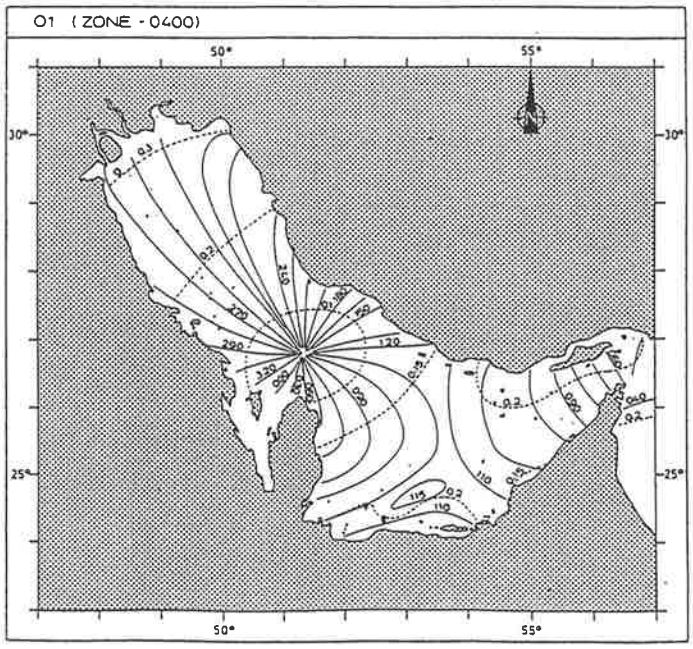

Figure 4.3: *The co-tidal chart for the O_1 harmonic constituent. Dashed lines are amplitude (m) and solid lines are phase (degrees) contours. The time zone is 0400 (Source: British Admiralty, reproduced by Danish Hydraulic Institute.)*

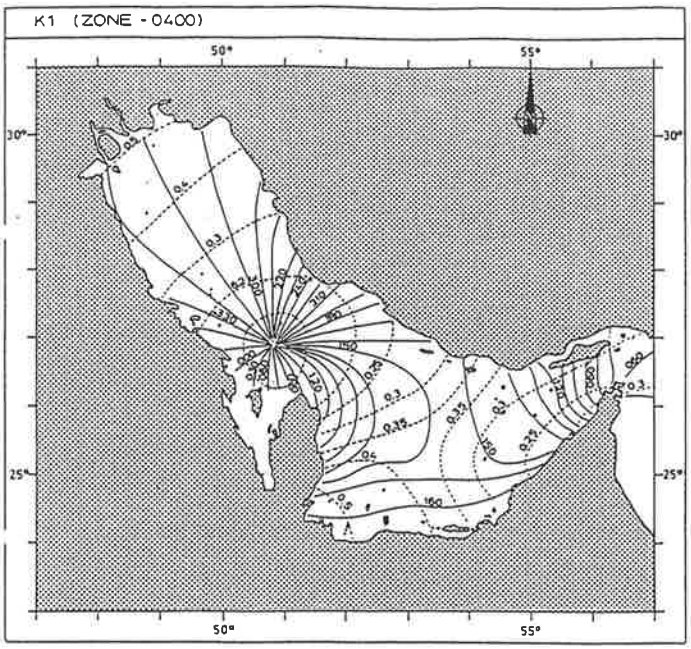

Figure 4.4: *The co-tidal chart for the K_1 harmonic constituent. Dashed lines are amplitude (m) and solid lines are phase (degrees) contours. The time zone is 0400 (Source: British Admiralty, reproduced by Danish Hydraulic Institute.)*

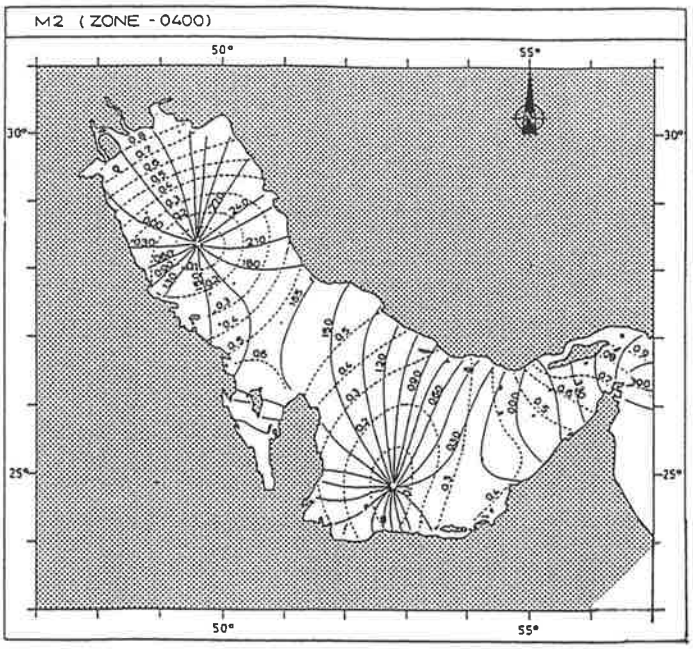

Figure 4.5: *The co-tidal chart for the M_2 harmonic constituent. Dashed lines are amplitude (m) and solid lines are phase (degrees) contours. The time zone is 0400 (Source: British Admiralty, reproduced by Danish Hydraulic Institute.)*

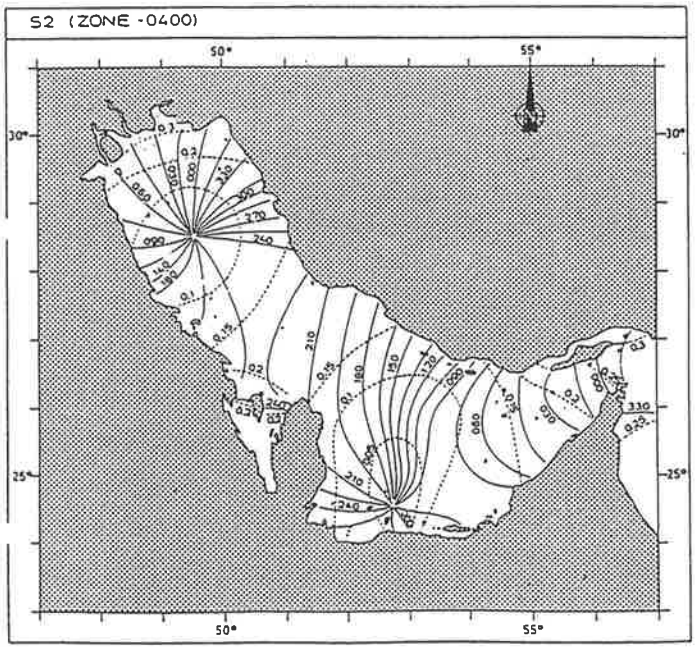

Figure 4.6: *The co-tidal chart for the S_2 harmonic constituent. Dashed lines are amplitude (m) and solid lines are phase (degrees) contours. The time zone is 0400 (Source: British Admiralty, reproduced by Danish Hydraulic Institute.)*

4.3 Review of Cartesian models of the Persian Gulf

Several depth-averaged Cartesian models of tides in the Persian Gulf already exist. The most important aspects of these models are included in Table 4.1. It should be pointed out that in Table 4.1 the *vertical/horizontal splitting* ((VHS)) scheme is a three-dimensional algorithm, described by Lardner and Cekirge (1988). In this approach, the surface elevation and depth-averaged velocity components are computed by using one of the existing two-dimensional schemes. These values are then used to compute the vertical velocity profiles by solving the linearized three-dimensional momentum equations.

Authors	year	Depth averaged (DA) or 3D	Numerical technique used	Bottom friction	Region modelled	Number of active or non-active grid element	Element dimension	Time step
Von Trepka	1968	DA	Hansen	quadratic law	whole Gulf	N/A	$14\times14\,km^2$	N/A
Lardner, Belen and Cekirge	1982	DA	semi-implicit finite difference	Chezy $c_1 ln(c_2 H + c_3)$ with $c_1 = 25$, $c_2 = c_3 = 1$	whole Gulf and Arabian shores	N/A	$20\times20\,km^2$ and $10 \times 10 km^2$	12 min
Lardner, Cekirge, and Gunay	1986	DA	N/A	Chezy ln form $c_2 = c_3 = 1$	whole Gulf and Gulf of Salwa	30×44 = 1320	$20\times20\,km^2$ and $5\times5\,km^2$	N/A
Chu, Barker and Akbar	1988	DA	semi-implicit	Equal Chezy 40-100$m^{\frac{1}{2}}$/sec	whole Gulf	31×45 = 1395	$19.05\times$ $19.05\,km^2$	N/A
El-Sabh and Murty	1988	DA	N/A	quadratic law	whole Gulf	$60\times$ 38 = 2280	$15\times15\,km^2$	6 min
Bashir, Khaliq, and Al-Hawaj	1989	DA	Hansen	quadratic law	whole Gulf	N/A	$16.67\times$ $18\,km^2$	N/A
Lardner, Al-Rabeh, Gunay and Cekirge	1989	3D	Crank-N	Chezy ln form $c_1 = 25$, $c_2 = c_3 = 1$	west coast of the Gulf	30×44 = 1320 and 12×35 = 4445	$20\times20\,km^2$ and $5\times5\,km^2$	N/A
Al-Rabeh, Gunay, and Cekirge	1990	3D/ VHS	semi-implicit/	Chezy ln form $c_1 = 25$ $c_2 = c_3 = 1$	whole Gulf and west coast of the Gulf	N/A	$20\times20\,km^2$ and $10\times10\,km^2$	N/A
Al-Rabeh and Gunay	1992	3D/ VHS	semi-implicit and Crank-N (in vertical)	Chezy ln form c_1, c_2, c_3	Safaniya	12×12 = 144	$2\times2\,km^2$	72 min
Proctor, Elliott and Flather	1992	DA	Proudman Oceanographic Laboratory	quadratic law	whole Gulf	N/A	$9\times9\,km^2$	N/A
Venkatesh and Murty	1994	DA	N/A	quadratic law	whole Gulf	$190\times$ 106 = 20140	$4.74\times$ $4.74\,km^2$	6 min

Table 4.1: *A summary of some Cartesian models of the Gulf. N/A means not available. Locations of Safaniya and the Gulf of Salwa are shown in Figure 4.1.*

Von Trepka (1968) investigates the tides in the Persian Gulf by using the hydrodynamical-numerical (HN) method of Hansen (1962); the model is non-linear. Cartesian coordinates with $14\,km \times 14\,km$ elements are used and the model is initially used to predict M_2, the dominant tidal constituent in the Gulf, ignoring non-linear interaction. Von Trepka is satisfied with the predictions for the amplitude of M_2, even in the complicated and very shallow coastline of the Bahrain area. The average difference between his predictions and the observed amplitudes is not more than $2.7\,cm$ and $18\ min$ [i.e. 8.7°] for the phases (von Trepka, 1968, p.61). Separate predictions for each of K_1, O_1 and S_2 are then performed but the results are not as good, since the amplitude error of these constituents is large.

Evidently nonlinear effects cannot be ignored if the minor tides are to be taken into account, and so an experiment is conducted wherein a Persian Gulf model comprised of $42\,km \times 42\,km$ elements is forced using seven constituents over a period of 29 days. Rather than performing a harmonic analysis of results, von Trepka compares his results with predictions of high and low water given in the German and English Tide Tables (ibid., p.62). At Kuwait Harbor the mean deviation was about $20\ min$ [i.e. 10°]. The maximal deviation was not more than $60\ min$ [i.e. 30°]. In most cases the difference in height was less than $10\,cm$. Only the low waters were computed to be too high, with a maximum difference of $36\,cm$ (ibid., p.62). In conclusion, von Trepka recommends using a finer grid model and more than seven constituents, and employing harmonic analysis of results in order to obtain prediction of the minor tides.

Figures 4.7 and 4.8 show the amplitude (m) and phase ($degrees$) contours respectively, for the M_2 tidal constituent of sea surface elevation predicted by Von Trepka.

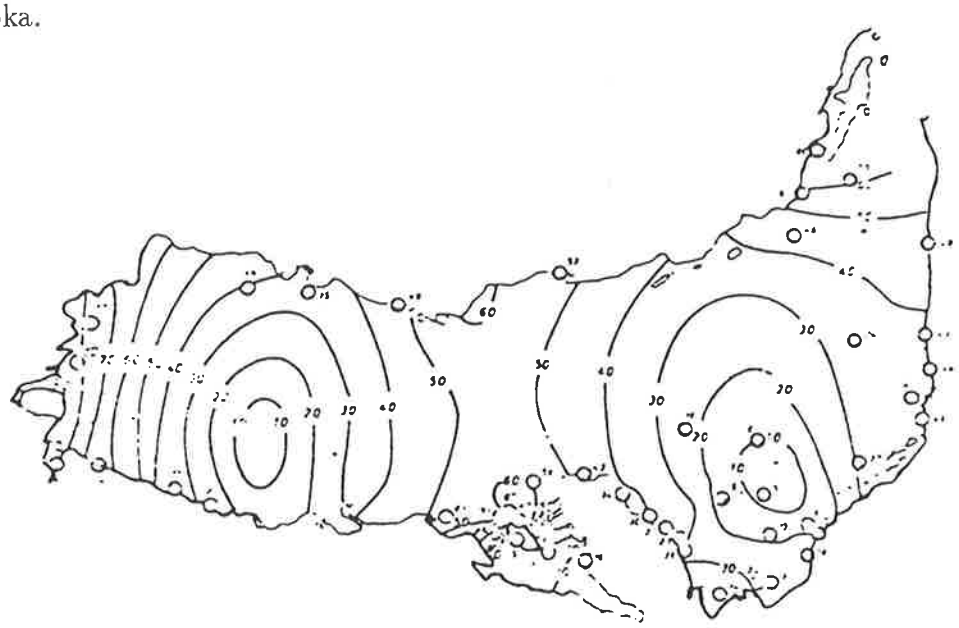

Figure 4.7: *The amplitude (cm) contours for the M_2 tidal constituent of sea surface elevation, predicted by Von Trepka (1968).*

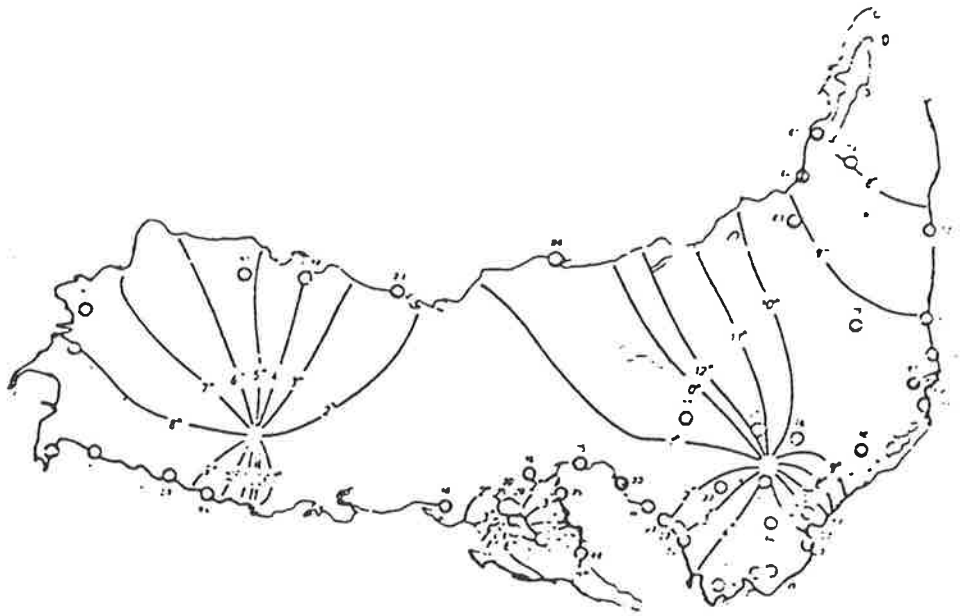

Figure 4.8: *The phase (degrees) contours for the M_2 tidal constituent of sea surface elevation, predicted by Von Trepka (1968).*

Lardner et al. (1982) developed a model by using the finite difference scheme of Leendertse (1967) to solve the depth-averaged equations. They constructed a three-block model consisting of two blocks using a coarse grid and one using a fine grid, to cover the shallow coastal areas, such as the area of Bahrain and the west coast of Qatar. They produced the co-tidal maps for K_1, M_2 and S_2. They believe that their computed amplitudes for M_2 are slightly too small (Le Provost, 1984, p.32 says by 10%) in a region of the Saudi Arabian coast on the northwest coast of Qatar and Abu Zabi, (south Figure 4.1), and is slightly too large on a region of the southern Iranian coastline around Jazireh-ye Hendorabi; otherwise the computed amplitudes are in good agreement with observation (ibid., p.438). The computed phases are also too low on the north-eastern coast of Qatar, and are somewhat high in the western half of the Gulf (ibid., p.438). However, they conclude that because of the method of computation (the amplitude values are computed as the average of all the maximum values of tidal elevation ζ and the phase values are computed from the time of the last maximum of ζ), the computed values of tidal phase vary irregularly. That is, they are not as reliable as amplitudes when compared with the observed values, although their shape of the contours are in reasonable agreement with the shape of the co-tidal lines shown in Figures 4.3–4.6.

In a later paper, Lardner et al. (1986) solved the depth-averaged equations using a different technique, namely, the method of characteristics. They applied the model to the Gulf, to predict the amplitudes and phases of constituents M_2 and K_1, by covering the region with elements of approximately $20\,km \times 20\,km$ mesh-size. They presented charts for the results of the amplitudes and phases of the M_2 and K_1

constituents by applying a tidal analysis to the output data and comparing the results with co-tidal charts, and indicated that phase contours of both M_2 and K_1 are in very good agreement (the observed and computed amplitudes at the eight tidal stations has been presented in the paper). They noted that the amplitude contours generally are as good, with the exception that the amplitude contours of both M_2 and K_1 are smaller than those of the Admiralty chart, at the head of the Gulf, and the contour of M_2 is too small in the Bahrain region and too large at the bottom of the Gulf of Salwa (ibid., p.1076). They considered that the discrepancies in certain areas occurred because of the rather coarse mesh used on the coastline (ibid., p.1076). Figures 4.9 and 4.10 indicate the amplitude (m) and phase ($degrees$) respectively, for the M_2 tidal constituent of sea surface elevation predicted.

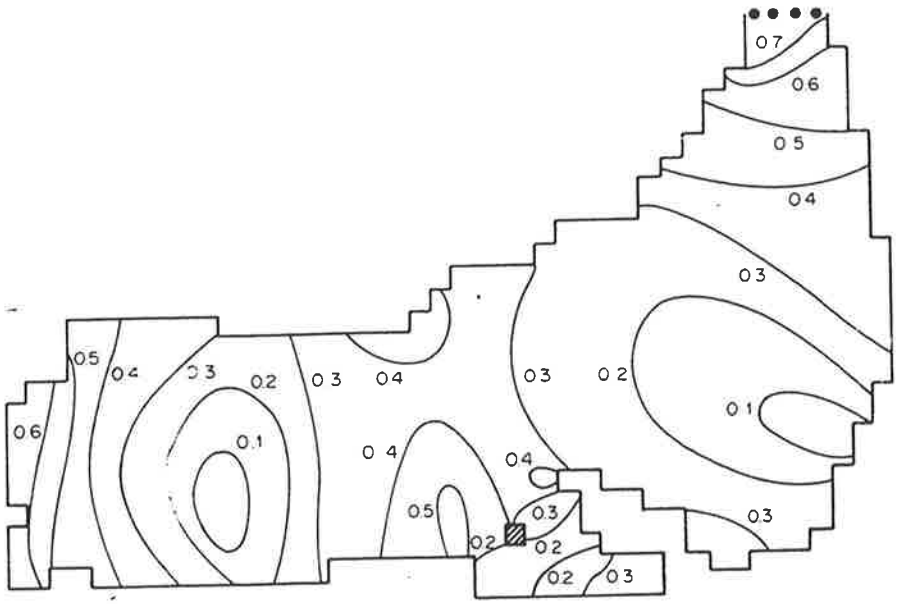

Figure 4.9: *The amplitude (m) contours for the M_2 tidal constituent of sea surface elevation, predicted by Lardner et al. (1986).*

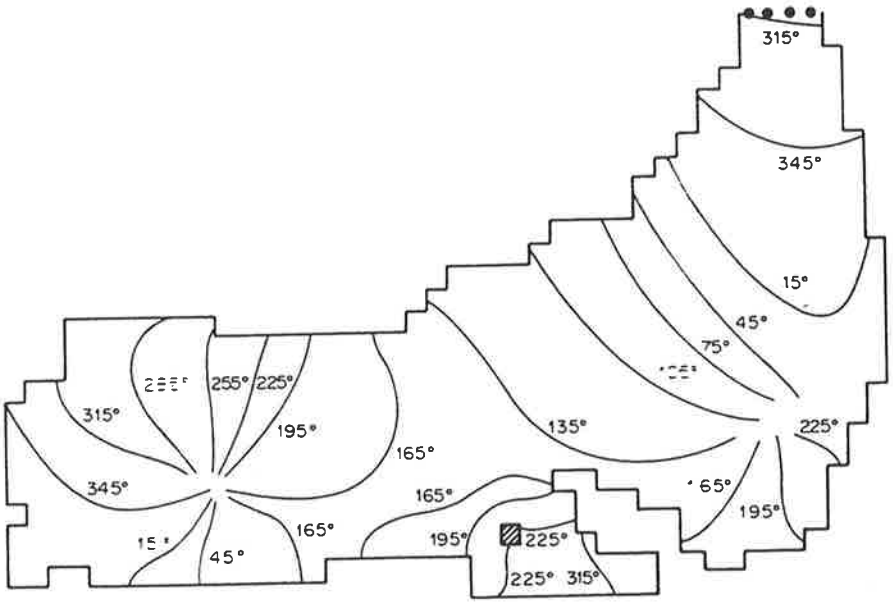

Figure 4.10: *The phase (degrees) contours for the M_2 tidal constituent of sea surface elevation, predicted by Lardner et al. (1986).*

Chu et al. (1988) constructed a Cartesian depth-averaged model and studied the tidal transport in the Gulf by using a coarse spatial resolution of 19.05 km. They used the velocity and depth information calculated from this hydrodynamic model to provide data to develop an Eulerian-Lagrangian transport model to study the flow and transport characteristics of the Gulf. The two-dimensional shallow water equations have been solved by using the Leendertse (1967) semi-implicit finite difference scheme. The data for the open boundary of the model and also for comparison were supplied by Admiralty tide tables and tidal stream tables, 1968. The data at Didamar Station in the Strait of Hormuz was used as the boundary condition, and for comparison with their model predictions they used the tide data of the four constituents M_2, S_2, K_1 and O_1 at 26 stations within the Gulf. They have not provided a table for the predictions and observed values for amplitudes and phases at the stations, but two plots of correlations of the tide ranges and phases were provided. They believed that the model results match fairly well with those given by the Admiralty Tide Table, except at a few shoreline stations along the Arabian coast, and considered that the coarse resolution of the coastline and bathymetry of the model may have caused the discrepancies at these stations.

Bashir et al. (1989) developed a two dimensional explicit finite difference model to reproduce the M_2 constituent of the tide in the Gulf. A difference between this method and schemes of, for example, Lardner et al. (1982) and von Trepka (1968) is that, in this model at the open boundary (strait of Hormuz), radiation type conditions are applied (Beckers and Neves, 1985 and Flather, 1976), in addition to

prescribing the tidal height (ibid., p296).

Lardner et al. (1989) described a three-dimensional hydrodynamic model for the Gulf. This paper was a continuation of Lardner et al. (1982, 1986), Cekirge et al. (1986) and Lardner and Cekirge (1987) and (1988), in which tidal and wind-driven currents were studied using the method of characteristics and the VHS technique. In this paper, they discussed the selection of appropriate values for the hydrodynamical parameters and presented an interpolation algorithm to compute velocity profiles at non-gridpoint positions.

Al-Rabeh et al. (1990) described a hydrodynamic model for wind-driven and tidal circulation of the Gulf. They extended the VHS model of Lardner and Cekirge (1988), and in particular they solved the depth-averaged equations by a finite difference scheme, based on that of Leendertse (1967), rather than solving them by the method of characteristics, which was done by Lardner and Cekirge (1988). Al-Rabeh et al. (1990) present two models, namely HYDRO1 and HYDRO2. Both models compute wind-driven and/or tidal circulation. HYDRO1 is for the whole Gulf and the HYDRO2 can be used for any particular area in the Gulf. The models are applied to compute the tidal heights at selected stations on the Saudi coastline.

Proctor et al. (1992) used the Proudman Oceanography Laboratory (PLO) depth-averaged tide-surge model for the whole Gulf, to provide environmental data on tides, currents and particle trajectories during the Gulf war. In this model the grid cells are approximately $9\,km \times 9\,km$. The open boundary of the model was located across the eastern end of the Strait of Hormuz. Along the open boundary ten tidal components, Q_1, O_1, P_1, K_1, μ_2, N_2, M_2, L_2, S_2 were specified.

Venkatesh and Murty (1994) developed a numerical model to investigate the movement of the 1991 oil spills in the Gulf. As a result of the 1991 Gulf war, more than 200 million gallons (ibid., p.2) of oil were spilled into the Gulf, causing the world's worst oil spill. The first spills occurred at the Al-Ahmadi oil terminal, off the Kuwaiti coast (see Figure 4.1). In this paper the simulations of the movement of oil from the Al-Ahmadi and Al-Bakr spills are described. The numerical model is used to compute the currents due to tides, winds and bathymetric influences. The open boundary of the model is set at the strait of Hormuz. This tidal model is a higher resolution version of El-Sabh and Murty (1988), that is, $4.74\ km \times 4.74,\ km$.

Some other numerical models of surges, and pollutant transport, also have been developed and applied to the Gulf. Table 4.2 summarizes some of these models.

Authors	year	Application	Region modelled
Murty and El-Sabh	1984	storm surges	whole the Gulf
Galt, Payton, Torgrimson and Watabatashi	1984	oil spill oil spill	whole the Gulf and Kuwait area
El-Sabh and Murty	1988	oil spill	whole the Gulf
Lardner, Lehr, Fraga and Sarhan	1988	pollutant transport	whole the Gulf
Cekirge, Al-Rabeh and Gunay	1989	oil spill	whole the Gulf
Proctor, Elliott and Flather	1992	oil spill	Kuwait area (Al-Ahmadi)
Spaulding, Anderson Isaji and Howlett	1993	oil spill	Al-Ahmadi
Venkatesh and Murty	1994	oil spill	Al-Ahmadi

Table 4.2: *A summary of some other numerical models of surges, and pollutant transport of the Gulf.*

4.4 Depth-averaged Cartesian model and its calibration

The Cartesian depth-averaged model of the Persian Gulf (which assumed the earth is locally flat) used the elements of $8.7\,km \times 9.7\,km$ mesh-size, that is, $2\Delta x = 8.7\,km$ and $2\Delta y = 9.7\,km$ and a time step of $\Delta t = 200sec.$

It was assumed that the Mercator projection of the spherical surface formed the Cartesian plan used. The British Admiralty maps 2837 and 2847 were used for the model. The value of Δx in the east-west direction was assumed to be that of the central point in the Gulf. The Cartesian grid contains 79×118 elements; 3199 active elements are used in the computations. The open boundary of the model is set at the eastern end of the Gulf (see dashed line in Figure 4.1), and the number of type 2 elements on the open boundary, is 12, so that the number of elements within the Gulf is 3187. Dashed line in Figure 4.1 shows the open boundary of the model, which is located at the eastern end of the Gulf. The first element from the left is labelled element number one and the second is number two and so on. The top

left and bottom right corner of the grid have a latitude of 30.37° N and 23.87° N, respectively

The ten tidal components Q_1, O_1, P_1, K_1, μ_2, N_2, M_2, L_2, S_2 and K_2, provided by Proctor et al. (1992), were used to produce open boundary tide-height input data. Table 4.3(a) shows the tide-height constants of the four major constituents at the elements on the open boundary and Table 4.3(b) indicates the amplitude and phase of the six minor constituents at the elements of the open boundary of the model Gulf. Tables 4.3(a) and 4.3(b) show that the constants were considered to vary linearly across the Gulf of Oman. The model was run for a simulated time of 32 days; the first three days of data were considered to include initial transients, so the tidal movement within the Gulf was represented by the last 29 days. Predictions for the 29 days can be used to determine tidal constants for 25 astronomical constituents (Easton, 1977, p.16), although the four major constituents O_1, K_1, M_2 and S_2 can be calculated from only 15 days of data (Easton, 1977, P.17). A criterion for using the minimum length of data required for analysis has been given in Pugh(1987, p.113).

Boundary	O_1		K_1		M_2		S_2	
element	amp	phase	amp	phase	amp	phase	amp	phase
1	0.235	330.3	0.390	350.0	0.759	170.4	0.292	204.2
2	0.239	330.6	0.395	349.8	0.763	169.9	0.293	203.0
3	0.243	330.8	0.400	349.6	0.767	169.3	0.295	201.9
4	0.247	331.1	0.404	349.4	0.771	168.8	0.296	200.8
5	0.251	331.3	0.409	349.3	0.776	168.3	0.298	199.6
6	0.255	331.6	0.413	349.0	0.780	167.8	0.300	198.5
7	0.259	331.8	0.418	348.9	0.784	167.3	0.302	197.4
8	0.263	331.9	0.423	348.7	0.789	166.7	0.304	196.3
9	0.267	332.2	0.428	348.5	0.794	166.3	0.306	195.3
10	0.271	332.4	0.432	348.4	0.799	165.8	0.309	194.2
11	0.275	332.6	0.437	348.2	0.803	165.3	0.311	193.2
12	0.279	332.8	0.441	348.0	0.808	164.8	0.314	192.2

Table 4.3(a): *Amplitude (cm) and phase (degree GMT) of the four major constituents at the elements of the open boundary of the Persian Gulf model. See also Table 4.3(b) for the remaining constituents used as the forcing data of the model. GMT means Greenwich Mean Time.*

The distribution of the observational stations used for calibration is shown in Figure 4.12, and Table 4.4 lists their latitude and longitude. Among the list of 84 stations there are 44 stations which have not been used in calibration because they have one or more of the following disadvantages; they are

(1) up rivers,

(2) in very shallow regions, or

(3) very close together.

It should be noted that in the situation where two stations are in close proximity, the station nearer to an elevation grid point has been selected.

Boundary element	Q_1		P_1		MU_2		N_2		L_2		K_2	
	amp	phase	amp	phase	amp	phase	amp	phase	amp	phase	amp	phase
1	0.029	317.0	0.130	350.0	0.031	109.4	0.167	153.4	0.031	190.4	0.078	204.2
2	0.030	317.3	0.132	349.8	0.031	108.9	0.168	152.9	0.032	189.9	0.078	203.0
3	0.030	317.5	0.132	349.6	0.031	108.3	0.169	152.3	0.032	189.3	0.079	201.9
4	0.031	317.8	0.135	349.4	0.032	107.8	0.170	151.8	0.032	189.8	0.079	200.8
5	0.032	318.0	0.136	349.3	0.032	107.3	0.171	151.3	0.032	188.2	0.079	199.6
6	0.032	318.2	0.138	349.0	0.032	106.8	0.172	150.8	0.032	187.8	0.080	198.5
7	0.033	318.5	0.139	348.9	0.032	106.3	0.173	150.3	0.032	187.2	0.081	197.4
8	0.033	317.7	0.141	348.7	0.033	105.7	0.174	149.8	0.033	186.7	0.081	196.3
9	0.033	318.9	0.142	348.5	0.033	105.2	0.175	149.2	0.033	186.2	0.082	195.3
10	0.034	319.1	0.144	348.4	0.033	104.8	0.176	148.8	0.033	185.8	0.082	194.2
11	0.034	319.3	0.146	348.2	0.033	104.3	0.177	148.3	0.033	185.3	0.083	193.3
12	0.035	319.5	0.147	348.0	0.033	103.8	0.178	147.8	0.033	184.8	0.084	192.2

Table 4.3(b): *Amplitude (cm) and phase (degree GMT) of the six minor constituents at the elements of the open boundary of the Persian Gulf model.*

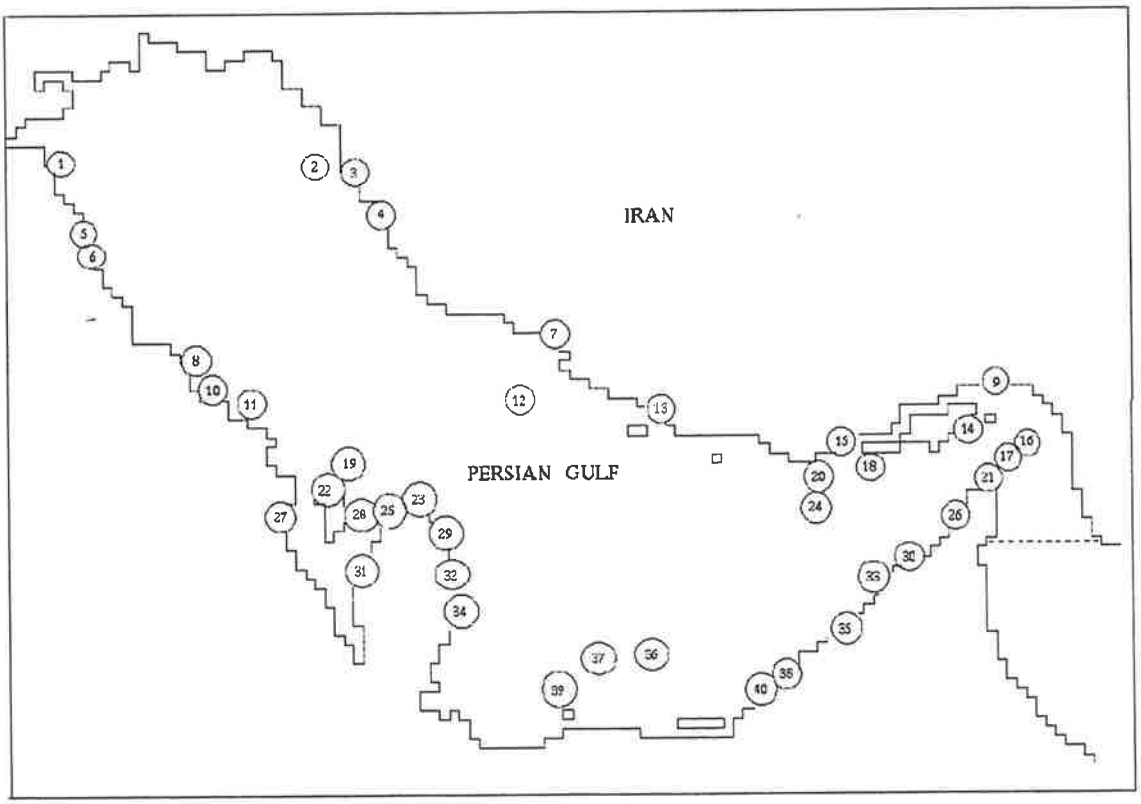

Figure 4.11: *The distribution of the 40 stations in the Gulf used for calibration.*

Reference	Tidal observation station	Map position Lat.(°N)	Long.(°E)
1	MINA-AL-AHMADI	29°4′	48°10′
2	KHARK ISLAND	29°16′	50°20′
3	BUSHEHR	28°54′	50°45′
4	LAVAR	28°15′	51°16′
5	RAS-AL-KHAFJI	28°25′	48°31′
6	RAS AL MISHAAB	28°7′	48°38′
7	ASALU	27°28′	52°37′
8	BERRI - DAWHAT ABU A	27°13′	49°43′
9	BANDAR ABBAS	27°11′	56°17′
10	RAS AL QULAAHY	26°51′	49°54′
11	TARUT BAY	26°39′	50°2′
12	JAZIRAT SHAIKH SHUAI	26°48′	53°23′
13	JAZIREH YE LAVAN	26°48′	52°23′
14	HENJAN	26°41′	55°54′
15	BANDAR LINGEH	26°33′	54°53′
16	LITTLE QUOIN ISLAND	26°28′	56°33′
17	KHOR KAWI	26°22′	56°22′
18	JEZIREH YE TUNBH	26°16′	55°18′
19	BAHRAIN APPROACH BEA	26°22′	50°47′
20	JEZIREH YE FORUR	26°15′	54°31′
21	KHASAB BAY	26°12′	56°15′
22	ZELLAQ	26° 3′	50°29′
23	JABAL FUWAIRT	26° 3′	51°22′
24	JAZIREH YE SIRRI	25°54′	54°33′
25	RUWAIS INSHORE	26°9′	51°13′
26	KHOR KHWAIR	25°58′	56°3′
27	QURAYAH	25°53′	50°7′
28	RAS ASHAIRIQ	25°59′	51°00′
29	RAS LAFFAN	25°54′	51°35′
30	UMM AL QAYWAYN	25°35′	55°35′
31	ZEKRIT	25°28′	50°51′
32	SUMAISMAH	25°34′	51°30′
33	AJMAN	25°25′	55°26′
34	AD DAWHAH	25°18′	51°31′
35	DUBAYY	25°16′	55°17′
36	ZARQA	24°53′	53°5′
37	ARDHANA	24°46′	52°34′
38	UMM AL NAR	24°26′	54°30′
39	DALMA, JAZIRAT	24°28′	52°19′
40	KHAWR ZUBAYYAH	24°20′	54°10′

Table 4.4: *Map position of the 40 selected stations used in calibrating the model of the Persian Gulf.*

4.4.1 Generating the mean sea level depths

The bathymetry for the region has been taken from the British Admiralty charts 2837 and 2847. Because the bathymetry on the charts was so sparse, depths at grid points were estimated by averaging over the region covered by the grid box surrounding each grid point. Since chart datum is Indian Spring Low Water ($ISLW$), and depths should be relative to Mean Sea Level (MSL), so MSL must be generated. By using an iterative process suggested by Mitchell (1985), MSL can be determined accurately. Having the $ISLW$ depth field as a zeroth estimate for MSL every where inside the model region and on the boundary line, and starting a 29 day simulation to predict tide heights at each elevation point of Type 1 in the model, a tidal analysis of the predictions provides a first estimate for MSL as,

$$MSL^{(1)} = ISLW + (O_1 + K_1 + M_2 + S_2)^{(1)}, \tag{4.1}$$

where the quantities in the bracket are amplitudes and superscript "$^{(1)}$" means values are obtained after the first iteration.

The $MSL^{(2)}$ as a second estimate is computed in a similar manner, by using the $MSL^{(1)}$ as the first estimate for the MSL field. The general mathematical procedure can be written as

$$MSL = \lim_{i\to\infty} MSL^{(i)} = ISLW + \lim_{i\to\infty} (O_1 + K_1 + M_2 + S_2)^{(i)}. \qquad (4.2)$$

This process generates MSL accurately. Figure 4.12 shows a bathymetric contour plot of the resulting MSL depth field of the Persian Gulf region. As this figure shows, the Arabian coasts are shallower than the Iranian coasts. The maximum depth of the Gulf is about $90\,m$, which appears in the Strait of Hormuz; the average depth of the Gulf is $32\,m$.

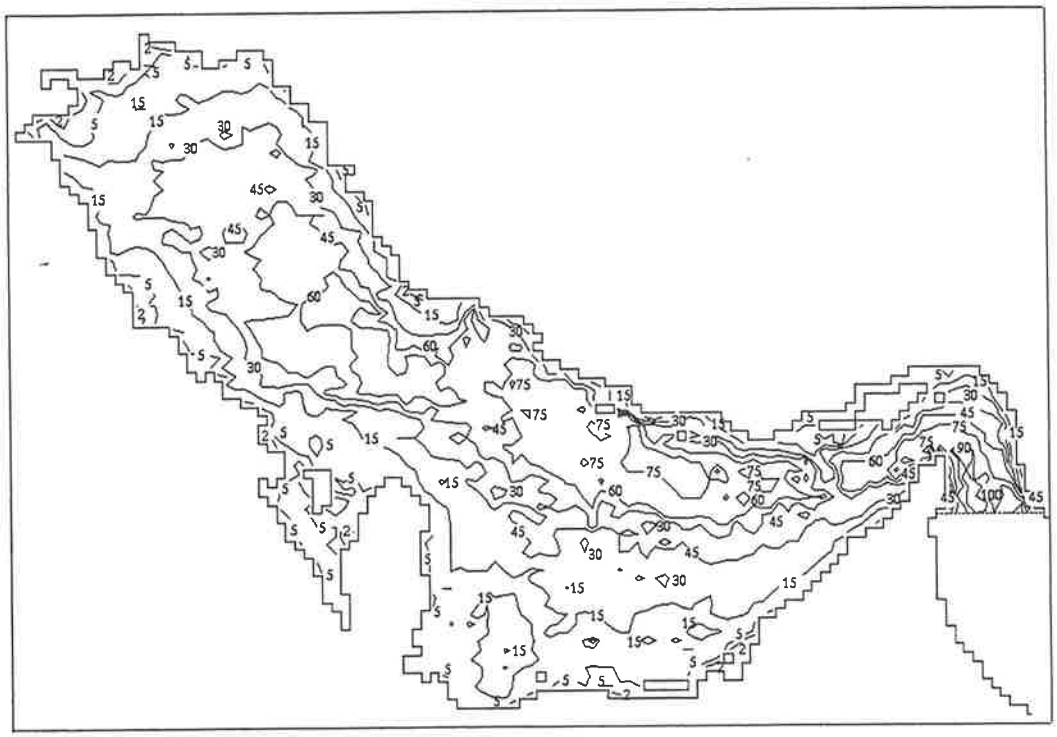

Figure 4.12: *Bathymetric contour plot in meters of the Persian Gulf.*

It should be noted that, along the open boundary, no such calculation is required, because the added amplitudes are provided by the forcing data. The value of $MSL^{(3)}$ was taken as a reasonable estimate for MSL because it was almost the same as $MSL^{(2)}$, to within $0.2\,m$.

The calibration of the depth-averaged model of the Persian Gulf was carried out as follows:
Before applying a model to a particular coastal region, the parameters in the model, namely, the bottom friction, C_b, and the reduced eddy viscosity coefficient, a, in the model are calibrated by comparing the model solutions against observations available at stations in the particular region. Most of the models are calibrated by an iterative trial and error scheme, that is, some initial values are assigned to the parameters of the model, which are then adjusted after several runs, by considering the error measure between model solutions and observations. The tide-height observations at stations listed in Table 4.4 were used in the process of the calibration the model.

The following error measure formulae were used in the calibration procedure (Bills, 1991, pp. 161-162).

(1) Absolute difference error: For constituent c, this error measure is

$$\varepsilon_c = \frac{1}{N}\sum_{s=1}^{N} |o_{c,s} - p_{c,s}| \tag{4.3}$$

where

- ε_c is the absolute difference in amplitude (cm) and phase between the ~~phase~~ observed (in *degrees*) and predicted results averaged over all interior calibration stations for tidal constituent c,
- N is the number of appropriate calibration stations,
- $o_{c,s}$ is the observed amplitude (cm) or phase (*degrees*) of constituent c at station s, and
- $p_{c,s}$ is the predicted amplitude (cm) or phase (*degrees*) of constituent c at stations s.

(2) Average absolute error: The overall average absolute amplitude error ε_a (cm) is

$$\varepsilon_a = \frac{1}{4}\sum_{c=1}^{4} \varepsilon_c \tag{4.4}$$

where ε_c, is the average absolute amplitude error defined for constituent c. An overall average absolute phase error ε_p (*degrees*) is defined in a similar way.

(3) Absolute complex difference error: An overall average absolute complex difference between observed and predicted tide-height, proposed by Mitchell (1985), is

$$\varepsilon = \frac{1}{4N}\sum_{c=1}^{4}\sum_{s=1}^{N} |[\mu_o exp(i\phi_o)]_{c,s} - [\mu_p exp(i\phi_p)]_{c,s}| \tag{4.5}$$

where

ε is the absolute complex difference (cm) between observed and predicted tide-heights averaged over all interior calibration stations for the four constituents O_1, K_1, M_2 and S_2,

$[\mu_o, \phi_o]_{c,s}$ are the observed amplitude (cm) and phase ($degrees$), respectively, of constituent c at station s, and

$[\mu_p, \phi_p]_{c,s}$ are the predicted amplitude (cm) and phase ($degrees$), respectively, of constituent c at station s.

This error measure takes lengths of the differences between complex vectors given by observed and predicted tide-heights and averages them over all interior calibration stations and the four constituents.

The absolute complex difference error is used to compare the results of different runs of the various values of bottom friction, C_b, and reduced horizontal eddy viscosity coefficient, a.

For the Persian Gulf a series of 16 simulations were carried out for different values of C_b, namely 0.0010, 0.0015, 0.0020 and 0.0025 with various values of a, that is, 0.0055, 0.01, 0.03 and 0.04, and an analysis of tide-heights was done for the selected tidal stations listed in Table 4.4. Table 4.5 shows the error measure ε resulting from 16 runs, when the third estimate for MSL was used. The optimal values for C_b and a were found to be 0.0015 and $0.03 sec^{-1}$, respectively, with associated error value of $\varepsilon = 5.376\, cm$. It should be noted that Proctor et al. (1992) used $C_b = 0.0015$ and El-Sabh and Murty (1988) chosed $C_b = 0.0025$. The optimal values have been used in all runs of the programs.

C_b \ a	0.0055	0.01	0.03	0.04
0.0010	5.958	5.874	5.853	5.861
0.0015	5.632	5.412	5.376	5.379
0.0020	5.653	5.592	5.516	5.446
0.0025	5.831	5.822	5.811	5.810

Table 4.5: *Error ε (cm), for various combinations of the values of quadratic friction, C_b, and reduced eddy coefficient a.*

4.5 Presentation of the results

In this section the tidal constants computed from the model and observations of tidal elevation are presented in Table 4.6. For comparison also the contour charts of tidal elevation for the four major tidal constituents, that is, diurnal tidal constituents O_1 and K_1 and the semi-diurnal constituents M_2 and S_2 are presented in Figures 4.13–4.20. The model used the values $C_b = 0.0015$ and $a = 0.03$.

Table 4.6 summarizes the results of model predicted amplitudes and phases, of O_1, K_1, M_2 and S_2 components with observation values at forty tidal stations

around the Gulf, identified in Table 4.4. The averaged complex difference error for the amplitude and phase of sea surface elevation is computed using equation 4.3, and included in Table 4.6. This error is $\varepsilon = 5.376\,cm$. The agreement between predicted and observed values is generally good, with amplitudes being in better agreement.

Observation station		O_1		K_1		M_2		S_2	
		amp	ph	amp	ph	amp	ph	amp	ph
1	Model	17.6	229.9	31.2	277.0	52.0	265.6	11.0	329.8
	Obs.	28.7	215.0	42.9	263.0	62.7	248.0	16.8	312.0
2	Model	17.1	206.6	31.7	247.2	39.3	166.3	14.3	207.7
	Obs.	25.7	192.0	38.8	233.0	36.4	149.0	12.8	196.0
3	Model	15.4	201.4	25.9	241.8	40.2	122.7	14.4	175.2
	Obs.	20.4	189.0	30.7	227.0	33.7	110.0	12.3	160.0
4	Model	11.9	179.4	18.5	214.9	42.3	82.3	14.9	131.3
	Obs.	18.0	171.0	25.3	209.0	49.7	68.0	17.7	117.0
5	Model	15.2	233.7	34.4	266.2	24.9	273.8	5.8	336.8
	Obs.	21.6	221.0	42.3	256.0	32.7	256.0	11.6	320.0
6	Model	14.9	237.0	28.0	337.1	15.7	294.5	3.3	353.7
	Obs.	21.0	221.0	38.0	259.0	25.0	276.0	8.0	335.0
7	Model	12.1	100.9	20.9	130.8	41.9	33.1	13.9	72.2
	Obs.	11.9	89.0	23.8	115.0	51.2	19.0	17.1	57.0
8	Model	8.6	245.8	11.0	291.3	36.0	49.2	12.2	125.1
	Obs.	14.0	227.0	17.0	273.0	44.0	37.0	16.0	107.0
9	Model	26.4	0.1	42.4	22.4	112.4	200.5	43.6	239.1
	Obs.	20.7	3.0	33.8	11.0	100.0	197.0	36.0	229.0
10	Model	4.9	238.1	10.1	292.1	39.1	56.8	12.5	113.7
	Obs.	10.0	218.0	18.0	274.0	48.0	36.0	16.0	93.0
11	Model	4.3	300.4	6.8	345.6	45.0	113.8	15.2	170.0
	Obs.	9.0	281.0	12.0	325.0	54.0	95.0	17.0	159.0
12	Model	14.5	80.6	24.4	101.6	37.8	334.9	14.3	20.9
	Obs.	15.0	55.0	29.0	94.0	30.0	335.0	12.0	10.0
13	Model	10.7	82.8	21.9	115.6	27.4	351.4	10.4	20.1
	Obs.	16.0	65.0	30.0	92.0	33.0	332.0	12.0	6.0
14	Model	22.9	358.2	38.8	28.4	88.9	201.7	35.6	246.3
	Obs.	20.0	14.0	29.0	28.0	73.0	204.0	25.0	247.0
15	Model	15.4	44.3	24.9	73.9	60.6	258.2	23.0	300.3
	Obs.	21.9	40.0	32.6	74.0	59.7	245.0	22.6	282.0
16	Model	24.0	344.5	42.1	14.9	89.3	185.8	35.2	231.4
	Obs.	20.4	355.0	28.7	359.0	76.8	185.0	27.4	221.0
17	Model	21.2	342.8	38.1	6.7	81.0	190.9	32.5	236.0
	Obs.	15.8	349.0	26.2	350.0	68.9	193.0	25.3	227.0
18	Model	16.4	24.8	26.1	57.1	62.2	234.0	24.6	276.9
	Obs.	18.9	38.0	29.3	64.0	59.1	229.0	20.1	266.0
19	Model	3.5	288.1	7.9	31.1	56.1	74.3	12.1	122.7
	Obs.	7.0	268.0	9.0	10.0	63.0	54.0	20.0	102.0
20	Model	14.1	61.3	28.9	103.6	35.1	273.5	10.1	314.2
	Obs.	22.3	41.0	37.5	85.0	45.1	258.0	15.2	294.0

Table 4.6: *Comparison of computed (Model) and observed (Obs.) results for amplitude (cm) and phase (degrees) for the four major tidal constituents at selected stations in the Persian Gulf.*

Observation station		O_1 amp	O_1 ph	K_1 amp	K_1 ph	M_2 amp	M_2 ph	S_2 amp	S_2 ph
21	Model	17.8	348.7	30.8	10.8	75.8	197.3	30.9	242.3
	Obs.	16.0	345.0	22.0	352.0	67.0	196.0	22.0	239.0
22	Model	1.7	47.5	2.7	121.7	11.3	195.1	4.6	259.5
	Obs.	1.8	36.0	1.2	116.0	4.9	196.0	2.1	273.0
23	Model	7.8	9.9	14.7	66.8	36.7	42.0	6.8	87.2
	Obs.	9.4	0.0	20.1	54.0	42.4	44.0	13.1	88.0
24	Model	10.4	44.6	15.3	95.4	37.6	251.3	13.6	294.8
	Obs.	17.6	31.0	24.5	77.0	39.0	235.0	14.5	279.0
25	Model	5.6	327.7	11.2	39.9	41.2	71.0	10.9	120.5
	Obs.	8.0	308.0	15.0	20.0	51.0	57.0	18.0	102.0
26	Model	11.5	15.5	19.7	19.8	60.8	207.6	25.2	251.9
	Obs.	16.0	28.0	21.0	29.0	62.0	210.0	20.0	250.0
27	Model	1.9	24.9	3.0	113.1	22.4	187.2	6.0	238.0
	Obs.	5.0	9.0	7.0	104.0	16.0	169.0	4.0	223.0
28	Model	2.9	328.7	5.3	36.5	31.6	90.4	4.1	143.2
	Obs.	3.7	301.0	7.0	16.0	41.7	72.0	11.3	128.0
29	Model	9.7	18.4	18.0	71.8	29.0	22.0	8.5	71.5
	Obs.	12.0	0.0	25.0	53.0	38.0	37.0	11.0	76.0
30	Model	9.8	23.9	11.1	51.2	43.6	227.8	17.6	270.1
	Obs.	17.0	33.0	20.0	74.0	45.0	234.0	15.0	267.0
31	Model	2.1	19.5	3.2	101.5	7.5	271.2	1.7	300.1
	Obs.	2.4	4.0	8.2	84.0	16.2	257.0	4.3	284.0
32	Model	14.8	33.5	26.8	81.4	35.3	31.2	13.9	77.5
	Obs.	15.0	17.0	34.0	64.0	34.0	37.0	11.0	67.0
33	Model	8.3	53.8	8.1	90.2	35.1	241.3	13.6	289.7
	Obs.	15.0	50.0	17.0	103.0	43.0	248.0	13.0	301.0
34	Model	16.0	37.6	28.8	90.7	38.0	42.7	14.6	98.6
	Obs.	16.4	28.0	36.2	72.0	32.1	51.0	10.8	82.0
35	Model	8.0	75.1	8.8	123.5	32.4	256.5	11.7	299.3
	Obs.	15.0	71.0	19.0	110.0	32.0	254.0	11.0	304.0
36	Model	14.4	80.4	24.7	109.0	17.7	284.3	7.6	353.6
	Obs.	16.3	62.0	35.8	95.0	11.2	266.0	4.0	337.0
37	Model	16.8	80.7	29.1	105.3	15.4	100.2	5.1	110.7
	Obs.	18.5	62.0	40.4	90.0	6.3	95.0	4.0	95.0
38	Model	7.0	125.2	14.0	169.3	14.0	342.6	2.0	12.0
	Obs.	12.0	114.0	22.0	151.0	25.0	323	8.0	26.0
39	Model	18.9	83.0	33.2	120.8	31.5	110.9	12.1	140.5
	Obs.	24.2	67.0	47.2	101.0	14.2	115.0	5.8	122.0
40	Model	12.6	97.0	21.1	136.8	44.6	303.9	16.4	358.0
	Obs.	19.0	81.0	30.0	120.0	37.0	289.0	15.0	343.0
Averaged complex differences		5.376							

Table 4.6(continued): *Comparison of computed (Model) and observed (Obs.) results for amplitude (cm) and phase (degrees) for the four major tidal constituents at selected stations in the Persian Gulf (see Table 4.1(a) for the remaining stations).*

The model was applied to predict the surface elevations for the principal diurnal O_1, K_1 and semi-diurnal M_2 and S_2 constituents. These components are dominant tidal constituents in the Persian Gulf. The contour charts of tide height predicted by the model are presented in Figures 4.13–4.20. These contours show lines of constant amplitude (m) and lines of constant phase (*degrees*). The co-phase lines are given in terms of time zone - 0400, to agree with the Admiralty chart 5081 (Figures 4.3–4.6). As the results show, two amphidromic points appear for the semi-diurnal

constituents M_2 and S_2, and one for the diurnal tide, O_1 and K_1. The bigger values of amplitudes are seen around the the Strait of Hormuz, and in particular the largest value is located at Bandar Abbas (Station 9 in Figure 4.11), and at the head of the Gulf. It should be noted that as Figures 4.13-4.16 show, the basic pattern of the O_1 tide is similar to that of the K_1 tide, because the period of the O_1 is close to the period of K_1, but the magnitude of the O_1 is nearly 20% lower. The same remarks can be made for the similarity of the M_2 and S_2 tides (Figures 4.17 and 4.19, and Figures 4.18 and 4.20). In this case the amplitude of the S_2 is approximately 30% of the M_2 values.

Comparing the resulting contours with the Admiralty chart, Figures 4.3–4.6, suggest that the locations of the amphidromic points and the basic pattern of the contours, predicted by the model are similar to those of the chart, but differ in certain important aspects. For example, modeled results for O_1 and M_2 phases show that in the Strait of Hormuz, near the open boundary, the tidal constituents are moving slower than Admiralty chart, while the K_1 constituent appears to be moving at the same speed, the reason may be a boundary effect.

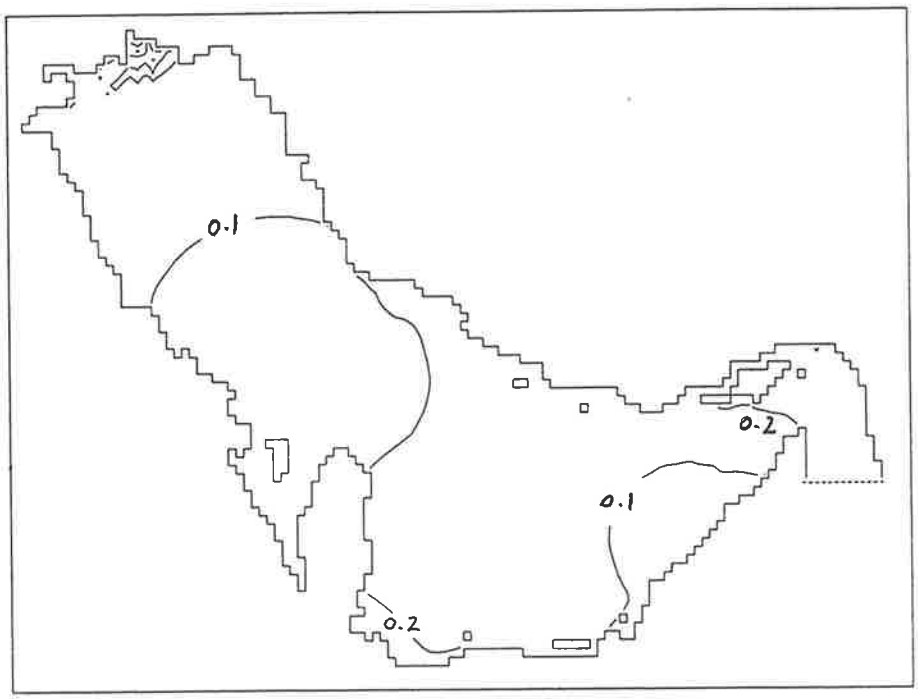

Figure 4.13: *Amplitude contours (m) for the O_1 tidal constituent of sea surface elevation in the Persian Gulf obtained from the Cartesian coordinate model.*

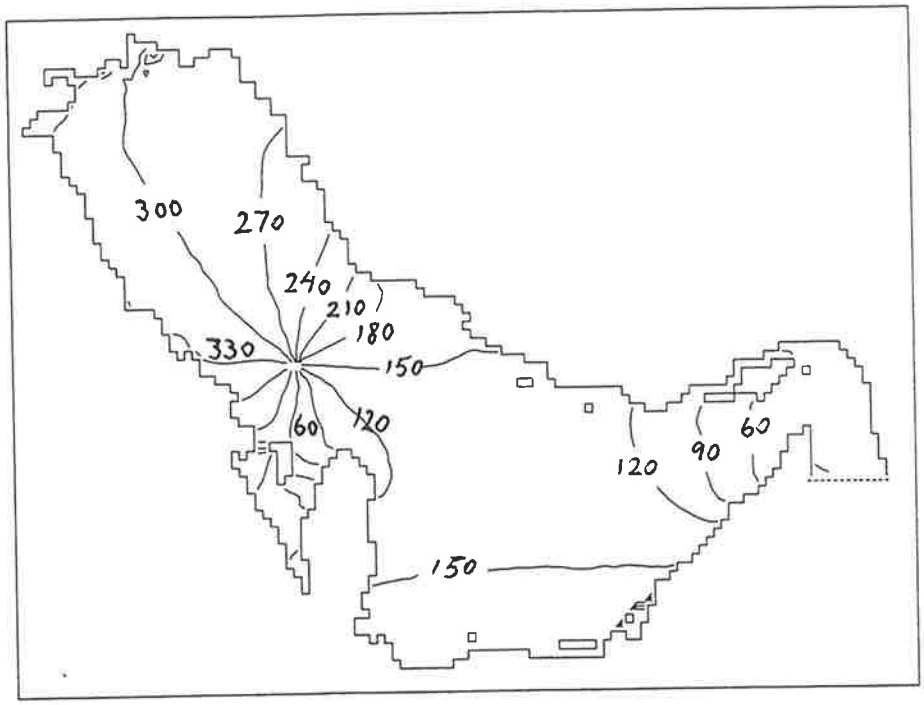

Figure 4.14: *Phase contours (degrees GMT) for the O_1 tidal constituent of sea surface elevation in the Persian Gulf obtained from the Cartesian coordinate model.*

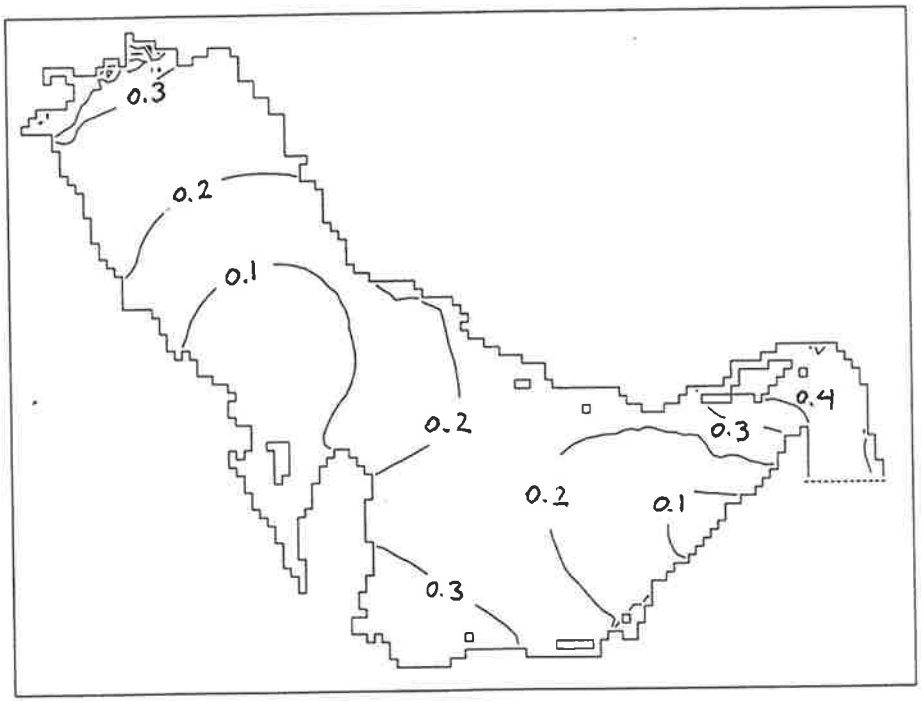

Figure 4.15: *Amplitude contours (m) for the K_1 tidal constituent of sea surface elevation in the Persian Gulf obtained from the Cartesian coordinate model.*

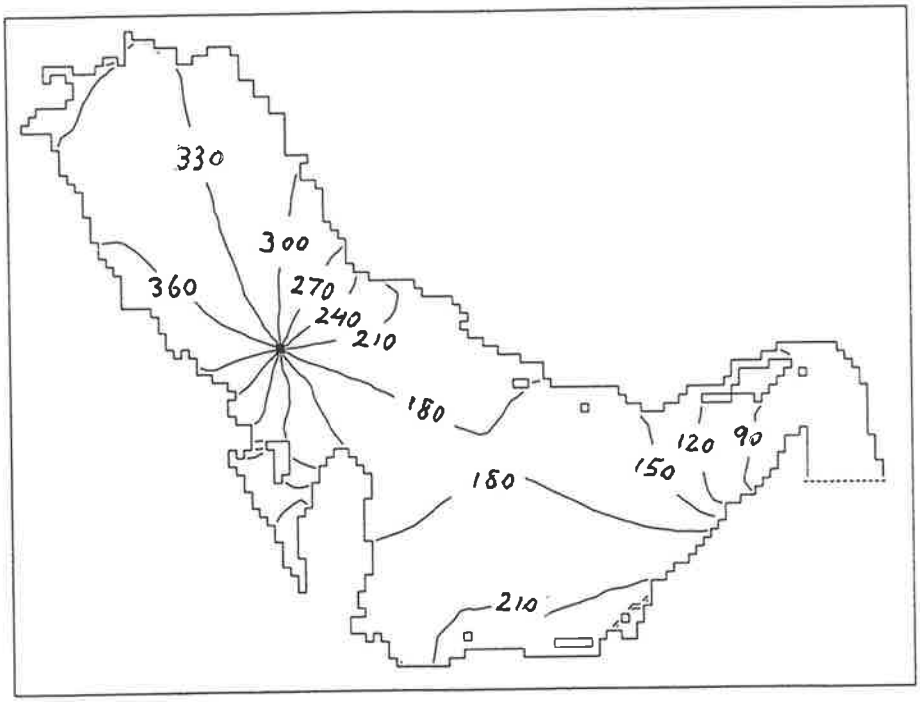

Figure 4.16: *Phase contours (degrees GMT) for the K_1 tidal constituent of sea surface elevation in the Persian Gulf obtained from the Cartesian coordinate model.*

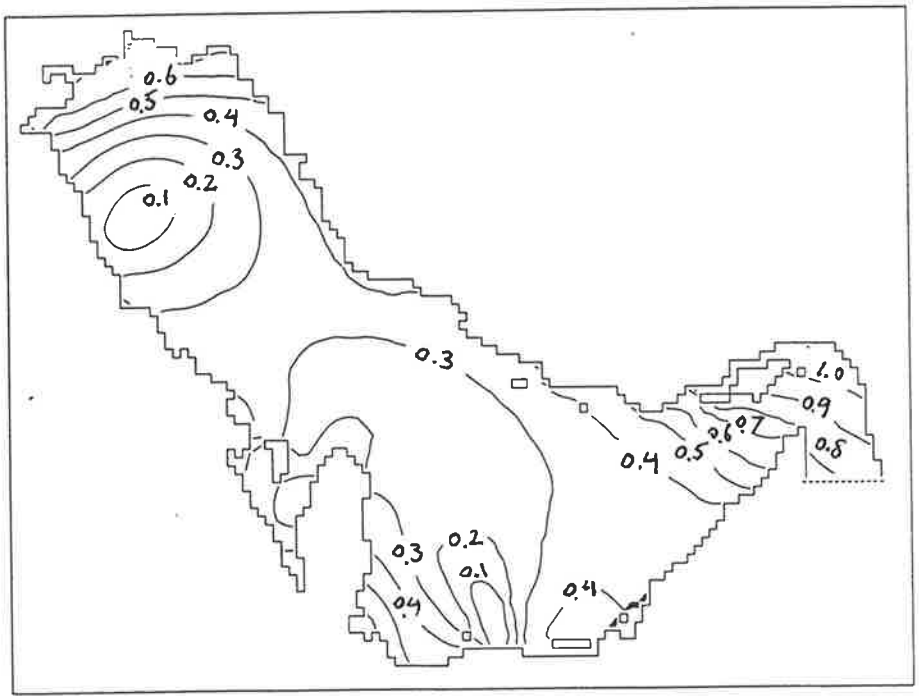

Figure 4.17: *Amplitude contours (m) for the M_2 tidal constituent of sea surface elevation in the Persian Gulf obtained from the Cartesian coordinate model.*

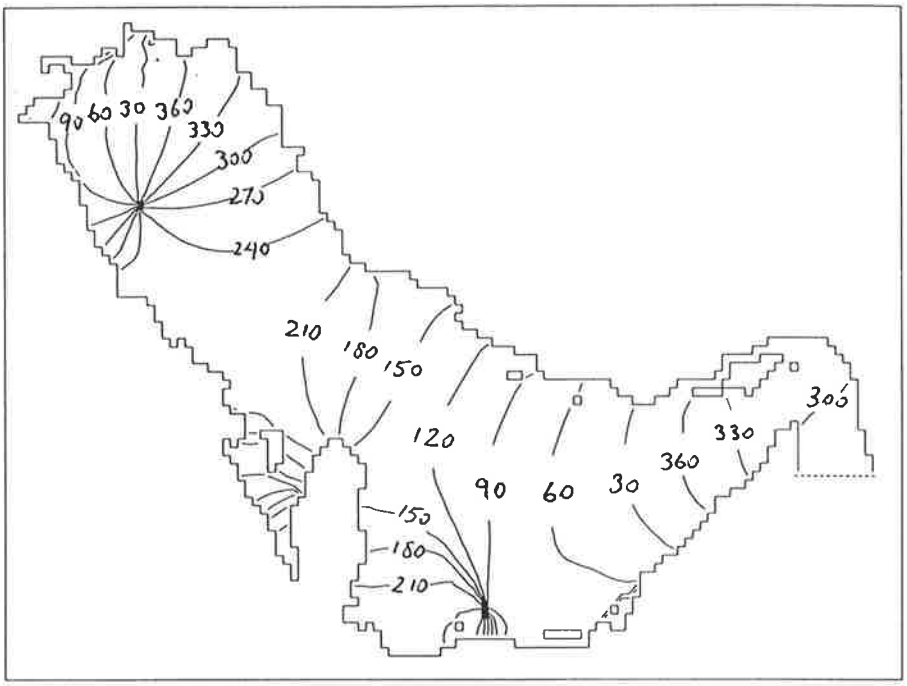

Figure 4.18: *Phase contours (degrees GMT) for the M_2 tidal constituent of sea surface elevation in the Persian Gulf obtained from the Cartesian coordinate model.*

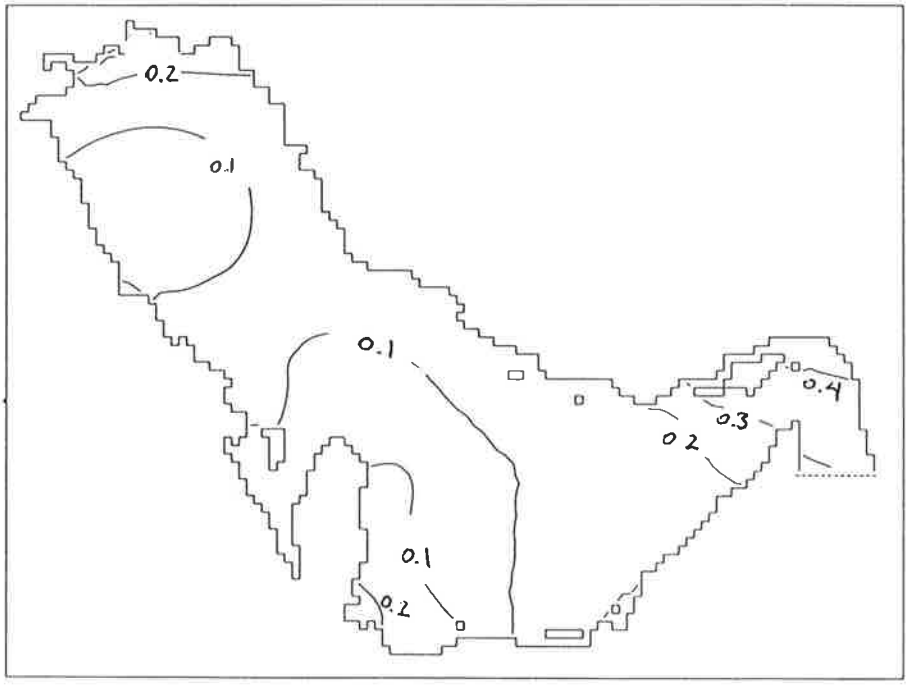

Figure 4.19: *Amplitude contours (m) for the S_2 tidal constituent of sea surface elevation in the Persian Gulf obtained from the Cartesian coordinate model.*

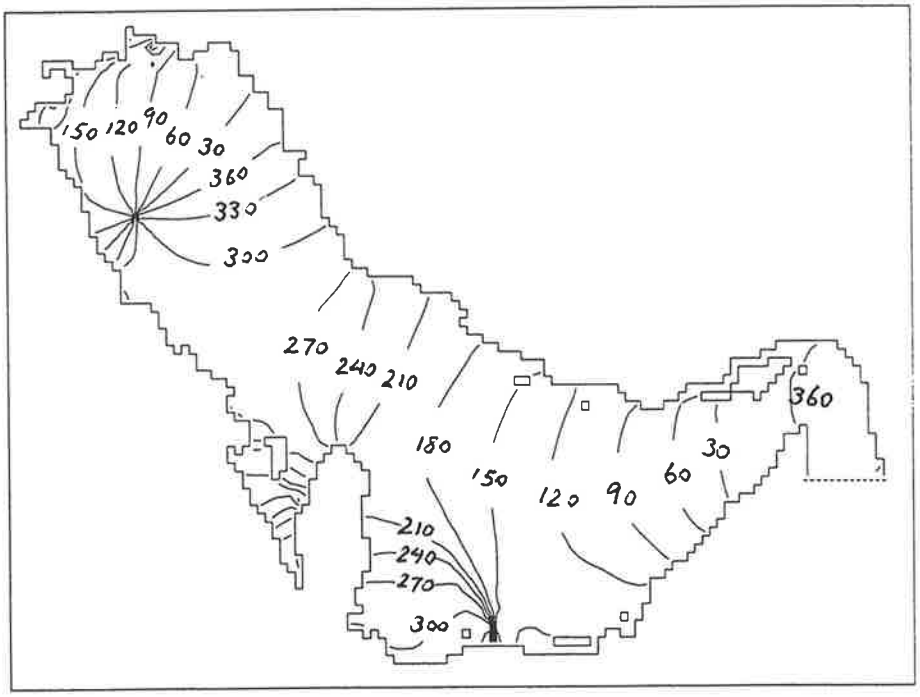

Figure 4.20: *Phase contours (degrees GMT) for the S_2 tidal constituent of sea surface elevation in the Persian Gulfobtained from the Cartesian coordinate model.*

4.6 Summary and discussion

A depth-averaged model of tides using Cartesian coordinates has been developed and applied to the Persian Gulf. The amplitudes and phases of the four major constituents, O_1, K_1, M_2 and S_2, have been reproduced and compared with Admiralty chart 5081. The locations of the amphidromic systems predicted by the model are almost the same, for all constituents, as those shown on the Admiralty chart, and the basic patterns of co-tidal and co-phase lines are similar, but computed phases for O_1 and M_2 show that in the Strait of Hormuz the tidal constituents are moving slower than the same constituents in the Admiralty chart. The predicted amplitudes at the selected stations are generally in better agreement than the predicted phases (see Table 6). It is expected to improve the performance of the model by using a spherical coordinate grid, since the Persian Gulf is too large to be approximated by a plane surface. Also the grid may be refined in certain regions, because the spatial variations in tides are very large in the Gulf, especially near the amphidromic regions, and because the coastline generally has a complicated shape and very variable bottom topography.

Chapter 5

A Depth-averaged Spherical Model of the Persian Gulf

5.1 Introduction

The depth-averaged Cartesian model of tides in the Persian Gulf was developed in Chapter 4. The amplitudes and phases of the four major constituents, O_1, K_1, M_2 and S_2, have been reproduced and compared with Admiralty chart 5081. Although there was generally good agreement between observed and computed tides from this model, the results can be improved by using a spherical coordinate grid since the Persian Gulf is large. Some researchers, for example Le Provost (1984), have already noticed that using spherical coordinates can improve the agreement between modelled and measured tide heights. This chapter discusses the development of a spherical depth-averaged model of the Persian Gulf.

5.2 Review of spherical models of the Persian Gulf

A number of spherical coordinate models of tides in the Persian Gulf have already been developed. In this section these works are discussed; Table 5.1 summarizes the important features of these models.

Evans-Roberts (1979) provided an extensive survey of tides in the Persian Gulf. He developed a spherical coordinate model with a mesh-size of $10'$ latitude and $10'$ longitude. He used a low-cost method to reproduce the M_2 and K_1, the most important tidal components in the Gulf. This method simulates the M_2 constituents and an artificial diurnal tide (AM_1) with the amplitude and phase of K_1 but period of exactly twice M_2. This produces a tide cycle which will repeat at intervals of approximately 24.8 hours. This is an economical method because the main features of the tides in the Gulf can be studied without the need to generate and analyse large quantities of results, but it should be pointed out that the other constituents such as S_2 and O_1 cannot be studied by this method; they can be approximated using the averaged ratios formula calculated for tidal amplitudes (see Bills, 1992,

p.142). The co-tidal map of M_2 produced by his model is presented in Figure 5.1. The amplitudes generated for M_2 are lower than those shown on the Admiralty chart 5081, but the phase contour lines are in good agreement. However, he believed that using the fairly coarse grid he used reduced the accuracy.

Authors	**Year**	**Depth averaged (DA) or 3D**	**Numerical technique used**	**Bottom friction used**	**Region modelled**	**Number of active or non-active grid element**	**Element dimension**
Evans-Roberts	1979	DA	N/A	N/A	whole Gulf	N/A	$10' \times 10'$
Hunter	1984	DA	explicit finite-difference	quadratic law	Kuwait waters	N/A	$2.5' \times 2.5'$
Elahi and Ashrafi	1992a	DA	explicit finite-difference	quadratic law	whole Gulf	39×54 = 2106	18×18km^2
Elahi and Ashrafi	1992b	DA	explicit finite-difference	quadratic law	whole Gulf	39×54 = 2106	18×18km^2

Table 5.1: *A summary of some spherical models of the Gulf. N/A means not available. Time steps are N/A.*

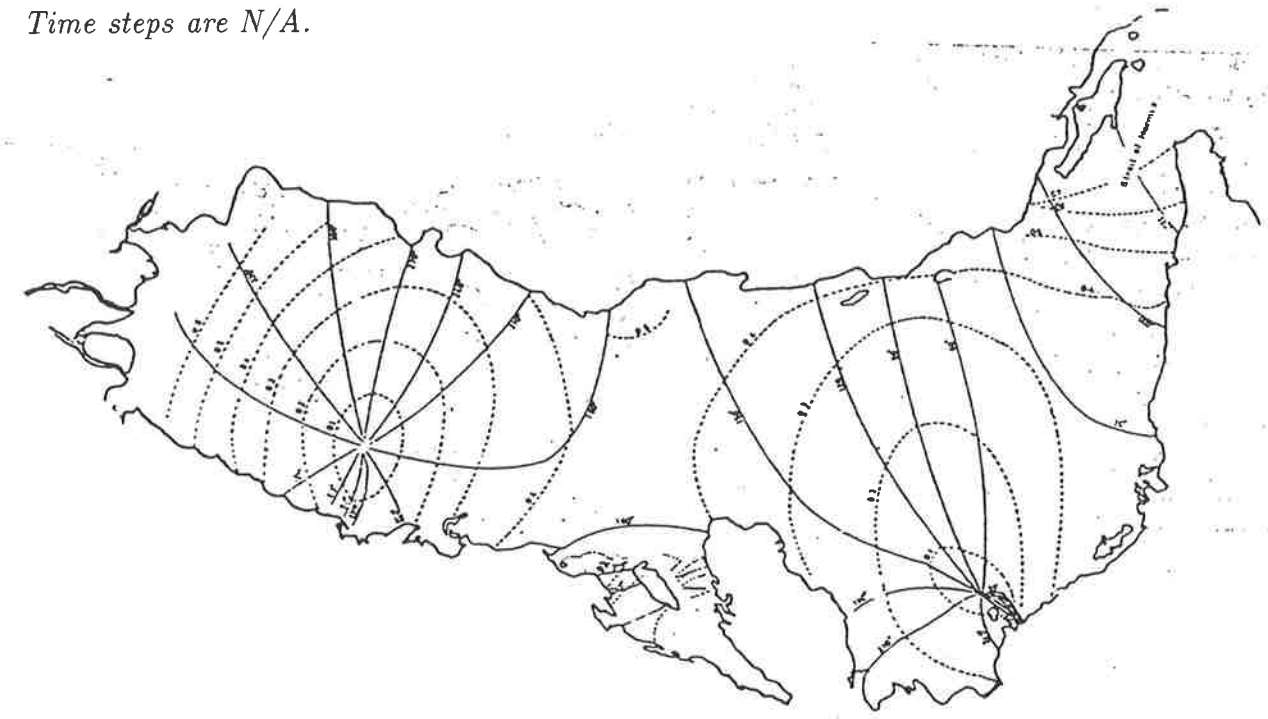

Figure 5.1: *Amplitude contours (dashed lines,(m)) and phase contours (solid lines, (degrees))for the M_2 tidal constituent of sea surface elevation in the Persian Gulf, produced by Evans-Roberts (1979, p.46).*

Hunter (1984) developed a depth-averaged spherical-coordinate numerical model to investigate the M_2 and K_1 tidal motions for Kuwaiti waters, the first time that this region has been modeled in detail. The depth-averaged velocities produced by the tidal model have been used as an input for developing a stratified model. An explicit finite difference scheme has been used to solve the depth-averaged equations –using a combination of forward and centered difference approximations. The non-linear effects due to the advective terms in the equations were included. He examined separately the two tidal constituents, M_2 and K_1, as was done by Von Trepka (1968). Because they were run separated the model neglected the non-linear interactions between M_2 and K_1. When Von Trepka was trying to reproduce the O_1 and S_2 components, he noted that the results were poor: the amplitude of the water elevations were always too large. He came to the conclusion that since the Persian Gulf is an extremely shallow sea the complete non-linear effects can not be neglected (ibid., p.61). In order to take into account the complete non-linear interaction between the different constituents, he prescribed a real prediction of sea surface elevations at the open boundary of the model by including seven constituents.

Hunter (1984) also ran the M_2 and K_1 components separately, by using a different bottom friction coefficient for each component. For testing the performance of the model he compared the model results with the observed harmonic constants at five tidal stations. From the initial runs of his model using an M_2 tidal input, Hunter found that the Admiralty chart 5081 of the Persian Gulf was possibly in error in Kuwaiti waters (ibid., p.15).

Elahi and Ashrafi (1992a) described a spherical-coordinate model to consider tides and currents in the Gulf. They solved the two-dimensional shallow water equations using an explicit finite difference scheme. Along the open boundary the elevations of four constituents, O_1, K_1, M_2 and S_2 were specified. They presented contour charts of amplitude and phase of the major components of tide-height. The locations of the amphidromic points are in reasonable agreements with the chart 5081 and the patterns of the contour lines are also similar. They report that around the coast of Bahrain the results are not encouraging.

Elahi and Ashrafi (1992a and 1992b) described a depth-averaged hydrodynamic numerical model. They have provided a table of comparison between the predicted and observed tidal constants at 18 stations around the Gulf (ibid., p.168) for the four major constituents.

There are some other spherical coordinate numerical models which have already been developed and applied to certain regions other than the Persian Gulf. Table 5.2 summarizes some of these models.

Authors	Year	Application	Region modelled
Zahel	1973	DA/ tides	world ocean
Flather and Davies	1976	DA/ storm surges	North Sea
Davies and Flather	1978	DA/ storm surges	North Sea
Flather	1981	DA/ storm surges	North Sea
Flather and Proctor	1983	DA/ storm surges	North Sea
Chilicka, Kowalik and Wierzbicki	1983	DA/ storm surges	Baltic Sea
Mitchell and Noye	1983	3D/ tides	Gulf of Carpentaria
Flather	1984	DA/ storm surges	North Sea
Fang and Yang	1988	DA/ tides	Korea Strait
Davies and Jones	1992	3D/ tides	Celtic and Irish Sea
Verboom, Ronde and Dijk	1992	DA/ storm surges	North Sea
Davies and Jones	1993	DA/ storm surges	Celtic and Irish Sea
Davies and Lawrence	1994	3D/ tides	Irish Sea

Table 5.2: *A summary of some spherical coordinate numerical models of other regions. DA means depth-averaged.*

5.3 Depth-averaged spherical tidal model

The spherical depth-averaged tidal model of the Persian Gulf developed for this thesis uses an element dimension of $5' \times 5'$ and a time step of $\Delta t = 200sec$. The top left and bottom right corner of the grid have coordinates of 30.37° and 48.55° and 23.87° and 53.58°, north latitude and east longitude, respectively. The positive ϕ-axis and λ-axis are directed north and east, respectively. The grid contains 79×118 elements; 3199 of which are used in the computations. The location of the open boundary is the same of that of the Cartesian model, that is the dashed line in Figure 4.1. The same set of open boundary data were used for the Cartesian model, is used for the spherical model (Tables 4.3(a) and 4.3(b)). The model runs for 29

days, after ignoring the first three days of simulation which are contaminated by initial transients. Predictions for the 29 days are saved hourly and then tidally analysed as described in Chapter 4 (Section 4.4).

The original Cartesian coordinate computer program (Section 3.1.4), has been converted to spherical coordinates to implement the finite difference form of the depth-averaged spherical tidal equations, including the additional terms resulting from the transformation into spherical coordinates.

5.4 Calibrating the model

This section discusses the approach and results of calibrating the spherical model. The model was applied to the Persian Gulf and calibrated with tidal data at the forty stations listed in Table 4.4. The model calibration was done using the trial-and-error scheme, in a similar manner to that used for calibrating the Cartesian model in Chapter 4. In this study the bottom friction, C_b and the reduced eddy viscosity coefficient, a, are calibrated.

Viscosity coefficients were formulated in equations (2.11)-(2.12) and are approximated in equations (3.55) and (3.58), respectively. In some tidal models of shallow seas the horizontal eddy viscosity terms are not included, for example, Flather and Heaps (1975), Blumberg (1977) and Lardner et al. (1982) and some others use global constants for the reduced eddy viscosity coefficient, for example, Noye et al. (1981, 1982). Greenberg (1983) used equation (2.10); the value of a in his model was set to $1.64\times10^{-3}sec^{-1}$. Schwiderski (1980) included the horizontal viscosity terms in his global models. He found that the value of the coefficients depends linearly on both the depth and the horizontal element sizes (see equations (2.11)-(2.12)).

Bills (1992) included the viscosity term in his Spencer Gulf model; the optimal value for reduced viscosity coefficient was found to be a=$0.0055sec^{-1}$, with a constant coefficient of quadratic friction $C_b = 0.0025$.

The objective of the calibration is to match the model solutions to the observations as closely as possible; to do this the mean absolute complex difference error measure, equation (4.5), is used. The bathymetric data used in the Cartesian model is for the spherical model. The calibrating experience of the Cartesian model is used to assign the appropriate start values for the parameters, which reduces the number of runs. For the Persian Gulf model a series of simulations were carried out for a range of C_b between 0.0010 and 0.0025 and different values of a, that is, 0.0005, 0.001, 0.002 and 0.003; then an analysis of tide-heights was carried out for the selected tidal stations listed in Table 4.4. The optimal values for C_b and a were found to be 0.0015 and $a = 0.001sec^{-1}$, respectively, with corresponding error of $\varepsilon = 4.347cm$. The value for C_b is the same as that of the Cartesian model, but the value of a for the Cartesian model of Chapter 4 was found to be $a = 0.03sec^{-1}$, which is larger comparing with the value of a in the spherical model. Table 5.3 shows the error measure ε resulting from 16 runs, and the values of C_b and a used in the calibration process. As this table shows, for different values of a the error varies

slightly, indicating that the model is not very sensitive to this parameter (see Bills, 1992, p.164). The optimal value is used in all runs of the programs. It should be noted that Elahi and Ashrafi (1992a) chose $C_b = 0.003$, and Proctor et al. (1992) used $C_b = 0.0015$, for their model of the Gulf.

C_b \ a	0.0005	0.001	0.002	0.003
0.0010	4.916	4.852	4.857	4.866
0.0015	4.512	4.347	4.348	4.349
0.0020	4.553	4.517	4.516	4.488
0.0025	4.879	4.860	4.851	4.840

Table 5.3: *Error ε (cm), for various combinations of values of quadratic friction, C_b, and reduced eddy coefficient a.*

5.5 Presentation of the results and discussion

In this section the model predictions for tidal elevations are presented. The predictions have been compared with the observational data at the forty stations shown in Table 4.4, and they are presented in Tables 5.1(a) and 5.1(b).

The tables show good agreement between predicted and observed values, especially the amplitudes.

The model was applied to simulate the tidal elevations of the four major tidal constituents, O_1, K_1, M_2 and S_2 constituents. The contour charts of amplitude and phase of the major components as predicted by the model, are presented in Figures 5.2–5.9. These contours show lines of constant amplitude (m) and lines of constant phase (*degrees*). The co-phase lines are given in GMT, time zone - 0400, to agree with the Admiralty chart, 5081 (Figures 4.3–4.6).

Observation station		O_1		K_1		M_2		S_2	
		amp	ph	amp	ph	amp	ph	amp	ph
1	Model	22.7	227.2	36.4	274.0	50.4	262.8	10.4	326.2
	Obs.	28.7	215.0	42.9	263.0	62.7	248.0	16.8	312.0
2	Model	19.0	204.9	31.3	246.6	36.9	161.0	12.4	210.8
	Obs.	25.7	192.0	38.8	233.0	36.4	149.0	12.8	196.0
3	Model	17.0	200.6	25.8	237.1	37.3	124.5	12.5	171.9
	Obs.	20.4	189.0	30.7	227.0	33.7	110.0	12.3	160.0
4	Model	12.4	180.8	19.3	220.3	41.7	70.6	13.5	127.8
	Obs.	18.0	171.0	25.3	209.0	49.7	68.0	17.7	117.0
5	Model	18.8	233.7	31.6	266.8	24.7	270.0	5.6	334.6
	Obs.	21.6	221.0	42.3	256.0	32.7	256.0	11.6	320.0
6	Model	18.4	232.4	31.1	271.1	17.7	290.6	2.6	347.6
	Obs.	21.0	221.0	38.0	259.0	25.0	276.0	8.0	335.0
7	Model	12.8	98.3	23.5	125.1	43.0	30.2	12.6	71.6
	Obs.	11.9	89.0	23.8	115.0	51.2	19.0	17.1	57.0
8	Model	9.8	238.8	11.2	283.3	36.0	49.5	11.4	119.7
	Obs.	14.0	227.0	17.0	273.0	44.0	37.0	16.0	107.0
9	Model	23.8	359.4	42.8	21.9	107.1	200.1	40.0	237.7
	Obs.	20.7	3.0	33.8	11.0	100.0	197.0	36.0	229.0
10	Model	6.9	227.3	9.7	285.1	39.6	48.1	12.0	105.5
	Obs.	10.0	218.0	18.0	274.0	48.0	36.0	16.0	93.0
11	Model	5.9	285.2	8.2	332.2	48.8	95.3	15.2	156.9
	Obs.	9.0	281.0	12.0	325.0	54.0	95.0	17.0	159.0
12	Model	15.7	63.5	28.1	104.8	33.0	331.9	12.0	17.5
	Obs.	15.0	55.0	29.0	94.0	30.0	335.0	12.0	10.0
13	Model	11.4	78.5	23.7	106.7	25.6	343.6	9.5	21.6
	Obs.	16.0	65.0	30.0	92.0	33.0	332.0	12.0	6.0
14	Model	22.1	10.2	37.6	31.6	82.6	201.9	31.9	246.3
	Obs.	20.0	14.0	29.0	28.0	73.0	204.0	25.0	247.0
15	Model	17.6	47.2	28.8	85.6	57.4	254.4	20.1	291.6
	Obs.	21.9	40.0	32.6	74.0	59.7	245.0	22.6	282.0
16	Model	22.0	344.9	34.6	10.7	85.3	185.9	32.4	230.7
	Obs.	20.4	355.0	28.7	359.0	76.8	185.0	27.4	221.0
17	Model	19.3	344.9	36.3	2.7	77.5	190.6	30.9	234.4
	Obs.	15.8	349.0	26.2	350.0	68.9	193.0	25.3	227.0
18	Model	18.6	29.3	29.5	66.1	63.2	233.5	23.1	272.4
	Obs.	18.9	38.0	29.3	64.0	59.1	229.0	20.1	266.0
19	Model	3.4	283.3	7.9	18.7	54.1	62.6	10.2	114.2
	Obs.	7.0	268.0	9.0	10.0	63.0	54.0	20.0	102.0
20	Model	13.7	56.2	27.3	103.3	34.2	274.3	9.1	310.8
	Obs.	22.3	41.0	37.5	85.0	45.1	258.0	15.2	294.0

Table 5.1(a): *Comparison of computed (Model) and observed (Obs.) results for amplitude (cm) and phase (degrees) for the four major tidal constituents at selected stations in the Persian Gulf (see Table 5.1(b) for the remaining stations.)*

Observation station		O_1		K_1		M_2		S_2	
		amp	ph	amp	ph	amp	ph	amp	ph
21	Model	17.9	351.7	30.5	6.1	75.0	197.4	28.9	242.0
	Obs.	16.0	345.0	22.0	352.0	67.0	196.0	22.0	239.0
22	Model	2.2	45.0	3.6	128.9	12.3	180.2	4.9	262.8
	Obs.	1.8	36.0	1.2	116.0	4.9	196.0	2.1	273.0
23	Model	7.8	11.5	16.3	69.6	31.2	51.4	7.0	92.8
	Obs.	9.4	0.0	20.1	54.0	42.4	44.0	13.1	88.0
24	Model	13.7	43.2	21.5	89.2	39.6	247.2	13.5	293.6
	Obs.	17.6	31.0	24.5	77.0	39.0	235.0	14.5	279.0
25	Model	5.3	322.8	11.9	39.2	43.6	72.4	9.9	117.0
	Obs.	8.0	308.0	15.0	20.0	51.0	57.0	18.0	102.0
26	Model	13.2	18.6	21.3	33.6	64.0	209.6	24.3	253.5
	Obs.	16.0	28.0	21.0	29.0	62.0	210.0	20.0	250.0
27	Model	2.3	23.1	3.6	120.0	24.9	184.6	6.3	234.9
	Obs.	5.0	9.0	7.0	104.0	16.0	169.0	4.0	223.0
28	Model	3.0	324.8	6.4	31.8	32.6	87.7	5.3	142.7
	Obs.	3.7	301.0	7.0	16.0	41.7	72.0	11.3	128.0
29	Model	9.8	12.8	20.1	64.3	24.3	34.3	7.9	77.2
	Obs.	12.0	0.0	25.0	53.0	38.0	37.0	11.0	76.0
30	Model	9.6	36.2	12.0	70.1	47.0	228.7	16.9	272.5
	Obs.	17.0	33.0	20.0	74.0	45.0	234.0	15.0	267.0
31	Model	2.8	14.8	4.4	96.2	9.3	247.2	2.5	294.9
	Obs.	2.4	4.0	8.2	84.0	16.2	257.0	4.3	284.0
32	Model	15.6	30.0	30.7	77.8	32.4	31.5	12.4	85.2
	Obs.	15.0	17.0	34.0	64.0	34.0	37.0	11.0	67.0
33	Model	9.0	53.8	10.6	99.8	41.1	240.1	14.1	290.4
	Obs.	15.0	50.0	17.0	103.0	43.0	248.0	13.0	301.0
34	Model	17.0	34.6	33.4	82.4	35.3	40.4	13.3	94.1
	Obs.	16.4	28.0	36.2	72.0	32.1	51.0	10.8	82.0
35	Model	9.4	80.2	12.4	121.1	38.0	252.4	12.5	300.8
	Obs.	15.0	71.0	19.0	110.0	32.0	254.0	11.0	304.0
36	Model	16.7	73.8	31.0	107.2	15.8	278.4	6.6	349.4
	Obs.	16.3	62.0	35.8	95.0	11.2	266.0	4.0	337.0
37	Model	18.7	76.6	35.3	102.8	16.7	86.4	5.9	107.0
	Obs.	18.5	62.0	40.4	90.0	6.3	95.0	4.0	95.0
38	Model	16.3	119.4	24.5	163.4	32.4	333.0	12.7	36.6
	Obs.	12.0	114.0	22.0	151.0	25.0	323.0	8.0	26.0
39	Model	20.5	78.1	39.5	112.5	30.8	105.2	12.5	137.8
	Obs.	24.2	67.0	47.2	101.0	14.2	115.0	5.8	122.0
40	Model	16.1	95.2	28.6	132.2	47.4	300.0	17.2	354.4
	Obs.	19.0	81.0	30.0	120.0	37.0	289.0	15.0	343.0
Averaged complex differences		4.347							

Table 5.1(b): *Comparison of computed (Model) and observed (Obs.) results for amplitude (cm) and phase (degrees) for the four major tidal constituents at selected stations in the Persian Gulf (see Table 5.1(a) for the remaining stations.)*

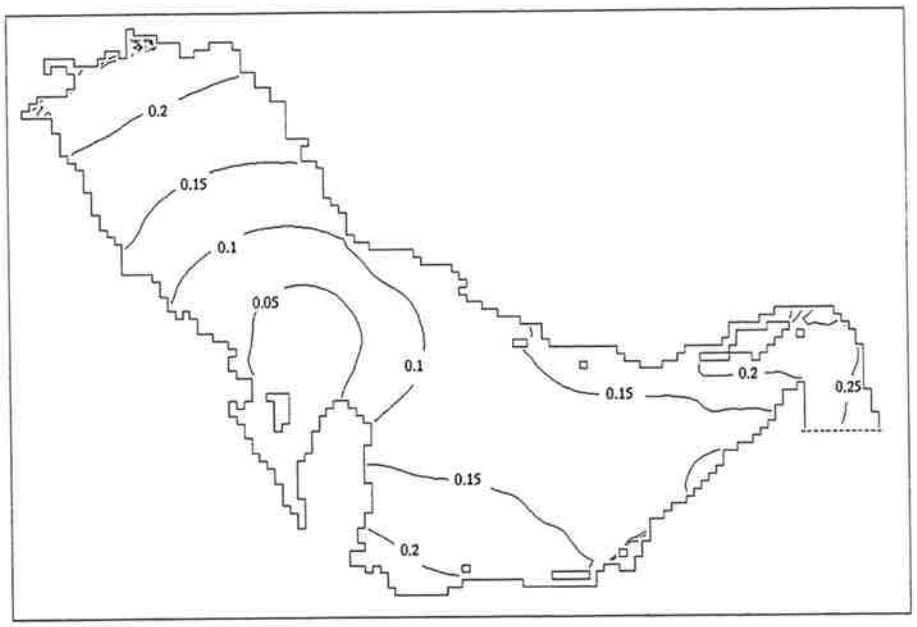

Figure 5.2: *Amplitude contours (m) for the O_1 tidal constituent of sea surface elevation in the Persian Gulf obtained from the spherical coordinate model.*

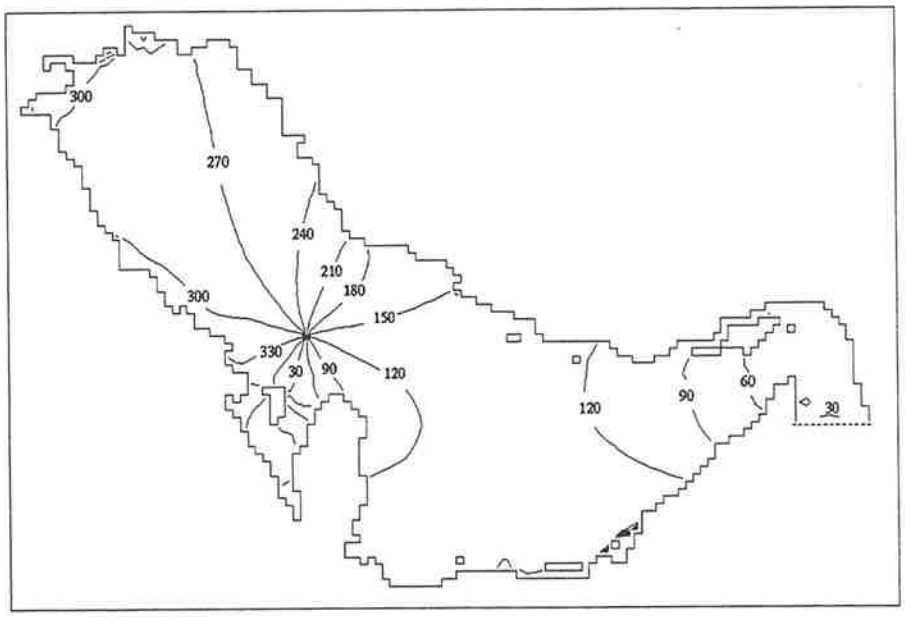

Figure 5.3: *Phase contours (degrees GMT) for the O_1 tidal constituent of sea surface elevation in the Persian Gulf obtained from the spherical coordinate model.*

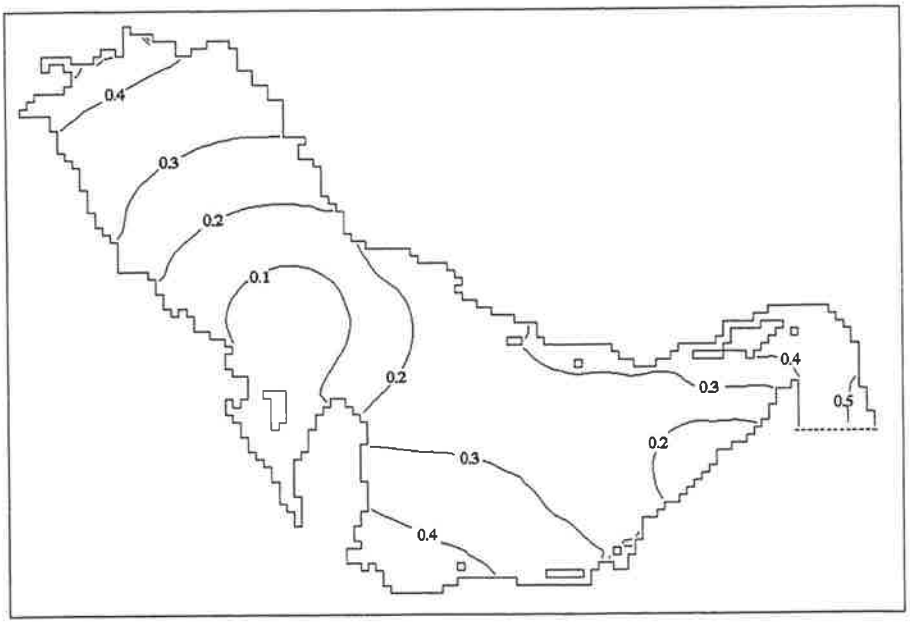

Figure 5.4: *Amplitude contours (m) for the K_1 tidal constituent of sea surface elevation in the Persian Gulf obtained from the spherical coordinate model.*

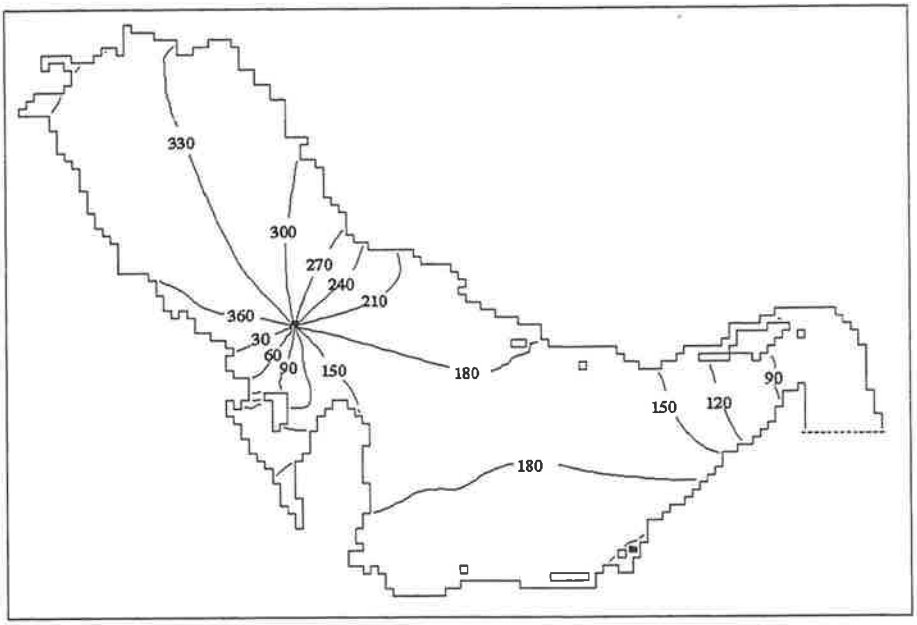

Figure 5.5: *Phase contours (degrees GMT) for the K_1 tidal constituent of sea surface elevation in the Persian Gulf obtained from the spherical coordinate model.*

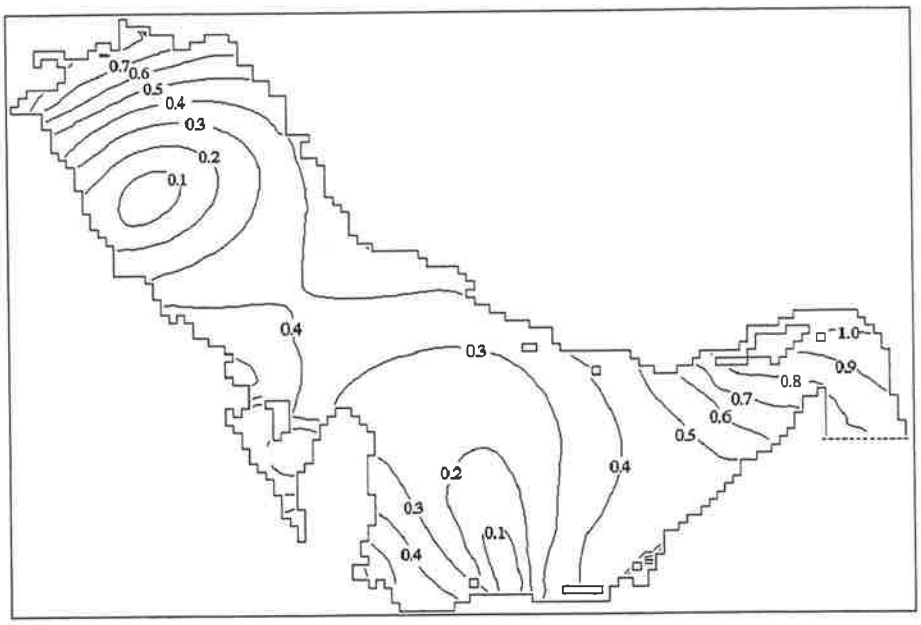

Figure 5.6: *Amplitude contours (m) for the M_2 tidal constituent of sea surface elevation in the Persian Gulf obtained from the spherical coordinate model.*

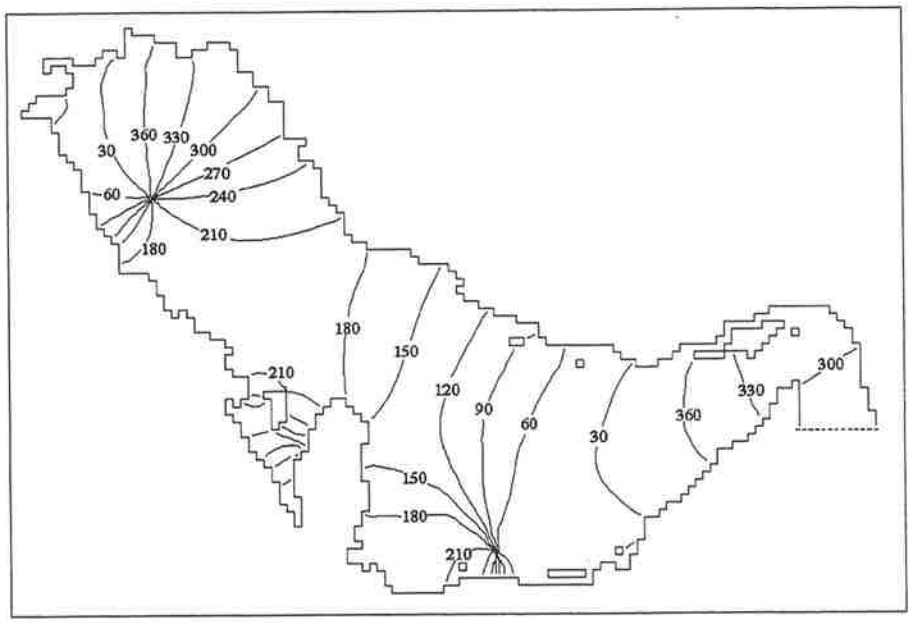

Figure 5.7: *Phase contours (degrees GMT) for the M_2 tidal constituent of sea surface elevation in the Persian Gulf obtained from the spherical coordinate model.*

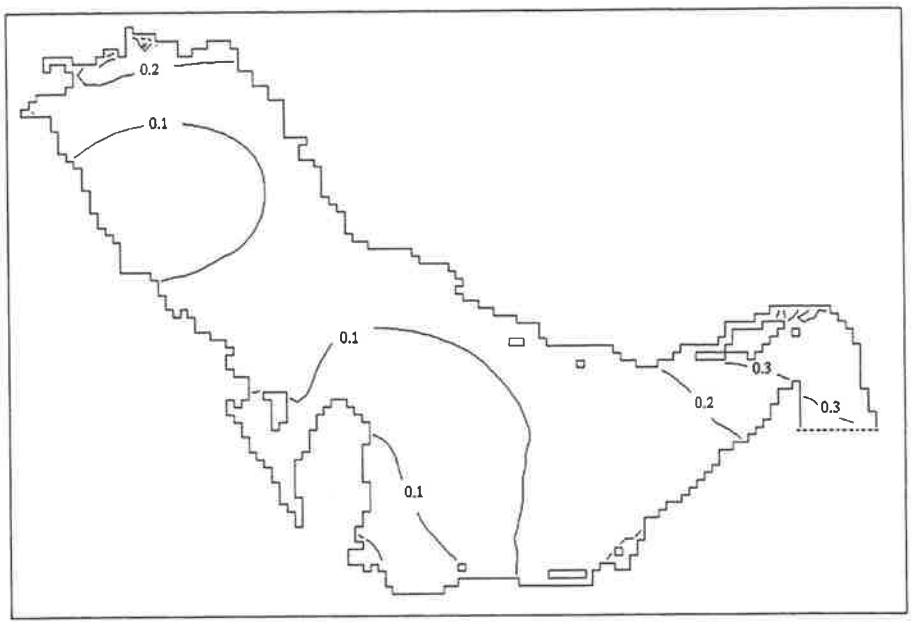

Figure 5.8: *Amplitude contours (m) for the S_2 tidal constituent of sea surface elevation in the Persian Gulf obtained from the spherical coordinate model.*

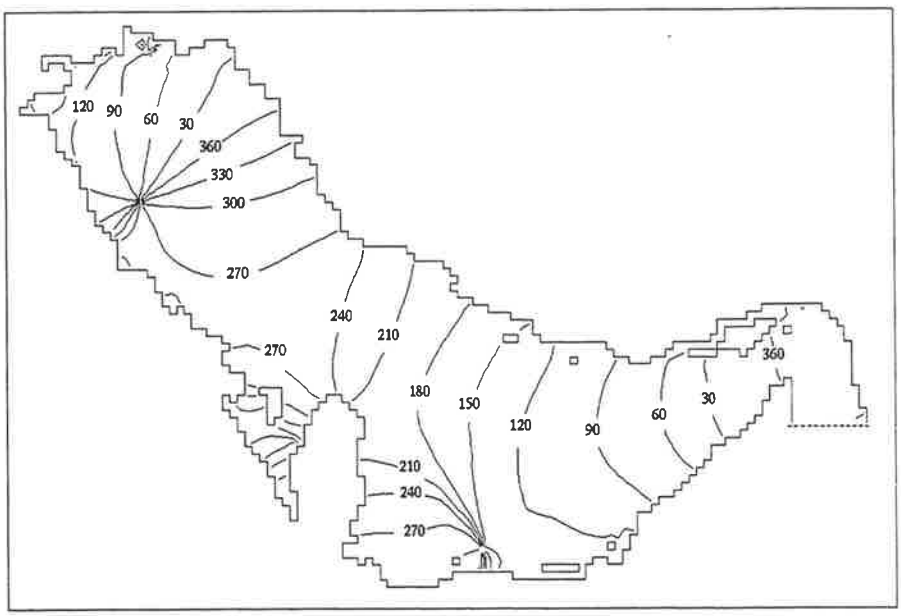

Figure 5.9: *Phase contours (degrees GMT) for the S_2 tidal constituent of sea surface elevation in the Persian Gulf obtained from the spherical coordinate model.*

The main features of the results and their comparison with the Admiralty chart are described in the following:

1. In the results

   - Two amphidromic points appeared for the semi-diurnal constituents, M_2 and S_2, and one for the diurnal components O_1 and K_1.
   - In general, the high amplitude values occur around the Strait of Hormuz, especially at Bandar Abbas (Station 9 in Figure 4.11) and the head of the Gulf.
   - The basic pattern of the O_1 constituent is similar to that for K_1, because the period of the O_1 is close to the period of K_1, but the magnitude of the O_1 is almost 20% lower.
   - The S_2 tide has a similar pattern to the M_2 for the same reasons, but in this case the amplitude of the S_2 is approximately 30% of the M_2 values.

2. When compared with the Admiralty chart

   - The location of the amphidromic points predicted by the model are similar to the Admiralty chart 5081.
   - The modeled results for O_1 and M_2 phases indicate that in the Strait of Hormuz, near the open boundary the phases are moving more slowly than those shown in the chart and they move anticlockwise through the Gulf.
   - The predicted phases for the K_1 constituent in the Strait of Hormuz are almost the same as those observed in the chart and they move clockwise in the Gulf.
   - The predicted phases for the S_2 constituent in the Strait of Hormuz appears to be slightly behind those shown in the chart and they move clockwise through the Gulf.

Chapter 6

Nested Spherical Model Development

6.1 Introduction

In this chapter a model that involves interactive nesting in space and time referred to as the **INST**(**IN**terpolated in **S**pace and **T**ime) model, is developed and used to compute the changes in tide heights and tidal currents in the Persian Gulf. The coastal regions of the Persian Gulf are shallow and complicated, suggesting that a high resolution grid is required to satisfactorily approximate these areas. It should be noted that a very fine grid over the whole Gulf is too computationally expensive, because the Gulf is very large and increasing the number of grid points causes a dramatic increase in the CPU time require to obtain solutions.

In this approach a fine grid has been superimposed over important regions of the coarse grid model. Having completed one sweep of the coarse model with a large time step, the information from that model is used as an open boundary condition to solve the tidal equations with a number of smaller time steps within the fine-grid regions. These time steps are an integral fraction of the coarse time step, and are chosen small enough to maintain the same average Courant-Friedrich-Lewy (CFL) number of both coarse and fine-grid models. Because of this, there is no large change in phase-speed of modelled tidal waves, with associated refraction and reflection, at the junction of the coarse and fine grids. This produces a smoother variation of wave properties each side of the interface between the fine and coarse grids.

6.2 Review of the literature

The idea of increasing resolution in a particular subregion of a model domain without running the fine grid model over the whole region has been considered by other researchers, and some nested models for oceanic applications have been developed, although most of the models developed are in the area of meteorology. These nested models fall into two categories, one-way nested or passive, and two-way nested or

interactive models, both of which will be described in this section. It should be pointed out that the **INST** model which is developed and described in this chapter, is a two-way model and involves interpolation in time as well as in space.

1. Meteorological models:

   Phillips and Shukla (1973) developed a nested grid system for weather prediction. They pointed out that there are two basic strategies which they refer to as one-way interaction and two-way interaction. In the one-way model the predictions are first made on a coarse grid, independent from the fine-grid calculations. Boundary values for the fine-grid region are obtained from what they have called a"history tape" of the coarse-grid predictions. The coarse-grid predictions do not use any information from the fine-grid predictions. In the two-way model the time integration proceeds simultaneously for the fine and coarse resolution mesh areas so that the two mesh areas interact dynamically with each other. In this way some of the computed values from the fine-grid are used in the coarse-grid. From the results of the numerical tests, they have found that in all cases the error for the two-way was smaller than for the one-way interaction and it was concluded that for the integration using the nested grid system, two-way interaction is more favorable.

   Kurihara et al. (1979) constructed a numerical technique to develop a two-way movable nested grid for meteorological applications. The grid points were not staggered and all meteorological variables have been defined at the same point. For this nested scheme, two types of dynamic interfaces were defined, the input dynamic interface at which the coarse grid model provides the boundary data for the fine grid model, and the feedback dynamic interface at which the predicted fine grid values were used to update the coarse grid region. In order to reduce the refraction and reflection of the waves at the interface between the two different mesh grids, they intentionally separated the input interface from the feedback dynamic interface. The main reason which supported their idea of separating interfaces was, since the fine grid boundary values are externally provided by interpolation from the coarse grid, so these values should not be used in the feedback procedure. In fact by separating the feedback interface the values which were internally predicted used in the feedback scheme. In the **INST** model developed in this thesis the wave refraction and reflection is reduced, because of the nesting in time which allows the Courant number for both grids to be approximately the same on each side of the interface.

   Zhang et al. (1986) presented a two-way nesting procedure. Like the others they also believed that by adding the nesting capability to a model a substantial improvement in the horizontal resolution is achieved, without using a fine grid mesh throughout the whole model domain. They used the idea of separated input interface from the feedback interface described by Kurihara et al. (1979) to reduce the interface noise.

2. Oceanographic models:

Ramming (1976) used the well-known basic model of the North Sea developed by Hansen (1956), and developed a nested North Sea model. He noted that to obtain a better approximation, it is necessary to refine the spatial grid in coastal regions as it may not be possible to obtain a good approximation of islands, flats, sands, coastal configurations and depth distribution from the model which uses a coarse grid. He believed that from the classical numerical models of the North Sea which already exist, very good results have been obtained, especially for the reproduction of storm surges and tides. He believed that this model with a grid size of 37 km could handle the problems concerning large areas and provides good topographical approximation. But he noted that to give answers to the more special questions of oceanography and neighboring sciences a new refined-grid model would have to be developed. In his nested model the refinement factor is always an odd number, because of using the Arakawa C-type staggered spatial grid. Ramming uses a refinement factor of three, and so a one-third model has been developed.

In order to provide more detailed tidal current information in some sensitive regions of the Persian Gulf, Lardner et al. (1982) developed a two-dimensional hydrodynamical tidal model for the Gulf. The horizontal eddy viscosity was considered to be zero. The model consisted of three blocks. The deep areas were covered by a coarse grid, which formed the first block; the shallow coastal areas were covered by a finer grid, which formed the second block; and the area of Ddahran, Bahrain and the west coast of Qatar were covered by a super-fine grid, which formed the third block. The three blocks were fitted together to form a single array. They used the finite difference scheme of Leendertse (1967) modified to study each of the above-mentioned regions of the Gulf. The only open boundary of the model was set at the Strait of Hormuz, which was contained in the first block. The tide heights at the open boundary of the second block at each time step were provided by the first block and the open boundary data for the third block, which was entirely located within the second block, was specified from the computed tide heights of the second block. In this model no spatial averaging of fine grid values was used for updating the values of grid points of the coarse region. This model may be classified as a two-way model. They reproduced the amplitudes and phases of three major constituents in the Gulf, namely K_1, M_2 and S_2 The pattern of co-amplitude and co-phase lines of the computed constituents were in reasonable agreement with the Admiralty chart 5081.

Greenberg (1983) uses two two-dimensional nonlinear numerical models to study the residual barotropic circulation generated by tides and winds in the Bay of Fundy and Gulf of Maine (ibid., p.885). A multi-grid nested model was used to examine the Bay and a coarse grid for the Gulf. In terms of nesting models this is classified as a two-way model. In this model the same time steps are used in both grids and no spatial averaging of fine grid values has been

used for updating the values of grid points of the coarse region.

In order to assess certain implementation aspects of the three-dimensional hydrodynamic model of the Persian Gulf developed by Lardner and Cekirge (1987, 1988), discussed in Section 4.3, Lardner et al. (1989) developed a two block model. In this model the Gulf was covered by a coarse grid block and the coastal areas of Saudi Arabia by fine grid block. This model is the extension of the model developed by Lardner et al. (1982) to three dimensions. It should be noted that in this model the advective terms were neglected.

In order to increase horizontal resolution in a subregion of the model domain, Spall and Holland (1991) developed an interactive nested model for oceanic application. They also classified the nested models as passive and interactive models. The refinement factor in the model is three. The feedback interfaces are separated from their dynamic interfaces and in order to give maximum information from the fine grid to the coarse grid they put the feedback interface as close as possible to the dynamic interface. They also note that, this agrees with the approach of Kurihara et al. (1979) and Zhang et al. (1986) in which the feedback interface is separated from the dynamical interface. In this model the coarse grid uses the same time step as the fine grid (Spall and Holland, 1991, p.209).

In order to investigate the covering (wetting) and uncovering (drying) of sand bars and shallow coastal flats that occur extensively throughout Northern Spencer Gulf in South Australia, Bills (1992) covered the region by a finer grid, that is, the element of the fine grid is one-third that of the coarse-grid element of the Spencer Gulf model. The open boundary forcing of the fine model has been taken from the solution field of the coarse model. This may be classified as a one-way model because the two models are not connected interactively.

6.3 Method of nesting

The spherical **INST** model described in this chapter uses the governing equations describing barotropic tidal motion in spherical coordinates, namely, equations (2.10)–(2.12). The code which has been adopted for use in the **INST** model procedure, is a considerably modified version of the spherical code, which was used in Chapter 5.

The **INST** model involves embedding a fine grid in space and time to cover a region within a coarse grid. The open boundaries of the fine grid model pass through elevation points and grid points of the coarse model. At the position b on the open boundary of the coarse model the sea surface elevations ζ_b is specified for all time by means of ten major tidal constituents, using the equation (2.1).

The elevations on the open boundary of the fine grid (interface between the two grids) are prescribed from the fine model, using the transferring algorithm described in Section 6.4.2

The grid matching technique, the levels in a time step of the coarse grid and the corresponding levels in time steps of the fine grid are now described.

6.3.1 Spatial and temporal refinements

The grid element, the basic unit of the grid, consists of three grid points, which are the free surface elevation ζ, and the horizontal velocity components u and v. They have the same meaning and locations as indicated in Figure 3.3, with the spatial refinement factor being an odd integer m which is defined by

$$m = \frac{\triangle\lambda_c}{\triangle\lambda_f}, \tag{6.1}$$

where $\triangle\lambda_c$ and $\triangle\lambda_f$ are the coarse and fine grid lengths, respectively.

In the present model the refinement factor is 3 so the scheme is called a one-third-refinement model. In the **INST** model refinement in time as well as space is carried out, so the coarse spatial model uses the large time steps and the fine spatial model the small time steps.

The general finite difference scheme used for both grids is three-level in time (Noye and Bills, 1992); Figure 6.1 shows the time levels in one time step of the coarse grid, and the corresponding levels in two equivalent time steps of the fine grid. It should be noted that the temporal refinement factor is defined by the integer p given by

$$p = \frac{\triangle t_c}{\triangle t_f}, \tag{6.2}$$

and in this model p is chosen to be 2.

6.3.2 The grid matching technique

The grid matching technique used in this approach, which embeds the fine grid within the coarse grid, is shown in Figure 6.2. The model uses nine fine grid elements embedded within a single coarse grid element in such a way that the elevation point within the coarse grid will coincide with the elevation point of the top left fine grid element. Each ζ_i, u_i and v_i coarse grid point will coincide with a fine grid point of a similar type.

The better definition provided by the fine grid allows the coast line to be modelled more accurately, or rapidly changing bathymetry to be incorporated in offshore areas.

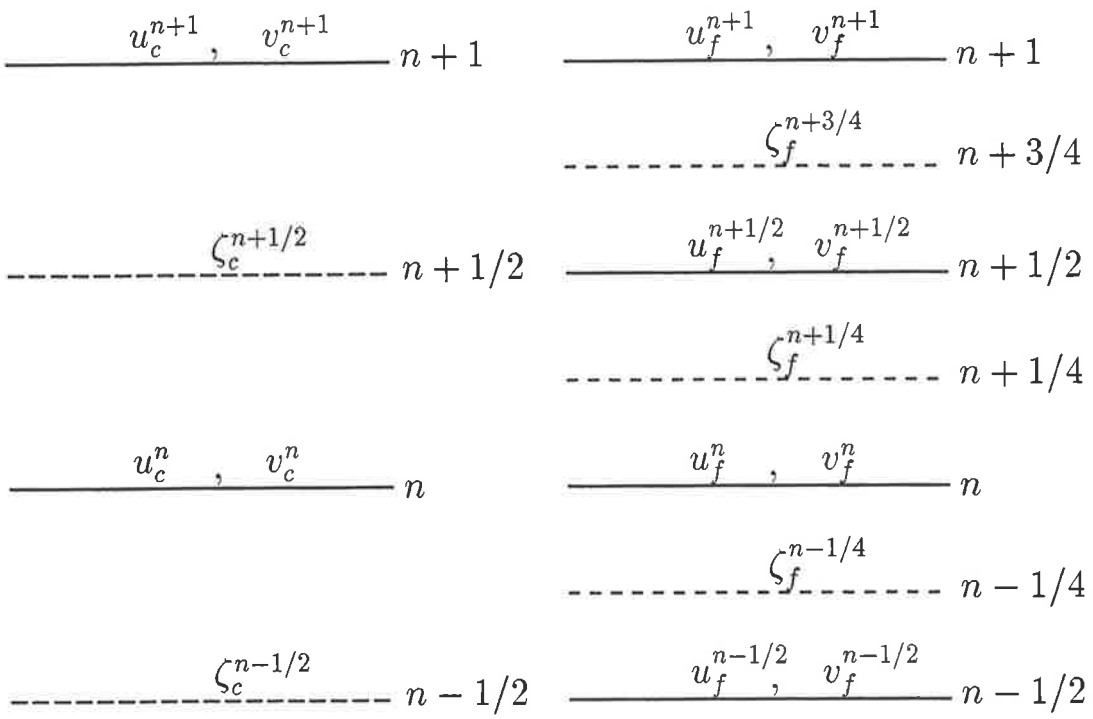

Figure 6.1: **(Left)** *Showing the time levels in each time step of the coarse grid and* **(Right)** *Showing the corresponding time levels in each time step of the fine grid. Sub-indices c and f stand for coarse and fine, respectively.*

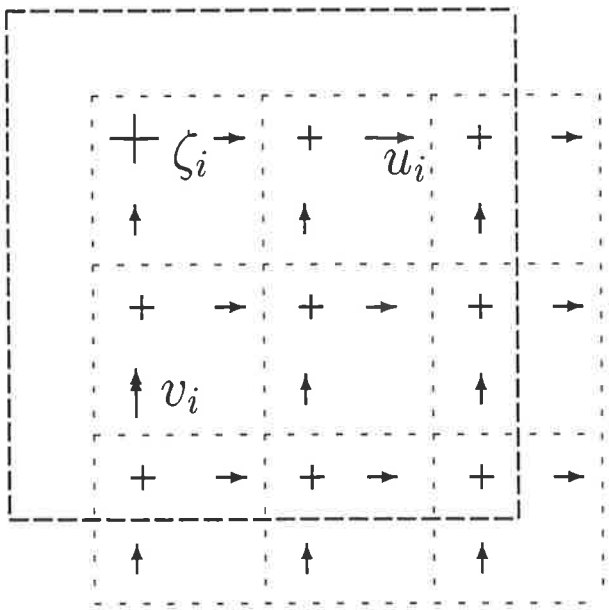

Figure 6.2: *The ith coarse grid element showing matching of the coarse and fine grids. Values for ζ_i, u_i and v_i are located in the appropriate places on the coarse and fine grid. For simplicity grids are drawn in a rectangular coordinate system.*

6.3.3 Initial and boundary conditions

The initial conditions used for both coarse and fine models are

$$\zeta = u = v = 0 \quad \text{at time } t = 0. \tag{6.3}$$

which means that the fluid is initially at rest. They are the same as those described in Section 3.2.3.
The boundary conditions used for the coarse and the fine grid of the **INST** model are the same as those explained in Section 3.2.2, but the forcing data for the fine model are specified as follows:
The elevations at the open boundary of the fine grid model (interface between two grids) are prescribed from the coarse grid model using the transferring algorithm explained in below.

At the end of each time step of the coarse grid model, the elevations at the open boundary points on the fine grid, which coincide with ζ grid points of the coarse grid, will be specified at the levels of time used in the fine grid by linear interpolation in time using the ζ value of the corresponding coarse grid point. For example ζ_{f1} and ζ_{f4} in Figure 6.3 use ζ_{c1} and ζ_{c2}. Data for the other fine grid elevation points, for example ζ_{f2}, ζ_{f3}, ζ_{f5} and ζ_{f6} in Figure 6.3, are obtained by interpolation in space from ζ_{f1} and ζ_{f4}.

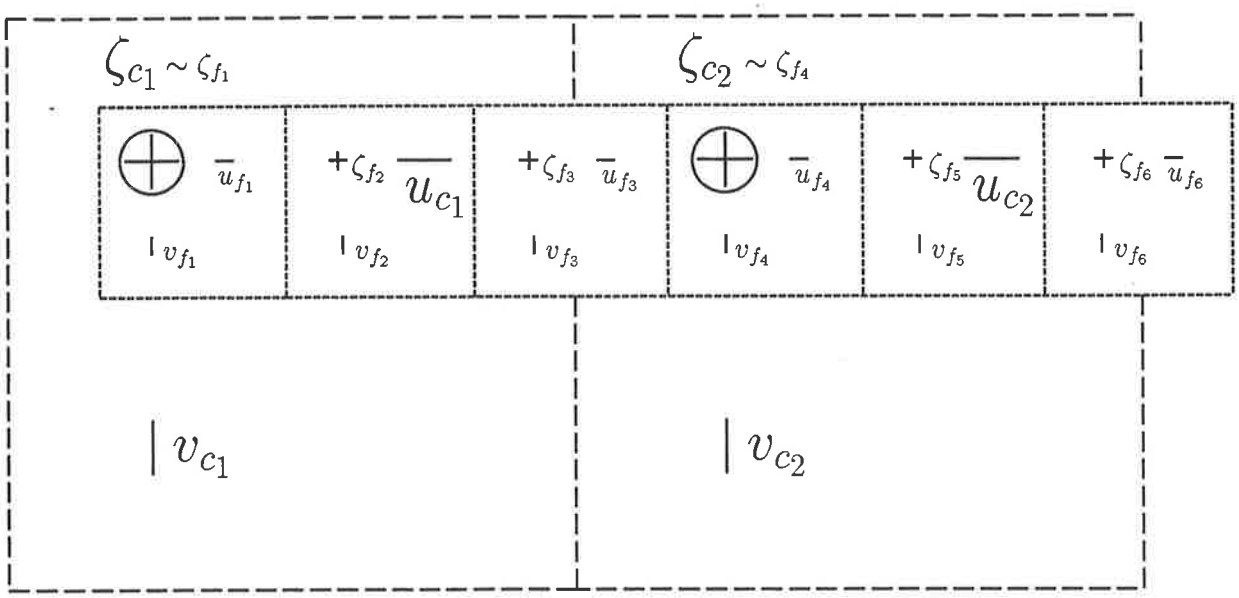

Figure 6.3: *Showing six fine grid elements on the open boundary of the fine grid, embedded within two coarse grid elements. The corresponding ζ grid points of the fine and coarse grids are circled. The ζ_{c_i}, u_{c_i} and v_{c_i} are the grid points of the coarse and ζ_{f_i}, u_{f_i} and v_{f_i} are of the fine model.*

6.4 Computational algorithms and automatic systems

In **INST** there are three computational algorithms, namely the algorithm for solving the governing equations, the transferring algorithm and the back transferring algorithm. In this section these algorithms are described.

6.4.1 Algorithm for solving the governing equations

The discretized form of the spherical tidal equations, (3.52), (3.54), and (3.57). are solved on the basis of the following mathematical algorithms. In these algorithms, and through the rest of this chapter, sub indices c and f which have been used with ζ, u and v, indicate the coarse and fine grid, respectively.

Based on Figure 6.1 the algorithms are:

(a) For the coarse model:

1. Solve the continuity equation (3.52) to find $\zeta_c^{n+1/2}$, using horizontal velocity components u_c^n and v_c^n at time level n, elevations at time level $(n-1/2)$ and the total depth H, at time level $(n-1/2)$.
2. Solve the momentum equations (3.54) and (3.57) for u_c^{n+1} and v_c^{n+1}, using $\zeta_c^{n+1/2}$ and u_c^n and v_c^n.

(b) For the fine model: The algorithm for the fine model requires more steps than the coarse model, depending on the temporal refinement factor defined in equation (6.3). The following illustrates the situation where the temporal refinement factor $p = 2$.

1. Solve equation (3.52) for $\zeta_f^{n+1/4}$ using u_f^n, v_f^n, $\zeta_f^{n-1/4}$ and certain values of $\zeta_c^{n+1/2}$ and $\zeta_c^{n-1/2}$, which coincide with the fine grid open boundary points.
2. Solve equations (3.54) and (3.57) for $u_f^{n+1/2}$ and $v_f^{n+1/2}$, using $\zeta_f^{n+1/4}$.
3. Solve equation (3.52) for $\zeta_f^{n+3/4}$ using $u_f^{n+1/2}$, $v_f^{n+1/2}$, $\zeta_f^{n+1/4}$ and certain values of $\zeta_c^{n+1/2}$ and $\zeta_c^{n-1/2}$, which coincide with the fine grid open boundary points.
4. Solve equations (3.54) and (3.57) for u_f^{n+1} and v_f^{n+1}, using $\zeta_f^{n+3/4}$.

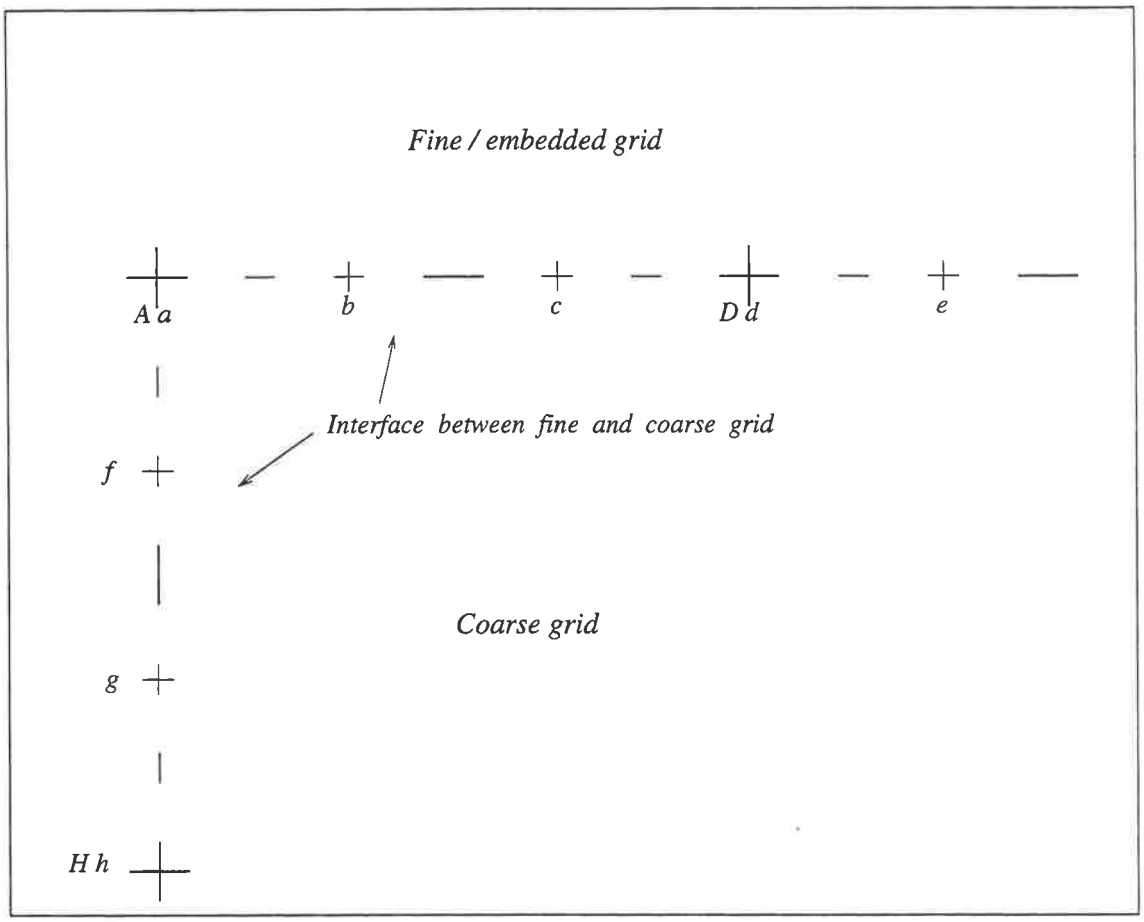

Figure 6.4: *Embedding the fine grid within the coarse grid. The larger bars and crosses are the overlapping grid points. The coordinates of the coarse grid are shown by capital letters and for the fine grid by lower case letters.*

6.4.2 Transferring algorithm

Figure 6.4 illustrates embedding the fine grid within the coarse grid. In this figure the larger bars and crosses are the overlapping grid points. The coordinates of the coarse grid are shown by capital letters and for the fine grid, by lower case letters. By using the figure and considering that the temporal refinement factor is $p = 2$, the transferring algorithm is described as follows:

1. After completing a sweep of the coarse model, that is, at the end of time level $n + 1$, and having the values of the overlapping coarse grid points, namely ${\zeta_A}^{n+1/2}$, ${\zeta_D}^{n+1/2}$ and ${\zeta_H}^{n+1/2}$, calculate ${\zeta_a}^{n+1/4}$, ${\zeta_d}^{n+1/4}$ and ${\zeta_h}^{n+1/4}$, by using the following interpolation in time:

$$ {\zeta_a}^{n+1/4} = (3{\zeta_A}^{n+1/2} + {\zeta_A}^{n-1/2})/4. \tag{6.4} $$

   Values of $\zeta_d^{n+1/4}$ and $\zeta_h^{n+1/4}$ can be calculated similarly

$$ {\zeta_d}^{n+1/4} = (3{\zeta_D}^{n+1/2} + {\zeta_D}^{n-1/2})/4, \tag{6.5} $$

and

$$\zeta_h{}^{n+1/4} = (3\zeta_H{}^{n+1/2} + \zeta_H{}^{n-1/2})/4, \tag{6.6}$$

2. Compute the values of elevations at the same overlapping fine grid points for the next half time level, using

$$\zeta_a{}^{n+3/4} = (5\zeta_A{}^{n+1/2} - \zeta_A{}^{n-1/2})/4, \tag{6.7}$$

$$\zeta_d{}^{n+3/4} = (5\zeta_D{}^{n+1/2} - \zeta_D{}^{n-1/2})/4, \tag{6.8}$$

and

$$\zeta_h{}^{n+3/4} = (5\zeta_H{}^{n+1/2} - \zeta_H{}^{n-1/2})/4. \tag{6.9}$$

3. Use linear interpolation in space to calculate the elevations at the other grid elements on the interface between the fine and coarse grids, namely $\zeta_b^{n+1/4}$, $\zeta_b^{n+3/4}$, $\zeta_c^{n+1/4}$, $\zeta_c^{n+3/4}$ and so on. The formula for the grid point b at the time level $n + 1/4$ is

$$\zeta_b^{n+1/4} = (2\zeta_a^{n+1/4} + \zeta_d^{n+1/4})/3 \tag{6.10}$$

and a similar formula can be used for the grid point f, using $\zeta_a^{n+1/4}$ and $\zeta_h^{n+1/4}$. For grid point c the equation is

$$\zeta_c^{n+1/4} = (\zeta_a^{n+1/2} + 2\zeta_d^{n+1/4})/3. \tag{6.11}$$

A similar formula applies for grid point g, using the data from a and h. If the elevation at e is just inside the grid, that is, the coastal boundary passes through the velocity of this grid, then $\zeta_e^{n+1/4}$ must be extrapolated from a and d, that is,

$$\zeta_e^{n+1/4} = (4\zeta_d^{n+1/4} - \zeta_a^{n+1/4})/3. \tag{6.12}$$

Similar formulae at each grid point can be used to obtain the values of ζ at the level $n + 3/4$.

6.4.3 Back transferring algorithm

At the end of each time step of simulation of the fine grid model, a spatially averaging procedure is used to estimate the corresponding coarse grid velocity points from the fine grid velocities. These averages are transferred back to the coarse grid model to provide a set of updated values for specific u and v velocity grid points within the coarse grid model to initiate the next time level within the overall model. The following example describes how this algorithm works.

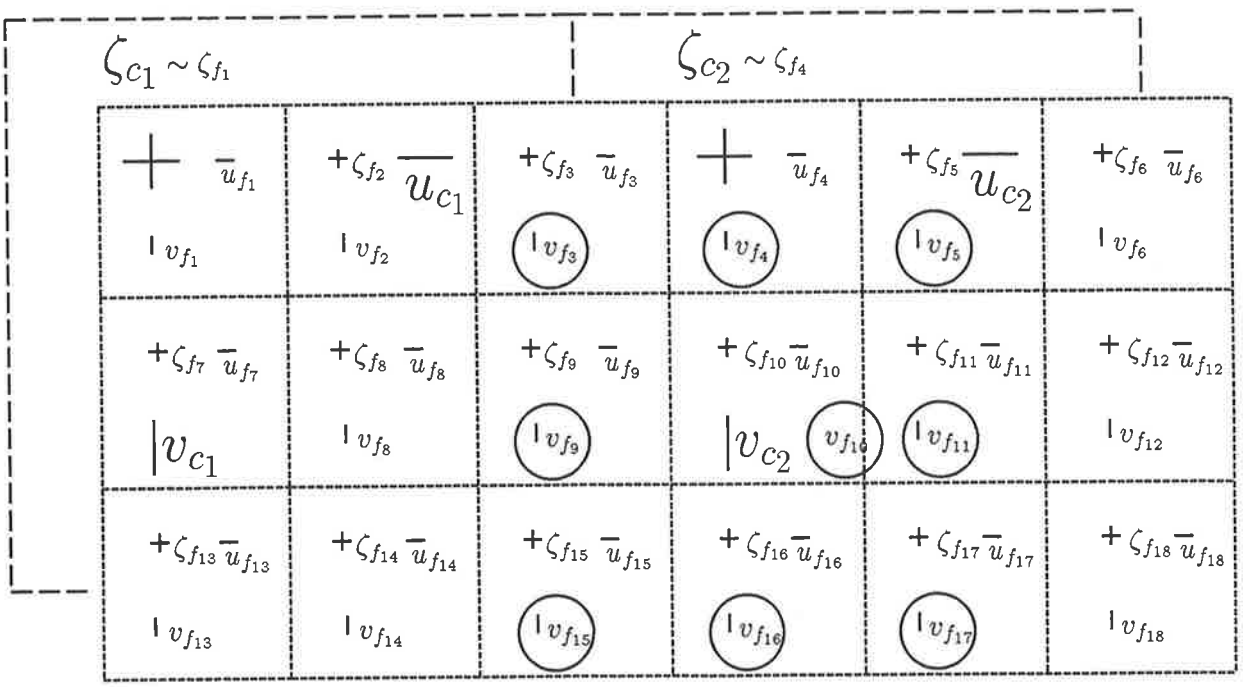

Figure 6.5: *The eighteen fine grid elements embedded within two coarse grid elements. Circled v_f velocities are used in the averaging procedure to update v_{c_2} coarse grid point.*

Figure 6.5 illustrates a schematic of the embedded 18 fine grids within two coarse grid elements away from the interface between two grids. In this figure the fine-grid velocity points, circled v_f velocities, are used in the averaging algorithm to update the v_{c_2} velocity, which is specified by |. This algorithm estimates the v_{c_2} velocity by obtaining an average from the corresponding fine-grid velocities, using the 9–point weighting function identified in matrix A, where

$$A = 1/16 \begin{bmatrix} 1 & 2 & 1 \\ 2 & 4 & 2 \\ 1 & 2 & 1 \end{bmatrix}$$

The averaging equation used in this scheme is

$$\begin{aligned} v_{c_2} &= (v_{f_3} + 2v_{f_4} + v_{f_5} \\ &+ 2v_{f_9} + 4v_{f_{10}} + 2v_{f_{11}} \\ &+ v_{f_{15}} + 2v_{f_{16}} + v_{f_{17}})/16. \end{aligned} \tag{6.13}$$

When a coarse-grid velocity point is on the open boundary of the fine grid the weight matrix becomes

$$1/8 \begin{bmatrix} -1 & -2 & -1 \\ 3 & 6 & 3 \end{bmatrix}.$$

Figure 6.6 illustrates the locations of two coarse-grid velocity points, u_{c_1} and u_{c_2} on the open boundary of the fine grid. The u_{c_1} is updated by using six fine-grid velocity points above it.

The averaging equation used is

$$u_{c_1} = (-u_{f_1} - 2u_{f_2} - u_{f_3} + 3u_{f_7} + 6u_{f_8} + 3u_{f_9})/8. \tag{6.14}$$

There are some remarks about averaging system which should be mentioned here. To find a good weighting function for the averaging procedure, the other types of the weighting matrix (Abramowitz and Stegun, 1964) have been tested, when a coarse velocity grid point is on the open boundary of the fine grid; finally the one described in Section 6.4.3 was selected and used in the model, because the results that are shown in Figures 6.10, 6.12 and 6.13, are better than the results obtained from using the other weighting functions. Other weighting functions have been tested including

(a)

$$1/12 \begin{bmatrix} 1 & 2 & 1 \\ 2 & 4 & 2 \end{bmatrix}.$$

For Figure 6.6 the averaging is then

$$\begin{aligned} u_{c_1} &= (u_{f_7} + 2u_{f_8} + u_{f_9} \\ &+ 2u_{f_{13}} + 4u_{f_{14}} + 2u_{f_{15}})/12. \end{aligned} \tag{6.15}$$

Note that this equation uses three grid points on the open boundary and three of the one row up.

(b)

$$1/8 \begin{bmatrix} 2 & 4 & 2 \end{bmatrix}.$$

Considering Figure 6.6 the averaging equation is

$$u_{c_1} = (2u_{f_{13}} + 4u_{f_{14}} + 2u_{f_{15}})/8. \tag{6.16}$$

This equation uses three grid points on the open boundary.

As suggested by Kurihara et al. (1979), using values on the boundary leads to instabilities. Each of these weighting function was tested and the most satisfactory solutions were found using equation (6.15).

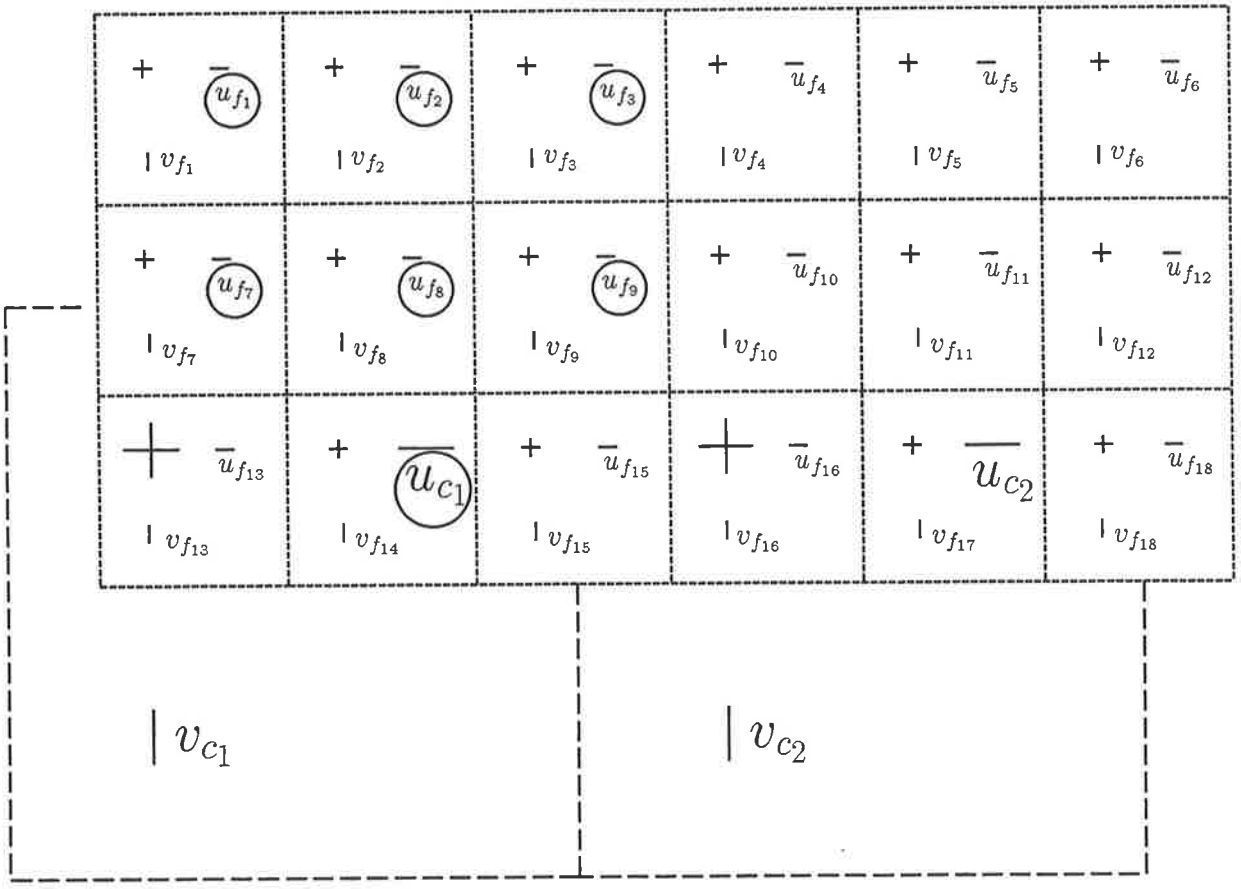

Figure 6.6: *The two coarse-grid velocity points, u_{c_1} and u_{c_2}, on the open boundary of the fine grid. The u_{c_1} is updated with six fine-grid velocity grid points.*

6.4.4 Stability criteria

The stability of the explicit finite difference scheme is assured provided that the usual Courant-Friedrich-Lewy (CFL) stability condition is met. This implies that the Courant number in each grid must be less than or equal to unity. The Courant number in two-dimensional Cartesian form is

$$C_2 = \Delta t\sqrt{gh}/\Delta s, \tag{6.17}$$

where

$$\Delta s = ((\Delta x)^{-2} + (\Delta y)^{-2})^{-1/2},$$

(see Flather and Heaps, 1975, Benque et al., 1982, Murty and El-Sabh, 1984, and Al-Rabeh et al., 1990).

The CFL condition is

$$C_2 = \frac{\Delta t\sqrt{gh_{max}}}{\Delta x \Delta y}\sqrt{(\Delta x)^2 + (\Delta y)^2} \leq 1, \tag{6.18}$$

where h_{max} is the maximum depth of the modeled region.

Equation (6.17) is used to obtain the optimum time step, that is,

$$\Delta t \leq \frac{\Delta x \Delta y}{\sqrt{g h_{max}}\sqrt{(\Delta x)^2 + (\Delta y)^2}}. \tag{6.19}$$

If $\Delta x = \Delta y$, equations (6.17) and (6.18) imply that

$$C_2 = \frac{\Delta t\sqrt{2gh_{max}}}{\Delta x} \leq 1, \tag{6.20}$$

and

$$\Delta t \leq \frac{\Delta x}{\sqrt{2gh_{max}}}. \tag{6.21}$$

By analogy of the Cartesian results, the Courant number in spherical form can be written as

$$C_2 = \frac{\Delta t\sqrt{gh_{max}}}{(R\Delta\lambda\cos\phi)(R\Delta\phi)}\sqrt{(R\Delta\lambda\cos\phi)^2 + (R\Delta\phi)^2} \leq 1, \tag{6.22}$$

or

$$C_2 = \frac{\Delta t\sqrt{gh_{max}}}{(R\Delta\lambda\cos\phi)(\Delta\phi)}\sqrt{(\Delta\lambda\cos\phi)^2 + (\Delta\phi)^2} \leq 1\,. \tag{6.23}$$

If $\Delta\lambda = \Delta\phi$ then

$$C_2 = \frac{\Delta t\sqrt{gh_{max}}}{R\Delta\lambda\cos\phi}\sqrt{\cos^2\phi + 1}\,. \tag{6.24}$$

To satisfy the stability condition in both fine and coarse grids it is required that the maximum Courant numbers in both grids be approximately the same, that is,

$$\sqrt{gh_c}\Delta t_c\sqrt{(\cos\phi)_c^2 + 1}/R\Delta\lambda_c(\cos\phi)_c \approx \sqrt{gh_f}\Delta t_f\sqrt{(\cos\phi)_f^2 + 1}/R\Delta\lambda_f(\cos\phi)_f, \tag{6.25}$$

where
h_c is the maximum depth in the coarse model,
h_f is the maximum depth in the fine model,
Δt_c, Δt_f are the time steps for the coarse and fine grids, respectively.
Using $m = \dfrac{\Delta\lambda_c}{\Delta\lambda_f}$, and choosing p as the temporal refinement factor, it can be seen that

$$p/m \approx \sqrt{h_f/h_c}\,, \tag{6.26}$$

so

$$p \approx m\sqrt{h_f/h_c}\,. \tag{6.27}$$

In the **INST** model of the Persian Gulf by considering $m = 3$, $h_c = 80\,m$ and $h_f = 20\,m$ the value of p using equation (6.26) is $p \approx 1.5$, in other words $\Delta t_c \approx \frac{3}{2}\Delta t_f$. The largest reasonable $p = 2$ has been chosen to minimize the simulation time, that is,

$$\Delta t_c = 2\Delta t_f. \tag{6.28}$$

Wave refraction as well as reflection may occur due to a change in phase speed at the interface of the two grids of different size (see Noye, 1984, p.298 and Roache, 1972, p.298). When a tidal wave passes through the interface, it is reflected or distorted. In order to minimize these effects and to assure a smooth variation on both sides of the boundary and over the boundary, it is necessary that the Courant number be approximately the same on each side of the interface.

It should be noted that, if the Courant number are almost equal in both sides of the interface the transition between the models are made properly, that is, refraction and reflection do not contaminated the computed patterns even near the boundary, so the objectives due to changing wave speeds would met properly. In other words when two grids are combined to form an embedded model, the solution obtained from the model is very similar to that of the fine grid.

At the interface between the fine and coarse grids $h_f \approx h_c$. Then the ratio of the Courant number numbers C_c and C_f in two grids will be

$$\frac{C_c}{C_f} = \frac{\Delta t_c \Delta \lambda_f}{\Delta t_f \Delta \lambda_c} = \frac{p}{m} = \frac{2}{3},$$

and this causes less distortion compared with using the same time step in both the fine and coarse regions, in which case C_c/C_f would be $1/3$.

$$\frac{C_c}{C_f} = \frac{2}{3},$$

and this causes less distortion compared with using the same time step in both fine and coarse region.

6.5 Numerical tests

In this section the application of the model in a rectangular bay is described. The aim of this application is to test the **INST** model. A rectangular bay of Figure 6.7 was chosen for this application and has been used for a fully coarse grid model, a fully fine grid model, and a nested model using the **INST** model. The contour plots of surface elevations obtained from the models are presented and compared with each other in order to verify the expectation that the contours resulting from the **INST** model are between the results of the fine and the coarse model and closer to that of fine model.

The coarse grid model of the region of Figure 6.7 uses a uniform grid of 0.25° latitude by 0.25° longitude. The time step $\Delta t_c = 400s$ is chosen for the coarse model. The depth is specified to be a constant $10m$. In this figure the coastal region of the shallow water which needs higher resolution is covered by a uniform grid of 0.0833° latitude by 0.0833° longitude, that is, $m = 3$, and the time step is $\Delta t_f = 200s$. The coastal boundaries of the embedded region coincide with those of the coarse model (solid lines passing through velocity grid points) and the open boundary of the fine grid model passes through those ζ grid points of the coarse model which are labelled

by a + sign. The u and v velocities which are inside the model and specified by — and |, respectively, will be updated by the back transferring (averaging) algorithm.

It should be noted that the coarse model is run until it hits the fine grid boundary.

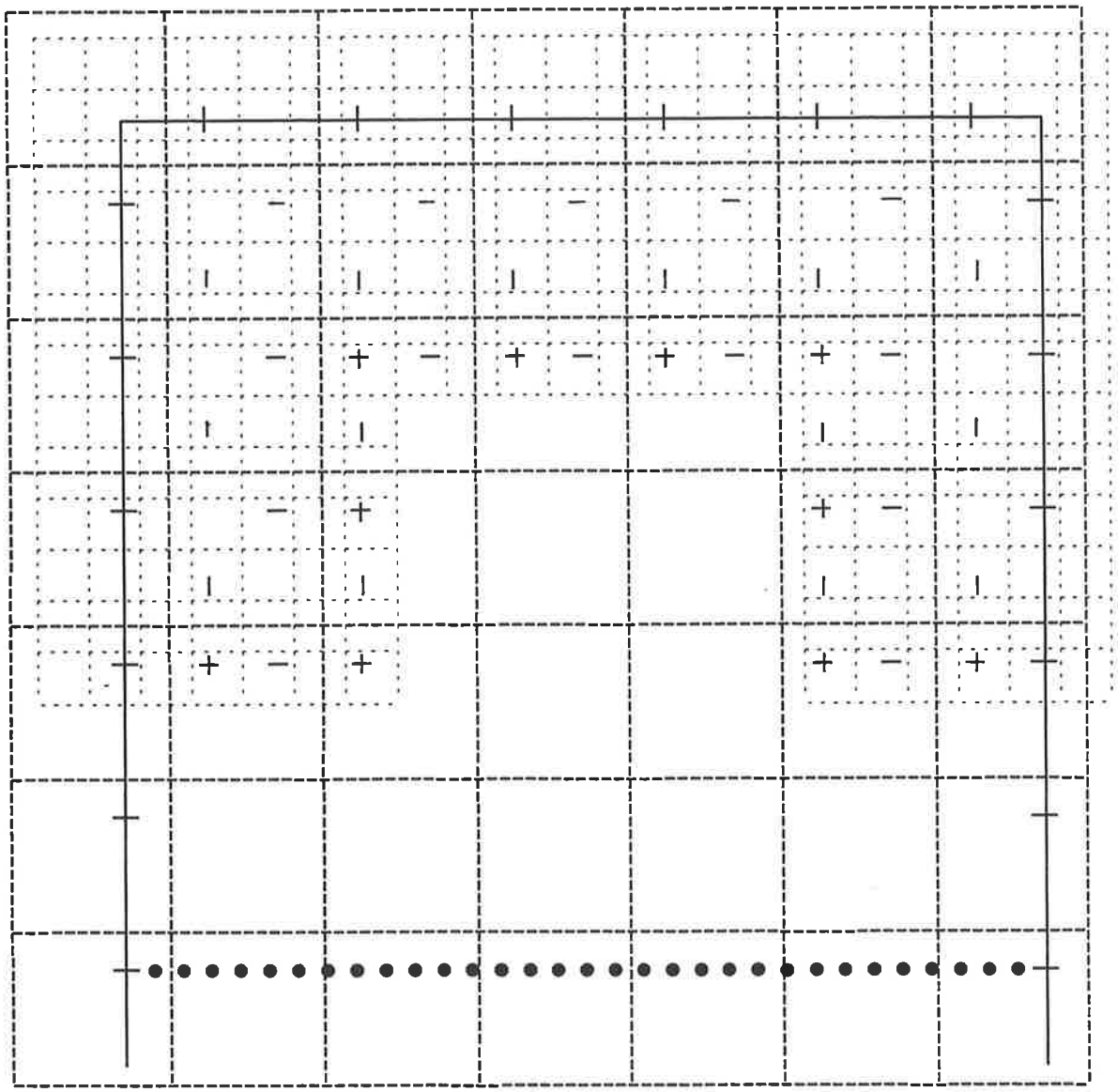

Figure 6.7: *A rectangular coastal model with embedded grids, coastal boundaries (solid lines), the open boundary of the coarse region (dotted lines), updated u and v velocities (−,| inside), and showing the open boundary of the fine model or interface between the grids (through the + signs).*

6.5.1 Automatic systems

As explained in Section 3.5, the region covered by the Noye and Bills (1992) model is labelled using four types of elements and each element is assigned one of the four integers 0, 1, 2 and 4. The numbering system in **INST** has been modified by adding three new types of elements, namely type 8, type 6 and type 5. The averaging scheme uses type 8 and type 6 elements and the replacing procedure is involved with the type 5. It should be pointed out that, instead of creating the replacing algorithm, the averaging system could be extended and used to update the other grid points, that is, those grids points which have already not been updated, no difference appears, but in terms of programming procedure it was easier to develop and use the replacing scheme, especially for complicated coastal boundaries such as those in the Persian Gulf. For this reason a new type of element, namely type 5, has been defined. In the input matrix of the coarse model those type 1 elements which must be replaced by new values computed using fine grid values, are replaced by the type 5. A similar substitution should be done for the corresponding elements in the input matrix of the fine grid. Figures 6.8 and 6.9 show the exact positions of the type 5 elements in the coarse and the fine models, respectively. These elements are used for the connection procedure of the two models. The open boundary of the fine model, that is, the interface between the coarse and the fine grids must be specified by using number 8. Figure 6.8 shows the position of the interface of the two models in Figure 6.7, in the input matrix of the coarse model. In the input matrix of the fine model the number 8 must be put exactly on the interface, but just over those grid points which have the same ζ points as the coarse grid, then between each two 8's the number 6 must be placed. The number of type 6's between each two type 8's is equal to $m - 1$. Figure 6.9 shows the location of these numbers in the type matrix of the fine grid. The reader may refer to Figure 6.7 to compare the positions of the relevant grids in the figures.

```
0 0 0 0 0 0 0 0
0 5 5 5 5 5 5 0
0 5 8 8 8 8 5 0
0 5 8 1 1 8 5 0
0 8 8 1 1 8 8 0
0 1 1 1 1 1 1 0
0 2 2 2 2 2 2 0
0 4 4 4 4 4 4 0
```

Figure 6.8: *The input matrix of the coarse model associated with Figure 6.7, showing the elements labelled 8 on the interface between the fine and the coarse model and the elements labelled 5 for use in the replacement scheme.*

```
0 0 0 0 0 0 0 0 0 0 0 0 0 0 0 0 0 0 0 0 0
0 0 0 0 0 0 0 0 0 0 0 0 0 0 0 0 0 0 0 0 0
0 0 1 1 1 1 1 1 1 1 1 1 1 1 1 1 1 1 1 1 0
0 0 1 5 1 1 5 1 1 5 1 1 5 1 1 5 1 1 5 1 0
0 0 1 1 1 1 1 1 1 1 1 1 1 1 1 1 1 1 1 1 0
0 0 1 1 1 1 1 1 1 1 1 1 1 1 1 1 1 1 1 1 0
0 0 1 5 1 1 8 6 6 8 6 6 8 6 6 8 1 1 5 1 0
0 0 1 1 1 1 6 4 4 4 4 4 4 4 4 6 1 1 1 1 0
0 0 1 1 1 1 6 4 4 4 4 4 4 4 4 6 1 1 1 1 0
0 0 1 5 1 1 8 4 4 4 4 4 4 4 4 8 1 1 5 1 0
0 0 1 1 1 1 6 4 4 4 4 4 4 4 4 6 1 1 1 1 0
0 0 1 1 1 1 6 4 4 4 4 4 4 4 4 6 1 1 1 1 0
0 0 6 8 6 6 8 4 4 4 4 4 4 4 4 8 6 6 8 6 0
0 0 4 4 4 4 4 4 4 4 4 4 4 4 4 4 4 4 4 4 0
```

Figure 6.9: *The input matrix of the fine model of Figure 6.7, showing the elements numbered 8 and 6 on the interface, the open boundary of the fine grid and elements labelled 5 for use in the replacement scheme.*

6.5.2 Test without Coriolis

A set of full non-linear equations in spherical coordinates, namely equations (3.50), (3.59) and (3.76), including all terms but the Coriolis force, are solved in a constant-depth rectangular bay. The Coriolis force excluded to verify that at all points across the model bay the tidal elevations are the same, and the tidal currents do not vary. In order to analyze the results obtained from the **INST** model, they are compared with the corresponding results predicted by the fine and the coarse models of the same computational domain. Different orientations of the interface between the three models also have been examined, to find out the exact behavior of the results through the embedded modelled region, compared with the fine and the coarse results.

The results from all four orientations (open boundary opening towards the north, south, east, and west) for each of the three models were the same for each orientation, so that only the results for the southerly facing boundary (Figure 6.7) are presented below.

Figure 6.10 illustrates the contour plots of the sea surface elevations resulting from the three models of the computational region of Figure 6.7, namely (a) is the fine, (b) is the **INST** and (c) is the coarse model.

The results shown in Figure 6.10 indicate that the elevations predicted by **INST** lie between the fine grid elevations and the coarse grid elevations. In addition, all the contours are linear, a result of Coriolis being excluded.

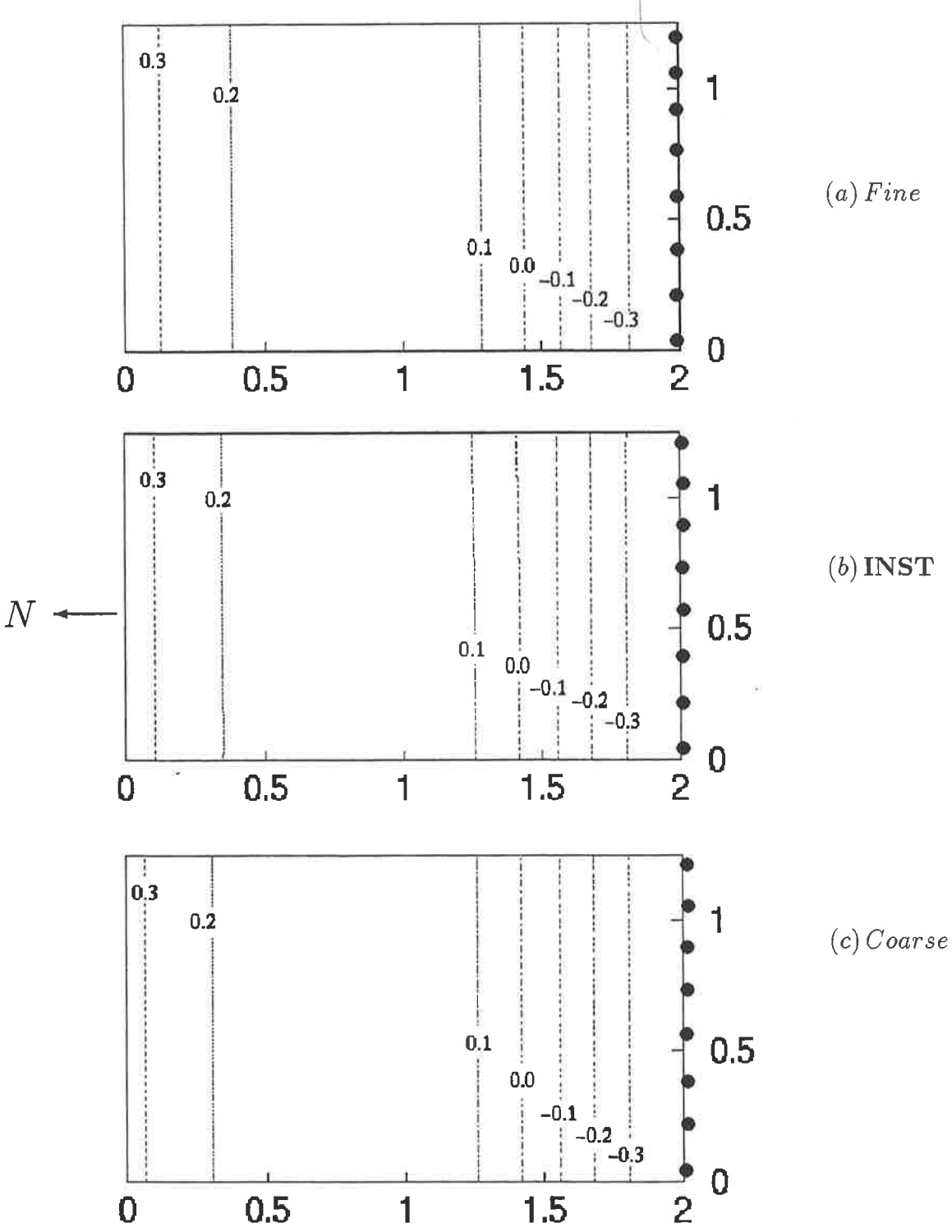

Figure 6.10: *Comparison of sea surface elevation contours for the rectangular bay of Figure 6.7 using (a) the fine grid, (b) the* **INST**, *and (c) the coarse grid, models. The dotted line on the right is the open boundary of the bay in each case. The Coriolis term is not included.*

6.5.3 Test with Coriolis

This section presents the results of testing the **INST** model when Coriolis is included. This test has been carried out to ensure that models work independent of orientation, and also to examine whether the **INST** results be between the coarse and the fine grid results, and are possibly closer to the fine results.

The rectangular bay illustrated in Figure 6.7 was modelled using four different orientations. Figure 6.11 shows two of these, namely the orientation with the open boundary facing south and that facing north. The three models, fine, **INST**, and coarse, were run with each of these orientations, and the results are shown in Figures 6.12 and 6.13. Both sets of results show that elevations resulting from applying the **INST** model lie between those resulting from the coarse and fine grid models. In addition, with the change in orientation, the change in Coriolis produced results that were mirror images of each other.

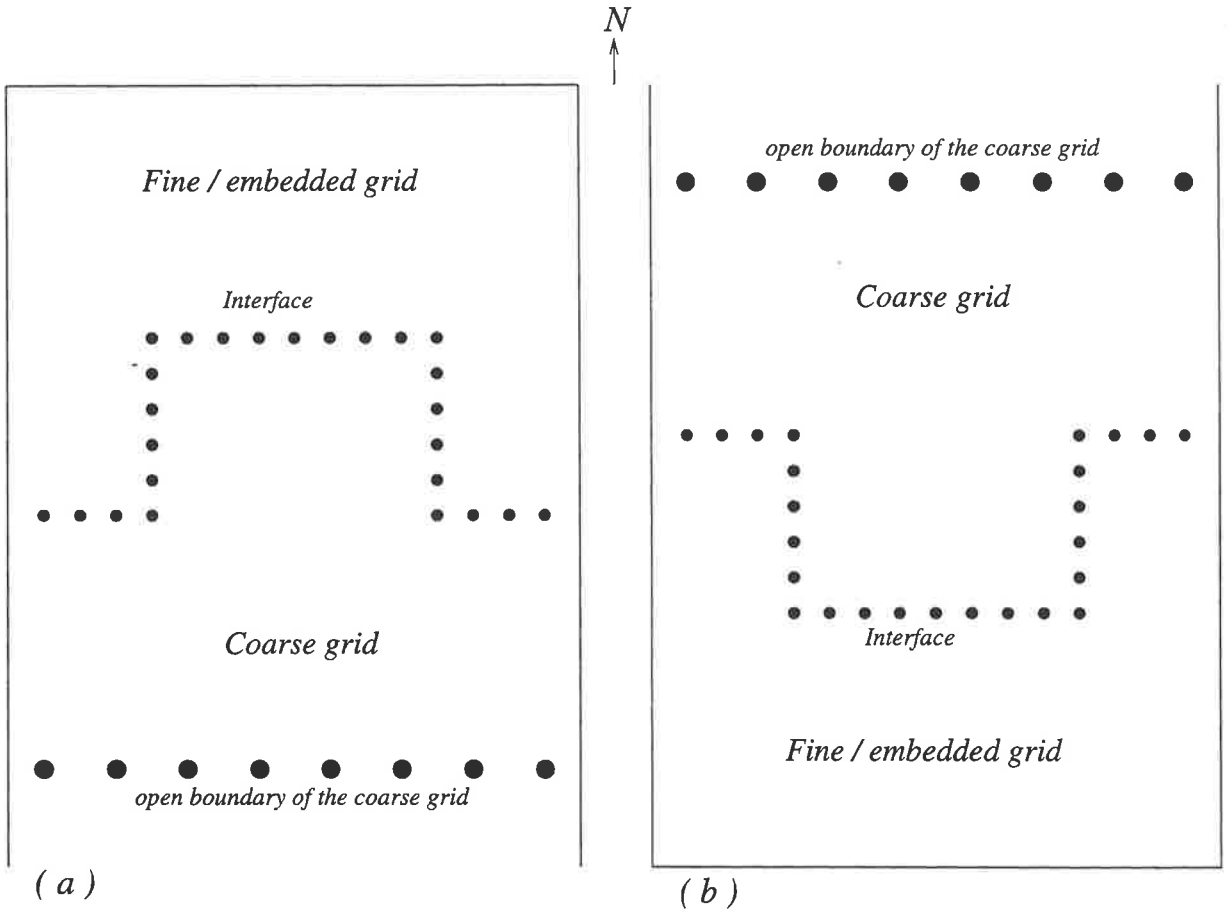

Figure 6.11: *A rectangular coastal model with embedded grids, showing (a) southerly, and (b) northerly facing open boundaries.*

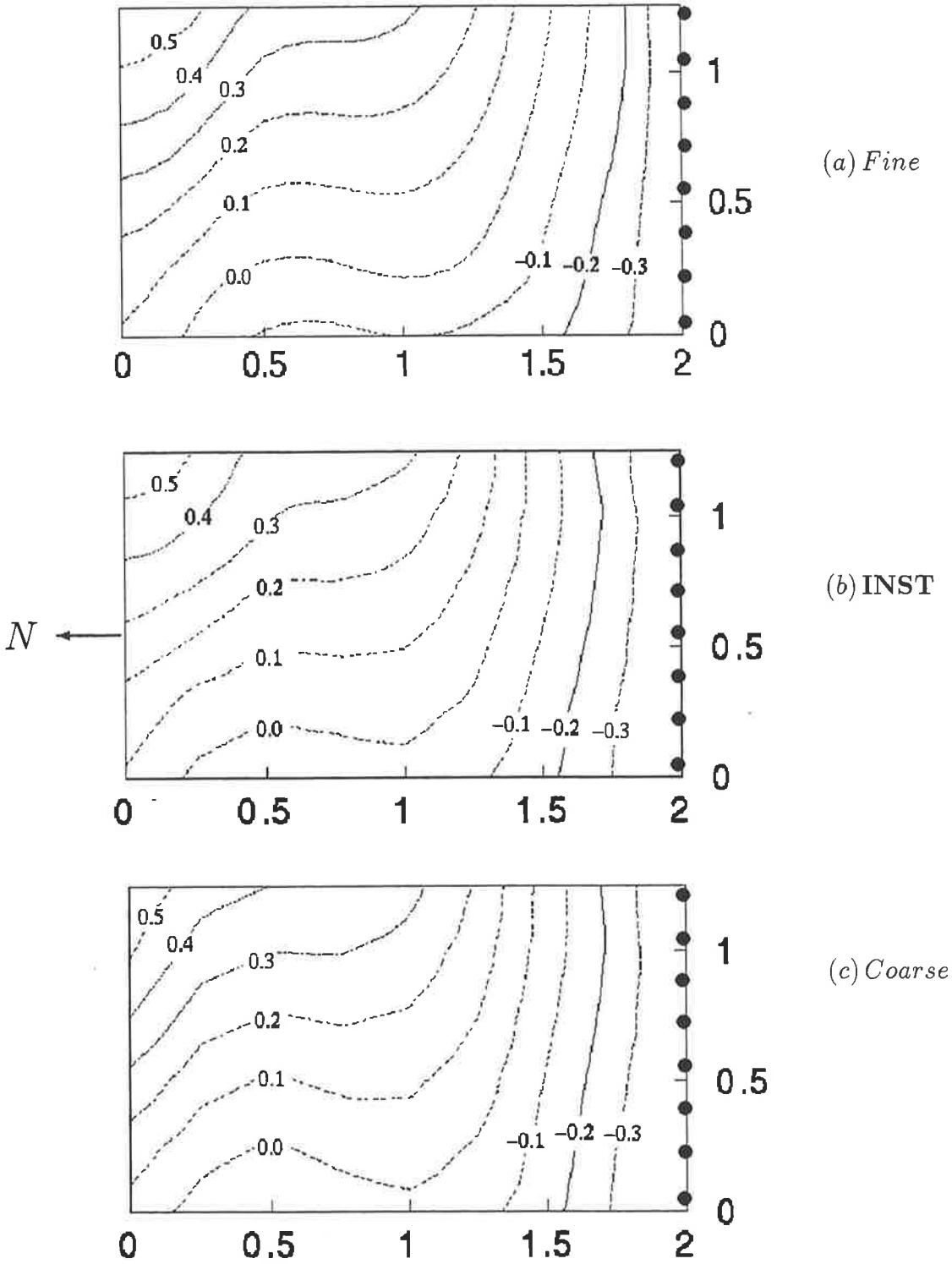

(a) *Fine*

(b) **INST**

(c) *Coarse*

Figure 6.12: *The* **INST** *contours of sea surface elevation f0r the rectangular bay model of Figure 6.11(a), compared with the contours for the same region, covered by fine and coarse grids. The Coriolis term is included. The dotted line is the open boundary of the bay.*

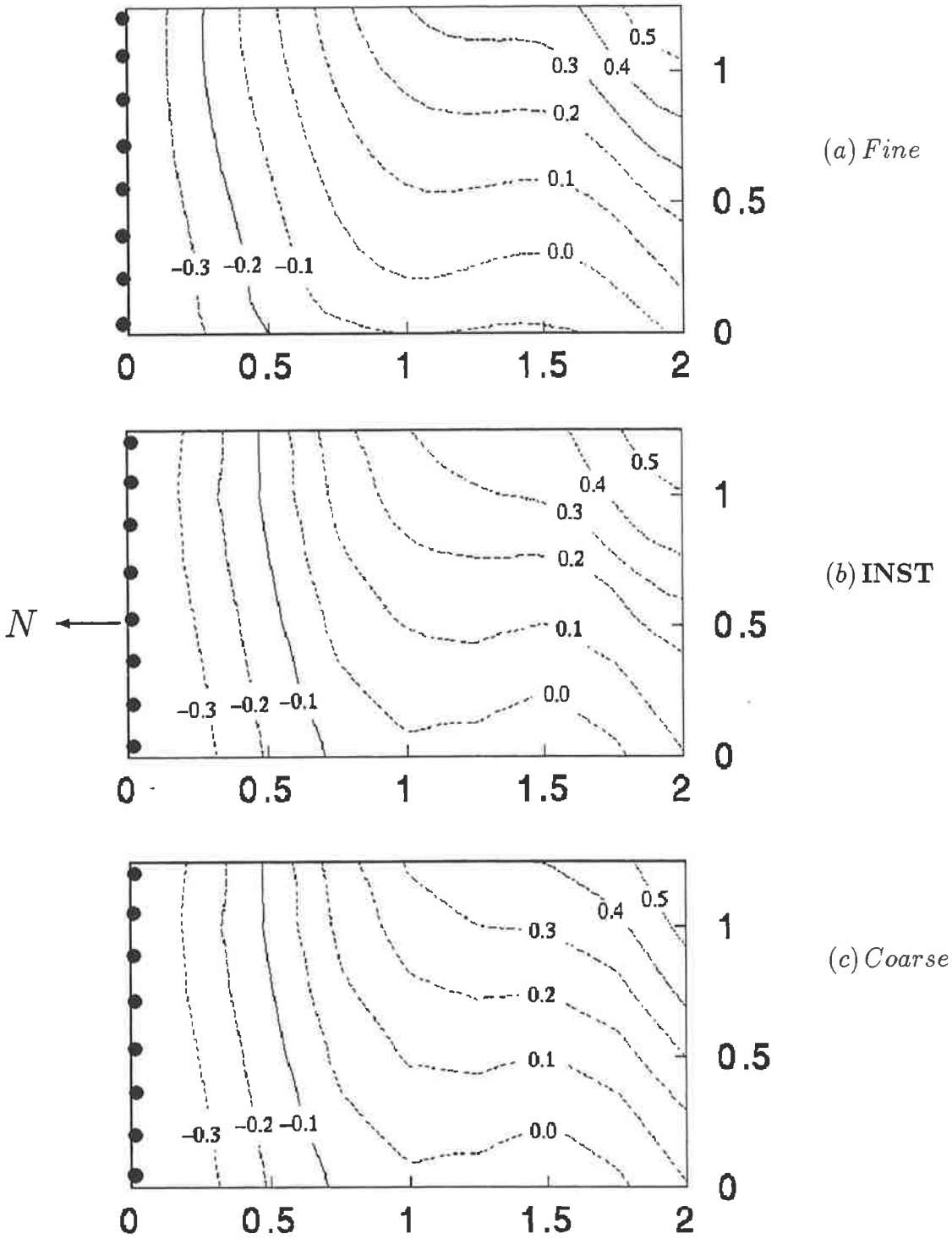

Figure 6.13: *The* **INST** *contours of sea surface elevation for the rectangular bay model of Figure 6.11(b), compared with the contours for the same region, covered by fine and coarse grids. The Coriolis term is included and the open boundary (dotted line) is on the left.*

Figure 6.14 shows the easterly and westerly facing open boundaries of the modelled bay. The results from using these orientations were basically the same as those found using the northerly and southerly orientations, and so they are not repeated here.

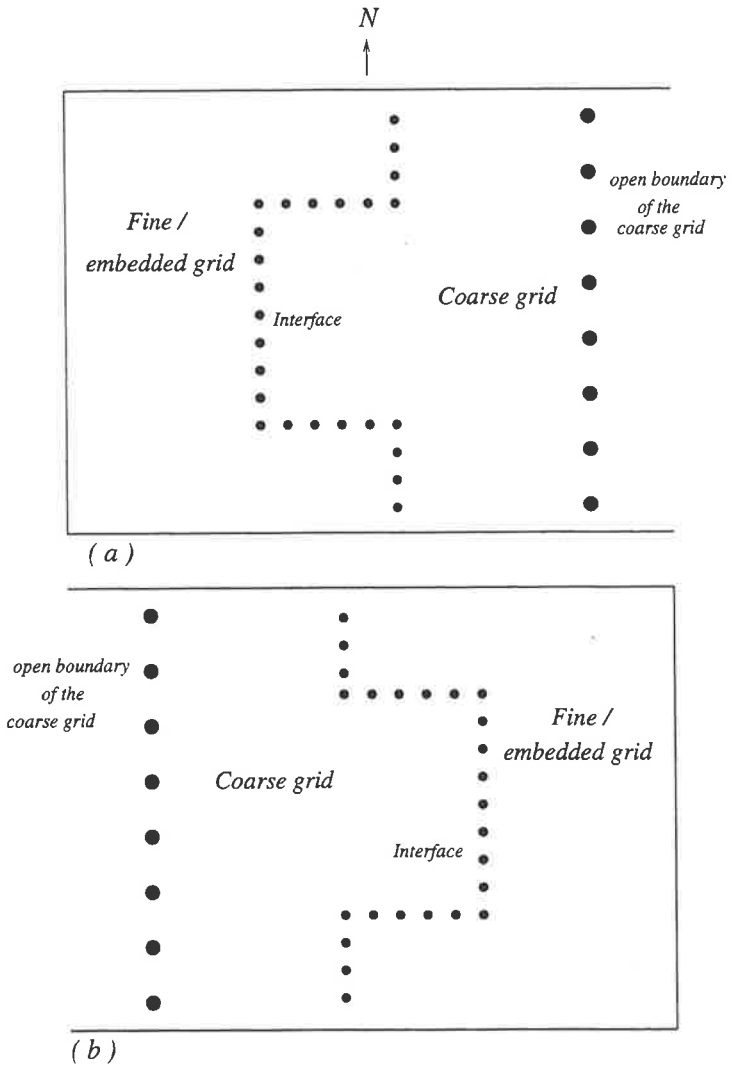

Figure 6.14: *A rectangular coastal model with embedded grids, showing easterly, (a), and westerly, (b), facing open boundaries.*

6.5.4 Summary and conclusion

The **INST** model was tested in a rectangular bay with different orientations of the interface between the fine and the coarse grids, that is, southerly, northerly, easterly and westerly facing open boundaries. The coarse, fine and the **INST** models have been applied to each orientation. Tests have been conducted to ensure the models work independently of the orientation of the open boundary, and to make sure that the **INST** results are between the coarse and the fine results, being closer to the

fine. The contour plots of the surface elevations obtained from the three models were compared with each other, and good agreement between the results through the embedded regions were shown. It should also be pointed out that the resulting contours from the southerly facing boundary model are the exact mirror image of those of the northerly model and similar results were found for the easterly and westerly models.

It should be noted that, because the Courant number has been almost equal in both sides of the interface the transition between the models has been made properly, that is, refraction and reflection do not contaminated the computed patterns even near the boundary, so the objectives due to changing wave speeds are met properly. In other words when two grids are combined to form an embedded model, the solution obtained from the model is very similar to that of the fine grid.

Chapter 7

The INST Model of the Persian Gulf

7.1 Introduction

This chapter discusses the application of the **INST** model to the Persian Gulf. From the application of a depth-averaged spherical coordinate model of the Persian Gulf, described in Chapter 5, close agreement between observed and computed tides was obtained, but to provide relevant information in shallow, complicated coastal areas, especially around the Iranian coast which has largely been neglected in the past, the grid was refined to improve the predictions in those regions.

Figure 7.1 shows the coastal regions of the coarse model of the Persian Gulf which are covered by the fine grid, in order to have a higher resolution within the shallow waters and reproduce the shape of the coastline more accurately. These regions of the Persian Gulf are important because of the shipping activities into and from islands and the coastal ports and the oil wells in coastal waters.

7.2 Numerical model

The coarse grid section of the **INST** model uses the same uniform grid ($5'$ latitude and $5'$ longitude) and a time step of $\Delta_c t = 200s$ as the spherical depth-averaged tidal model of the Persian Gulf described in Chapter 5. The fine grid covers the shaded area of Figure 7.1 and uses a uniform grid which is $(5/3)'$ square. The fine grid has been generated on the basis of the grid matching technique, described in Section 6.3.2. Using this technique the coastal boundaries of the coarse and the fine grids have different shapes; Figures 7.2 and 7.3 illustrate this, in particular around the head of the Gulf and in the Bahrain area.

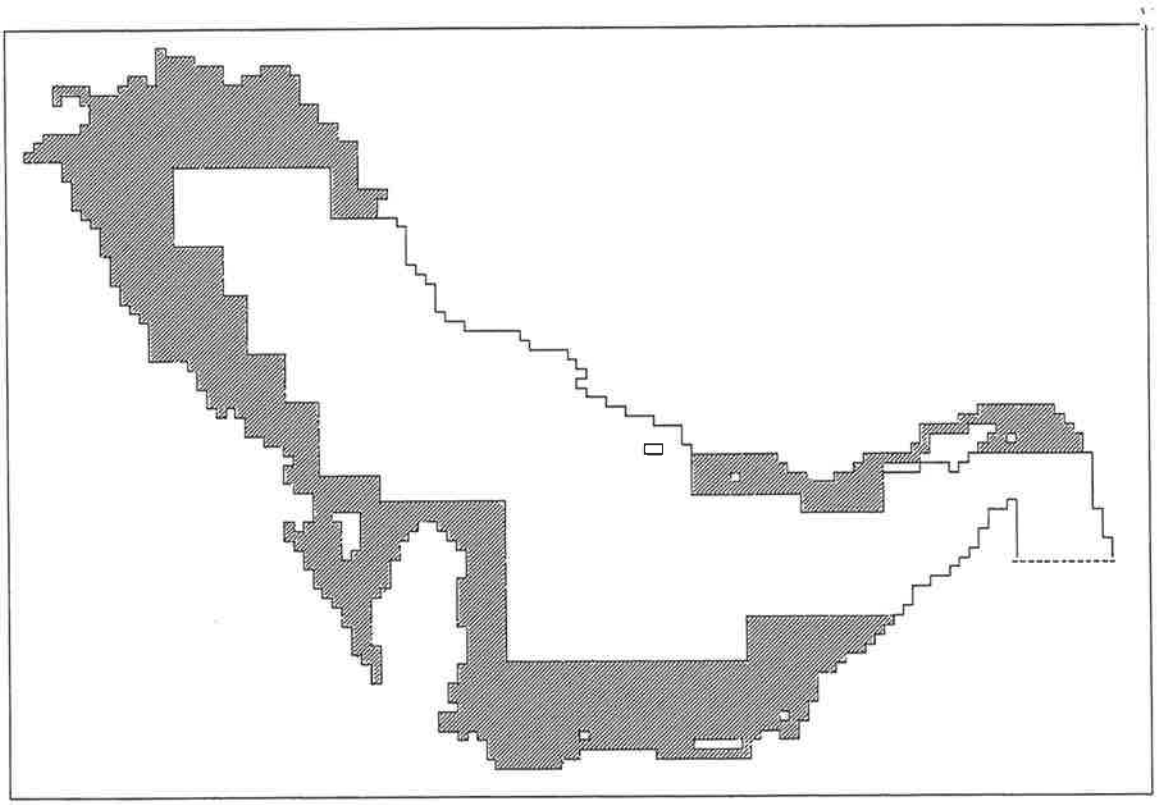

Figure 7.1: *The shallow coastal regions of the coarse model of the Persian Gulf which are covered by the fine grid of the* **INST** *model.*

The embedded fine grid contains 8383 grid elements that lie within the embedded regions. The time step used, as described in Section 6.4.4, is half of that of the coarse model, that is, $(\Delta t)_f = 100s$.

The bathymetry for the embedded fine grid has been developed for the 8383 elevation grid points, from the bathymetry of the coarse model using bivariate interpolation, three and four point formulae. The four point formula interpolates the value of a function f at a point (x, y), which lies in a grid square with vertices of (x_1, y_1), (x_2, y_1), (x_2, y_2) and (x_1, y_2) (see Figure 7.4), that is,

$$f(x,y) = \alpha_1 f(x_1,y_1) + \alpha_2 f(x_2,y_1) + \alpha_3 f(x_2,y_2) + \alpha_4 f(x_1,y_2)$$

where α_i, $i = 1, 2, 3, 4$, are the coefficients of the interpolation function described in Abramowitz et al. (1964, p.882) and Press et al. (1989, p.117), they are combinations of the the functions described in Section 6.4.2.

The three points formula defined similarly (see Abramowitz et al. 1964, p.882).

The value $C_b = 0.0015$ is used for the quadratic friction coefficient, for both the coarse and fine grids.

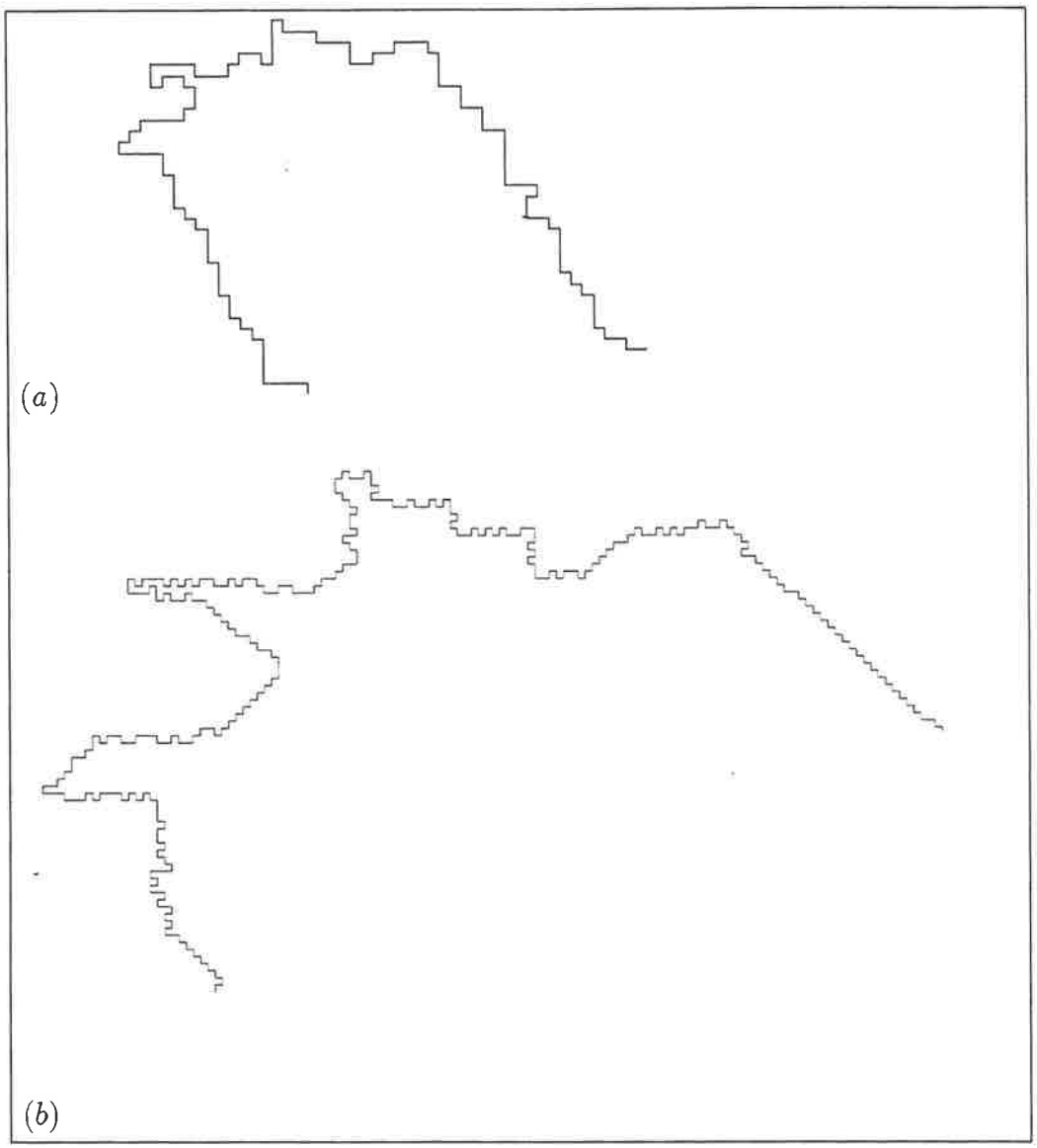

Figure 7.2: *The coastal boundary near the head of the Persian Gulf, (a), as covered by the coarse grid and (b), as covered by the fine grid in the* **INST** *model.*

The reduced eddy viscosity coefficient for the fine model was chosen to be three times that of the coarse model, because the refinement factor in this model is $m = 3$ and because a depends on $\Delta\lambda$, equations 2.11–2.12. In this way the horizontal eddy viscosity did not change abruptly at the interface between the fine and coarse grids.

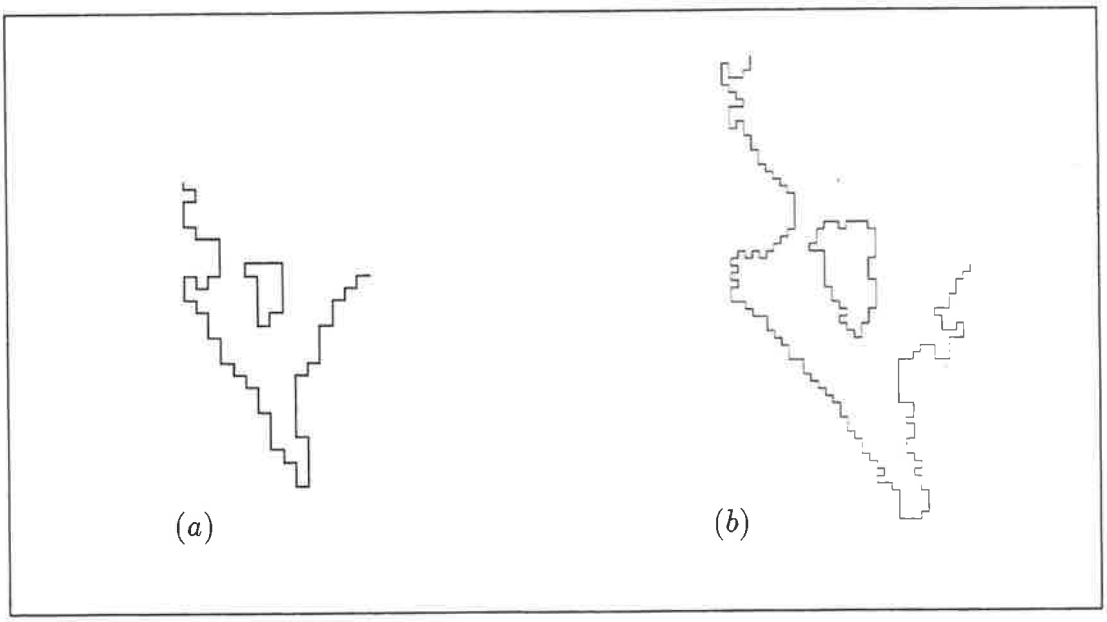

Figure 7.3: *The coastal boundary of the Bahrain coast in the Persian Gulf, (a), as covered by the coarse grid and (b), as covered by the fine grid in the* **INST** *model.*

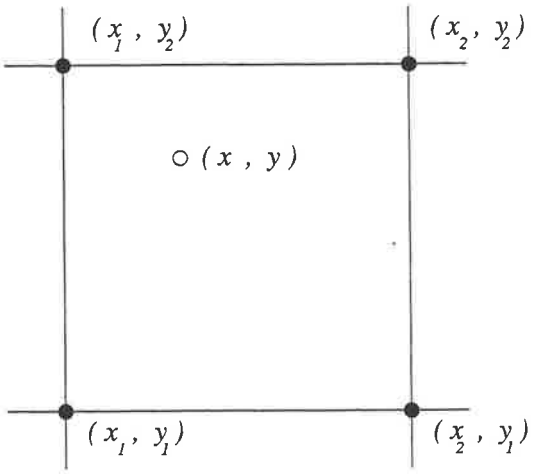

Figure 7.4: *The labeling of points used in the four point interpolation formula.*

7.3 Presentation of the results

In this section model predictions for tidal elevations and depth-averaged tidal currents are presented. The main interpretations of the predictions are by means of contour charts of tidal elevations and ellipse plots of the depth-averaged currents for the diurnal constituents O_1 and K_1 and the semi-diurnal constituents M_2 and S_2.

The model was run for a simulated time of 32 days, the first three days of predictions are ignored (as initial transients). Predictions for the remaining 29 days were saved hourly and were tidally analysed.

7.3.1 Sea surface elevations

In this section the tidal constants computed from the **INST** model are compared with the observations of tidal elevation at the forty stations identified in Table 4.4. They are also compared with the predictions from the Cartesian model of Chapter 4 and the spherical model of Chapter 5. Table 7.1 summarizes the results of the three models. The absolute complex differences error, described in Chapter 4, for the computed values are obtained and are included in Table 7.1. The errors for the Cartesian, the spherical and the **INST** models are $\varepsilon = 5.3\,cm$, $\varepsilon = 4.3\,cm$ and $\varepsilon = 3.75\,cm$, respectively. The errors show that a steady improvement is achieved using the later models. The computed values obtained from the **INST** model have only small deviations from the observed values; the absolute difference in phase generally is less than 12° and for the amplitudes in most of the stations the differences are less than $5\,cm$. The computed results compare favourably with the observations; at 90% of the stations both the amplitude and phase for results from the **INST** model are better than the same results obtaining from the other two models.

The co-amplitude and co-phase lines for the principal diurnal O_1, K_1 and semi-diurnal M_2 and S_2 constituents have been predicted by the **INST** model. They are presented in Figures 7.5–7.12 and compared with Admiralty chart 5081 (see Figures 4.3–4.6). The Admiralty chart has been constructed from observations available at a number of locations along the coast and a limited number of points within the Gulf. The chart only provides approximations to the true tidal conditions within the Gulf. However, the Admiralty chart at a location may be very accurate (if much data was available) or very inaccurate (if little data was available).

The location of the amphidromic points predicted by the model are similar to the Admiralty chart but differ in certain important aspects. Modeled results for M_2 phases suggest that the tidal constituent is moving more slowly through the Strait of Hormuz than shown on the Admiralty chart, while the K_1 constituent appears to be moving at the same speed, this is probably a function of the boundary condition in the Strait of Hormuz.

It should be mentioned that Hunter (1984), using an M_2 tidal input, notes that "the Admiralty co-tidal chart of the Gulf was considerably in error in Kuwait waters". The **INST** results confirm Hunter's comment, as the location of the amphidromic point in the Kuwait area is not exactly the same as that shown in the Admiralty chart. Also the **INST**-modeled predictions for the M_2 amplitude in this region are lower than those of the chart in the same region, the same being true for O_1, K_1 and S_2 (see Figures 7.5–7.12 and 4.3–4.6). In the case of phases, as Figures 7.10 and 4.5 show, the constituents in this area are not moving with the same speed as that shown in the Admiralty chart.

Observation station		O_1		K_1		M_2		S_2	
		amp	ph	amp	ph	amp	ph	amp	ph
1	Obs.	28.7	215.0	42.9	263.0	62.7	248.0	16.8	312.0
	INST	24.2	220.6	35.7	270.5	56.0	254.7	12.8	320.3
	sph.	22.7	227.2	36.4	274.0	50.4	262.8	10.4	326.2
	Car.	17.6	229.9	31.2	277.0	52.0	265.6	11.0	329.8
2	Obs.	25.7	192.0	38.8	233.0	36.4	149.0	12.8	196.0
	INST	20.6	201.4	33.5	242.2	36.0	156.2	13.1	206.3
	sph.	19.0	204.9	31.3	246.6	36.9	161.0	12.4	210.8
	Car.	17.1	206.6	31.7	247.2	39.3	166.3	14.3	207.7
3	Obs.	20.4	189.0	30.7	227.0	33.7	110.0	12.3	160.0
	INST	18.2	197.3	26.8	232.4	36.3	119.0	12.5	166.3
	sph.	17.0	200.6	25.8	237.1	37.3	124.5	12.5	171.9
	Car.	15.4	201.4	25.9	241.8	40.2	122.7	14.4	175.2
4	Obs.	18.0	171.0	25.3	209.0	49.7	68.0	17.7	117.0
	INST	14.4	176.5	22.5	218.2	41.9	69.0	15.3	128.0
	sph.	12.4	180.8	19.3	220.3	41.7	70.6	13.5	127.8
	Car.	11.9	179.4	18.5	214.9	42.3	82.3	14.9	131.3
5	Obs.	21.6	221.0	42.3	256.0	32.7	256.0	11.6	320.0
	INST	20.4	225.0	30.6	260.3	26.8	270.0	7.5	330.2
	sph.	18.8	233.7	31.6	266.8	24.7	270.0	5.6	334.6
	Car.	15.2	233.7	34.4	266.2	24.9	273.8	5.8	336.8
6	Obs.	21.0	221.0	38.0	259.0	25.0	276.0	8.0	335.0
	INST	19.5	228.0	32.6	265.0	20.0	288.2	3.5	345.2
	sph.	18.4	232.4	31.1	271.1	17.7	290.6	2.6	347.6
	Car.	14.9	237.0	28.0	337.1	15.7	294.5	3.3	353.7
7	Obs.	11.9	89.0	23.8	115.0	51.2	19.0	17.1	57.0
	INST	11.2	97.2	23.5	122.5	41.0	28.3	14.5	68.6
	sph.	12.8	98.3	23.5	125.1	43.0	30.2	12.6	71.6
	Car.	12.1	100.9	20.9	130.8	41.9	33.1	13.9	72.2
8	Obs.	14.0	227.0	17.0	273.0	44.0	37.0	16.0	107.0
	INST	12.0	235.0	13.5	284.5	38.5	49.0	13.2	120.1
	sph.	9.8	238.8	11.2	283.3	36.0	49.5	11.4	119.7
	Car.	8.6	245.8	11.0	291.3	36.0	49.2	12.2	125.1
9	Obs.	20.7	3.0	33.8	11.0	100.0	197.0	36.0	229.0
	INST	23.0	0.1	40.0	18.4	106.0	200.0	39.2	235.6
	sph.	23.8	359.4	42.8	21.9	107.1	200.1	40.0	237.7
	Car.	26.4	0.1	42.4	22.4	112.4	200.5	43.6	239.0
10	Obs.	10.0	218.0	18.0	274.0	48.0	36.0	16.0	93.0
	INST	7.2	225.3	11.4	283.2	41.5	49.0	14.0	101.2
	sph.	6.9	227.3	9.7	285.1	39.6	48.1	12.0	105.5
	Car.	4.9	238.1	10.1	292.1	39.1	56.8	12.5	113.7
11	Obs.	9.0	281.0	12.0	325.0	54.0	95.0	17.0	159.0
	INST	6.5	284.5	9.2	330.1	50.0	95.5	16.0	157.3
	sph.	5.9	285.2	8.2	332.2	48.8	95.3	15.2	156.9
	Car.	4.3	300.4	6.8	345.6	45.0	113.8	15.2	170.0
12	Obs.	15.0	55.0	29.0	94.0	30.0	335.0	12.0	10.0
	INST	15.5	62.3	29.4	102.5	32.5	332.5	12.0	15.5
	sph.	15.7	63.5	28.1	104.8	33.0	331.9	12.0	17.5
	Car.	14.5	80.6	24.4	101.6	37.8	334.	14.3	20.0
13	Obs.	16.0	65.0	30.0	92.0	33.0	332.0	12.0	6.0
	INST	12.6	79.0	24.5	106.0	27.5	340.0	10.5	20.0
	sph.	11.4	78.5	23.7	106.7	25.6	343.6	9.5	21.6
	Car.	10.7	82.8	21.9	115.6	27.4	351.4	10.4	20.1

Table 7.1: *Comparison of computed (INST), spherical (sph.), Cartesian (Car.) and observed (Obs.) results for amplitude (cm) and phase (degrees GMT) for the four major tidal constituents at selected stations in the Persian Gulf. (see Table 4.4 for the names and locations of each of the observation stations.)*

Observation station		O_1		K_1		M_2		S_2	
		amp	ph	amp	ph	amp	ph	amp	ph
14	Obs.	20.0	14.0	29.0	28.0	73.0	204.0	25.0	247.0
	INST	22.0	12.5	36.0	29.5	80.1	202.0	30.0	246.5
	sph.	22.1	10.2	37.6	31.6	82.6	201.9	31.9	246.3
	Car.	22.9	358.2	38.8	28.4	88.9	201.7	35.6	246.3
15	Obs.	21.9	40.0	32.6	74.0	59.7	245.0	22.6	282.0
	INST	18.5	46.0	30.1	80.0	58.4	250.0	20.0	290.0
	sph.	17.6	47.2	28.8	85.6	57.4	254.4	20.1	291.6
	Car.	15.4	44.3	24.9	73.9	60.6	258.2	23.0	300.3
16	Obs.	20.4	355.0	28.7	359.0	76.8	185.0	27.4	221.0
	INST	22.0	351.0	32.5	10.2	83.5	185.0	31.0	226.0
	sph.	22.0	344.9	34.6	10.7	85.3	185.9	32.4	230.7
	Car.	24.0	344.5	42.1	14.9	89.3	185.8	35.2	231.4
17	Obs.	15.8	349.0	26.2	350.0	68.9	193.0	25.3	227.0
	INST	17.5	345.6	33.2	1.3	75.0	192.0	28.5	230.0
	sph.	19.3	344.9	36.3	2.7	77.5	190.6	30.9	234.4
	Car.	21.2	342.8	38.1	6.7	81.0	190.9	32.5	236.0
18	Obs.	18.9	38.0	29.3	64.0	59.1	229.0	20.1	266.0
	INST	19.0	28.5	29.0	65.0	60.0	232.3	21.2	270.0
	sph.	18.6	29.3	29.5	66.1	63.2	233.5	23.1	272.4
	Car.	16.4	24.8	26.1	57.1	62.2	234.0	24.6	276.9
19	Obs.	7.0	268.0	9.0	10.0	63.0	54.0	20.0	102.0
	INST	5.5	280.3	8.5	17.0	55.0	60.2	13.5	110.5
	sph.	3.4	283.3	7.9	18.7	54.1	62.6	10.2	114.2
	Car.	3.5	288.	7.9	31.1	56.1	74.3	12.1	122.7
20	Obs.	22.3	41.0	37.5	85.0	45.1	258.0	15.2	294.0
	INST	15.0	54.0	30.3	100.2	36.5	271.0	11.5	304.2
	sph.	13.7	56.2	27.3	103.3	34.2	274.3	9.1	310.8
	Car.	14.1	61.3	28.9	103.6	35.1	273.5	10.1	314.2
21	Obs.	16.0	345.0	22.0	352.0	67.0	196.0	22.0	239.0
	INST	17.0	349.4	28.5	5.3	72.6	196.5	26.0	240.0
	sph.	17.9	351.7	30.5	6.1	75.0	197.4	28.9	242.0
	Car.	17.8	348.7	30.8	10.8	75.8	197.3	30.9	242.3
22	Obs.	1.8	36.0	1.2	116.0	4.9	196.0	2.1	273.0
	INST	2.0	42.0	3.0	124.0	10.7	185.6	4.0	264.5
	sph.	2.2	45.0	3.6	128.9	12.3	180.2	4.9	262.8
	Car.	1.7	47.5	2.7	121.7	11.3	195.1	4.6	259.5
23	Obs.	9.4	0.0	20.1	54.0	42.4	44.0	13.1	88.0
	INST	8.2	10.0	17.3	65.2	33.5	48.5	8.5	90.0
	sph.	7.8	11.5	16.3	69.6	31.2	51.4	7.0	92.8
	Car.	7.8	9.9	14.7	66.8	36.7	42.0	6.8	87.2
24	Obs.	17.6	31.0	24.5	77.0	39.0	235.0	14.5	279.0
	INST	15.8	40.2	20.0	86.5	39.0	243.2	14.0	289.0
	sph.	13.7	43.2	21.5	89.2	39.6	247.2	13.5	293.6
	Car.	10.4	44.6	15.3	95.4	37.6	251.3	13.6	294.8
25	Obs.	8.0	308.0	15.0	20.0	51.0	57.0	18.0	102.0
	INST	6.8	318.2	12.2	35.5	45.7	70.0	11.4	114.0
	sph.	5.3	322.8	11.9	39.2	43.6	72.4	9.9	117.0
	Car.	5.6	327.7	11.2	39.9	41.2	71.0	10.9	120.5
26	Obs.	16.0	28.0	21.0	29.0	62.0	210.0	20.0	250.0
	INST	15.0	22.1	21.0	31.5	62.5	210.0	23.5	251.5
	sph.	13.2	18.6	21.3	33.6	64.0	209.6	24.3	253.5
	Car.	11.5	15.5	19.7	19.8	60.8	207.6	25.2	251.9

Table 7.1(cont.): *Comparison of computed (INST), spherical (sph.), Cartesian (Car.) and observed (Obs.) results for amplitude (cm) and phase (degrees GMT) for the four major tidal constituents at selected stations in the Persian Gulf.*

Observation station		O_1		K_1		M_2		S_2	
		amp	ph	amp	ph	amp	ph	amp	ph
27	Obs.	5.0	9.0	7.0	104.0	16.0	169.0	4.0	223.0
	INST	3.5	20.4	4.8	117.2	23.2	180.2	5.4	
	sph.	2.3	23.1	3.6	120.0	24.9	184.6	6.3	234.9
	Car.	1.9	24.9	3.0	113.1	22.4	187.2	6.0	238.0
28	Obs.	3.7	301.0	7.0	16.0	41.7	72.0	11.3	128.0
	INST	3.0	318.6	6.5	29.4	34.8	83.5	7.2	140.0
	sph.	3.0	324.8	6.4	31.8	32.6	87.7	5.3	142.7
	Car.	2.9	328.7	5.3	36.5	31.6	90.4	4.1	143.2
29	Obs.	12.0	0.0	25.0	53.0	38.0	37.0	11.0	76.0
	INST	11.2	10.0	22.5	60.3	26.5	36.4	8.7	76.3
	sph.	9.8	12.8	20.1	64.3	24.3	34.3	7.9	77.2
	Car.	9.7	18.4	18.0	71.8	29.0	22.0	8.5	71.5
30	Obs.	17.0	33.0	20.0	74.0	45.0	234.0	15.0	267.0
	INST	11.3	34.6	14.3	72.3	46.3	230.5	15.8	270.0
	sph.	9.6	36.2	12.0	70.1	47.0	228.7	16.9	272.5
	Car.	9.8	23.9	11.1	51.2	43.6	227.8	17.6	270.1
31	Obs.	2.4	4.0	8.2	84.0	16.2	257.0	4.3	284.0
	INST	2.5	10.5	6.2	92.5	11.7	251.4	3.4	290.2
	sph.	2.8	14.8	4.4	96.2	9.3	247.2	2.5	294.9
	Car.	2.1	19.5	3.2	101.5	7.5	271.2	1.7	300.1
32	Obs.	15.0	17.0	34.0	64.0	34.0	37.0	11.0	67.0
	INST	15.3	27.2	32.5	74.1	33.2	33.2	11.5	80.1
	sph.	15.6	30.0	30.7	77.8	32.4	31.5	12.4	85.2
	Car.	14.8	33.5	26.8	81.4	35.3	31.2	13.9	77.5
33	Obs.	15.0	50.0	17.0	103.0	43.0	248.0	13.0	301.0
	INST	11.2	52.5	12.4	100.3	41.5	242.5	13.6	293.5
	sph.	9.0	53.8	10.6	99.8	41.1	240.1	14.1	290.4
	Car.	8.3	53.8	8.1	90.2	35.1	241.3	13.6	289.7
34	Obs.	16.4	28.0	36.2	72.0	32.1	51.0	10.8	82.0
	INST	16.5	32.3	34.0	80.4	33.5	41.5	11.5	92.0
	sph.	17.0	34.6	33.4	82.4	35.3	40.4	13.3	94.1
	Car.	16.0	37.6	28.8	90.7	38.0	42.7	14.6	98.6
35	Obs.	15.0	71.0	19.0	110.0	32.0	254.0	11.0	304.0
	INST	11.5	77.5	14.3	119.0	36.0	253.0	12.0	300.0
	sph.	9.4	80.2	12.4	121.1	38.0	252.4	12.5	300.8
	Car.	8.0	75.1	8.8	123.5	32.4	256.5	11.7	299.3
36	Obs.	16.3	62.0	35.8	95.0	11.2	266.0	4.0	337.0
	INST	16.0	69.0	33.2	105.3	13.5	274.5	6.0	345.3
	sph.	16.7	73.8	31.0	107.2	15.8	278.4	6.6	349.4
	Car.	14.4	80.4	24.7	109.0	17.7	284.3	7.6	353.6
37	Obs.	18.5	62.0	40.4	90.0	6.3	95.0	4.0	95.0
	INST	18.5	72.5	37.2	99.2	15.5	89.0	5.4	102.6
	sph.	18.7	76.6	35.3	102.8	16.7	86.4	5.9	107.0
	Car.	16.8	80.7	29.1	105.3	15.4	100.2	5.1	110.7
38	Obs.	12.0	114.0	22.0	151.0	25.0	323	8.0	26.0
	INST	14.6	116.0	24.0	160.4	29.4	330.0	11.0	33.2
	sph.	16.3	119.4	24.5	163.4	32.4	333.0	12.7	36.6
	Car.	7.0	125.2	14.0	169.3	14.0	342.6	2.0	12.0
39	Obs.	24.2	67.0	47.2	101.0	14.2	115.0	5.8	122.0
	INST	22.0	74.2	41.5	109.4	29.0	100.3	11.2	133.2
	sph.	20.5	78.1	39.5	112.5	30.8	105.2	12.5	137.8
	Car.	18.9	83.0	33.2	120.8	31.5	110.9	12.1	140.5

Table 7.1(cont.): *Comparison of computed (INST), spherical (sph.), Cartesian (Car.) and observed (Obs.) results for amplitude (cm) and phase (degrees GMT) for the four major tidal constituents at selected stations in the Persian Gulf.*

Observation station		O_1 amp	O_1 ph	K_1 amp	K_1 ph	M_2 amp	M_2 ph	S_2 amp	S_2 ph
40	Obs.	19.0	81.0	30.0	120.0	37.0	289.0	15.0	343.0
	INST	17.8	92.4	30.0	128.0	44.0	296.2	16.0	350.1
	sph.	16.1	95.2	28.6	132.2	47.4	300.0	17.2	354.4
	Car.	12.6	97.0	21.1	136.8	44.6	303.9	16.4	358.0

Averaged complex differences	INST	sph.	Car.
	3.75	4.3	5.3

Table 7.1(cont.): *Comparison of computed (INST), spherical (sph.), Cartesian (Car.) and observed (Obs.) results for amplitude (cm) and phase (degrees GMT) for the four major tidal constituents at selected stations in the Persian Gulf.*

As Figures 7.5 and 7.7 show, the basic pattern of amplitude contours for the O_1 constituent is similar to that for K_1; this is the same for phase contours (see Figures 7.6 and 7.8) because the period of the O_1 is close to the period of the K_1 constituent, but the magnitude of the O_1 is almost 22% lower. The S_2 tide has a similar pattern to the M_2 for the same reasons, but in this case the amplitude of the S_2 is approximately 35% of the M_2 values. The results show that the larger values of the constituents are observed around the Strait of Hormuz, especially the biggest value appearing at Bandar Abbas and the head of the Gulf. In general the pattern of the model results are similar with the Admiralty chart. It should also be noted that the model predictions show reasonable agreement with the patterns of previous models (for example Von Trepka (1968), Figures 4.7-4.8, Lardner et al. (1986), Figures 4.9-4.10).

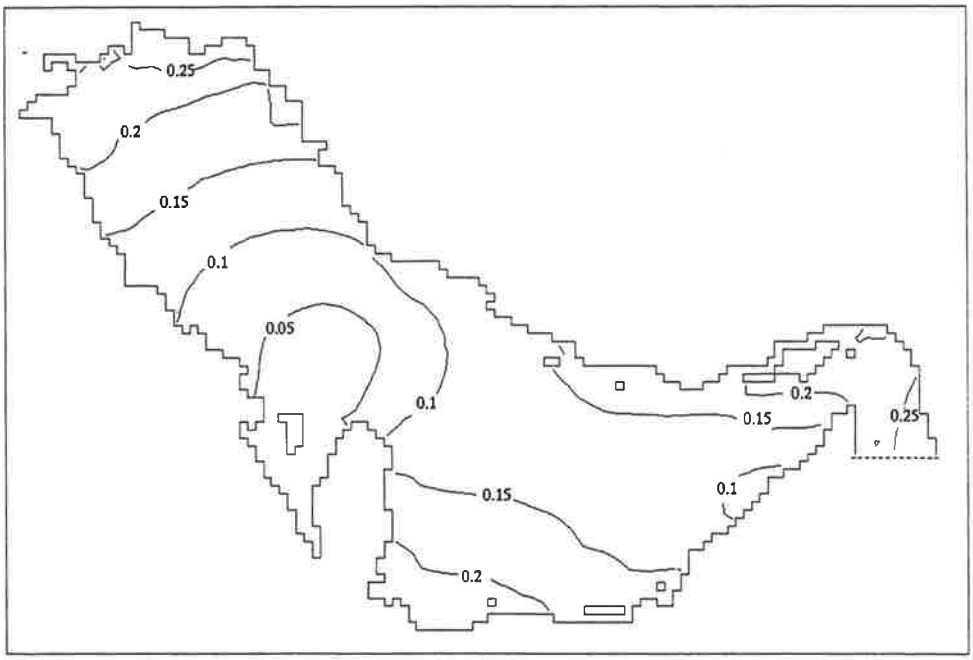

Figure 7.5: *Amplitude contours (m) for the O_1 tidal constituents of sea surface elevation from the* **INST** *model.*

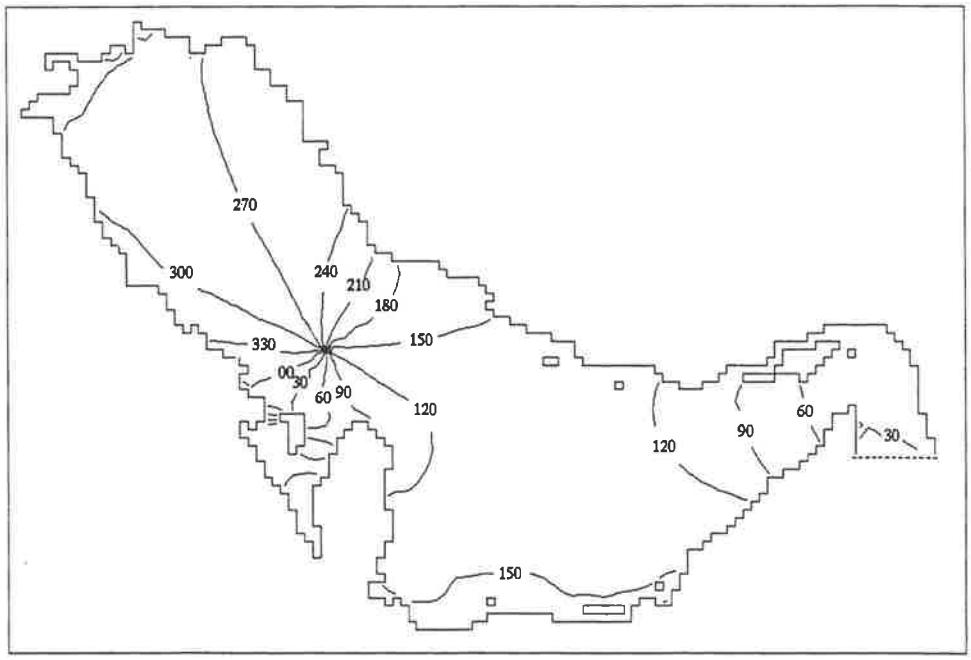

Figure 7.6: *Phase contours (degrees GMT) for the O_1 tidal constituents of sea surface elevation from the* **INST** *model.*

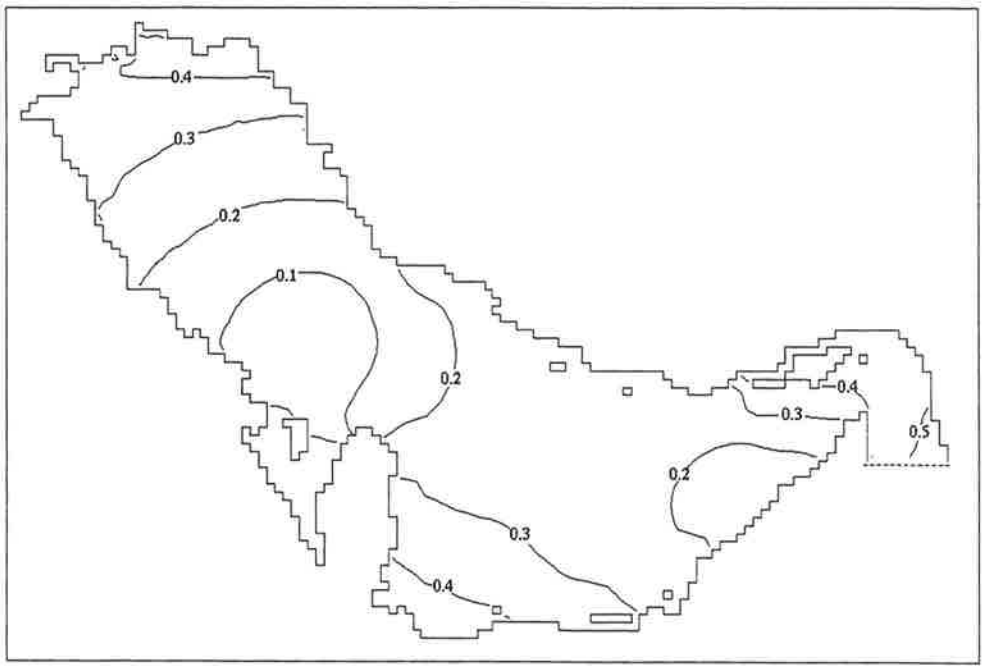

Figure 7.7: *Amplitude contours (m) for the K_1 tidal constituent of sea surface elevation from the* **INST** *model.*

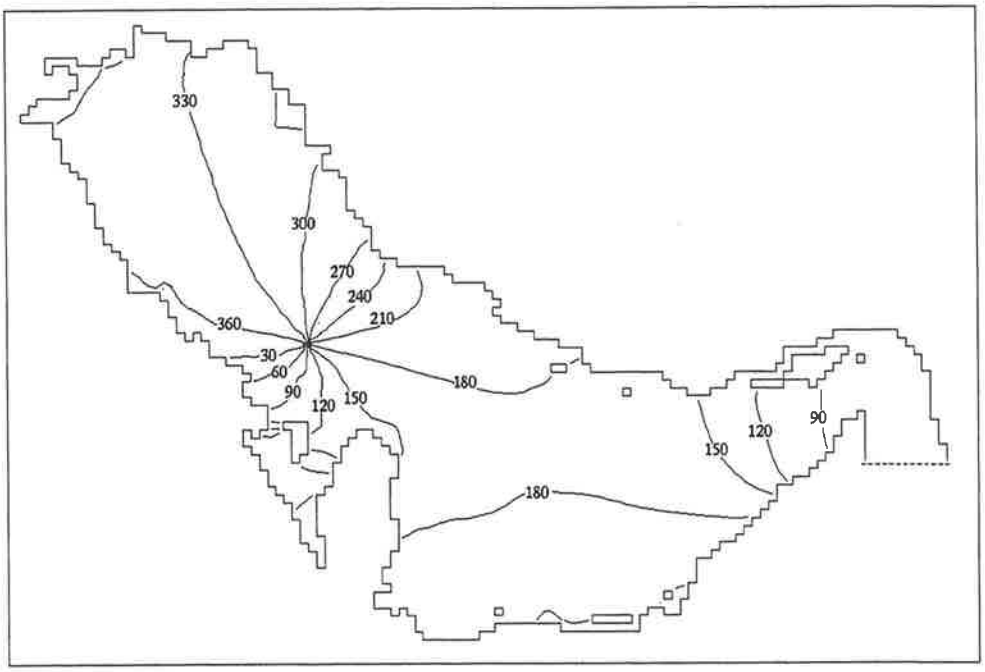

Figure 7.8: *Phase contours (degrees GMT) for the K_1 tidal constituent of sea surface elevation from the* **INST** *model.*

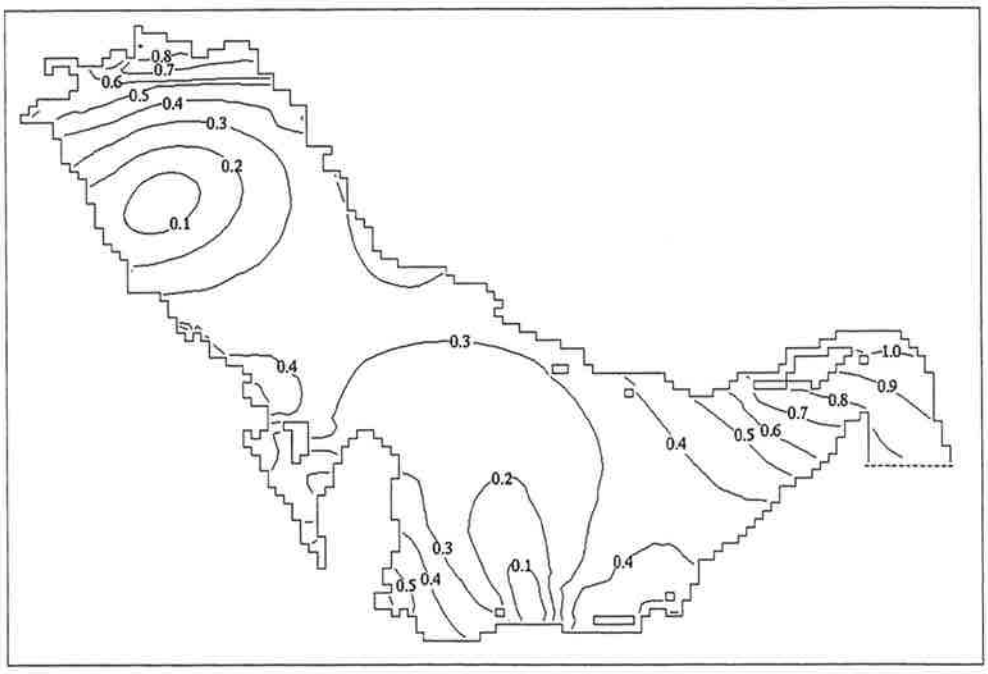

Figure 7.9: *Amplitude contours (m) for the M_2 tidal constituent of sea surface elevation from the* **INST** *model.*

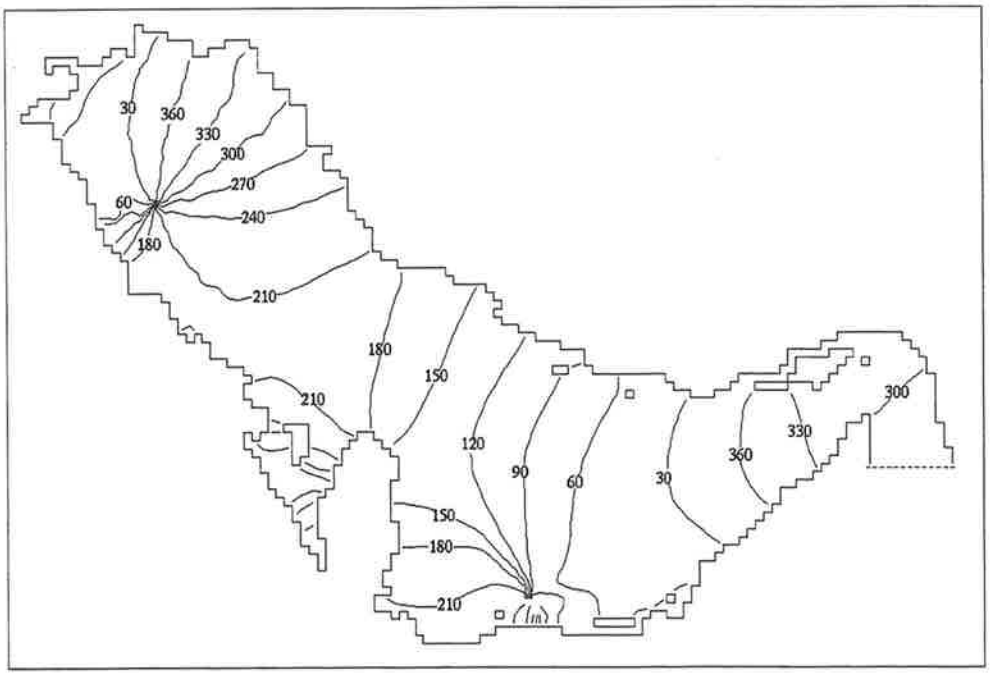

Figure 7.10: *Phase contours (degrees GMT) for the M_2 tidal constituent of sea surface elevation from the* **INST** *model.*

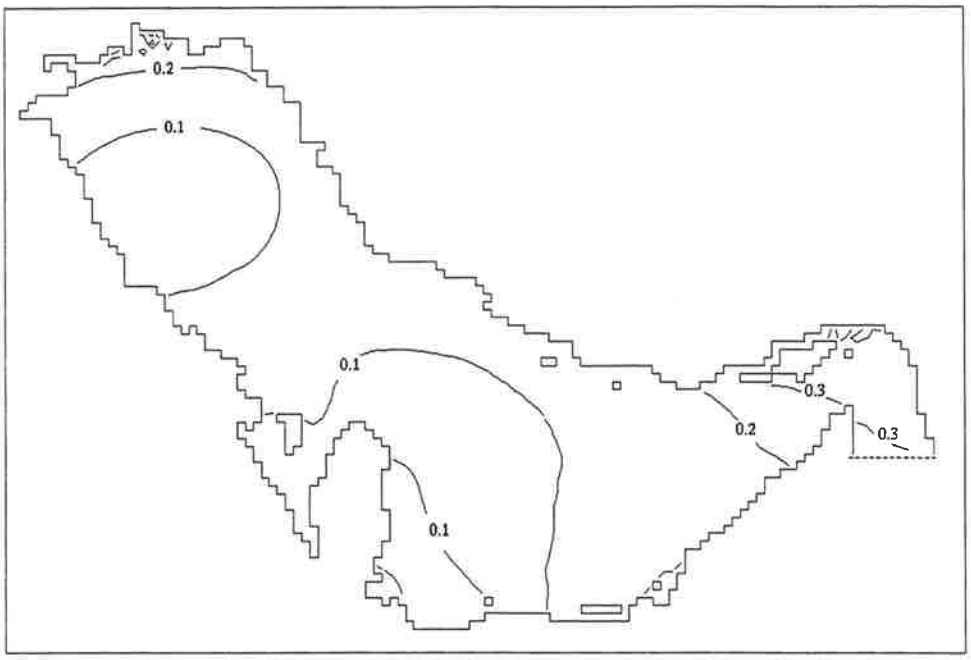

Figure 7.11: *Amplitude contours (m) for the S_2 tidal constituents of sea surface elevation from the* **INST** *model.*

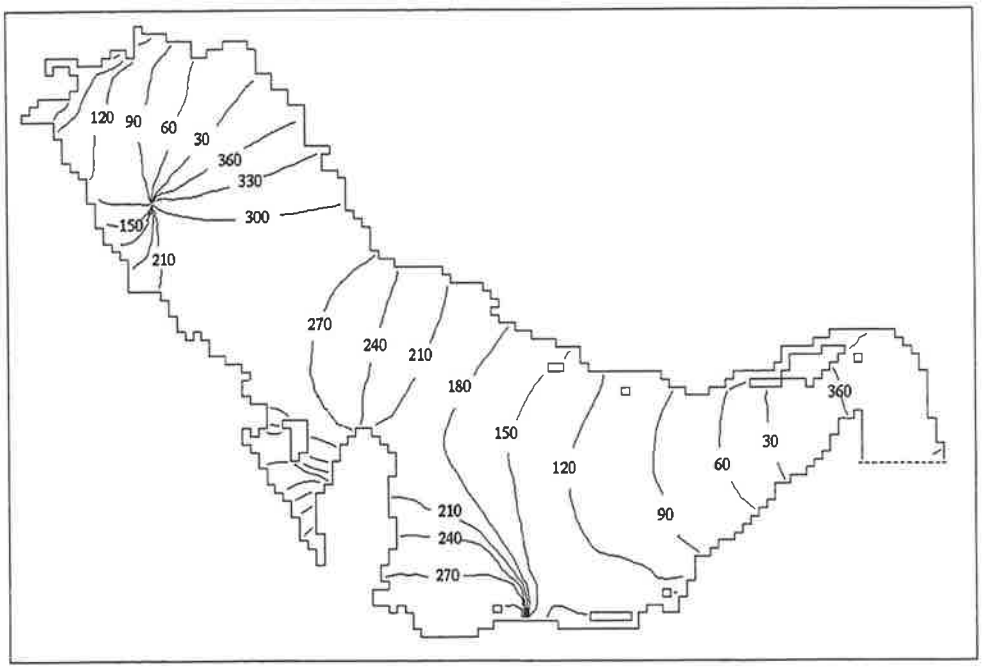

Figure 7.12: *Phase contours (degrees GMT) for the S_2 tidal constituents of sea surface elevation from the* **INST** *model.*

7.3.2 Elevation contours at a given time

Snapshots of sea surface elevation predicted by the model at the end of each of the first six hours of a 12 hr tidal period are presented in Figures 7.13–7.18. As Figure 7.13 shows, at the beginning on the head of the Gulf the value for surface elevation is $0.8m$ above MSL and in the Strait of Hormuz it is $0.6m$ below MSL. At the middle of the Gulf this figure shows that the value for sea surface elevation is $0.2m$ above the MSL. For the next hours the tidal wave moves into the Gulf. The elevation increases at the middle of the Gulf and decreases at the head (Figures 7.16–7.18). In particular the position of the zero elevation has moved from the middle of the Gulf to the head of the Gulf (see Figures 7.13 and 7.18, respectively). Figure 7.18 also shows a minimum value of $0.6m$ below MSL for the surface elevation at the head. As the process suggests, over the next six hours the sea surface elevation increases at the head and decreases in the Strait of Hormuz until the elevation reaches a maximum value at the head of the Gulf, then the process is repeated.

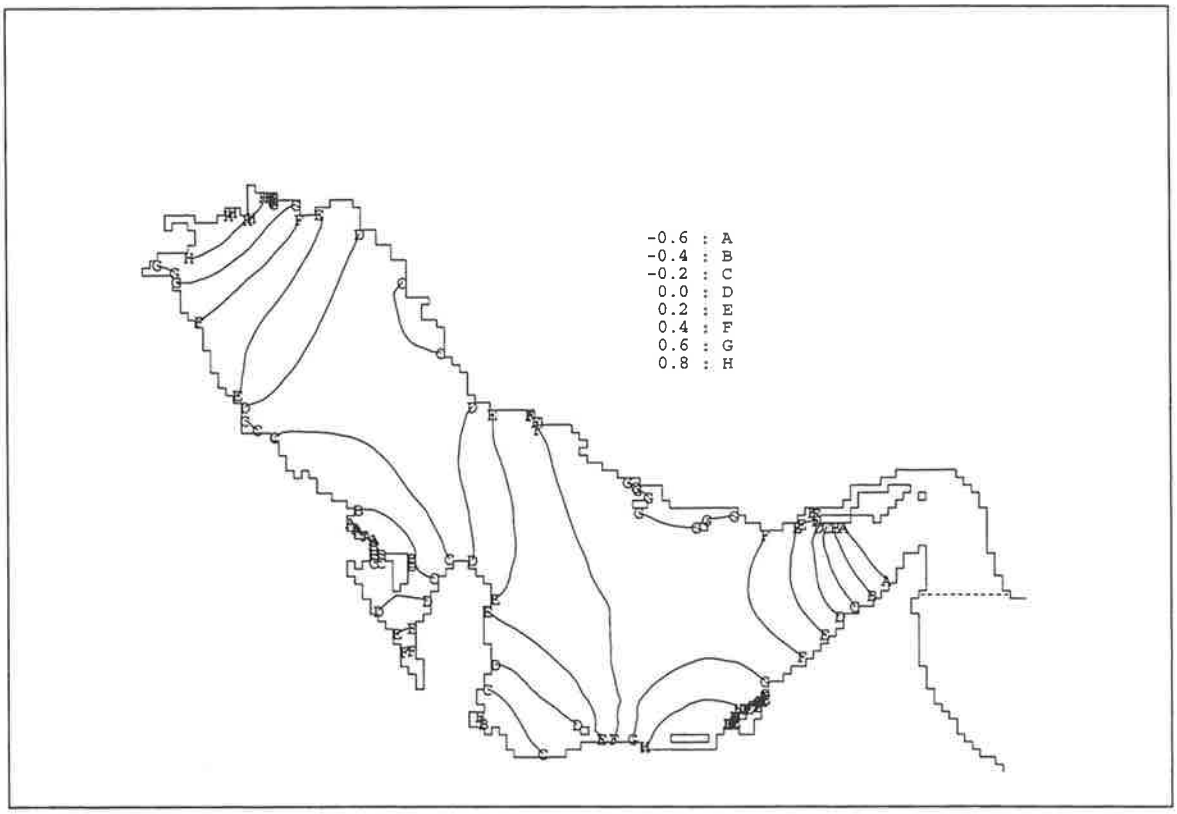

Figure 7.13: *Contours of sea surface elevation (m) in the Persian Gulf at the beginning hour of a five hour period.*

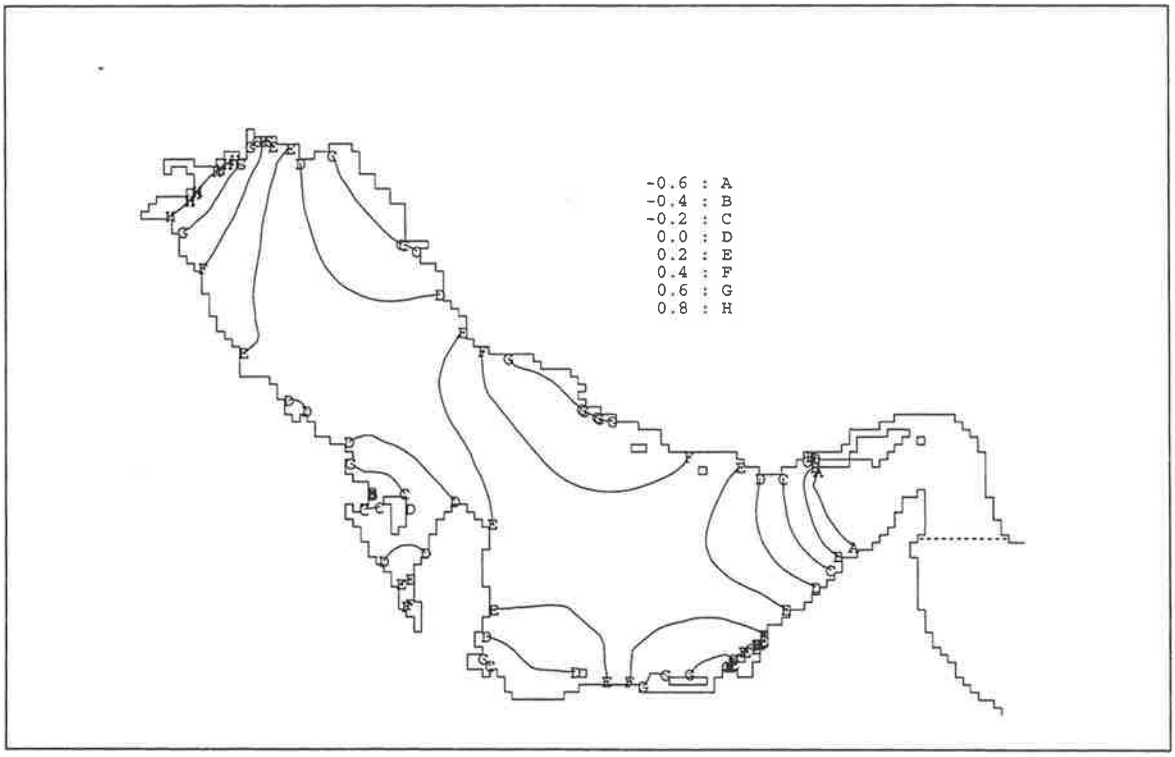

Figure 7.14: *Contours of sea surface elevation (m) in the Persian Gulf at the end of the first hour of a five hour period.*

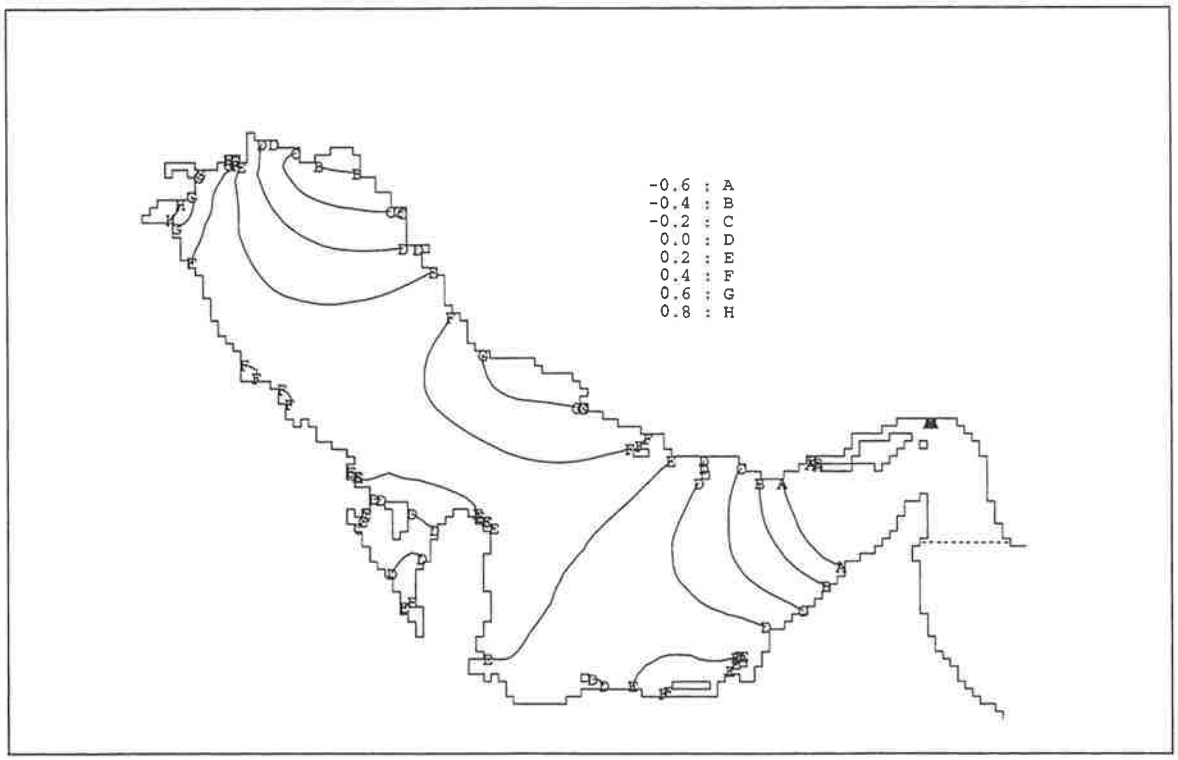

Figure 7.15: *Contours of sea surface elevation (m) in the Persian Gulf at the end of the second hour of a five hour period.*

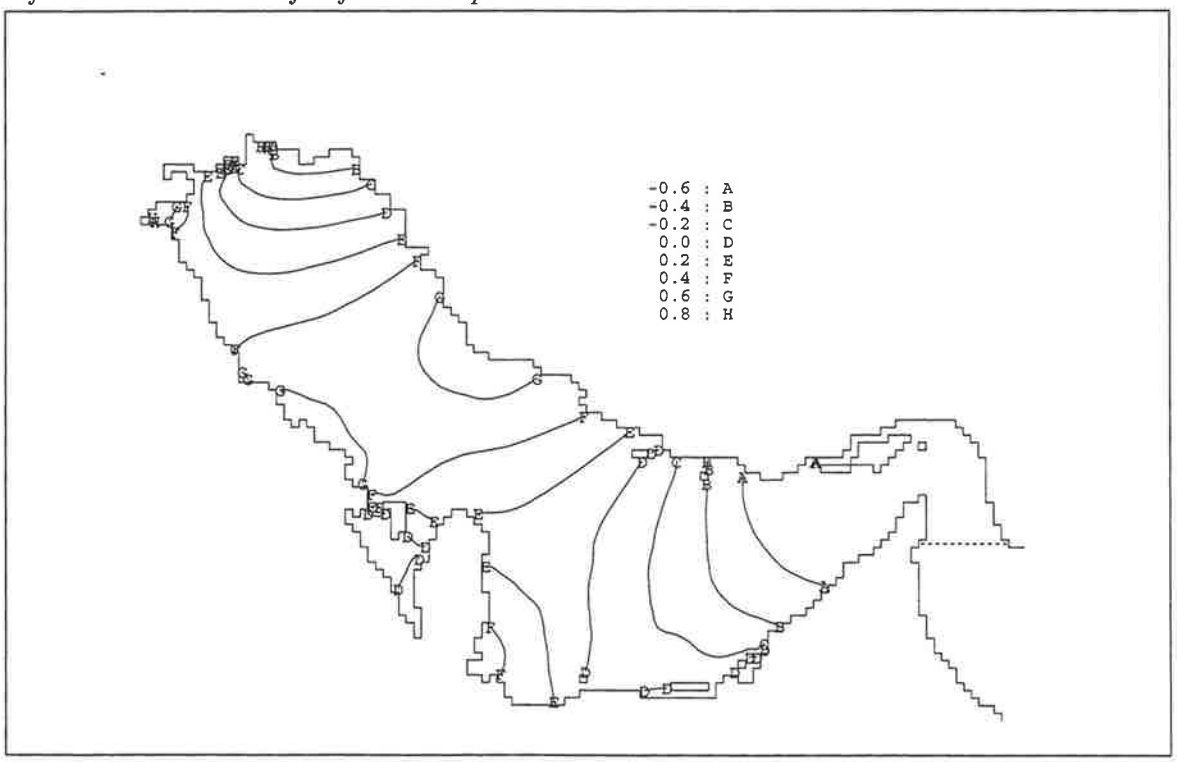

Figure 7.16: *Contours of sea surface elevation (m) in the Persian Gulf at the end of the third hour of a five hour period.*

Figure 7.17 shows that near Jazireh-ye Lavan (see Figure 4.1) along the Iranian coast, the value for surface elevation is $0.6m$ below MSL, which gradually increases along the Iranian coast to reach a maximum value of $0.8m$ above MSL near Lavar (Station 4 in Table 4.4). The value for surface elevation also keeps rising along the Qatar coast (see Figure 4.1) . It is at its highest value of $0.6m$ above MSL at the left corner of the United Arab Emirates.

Figure 7.17 also indicates that the surface elevation is relatively high, $0.6m$, at Bushehr Port in the Iranian side (Station 3 in Table 4.4) and diminishes through the head of the Gulf; near Kuwait the elevation is zero.

Figure 7.18 shows a minimum value of $0.6m$ at Bandar Abbas near the Strait of Hormuz (station 9 in Table 4.4) and Jazireh-ye Lavan (Station 13 in Table 4.4), at the sixth hour of a five hour period, and gradually increases along the Iranian coast and along the Qatar coast (see Figure 4.1). This figure shows that in the Bahrain area the surface elevation diminishes to a value of zero (along the Gulf of Salwa).

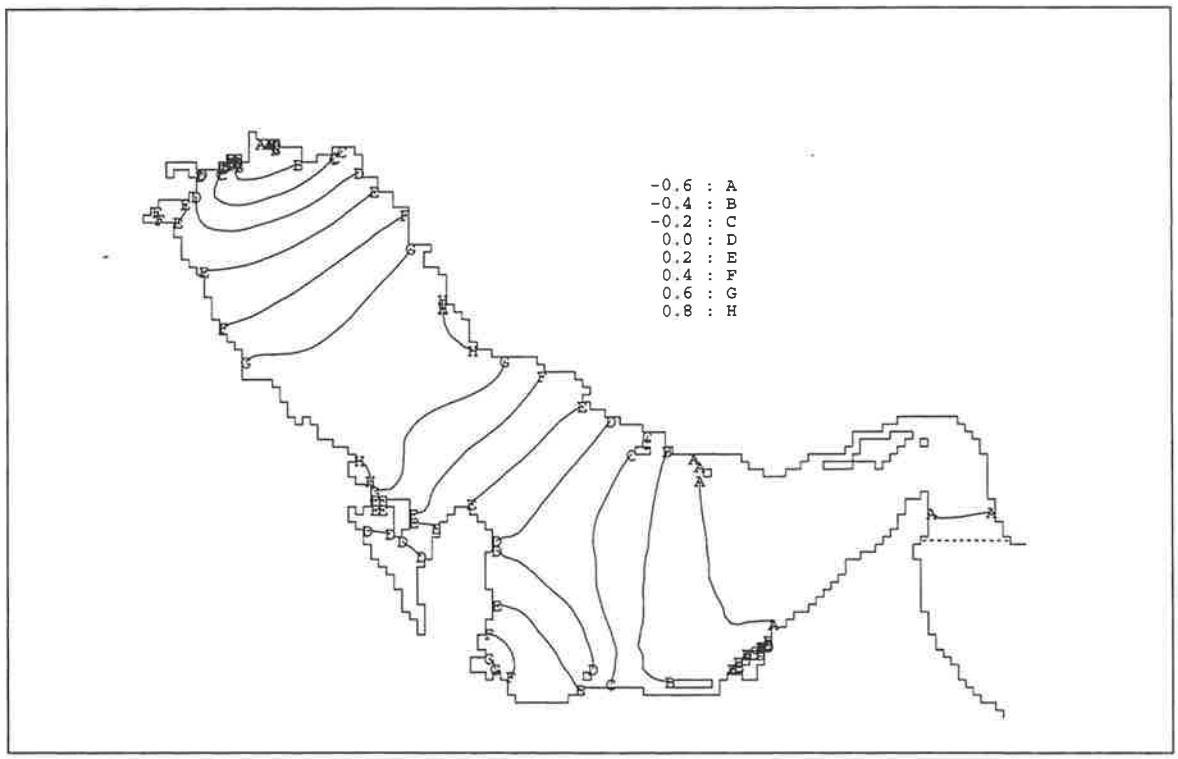

Figure 7.17: *Contours of sea surface elevation* (m) *in the Persian Gulf at the end of the fourth hour of a five hour period.*

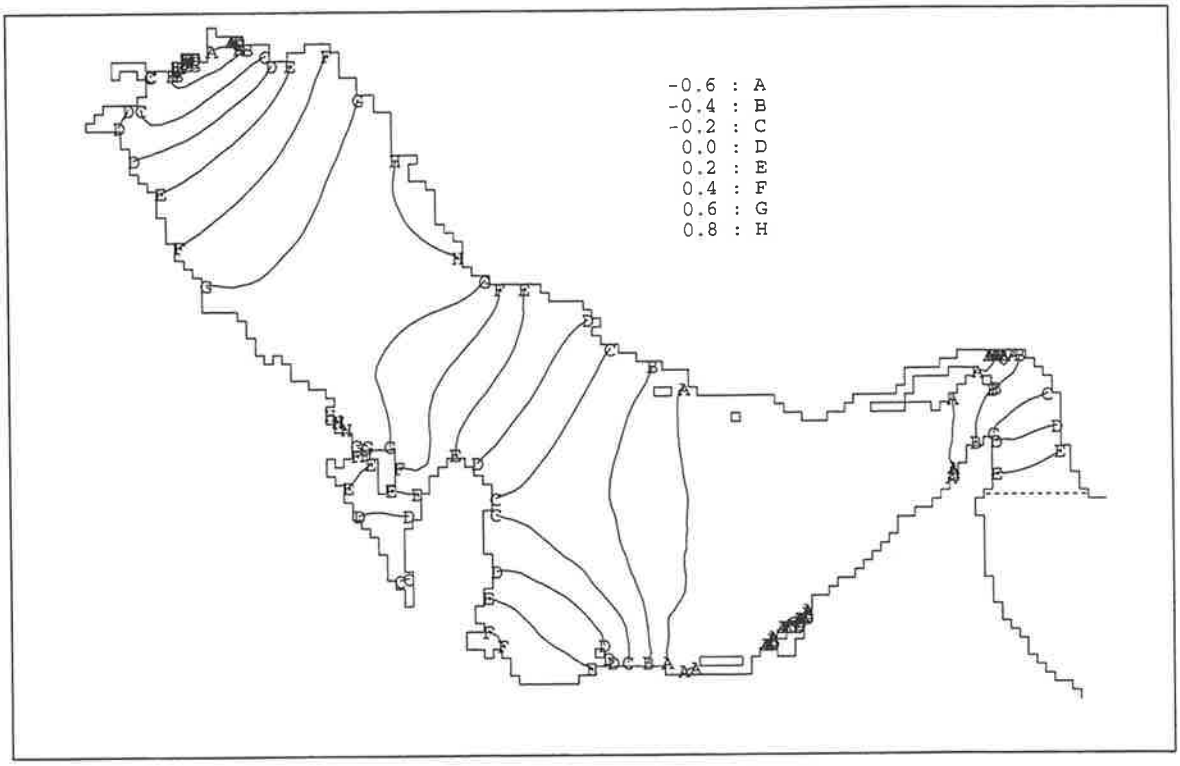

Figure 7.18: *Contours of sea surface elevation (m) in the Persian Gulf at the end of the five hour of a five hour period.*

7.3.3 Depth-averaged tidal current ellipses

In this section the model predicted tidal current ellipses for the O_1, K_1, M_2 and S_2 constituents are presented in Figures 7.19–7.22, respectively. The current ellipse plots show the behaviour of the depth-averaged current over a complete tidal cycle.

A comparison is made between predictions from the **INST** and the spherical model of Chapter 5 (coarse model of the **INST**). As no published reports of observational data on tidal currents exist for the Gulf no comparisons can be made between observed and simulated currents. The discussions below are based on the good comparisons for the tidal elevations. The tidal ellipses predicted by the **INST** model are similar to those of the spherical model for each constituent, see for example Figures 7.19(a) and 7.19(b). The current patterns between the two diurnal tidal ellipses, O_1 and K_1 are similar in each model, see for example Figures 7.19(a) and 7.20(a). Also the similarity in current pattern is clearly noted for the semi-diurnal tidal ellipses, see for example Figures 7.21(a) and 7.22(a).

Figures 7.19–7.22 indicate that the ellipses for all constituents have longitudinal and circular movement. The circular movement generally appears in the Strait of Hormuz, at the head region and near the United Arab Emirates coast. Figures 7.21 and 7.22 show a group of clockwise rotating ellipses for the M_2 and S_2 tidal constituents near Abu Zabi and Dubayy (see Figure 4.1) and another group of anticlockwise rotating ellipses at the head of the Gulf. The circular movement suggests that the particle paths are not totally periodic, that is, they do not return to same initial point.

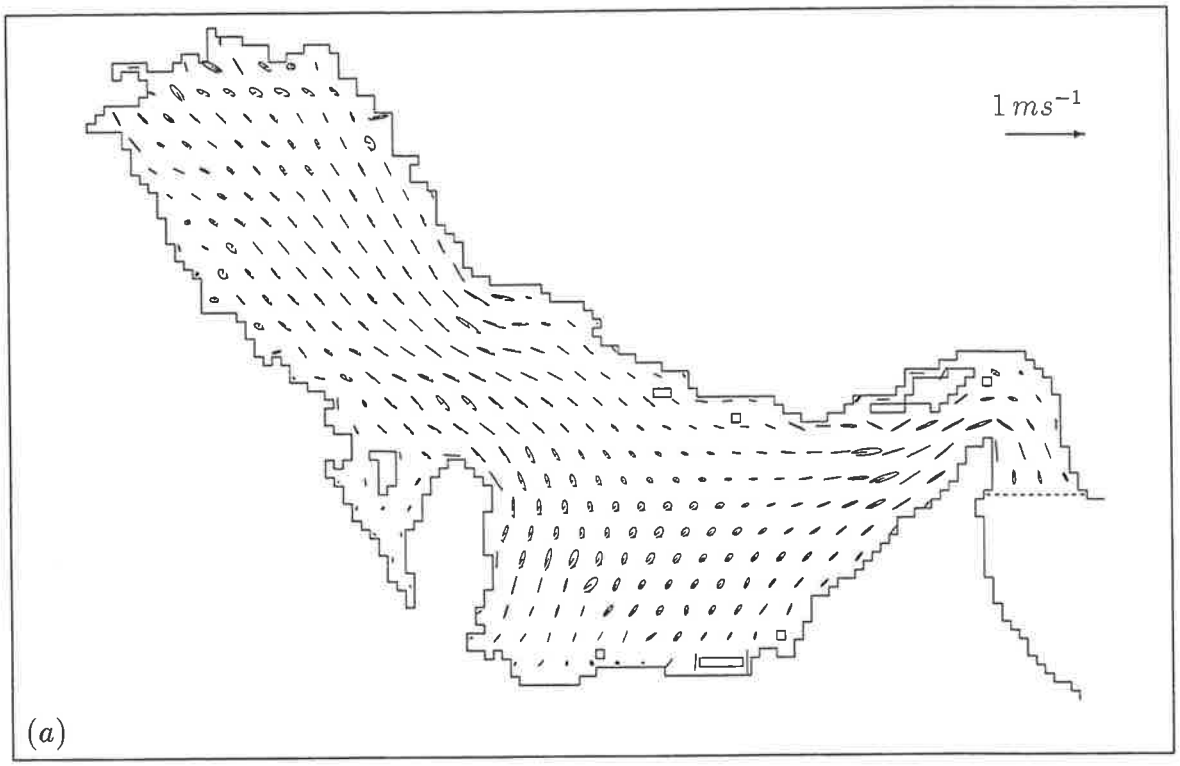

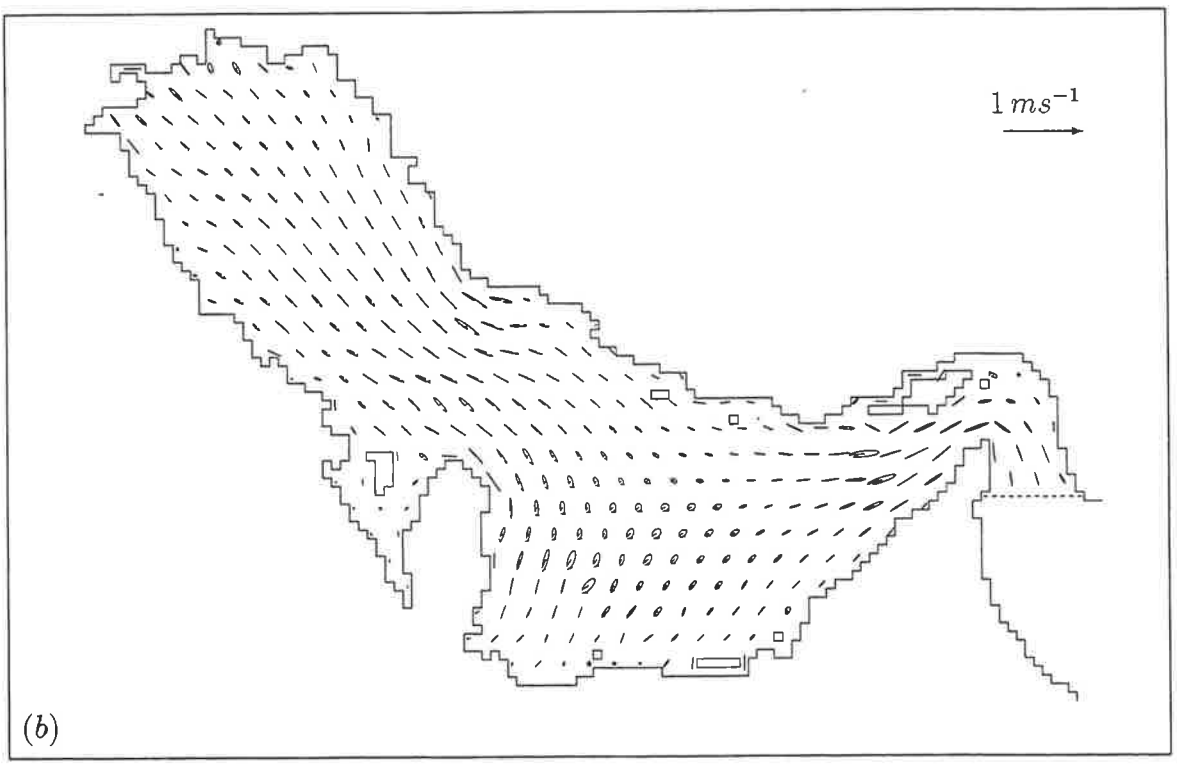

Figure 7.19: *Tidal current ellipses* (ms^{-1}) *for the* O_1 *tidal constituent of depth-averaged current for the (a)* **INST** *and (b) coarse tidal models of the Persian Gulf. Note that the scale is different to that used in the later figures.*

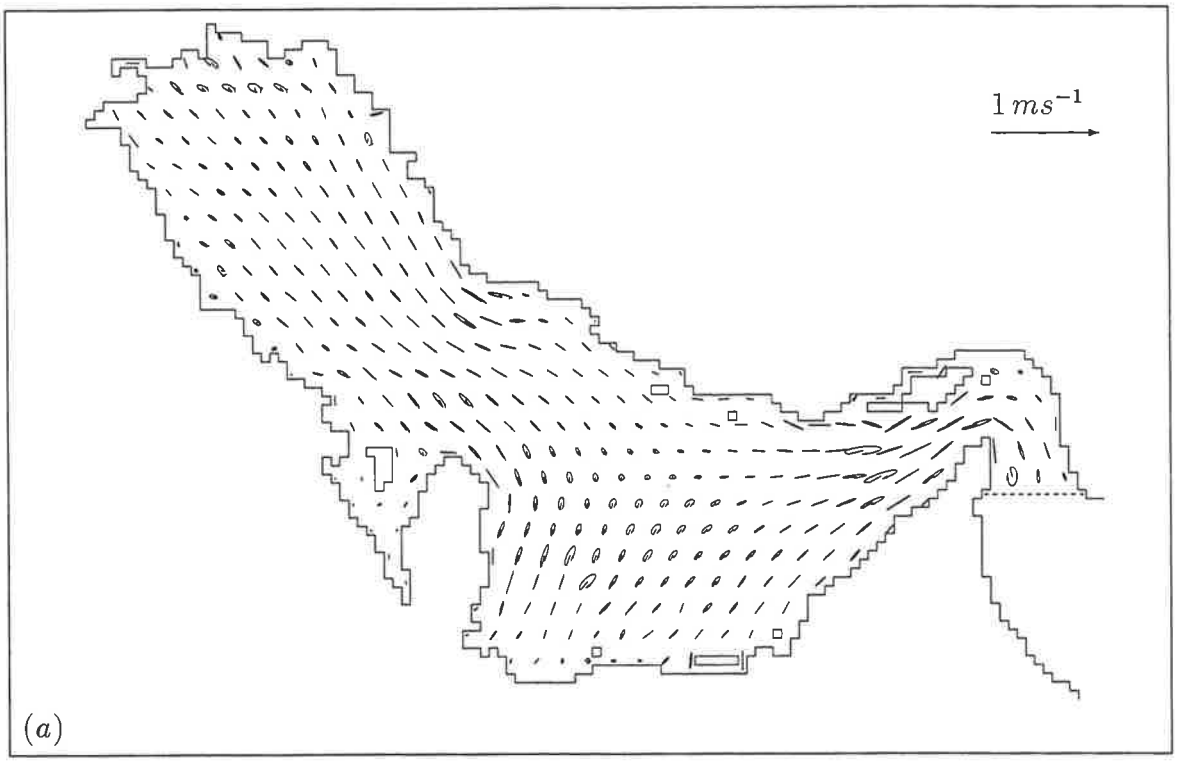

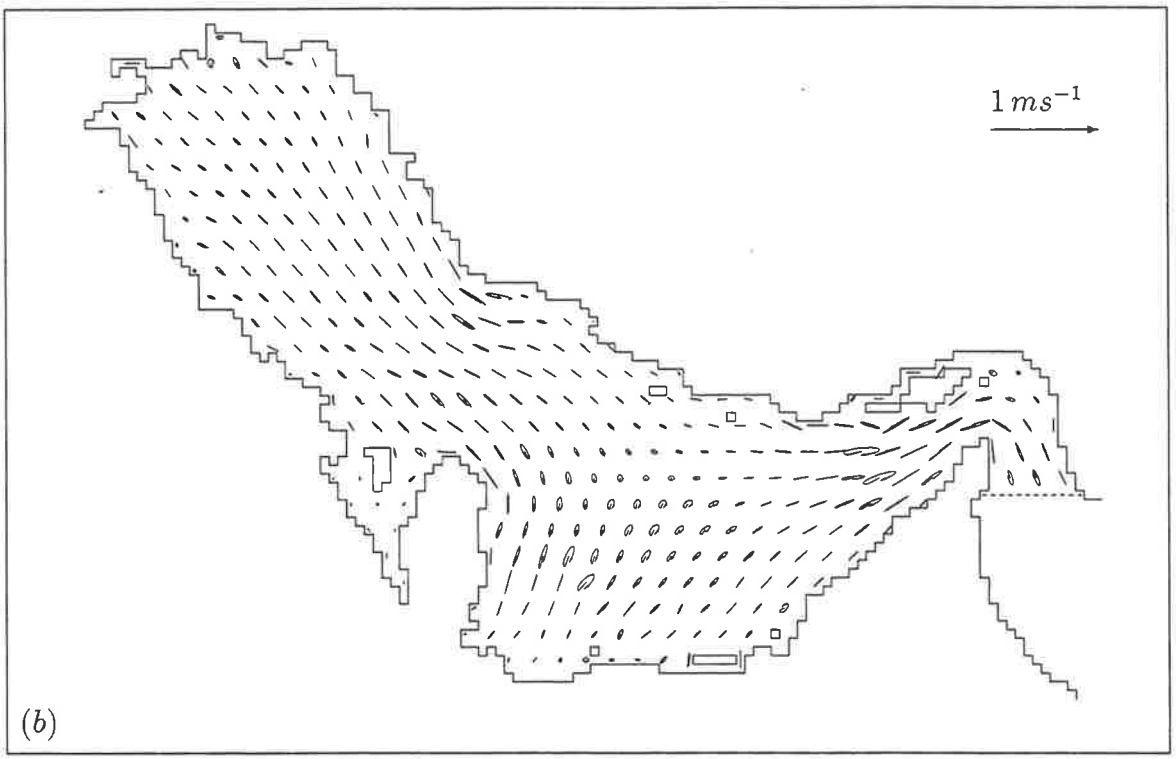

Figure 7.20: *Tidal current ellipses* (ms^{-1}) *for the* K_1 *tidal constituent of depth-averaged current for the (a)* **INST** *and (b) coarse tidal models of the Persian Gulf.*

7.3.4 The diurnal ellipses O_1 and K_1

Comparison of the O_1 tidal ellipses (Figure 7.19) with the K_1 ellipses (Figure 7.20) indicates that the K_1 current is stronger than the O_1 current (note that the scale of the O_1 plot in Figure 7.19 is different from that in Figure 7.20). The behaviour of both constituents is similar everywhere within the Gulf.

The diurnal current is strongest in the Strait of Hormuz and at the middle of the Gulf. It is weak close to the coastal boundaries, where the water is shallower.

As Figures 7.19 and 7.20 show these currents are stronger along the Iranian coast than the Arabian side, because the Arabian side is shallower. Through the head of the Gulf these currents have longitudinal movement, while from the open boundary toward the middle of the Gulf they generally show a circular movement. In the figures a group of anticlockwise rotating currents is seen in the south of the Gulf, toward United Arab Emirates. This continues on the western coast of Qatar. Near the Khark island (Station 2 in Table 4.4) on the Iranian side the current movement is longitudinal, changing to circular towards the end of the Gulf.

The coarse model predictions for the O_1 tidal current ellipses, Figure 7.19(b), are different at the top of the Gulf from the **INST** model results, Figure 7.20(b).

In general the strongest currents appear in the middle of the Gulf and also in the Strait of Hormuz.

7.3.5 The semi-diurnal ellipses M_2 and S_2

Figures 7.21 and 7.22 show the results for the M_2 and S_2 tidal constituents, respectively. They have similar current patterns, but the M_2 currents are stronger than the S_2, (note the change of scale for the S_2). They also exhibit similar behaviour everywhere in the Gulf.

The semi-diurnal currents are strongest from the open boundary through the middle of the Gulf and also at the head of the Gulf. They are weak near Lavar and Ras Al Qulaahy (station 10 in Table 4.4) on the Arabian side. Through the middle part of the Gulf, near the Iranian side, and around Lavar and Ras Al Qulaahy, these currents exhibit longitudinal movement, while in the other parts of the Gulf they are more circular, such as at head of the Gulf and in the United Arab Emirate area. These figures indicate a group of anticlockwise rotating currents in the Strait of Hormuz toward the coast of Qatar and another group of clockwise rotating currents at the head of the Gulf. The figures also show that there is a group of clockwise rotating currents near the coast of Bahrain. Around the Khark Island (Station 2 in Table 4.4) the tidal current movement is circular and keeps a similar movement toward the end of the Gulf, except along the Kuwait region which tends to be longitudinal and weaker than the currents on the opposite side.

In general the semi-diurnal current is stronger on the Iranian side and weaker in certain regions of the middle of the Gulf compared with the currents at the head or near the United Arab Emirate coast.

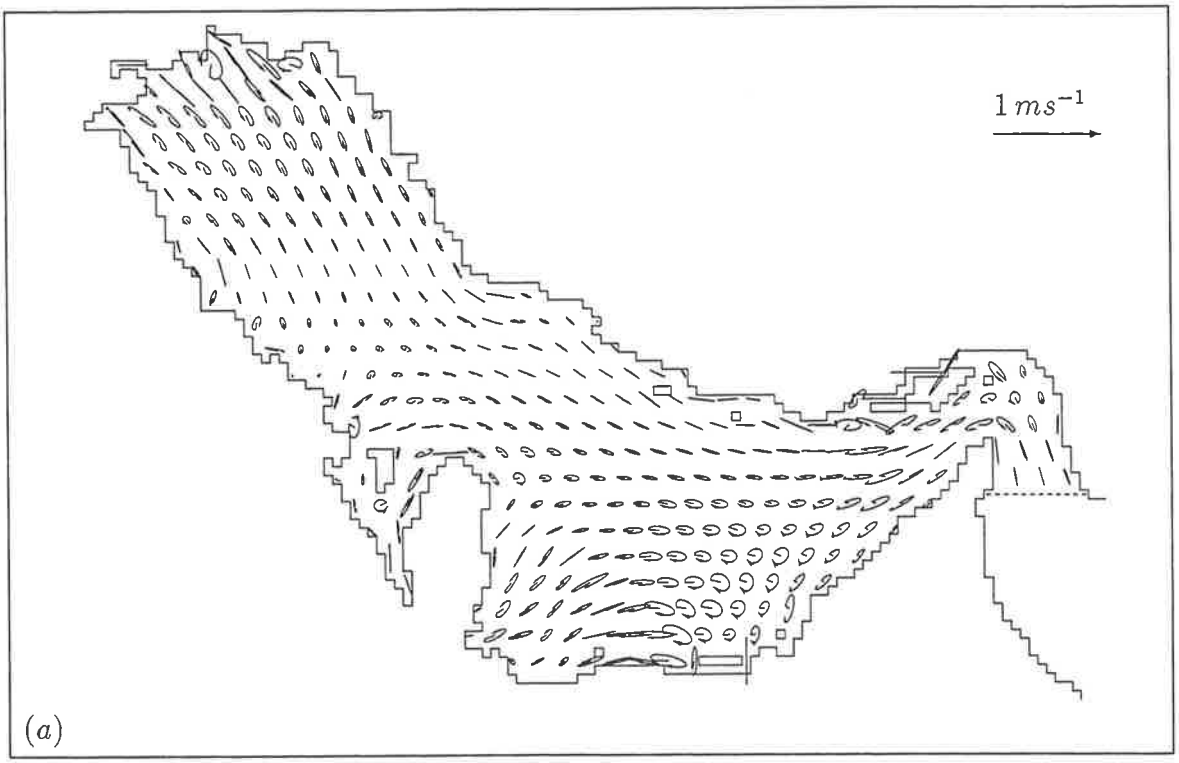

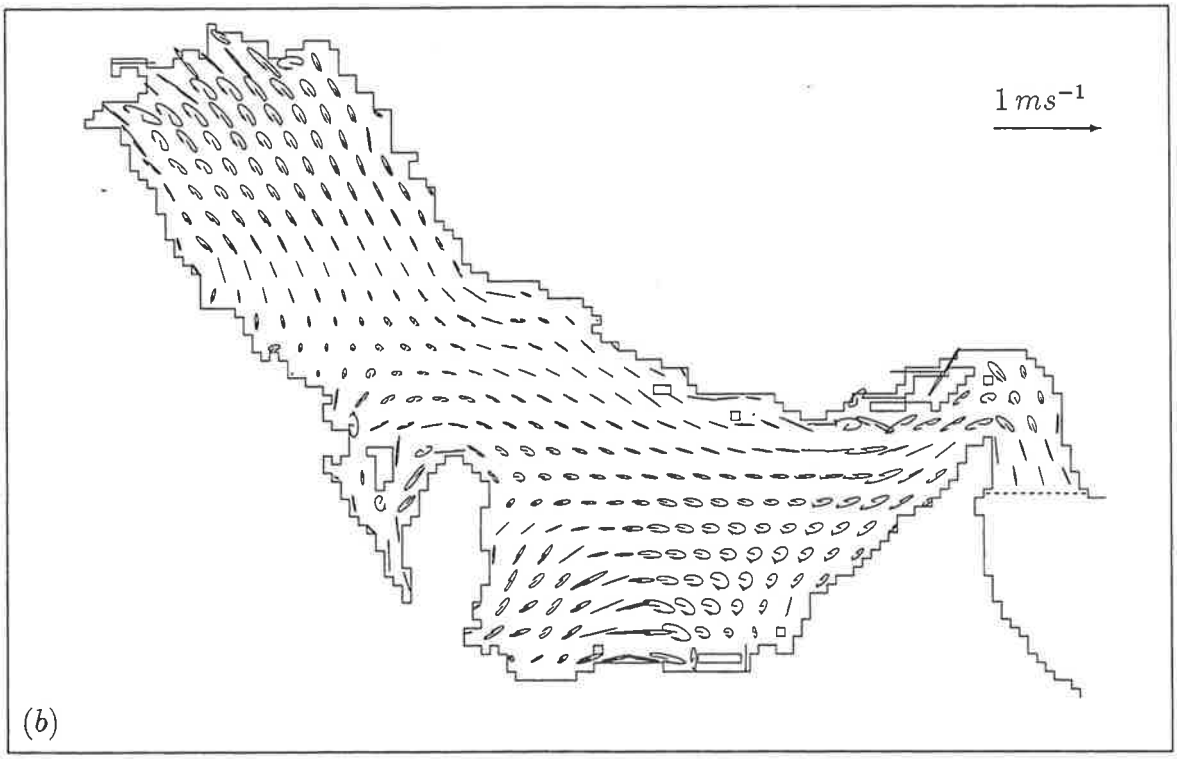

Figure 7.21: *Tidal current ellipses* (ms^{-1}) *for the* M_2 *tidal constituent of depth-averaged current for the (a)* **INST** *and (b) coarse tidal models of the Persian Gulf.*

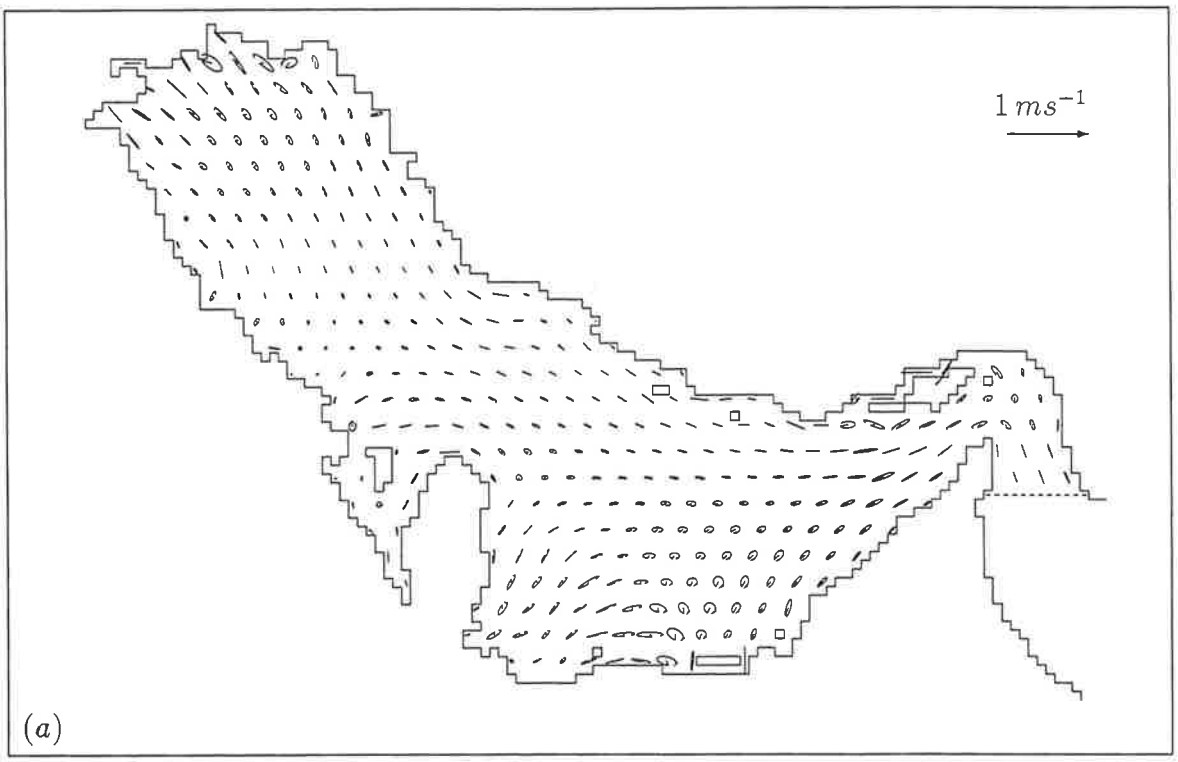

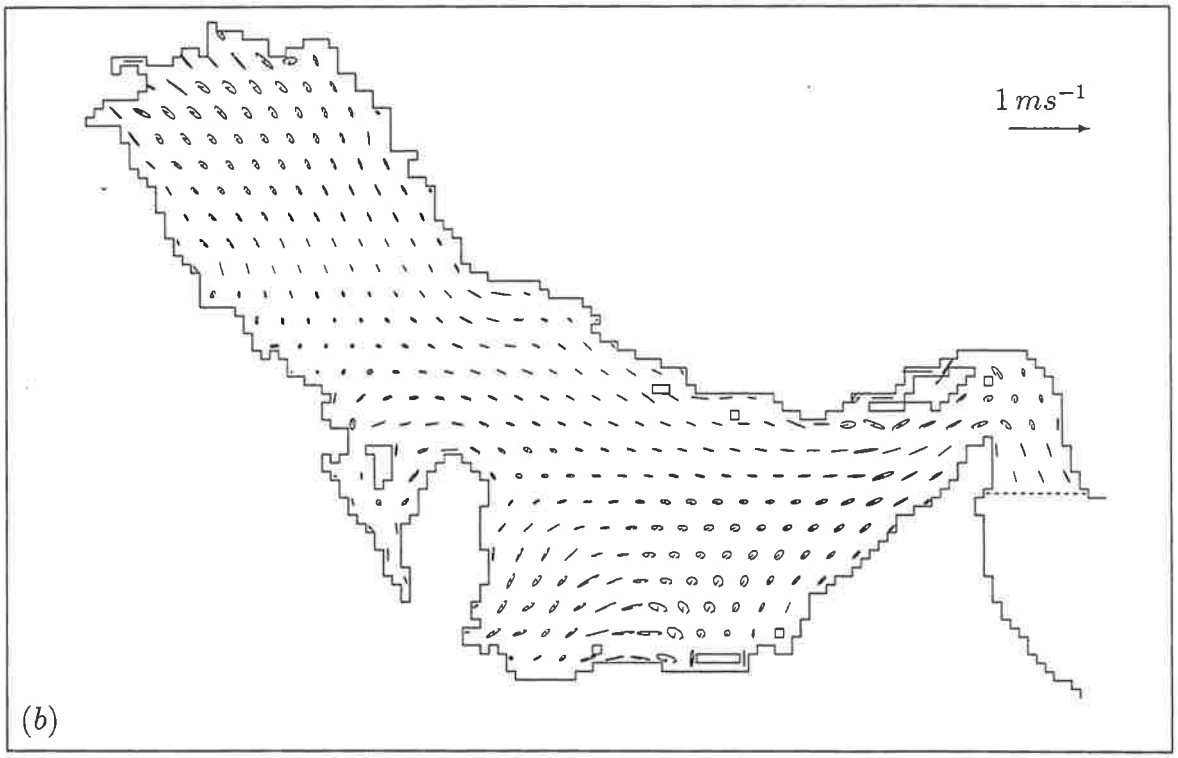

Figure 7.22: *Tidal current ellipses* (ms^{-1}) *for the* S_2 *tidal constituent of depth-averaged current for the (a)* **INST** *and (b) coarse tidal models of the Persian Gulf. Note the change of scale relative to the previous figures.*

As Figures 7.21–7.22 indicate the strongest currents appear around Zarqa and Ardhana (Stations 36 and 37 in Table 4.4), near Kuwaiti waters and in the Strait of Hormuz.

It should be noted that the predictions of the coarse model for the S_2 tidal ellipses, Figure 7.22(b), are different at the top of the Gulf from those shown by the **INST** model, Figure 7.22(a). The differences are due to the grid refinement in that region. Similar differences can be seen for the M_2 tidal ellipses in Figure 7.21(b), for the coarse model, and in Figure 7.21(a), for the **INST** model.

7.3.6 Depth-averaged velocity vectors at a given time

This section presents snapshots of depth-averaged current predictions resulting from the **INST** model of the Persian Gulf, for the first six hours of a 12 hr tidal cycle, Figures 7.23–7.28. For clarity, only velocity vectors at every ninth grid point on every ninth line of the fine grid data has been drawn, and velocity vectors at every third grid point on every third line of the coarse grid data has been drawn.

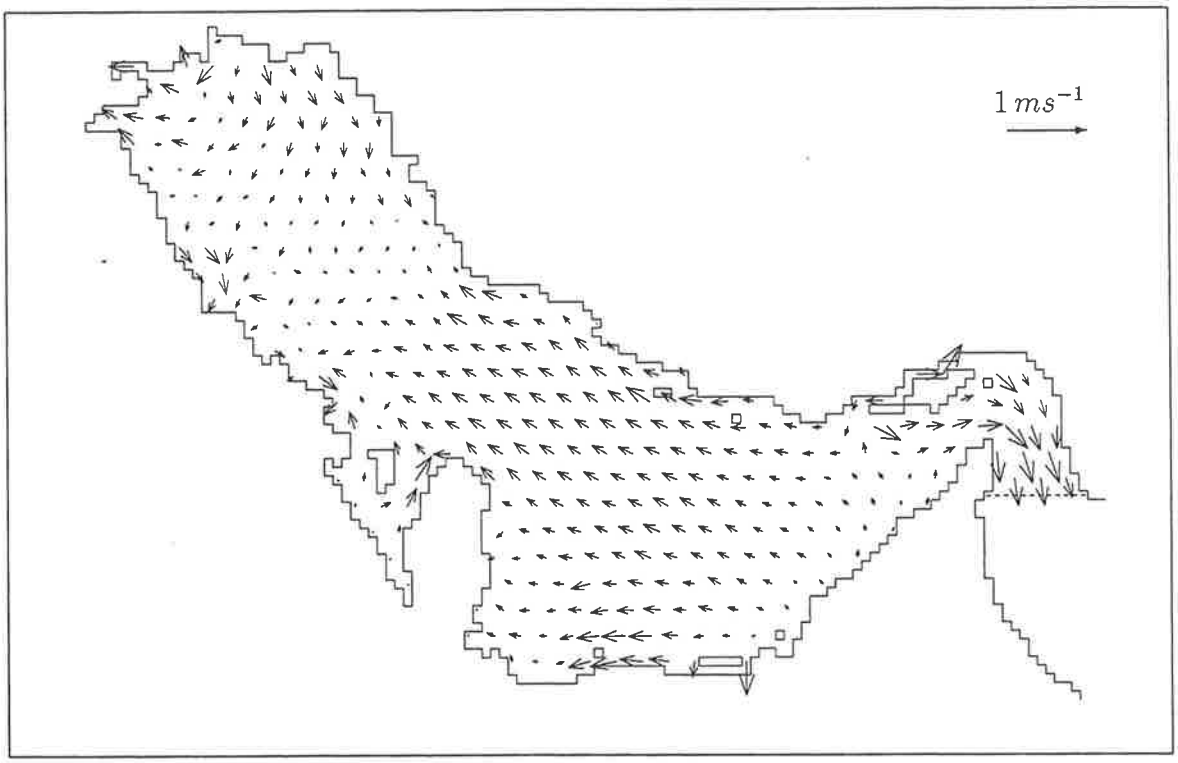

Figure 7.23: *Depth-averaged tidal current* (ms^{-1}) *vectors in the Persian Gulf at the end of the first hour of a six hour simulation using the* **INST** *model.*

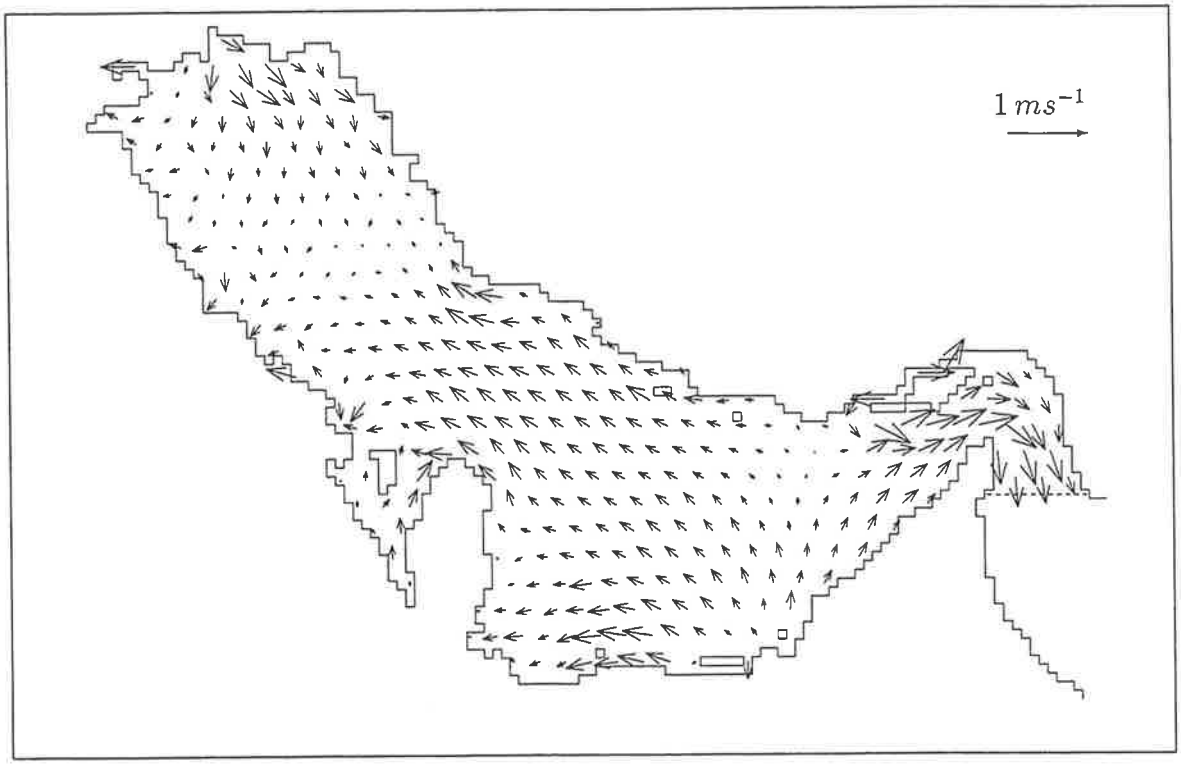

Figure 7.24: *Depth-averaged tidal current (ms^{-1}) vectors in the Persian Gulf at the end of the second hour of a six hour simulation using the* **INST** *model.*

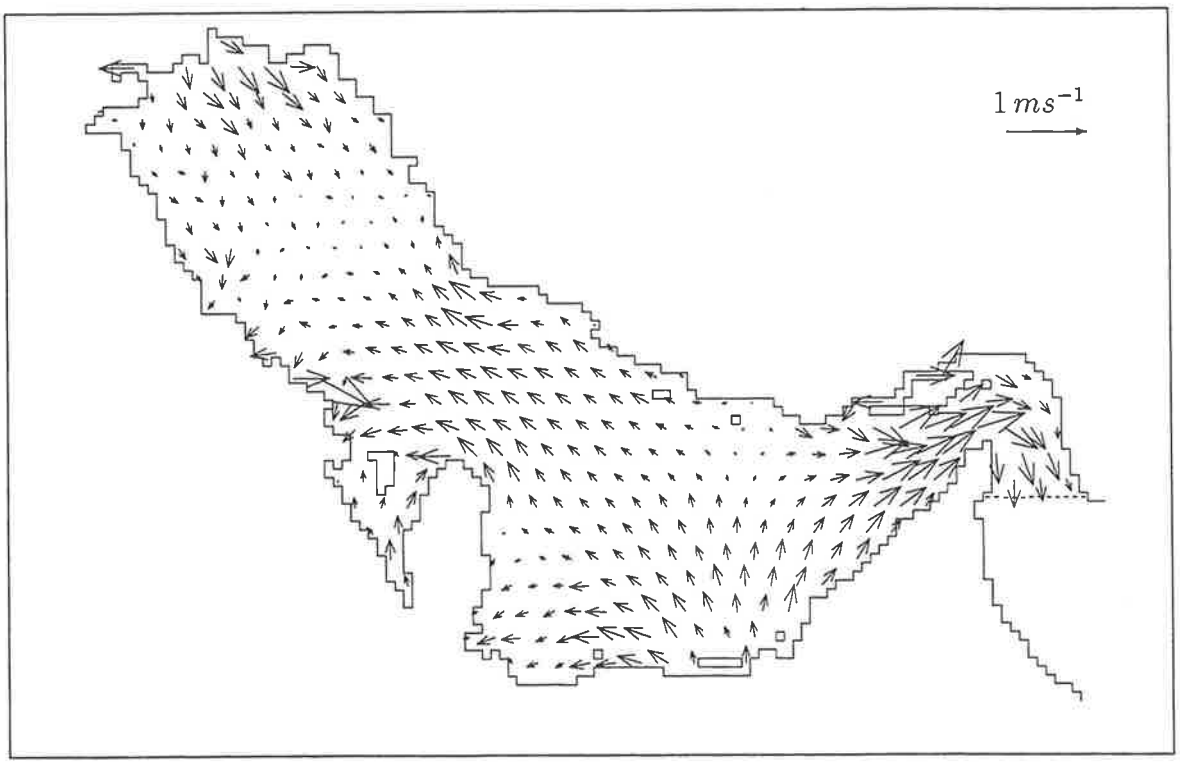

Figure 7.25: *Depth-averaged tidal current (ms^{-1}) vectors in the Persian Gulf at the end of the third hour of a six hour simulation using the* **INST** *model.*

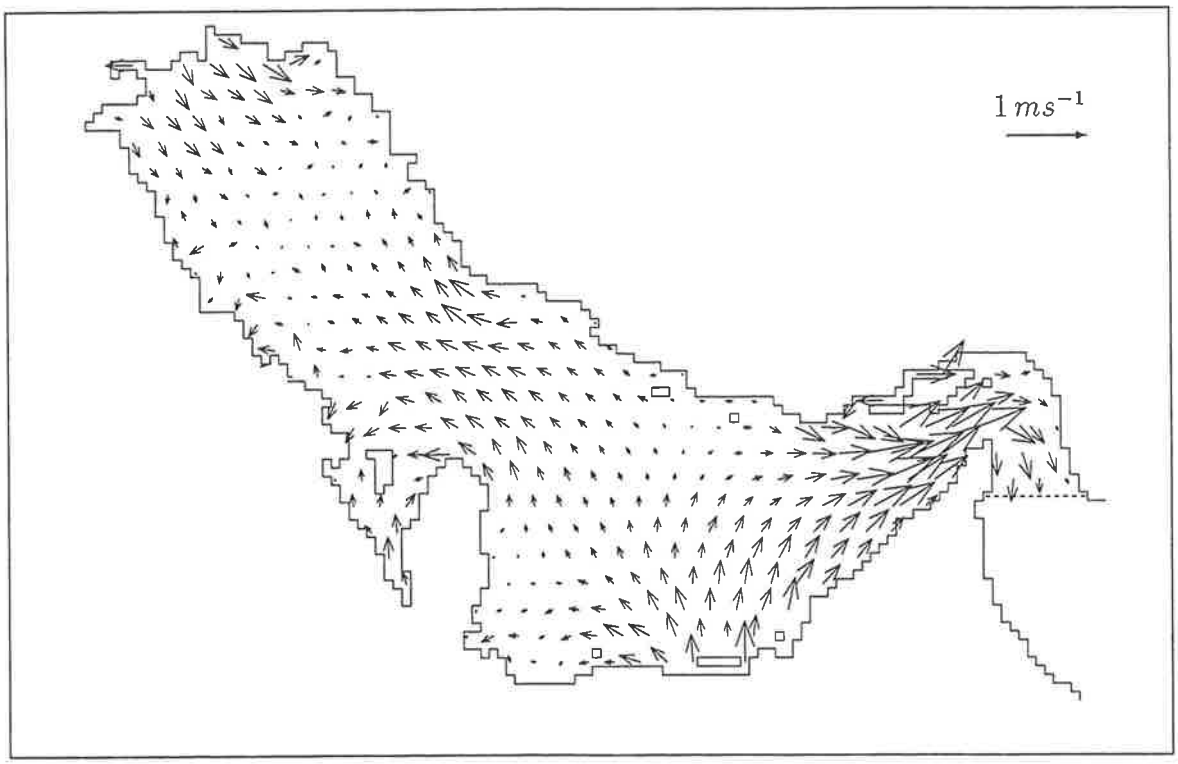

Figure 7.26: *Depth-averaged tidal current* (ms^{-1}) *vectors in the Persian Gulf at the end of the fourth hour of a six hour simulation using the* **INST** *model.*

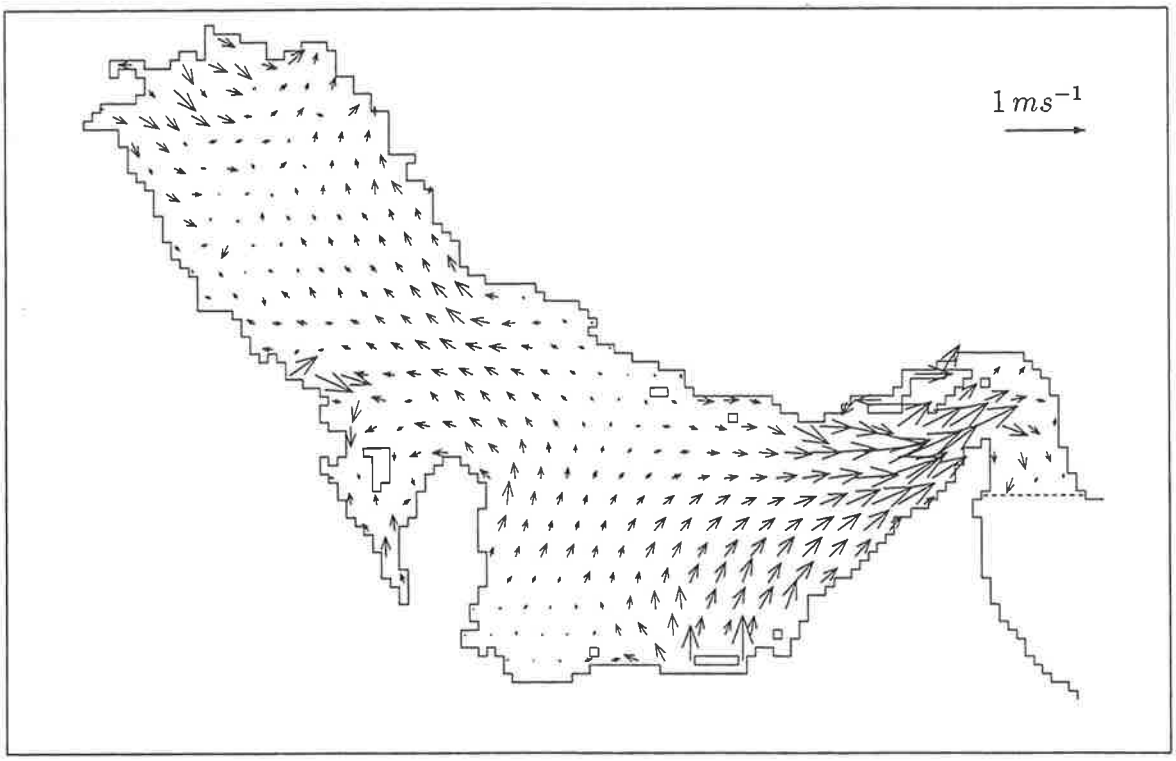

Figure 7.27: *Depth-averaged tidal current* (ms^{-1}) *vectors in the Persian Gulf at the end of the fifth hour of a six hour simulation using the* **INST** *model.*

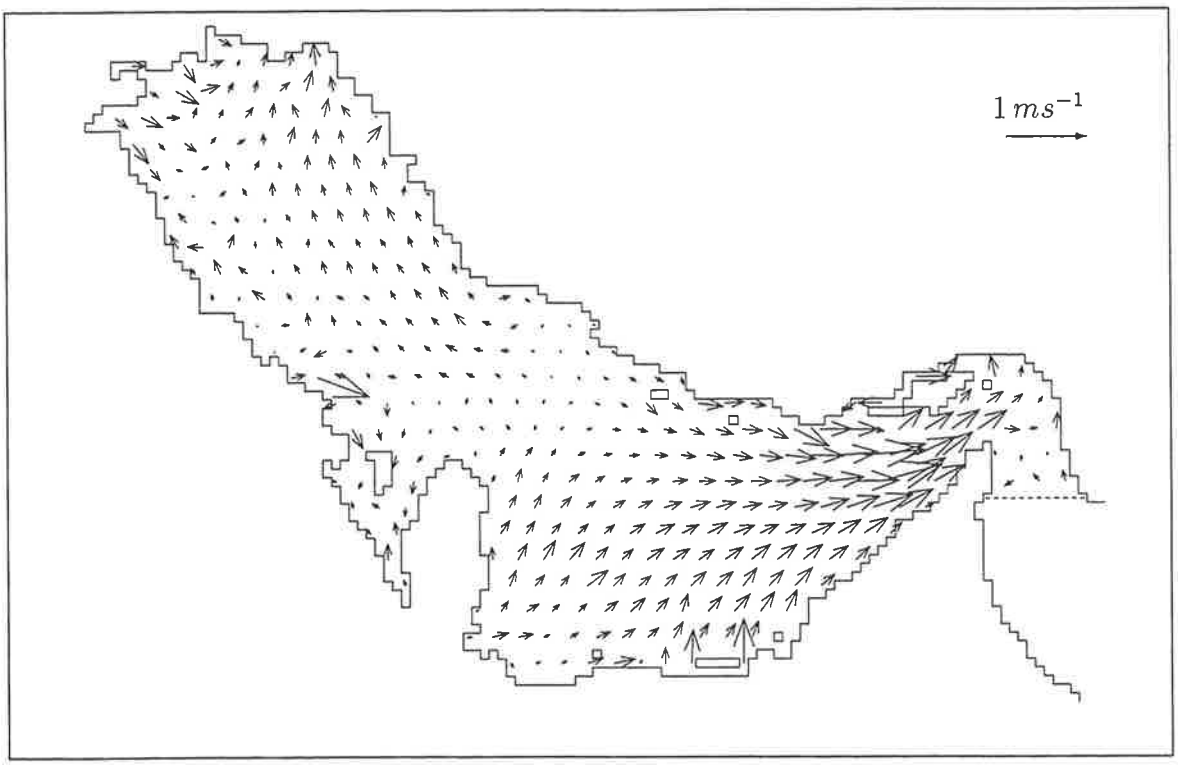

Figure 7.28: *Depth-averaged tidal current* (ms^{-1}) *vectors in the Persian Gulf at the end of the sixth hour of a six hour simulation using the* **INST** *model.*

It can be seen that the tidal current field in the Gulf is quite complicated with strong velocities occurring around the middle of the Gulf, near Bahrain, and in the Strait of Hormuz. Velocities are weak nearly at the middle of the Gulf, around Ras Al Qulaahy and Turut bay in the Arabian side (Stations 10 and 11 in Table 4.4, respectively) and near Lavar in the Iranian side (Station 4 in Table 4.4). The figures show that most of the water mass enters and exits the Gulf along the Iranian coast, while the water along the Arabian coast moves more slowly, as the velocity is a function of depth of the water and the Arabian coast is shallower than the Iranian coast. It should also be noted that throughout the centre of the northwestern region of the Gulf, a weak return flow is seen. This continues towards the northwest where it approaches the coast. In the central area of the northern Gulf there is a weak flow of magnitude 0.04–0.08 ms^{-1}.

As Figures 7.23–7.28 indicate the velocities produced in the middle and at the top of the head of the Gulf are relatively large, but the largest velocities exist in the Strait of Hormuz, where the water has maximum depth. Along the coastal regions the velocities are smaller, because these regions are shallower than the other parts of the Gulf.

7.3.7 Depth-averaged velocity residuals

A residual current is defined as the part of the velocity that is left after removal of all tidal oscillations. The purpose of producing residual plots is to present the broad regions where model generation of non-linear constituents takes place. The residuals are a consequence of the non-linearity of the model. So a fully linear model would predict zero residual tidal circulation.

The predicted four major tidal constituents of depth-averaged velocity fields are used to reconstitute a time series of velocity for a 29 day period at each computational point. This series is then subtracted from the raw velocity predictions of the numerical model at the corresponding computational points. The difference is

then averaged by dividing by the number of hourly data points (697) it represents. The result which is plotted as a vector shows the contribution to the mean 29-day circulation due to the non-linearity of the model.

The residual vectors for the velocity obtained from the **INST** model are shown in Figure 7.29(a). Large residuals are predicted through the head of the Gulf and the Strait of Hormuz. *The pattern of residuals around the northern part of the Gulf shows large values in areas which do not coincide with the interface between the two grids; also note that area D is not along the fine grid open boundary.*

The residual plots for the coarse model (spherical model of Chapter 5) are presented in Figure 7.29(b). There are some differences between the pattern of residuals resulting from the two models. At the head of the Gulf region, **A**, the coarse model predicts larger values compared with the predictions of the **INST** model in the same area. In the north-east of Bahrain, **B**, large residuals are predicted by the coarse model, while in the same region **INST** shows small values. Around the Strait of Hormuz, **C**, quite different residuals are also predicted by the models. The coarse model shows large values and the **INST** model predicts smaller residuals which are parallel to the coastline. Around the Saudi coast line, **D**, which is very shallow, large values are shown by the **INST** model compared with the values predicted by the coarse model in the same region.

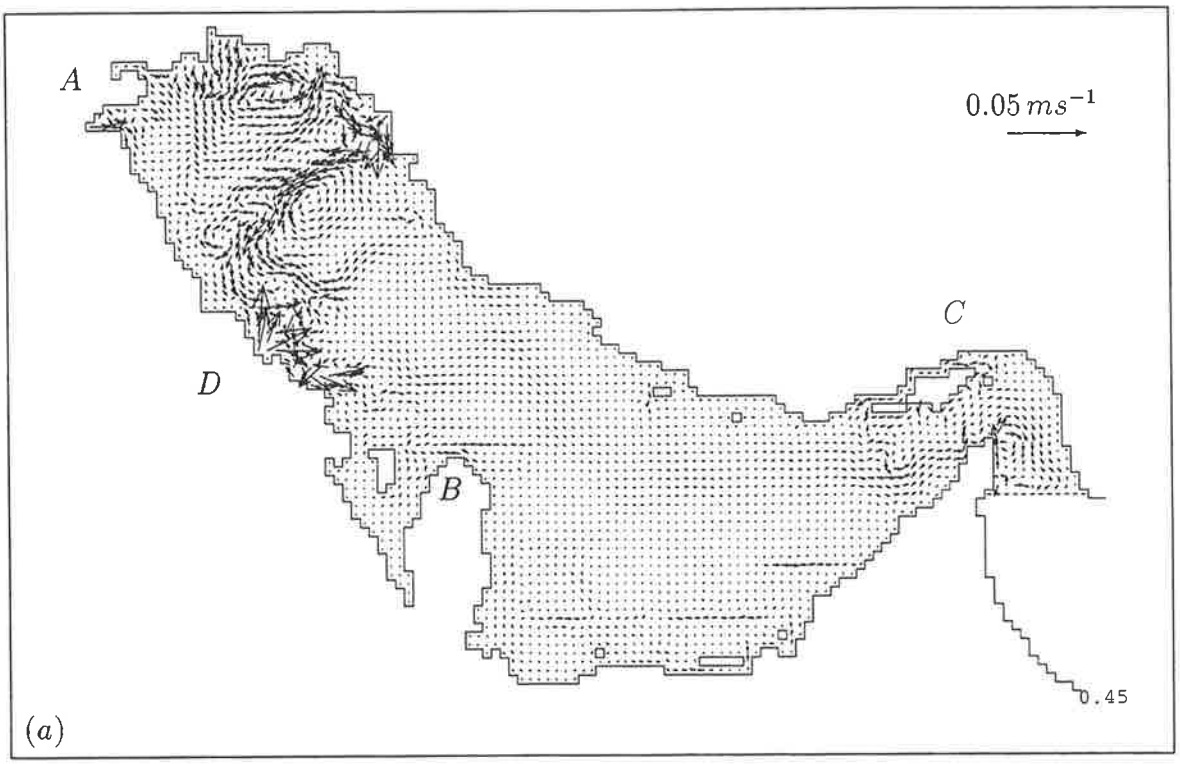

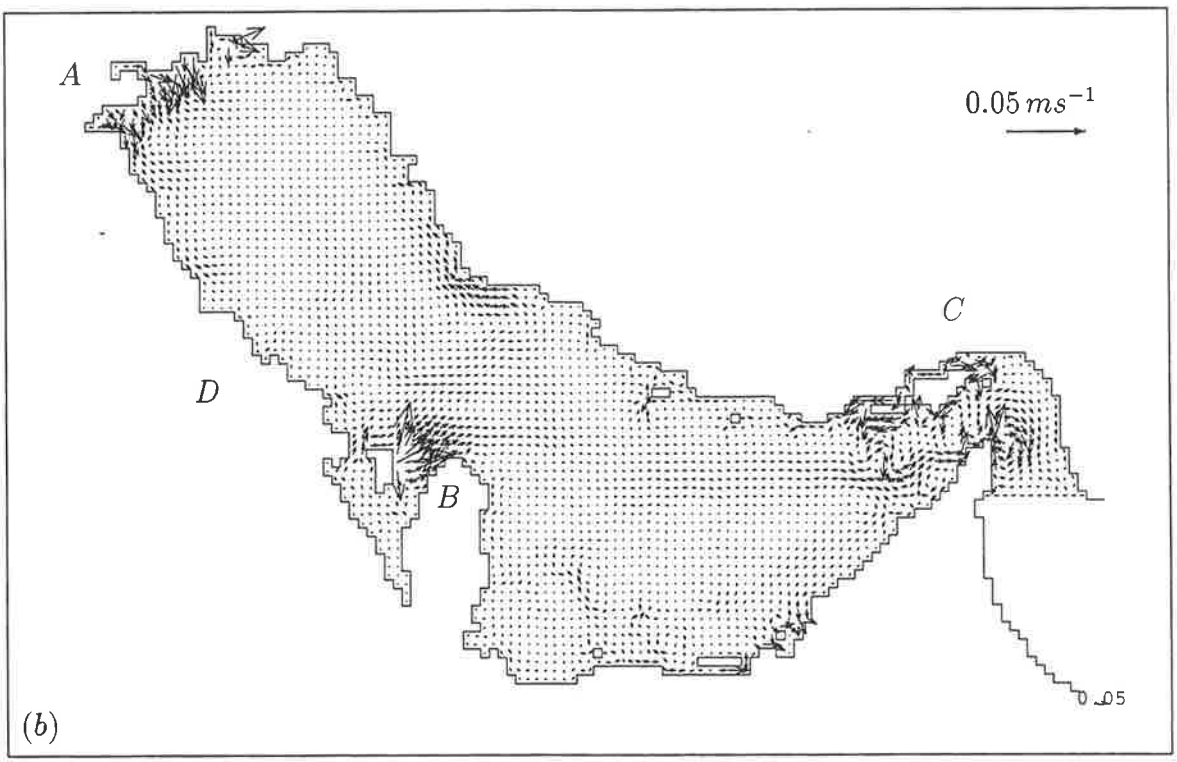

Figure 7.29: *Depth-averaged velocity residuals for a 29 day period for the (a)* **INST** *and (b) coarse tidal models of the Persian Gulf.*

Chapter 8

Summary and conclusion

This thesis discusses the development of a nested finite difference model of tidal flow in coastal regions and the application of this model to the Persian Gulf, together with comparisons between this model and two simpler models, a Cartesian coordinate model and a spherical coordinate model.

Chapter 2 discusses the characteristics of tidal dynamics in shallow seas as well as the physical meaning of each term in the depth-averaged Cartesian and spherical tidal equations.

The basic idea of finite difference techniques is presented in Chapter 3. In this chapter the finite difference techniques used to solve the governing equations in Cartesian and spherical coordinates are explained. An explicit finite-difference scheme based on the Arakawa C spatial grid is used to solve the tidal equations. The Arakawa C grid is used because it allows spatial derivatives to be conveniently approximated in second-order central difference form and land boundaries can be represented simply, by means of straight-line segments parallel to the coordinate axes.

A grid staggered in time as well as in space is also used and these are described in this chapter.

The finite difference code described in Bills (1992) has been chosen for solving the governing equations. The programs, written in Fortran 77, have been converted from the original Cartesian coordinates to spherical coordinates. The code has also been modified to produce the nested model of Chapter 6.

The development of a Cartesian depth-averaged model of the Persian Gulf is presented in Chapter 4. The model used elements of $8.7km \times 9.7km$ mesh size and a time step of $200sec.$ The ten components Q_1, O_1, P_1, K_1, μ_2, N_2, M_2, L_2, S_2 and K_2 were used to produce open boundary tide-height input data.

The amplitudes and phases of the four major constituents, O_1, K_1, M_2 and S_2 have been reproduced and compared with Admiralty chart 5081. Existing information on tides in the Persian Gulf is based primarily on the Admiralty chart. The data which has been used in this thesis were provided by the Admiralty chart, the National Tidal Facility at the Flinders University of South Australia and Proctor et al. (1992). The chart has been constructed from observations available at a number

of sites along the coast and a limited number of points within the Gulf. The Admiralty chart forms an initial basis for understanding tidal movement in the Persian Gulf and for comparison with mathematical models developed within this thesis and by other researchers whose work is reviewed in Section 4.3. The observational data, sets of harmonic constituents for O_1, K_1, M_2 and S_2, for 84 tidal stations in the Gulf was supplied by the National Tidal Facility at the Flinders University of South Australia. From this list, 40 stations have been used in the calibration process.

The amplitudes and phases of the four major constituents, O_1, K_1, M_2 and S_2 have been reproduced and compared with Admiralty chart 5081. The locations and the patterns of the amphidromic points predicted by the model are similar to those shown on the Admiralty chart, and the basic patterns of co-tidal and co-phase lines are the same, but computed phases for O_1 and M_2 show that in the Strait of Hormuz the tidal constituents are moving slower than the same constituents in the Admiralty chart. The predicted amplitudes, at the selected stations, are general in better agreement than the predicted phases. A series of simulations were carried out for different values of C_b and a. The optimal values for C_b and a were found to be 0.0015 and $0.03 sec^{-1}$, respectively, with associated error value of $\varepsilon = 5.3\, cm$.

It was determined that the performance of the model could be to improved by two changes. Firstly, a spherical coordinate grid could be used, since the Persian Gulf is too large to be approximated by a plane surface. Secondly, the grid could be refined in certain regions, because the spatial variations in tides are very large in the Gulf, especially near the amphidromic regions, and because the coastline has a complicated shape in most of the regions.

The depth-averaged tidal model in spherical coordinates is developed in Chapter 5 and applied to the Persian Gulf. The model uses an element dimension of $5' \times 5'$ and a time step of $\Delta t = 200 sec$. The same set of open boundary data, used for the Cartesian model, is used for tidal reproduction. The original Cartesian coordinate computer code has been converted to spherical coordinates to implement the finite difference form of the Persian Gulf spherical tidal equations. A calibration was done in order to determine optimal values for the quadratic bottom coefficient C_b, and the reduced horizontal eddy coefficient a. This was done by obtaining a minimum overall average absolute complex difference between tide-height predictions and observations. The optimal values for C_b and a were found to be 0.0015 and $a = 0.001 sec^{-1}$, respectively, with corresponding error of $\varepsilon = 4.3 cm$. The tidal data which were used in the calibration process were the same as those used in the Cartesian model. The predictions at most of stations are now closer to the observations, when they are compared with the corresponding stations used in the Cartesian model. The improvements in the results indicate the effect of considering the earth's curvature in the Persian Gulf model. The contour charts of tidal elevation for the four major tidal constituents, that is, O_1, K_1, M_2 and S_2 are produced. These contours have been compared with the Admiralty chart. In general the behaviour of the contours comparing with the Admiralty chart are similar to that obtained from the Cartesian model.

From the application of a depth-averaged spherical coordinate model of the Per-

sian Gulf, described in Chapter 5, reasonably close agreement between observed and computed tides was obtained, but to solve coastal engineering problems and to provide relevant answers for the other questions in the shallow and complicated coastal areas, it was necessary to refine the grid to improve the predictions and have a better approximation in those regions. In order to achieve this a new model was proposed, which has the advantage of having a finer spatial grid in areas where high resolution is required together with a fine grid in time in these regions, without using the fine grid everywhere with very small time steps. It should be noted that a very fine grid over whole the Gulf is too computationally expensive, because the Gulf is very large and increasing the number of grid points causes CPU time to be too excessive. To achieve the above aims, an **IN**terpolated in **S**pace and **T**ime model, the **INST** model, is developed in Chapter 6. This model basically involves embedding a fine grid in space and time to cover a region within a coarse grid. The general finite difference scheme used for both grids is three-level in time. Two basic algorithms, referred to as the transferring and back-transferring algorithms, are used. The first algorithm is used to prescribe elevations on the open boundary of the fine model; the second algorithm is used to provide the feedback of values on the fine grid to the coarse grid.

To satisfy the stability condition in both fine and coarse grids also to insure wave stability it is required that the maximum Courant numbers in both grids be approximately the same. Because this condition was met in both sides of the interface the transition between the models has been made properly, that is, refraction and reflection do not contaminated the computed patterns even near the boundary.

In order to test the **INST** model it has been applied to a rectangular bay. The bay has been used for a fully coarse grid model, a fully fine grid model, and a nested model using the **INST** model. A set of full non-linear equations in spherical coordinates including all terms but the Coriolis force, are solved in the bay. In order to find out the exact behavior of the results through the modelled region, different orientations of the interface between the two models also have been examined. The results from the **INST** model are compared with the corresponding results predicted by the fine and the coarse models of the same computational domain. The contour plots of surface elevations obtained from the models are compared with each other. The results show that the model works well, because contours resulting from the **INST** be between the results of the fine and the coarse model and are closer to those of the fine model.

The **INST** model has been tested also with Coriolis included. This test has been carried out to ensure that the model works independently of the orientation, and also to examine whether the **INST** results be between the coarse and the fine results. The contour plots of the sea surface elevations of the fine, the **INST**, and the coarse models were compared with each other; good agreement between the results was found.

The application of the **INST** model to the Persian Gulf is discussed in Chapter 7. The coarse grid section of the **INST** model uses the same uniform grid ($5'$ latitude and $5'$ longitude) and a time step of $200sec.$ as the spherical depth-averaged tidal

model of the Persian Gulf described in Chapter 5. Regarding the grid matching technique, the coastal boundaries of the coarse and the fine grids have different shapes. In addition over the fine grid, there are 9 times as many grid points as for the coarse grid, so with this technique the coastline is modelled much more realisticly.

The predictions from the **INST** model are represented by contour charts of the tidal elevation and ellipse plots of the depth-averaged current for the diurnal constituents O_1 and K_1 and the semi-diurnal constituents M_2 and S_2. The tidal results computed from the **INST** model are compared with the observations of tidal elevation at forty stations throughout the Gulf. The results are also compared with the predictions from the Cartesian model of Chapter 4 and the spherical model of Chapter 5. The absolute complex differences error was found to be $\varepsilon = 3.7\,cm$ for the **INST** model Compared with the corresponding error values obtained, namely $\varepsilon = 5.3\,cm$ for the Cartesian and $\varepsilon = 4.3\,cm$ for the spherical model, respectively. For 90% of the stations both the amplitude and phase for results from the **INST** model are better than the same results obtained from the other two models. The co-amplitude and co-phase lines for the principal diurnal O_1 and K_1 and semi-diurnal M_2 and S_2 constituents have been predicted by the model. They are compared with Admiralty chart 5081. The location of the amphidromic points predicted by the **INST** model and the basic pattern of amplitude and phase contours are generally similar to the Admiralty chart. But the detailed results show that the predictions from all three models developed in this thesis differ with the Admiralty chart in certain important aspects. For example, modeled results for M_2 phases suggest that the tidal constituent is moving more slowly through the Strait of Hormuz than shown on the Admiralty chart probably because of the boundary conditions. Also the modeled predictions for the M_2 amplitude in the Kuwait area are lower than those shown on the chart. The same is true for the O_1, K_1 and S_2 constituents.

The model-predicted tidal current ellipses for the O_1, K_1, M_2 and S_2 constituents are given in this chapter. As no published reports of observational data on tidal currents exist for the Gulf, no comparisons can be made between observed and simulated currents. A comparison is made between predictions from the **INST** model and the spherical model of Chapter 5. The diurnal ellipses predicted by the **INST** model are generally similar to those of the spherical model for each constituent. The current patterns for the tidal ellipses associated with the two diurnal constituents, O_1 and K_1, are similar in each model. Also the similarity in current pattern is clearly noted for the tidal ellipse for the semi-diurnal constituents. On comparison of the O_1 tidal ellipses with the K_1 ellipses it is apparent that K_1 current is stronger than the O_1 current. The behaviour of both constituents is similar everywhere within the Gulf. The diurnal current is strongest in the Strait of Hormuz and at the middle of the Gulf. It is weak close to the coastal boundaries, where the water is shallower. In general the strongest current appeared at the middle of the Gulf and also in the Strait of Hormuz.

The semi-diurnal ellipses M_2 and S_2 show similar current patterns, but the M_2 current is stronger than the S_2. The semi-diurnal current is strongest from the open

boundary through the middle of the Gulf and also at the head of the Gulf. Through the middle part of the Gulf, near the Iranian side, these currents exhibit longitudinal movement, while in the other parts of the Gulf they are more circular, such as at the head of the Gulf and in the United Arab Emirate region. The results also indicate a group of anticlockwise rotating currents in the Strait of Hormuz toward the coast of Qatar and another group of clockwise rotating currents at the head of the Gulf. The results also show that there is a group of clockwise rotating currents near the coast of Bahrain. It should be noted that the predictions of the coarse model for the S_2 tidal ellipses at the top of the Gulf are different from those shown by the **INST** model. The differences are due to the grid refinement in that region.

Snapshots of depth-averaged current predictions resulting from the **INST** model of the Gulf are presented in Chapter 7. They show the behaviour of the velocity fields for the first six hours of a 12 hr tidal cycle. The tidal current field in the Gulf is quite complicated with strong velocities occurring around the middle of the Gulf near, Bahrain, and in the Strait of Hormuz. Velocities are weak in the middle of the Gulf. Because the velocity is a function of depth and the Arabian coast is shallower than the Iranian coast, it is noted that most of the water appears to enter and exit the Gulf along the Iranian coast.

The results presented in this chapter suggest that the velocities produced in the middle and at the top of the head of the Gulf are relatively large, but the largest velocities exist in the Strait of Hormuz, where the water has its maximum depth. Along the coastal regions the velocities are smaller, because these regions are shallower than the other parts of the Gulf.

Chapter 7 also presents the residual vectors for velocity obtained from the **INST** model. Large residuals are predicted through the head of the Gulf and in the Strait of Hormuz. A comparison between the residual plot for the coarse model and that of the **INST** model indicate that, at the head of the Gulf, the coarse model has predicted larger values compared with the prediction of the **INST** model in that region. In the north-east of Bahrain, large residuals predicted by the coarse model are not shown in the **INST** model. The predicted residuals by around the Strait of Hormuz are different within each model.

In summary the spherical model of the Persian Gulf works better than the Cartesian model, and **INST** model predictions at the observational stations are closer to the observational data compared with the predictions of the other two models. Also it should be pointed out that with the technique used in the **INST** model, much more information on tidal elevations and velocities is available in regions over the embedded grid is developed. This provides more information to engineers and developers for coastal regions, as well as for shipping and environmental concerns near off shore islands.

Bibliography

Abramowitz, M. and Stegun, I. A. (1964), Handbook of mathematical functions with formulas, graphs and mathematical tables. National Bureau of standards, Applied Mathematics series 55, 1046pp..

Al-Rabeh, A. H., Gunay, N. and Cekirge, H. M. (1990), "A hydrodynamic model for wind-driven and tidal circulation in the Arabian Gulf", Applied Mathematical Modelling, **14**, pp. 410–419.

Al-Rabeh, A. H. and Gunay, N. (1992), "On the application of a hydrodynamic model for a limited sea area", Coastal engineering, **17**, pp. 173–194.

Arakawa, A. and Lamb, V. R. (1977), "Computational design of the basic dynamical processes of the UCLA general circulation model", Methods in Computational Physics, **17**, pp. 173–265.

Bashir, M., Khaliq, A. Q. M. and Al-Hawaj, A. Y. (1989), "An explicit finite difference model for tidal flows in the Arabian Gulf", in "Computational Techniques and Applications: CTAC-89", eds. W. L. Hogarth and J. Noye, Hemisphere publishing corporation, pp. 295–302..

Beckers, P. M. and Neves, R. J. (1985), "A semi-implicit tidal model of the north European continental shelf", Applied Mathematical Modelling, **9**, pp. 395–402.

Benque, J. P., Cunge, J. A., Feuillet, J., Hauguel, A. and Holly, F. M. (1982), "New method for tidal current computation", Journal of the Waterway, Port, Coastal and Ocean Division, ASCE, **108**, No. ww3, pp. 396–417.

Bills, P. J. (1992), "Barotropic depth-averaged and three-dimensional tidal programs for shallow seas.", Ph. D. thesis, The Department of Applied Mathematics, The university of Adelaide, South Australia.

Bills, P. J. and Noye, B. J. (1984), "Verification of a three-dimensional tidal model for coastal seas", in Computational Techniques and Applications: CTAC-83, eds. J. Noye and C. Fletcher, Elsevier Science Publishers B. V. (North-Holland), pp. 394–410.

Bills, P. J. and Noye, B. J. (1986), "Tides of Spencer Gulf, South Australia", in Computational Techniques and Applications: CTAC-85, eds. J. Noye and R. May, Elsevier Science Publishers B. V. (North-Holland), pp. 519–531.

Bills, P. J. and Noye, B. J. (1987), "An investigation of open boundary conditions for tidal models of shallow seas", in Numerical Modelling: Applications to Marine Systems, ed. J. Noye, Elsevier Science Publishers B. V. (North-Holland),

pp. 159–194.

Bills, P. J. and Noye, B. J. (1992), "Model of a coastal sea with tidal flats", in Computational Techniques and Applications: CTAC-91, eds. J. Noye, B. Benjamin and L. Colgan, pp. 117–126.

Blumberg, A. F. (1977), "Numerical tidal model of Chesapeake Bay", Journal. Hydraulics Division, American Society of Civil Engineers, **103**, No. HY1, pp. 1–10.

Blumberg, A. F. and Mellor, G. L. (1980), "A coastal ocean numerical model", J. Sundermann and K. P. Holz (eds.), Mathematical Modelling of Estuarine Physics. Lecture Notes on Coastal and Estuarine Studies, **1**, Springer-Verlag, pp. 203–219.

Blumberg, A. F. and Mellor, G. L. (1983), "Diagnostic and prognostic numerical circulation studies of the South Atlantic Bight", Journal of Geophysical Research, **88**, No. C8, pp. 4579–4592.

Casulli, V. (1990), "Numerical simulation of shallow water flow", in Computational Methods in Surface Hydrology, eds. Gambolati, G., Rinaldo, A., Brebbia, C. A., Gray, W. G. and Pinder, G. F., Springer, Berlin, pp. 13–22.

Casulli, V. and Cheng, R. T. (1992), "Semi-implicit finite difference methods for three-dimensional shallow water flow", International Journal for Numerical Methods in Fluids, **15**, No. 6, pp. 629–648.

Cekirge, H. M., Al-Rabeh, A. H. and Gunay, N. (1989), "Determining the wind-driven surface currents for prediction of movements of oil slicks in the Arabian Gulf", Computers and Mathematics with Applications, **17**, No. 11, pp. 1449–1453.

Cekirge, H. M., Lardner, R. W. and Fraga, R. J. (1986), "Adaption of the solution of the two-dimensional tidal equations using the method of characteristics to wind-induced currents and storm surges", Computers and Mathematics with Applications, **12A**, No. 10, pp. 1081–1090.

Chilicka, Z., Kowalik, Z., and Wierzbicki, Z. (1983), "Construction of a numerical model of storm surges with a refined grid", Oceanologia, No. 16, pp. 5–15.

Chu, W., Barker, B. L. and Akbar, A. M. (1988), 'Modeling tidal transport in the Arabian Gulf", in Journal of Waterway, Port, Coastal and Ocean Engineering, ASCE, **114**, No. 4, pp. 455–471.

Crisp, D. J. (1976), "Prospects of marine science in the Gulf area - the background paper", Marine Sciences in the Gulf Area, UNESCO Technical Papers in Marine Science, **26**, pp. 19–38.

Davies, A. M. and Flather, R. A. (1977), "Computation of the storm surge of 1 to 6 April 1973 using numerical models of the north west European continental shelf and the North Sea", Deutsches Hydrographische Institut, Z. **30**, pp.139–162.

Davies, A. M. and Flather, R. A. (1978), "Application of numerical models of the north west European continental shelf and the North Sea to the computation of the storm surges of November to December 1973", Deutsches Hydrographische Institut, Z. Erg. -H, A, No. 14.

Davies, A. M. and Jones, J. E. (1992), "A three dimensional model of the M_2, S_2, N_2, K_1 and O_1 tides in the Celtic and Irish seas", Progress in oceanography. **29**, pp. 197–234.

Davies, A. M. and Jones, J. E. (1993), "On improving the bed stress formulation in storm surge models", Journal of Geophysical Research, **98**, No. C4, pp. 7023–7038.

Davies, A. M. and Lawrence, J. (1994), "The response of the Irish sea to boundary and wind forcing: Results from a three-dimensional hydrodynamic model", Journal of Geophysical Research, **99**, No. C11, pp. 22665–22687.

Easton, A. K. (1977), "Selected programs for tidal analysis and prediction", Technical Report No. 9,The Flinders Institute for Atmospheric and Marine Sciences, The Flinders University of South Australia, Australia.

Elahi, K. Z. and Ashrafi, R. A. (1992a), "Tidal modelling of the Arabian Gulf", in Hydraulic and Environmental Modelling: Coastal Waters, eds. Falconer, R. A., Chandler-Wilde, S. N. and Liu, S. Q., **1**, pp. 89–98.

Elahi, K. Z. and Ashrafi, R. A. (1992b), "Computer modelling of the tides of the Arabian Gulf", in Computer Modelling of Seas and Coastal Regions, ed. Partridge, P. W., Elsevier Applied Science, pp. 161–173.

El-Sabh, M. I. and Murty, T. S. (1988), "Simulation of the movement and dispersion of oil slicks in the Arabian Gulf", Natural Hazards, **1**, pp. 197–219.

Evans-Roberts, D. J. (1979), "Tides in the Persian Gulf region", Consulting engineer, **43**, No. 6, pp. 46–48.

Fang, G. and Yang, J. (1988), "Modeling and prediction of tidal currents in the Korea Strait", Progress in oceanography, **21**, pp. 307–318.

Flather, R. A. (1976), "A tidal model of the North-West European Continental Shelf", Memoires. Societe Royale des Sciences de Liege, 6^e série, tome X, pp. 141–164.

Flather, R. A. (1981), "Practical surge prediction using numerical models", in Floods Due to High Winds and Tides, ed. D. H. Peregrine. London: Academic Press, pp. 21–43.

Flather, R. A. (1984), "A numerical model investigation of the storm surge of 31 January and 1 February 1953 in the north sea", Quarterly Journal of the Royal Meteorological Society, **110**, pp. 591–612..

Flather, R. A. and Davies, A. M. (1976), "Note on a preliminary scheme for storm surge prediction using numerical models", Quarterly Journal of the Royal Meteorological Society, **102**, No. 431, pp. 123–132.

Flather, R. A. and Heaps, N. S. (1975), "Tidal computations for Morecambe Bay", Geophysical Journal of the Royal Astronomical Society, **42**, pp. 489–517.

Flather, R. A. and Proctor, R. (1983), "Prediction of North Sea storm surges using numerical models: recent developments in U.K.", in North Sea Dynamics, ed. by Sündermann/Lenz, Springer-Verlag Berlin Heidelberg, pp. 299–317.

Galt, J. A., Payton, D. L., Torgrimson, G. M. and Watabayashi, G. (1984), "Applications of trajectory analysis for the Nowruz oil spill", in Oceanographic Modelling of the Kuwait Action Plan (KAP) Region, ed. M.I. El-Sabh ,

UNESCO Reports in Marine Science, No. 28, pp. 55–66.

Greenberg, D. A. (1983), "Modeling the mean barotropic circulation in the Bay of Fundy and Gulf of Maine", Journal of Physical Oceanography, **13**, pp. 886–904.

Hansen, W. (1962), "Hydrodynamical methods applied to oceanographic problems", in Proceeding of the Symposium on Mathematical and Hydrodynamic Methods of Physical Oceanography, Sept. 1961, Mitt. Inst. Meeresk. Univ. Hamburg, No. 1, pp. 25–34.

Heaps, N. S. (1969), "A two-dimensional numerical sea model", Philosophical Transactions of the Royal Society of London. Series A. Mathematical and Physical Sciences, **265**, pp. 93–137.

Heaps, N. S. (1973), "Three-dimensional numerical model of the Irish Sea", Geophysical Journal. Royal Astronomical Society, **35**, pp. 99–120.

Hunter, J. R. (1982), "The physical oceanography of the Arabian Gulf: A review and theoretical interpretation of previous observations", Proceeding of the Conference on Marine Environmental and Pollution, Kuwait, pp. 1–23.

Hunter, J. R. (1984), "Tidal and stratification/mixing models of Kuwait waters", in Kuwait Bulletin of Marine Science, No. 5, pp. 11–35.

Kowalik, Z. and Murty, T. S. (1993). Numerical Modeling of Ocean Dynamics, Advanced Series on Ocean Engineering, Vol. 5, Singapore: World Scientific.

Kurihara, Y., Tripoli, G. J. and Bender, M. A. (1979), "Design of a movable nested-mesh primitive equation model", Monthly Weather Review, **107**, pp. 239–249.

Lardner, R. W., Al-Rabeh, A. H., Gunay, N. and Cekirge, H. M. (1989), "Implementation of the three-dimensional hydrodynamic model for the Arabian Gulf", Advances in Water Resources, **12**, pp. 2–8.

Lardner, R. W., Belen, M. S. and Cekirge, H. M. (1982), "Finite difference model for tidal flows in the Arabian Gulf", Computers and Mathematics with Applications, **8**, No. 6, pp. 425–444.

Lardner, R. W. and Cekirge, H. M. (1987), "An efficient three-dimensional algorithm for the computation of wind-driven circulation", J. Engng. Analysis, **4**, pp. 89–94.

Lardner, R. W. and Cekirge, H. M. (1988), "A new algorithm for three-dimensional tidal and storm surge computations", Applied Mathematical Modelling, **12**, pp. 471–481.

Lardner, R. W., Cekirge, H. M. and Gunay, N. (1986), "Numerical solution of the two-dimensional tidal equations using the method of characteristics", Computers and Mathematics with Applications, **12A**, No. 10, pp. 1065–1080.

Lardner, R. W., Lehr, W. J., Fraga, R. J. and Sarhan, M. A. (1988), "A model of residual currents and pollutant transport in the Arabian Gulf", Applied Mathematical Modelling, **12**, pp. 379–390.

Leendertse, J. J. (1967), Aspects of a Computational Model for Long-Period Water-Wave Propagation, The Rand Corporation, Report RM–5294–PR.

Leendertse, J. J. (1970), A Water-Quality Simulation Model for Well-Mixed Es-

tuaries and Coastal Seas: Vol. I, Principles of Computation, The Rand Corporation, RM–6230–RC.

Lehr, W.J. (1984), "A brief survey of oceanographic modelling and oil spill studies in the KAP region", Oceanographic Modelling of the Kuwait Action Plan (KAP) Region, ed. M.I. El-Sabh, UNESCO Reports in Marine Science, No. 28, pp. 4–11.

Le Provost, C. (1984), "Model for tides in the KAP region", in Oceanographic modelling of the Kuwait Action Plan (KAP) region, ed. M. I. El-Sabh, UNESCO reports in marine science, No. 28, pp. 25–36.

Matthews, K. (1996), A Spherical Coordinates Tidal Model of the Great Australian Bight using a new Coastal Boundary Representation, Ph. D. thesis, The Department of Applied Mathematics, The University of Adelaide, South Australia.

Mitchell, W. L. and Noye, B. J. (1983), Numerical Predictions of Tides and Currents in the Gulf of Carpentaria, Report to Marine Sciences and Technologies Scheme, Project 80-2027R, The University of Adelaide, South Australia.

Murty, T. S. and El-Sabh, M. I. (1984), "Storm tracks, storm surges and sea state in the Kuwait Action Plan (KAP) region ", in Oceanographic Modelling of the Kuwait Action Plan (KAP) Region, ed. M.I. El-Sabh, UNESCO Reports in Marine Science, No. 28, pp. 12–24.

Noye, B. J. (1984), Computational Techniques for Differential Equations, ed. J. Noye, North-Holland Mathematics Studies No. 83, 679pp..

Noye, B. J. and Bills, P. J. (1990), "A three-dimensional tidal model for coastal seas", in Proceedings of the Third Australian Supercomputer Conference, The University of Melbourne, Australia, December 3–6, 1990.

Noye, B. J. and Bills, P. J. (1992), "A three-dimensional tidal model for coastal seas", in Computational Techniques and Applications: CTAC-91, eds. J. Noye, B. Benjamin and L. Colgan, pp. 373–384.

Noye, B. J., May, R. L. and Teubner, M. D. (1981), "Three-dimensional numerical model of tides in Spencer Gulf", Ocean Management, **6**, pp. 137–147.

Noye, B. J., May, R. L. and Teubner, M. D. (1982), "A three-dimensional tidal model for a shallow gulf", in "Numerical Solutions of Partial Differential Equations", ed. J. Noye (North-Holland), pp. 417–436.

Phillips, N. A. and Shukla, J. (1973) "On the strategy of combining coarse and fine grid meshes in numerical weather prediction", Journal of Applied Meteorology, **12**, pp. 763–770.

Pond, S. and Pickard, G. L. (1993), Introductory Dynamical Oceanography (2nd edition). Pergamon press.

Press, W. H, Flannery, B. P., Teukolsky, S. A. and Vetterling, W. T. (1989), Numerical Recipes. Cambridge University Press.

Proctor, R., Elliott, A. and Flather, R. A. (1992), "Predictions and observations of the Arabian Gulf oil slick", J.N.S., **17**, No. 4, pp. 215–227.

Pugh, D. T. (1987), Tides, Surges and Mean-sea level. Wiley.

Ramming, H-G. (1976), "A nested north sea model with fine resolution in shallow

coastal areas", Memoires. Societe Royale des Sciences de Liege 10, pp. 9–26.

Ramming, H-G. and Kowalik, Z. (1980), Numerical Modelling of Marine Hydrodynamics: Applications to Dynamic Physical Processes, Elsevier Oceanography Series, **26**, 368 pp.

Roache, P. J. (1972), Computational fluid dynamics, Hermosa Publisher, Albuquerque, New Mexico, 446pp.

Schwiderski, E. W. (1980), "Ocean Tides, part 1: Global Ocean tidal equations", Marine Geodesy,, **3**, pp. 161–217.

Semtner, A. J. (1986), "Finite difference formulation of a world ocean model", ed. J. J. O'Brien, Advanced Physical Oceanographic Numerical Modelling, pp. 187–202. Reidel Publishing Co.

Spall, M. A. and Holland, W. R. (1991), "A nested primitive equation model for oceanic applications", Journal of Physical Oceanography, **21**, pp. 205–220.

Spaulding, M. L., Anderson, E. L., Isaji, T. and Howlett, E. (1993), "Simulation of the oil trajectory and fate in the Arabian Gulf from the Mina Al Ahmadi spill", Marine Environmental Research, **36**, No. 2, pp. 79–115.

Stevens, M. and Noye, J. (1984), "An improved three-dimensional tidal model for a shallow gulf", in Computational Techniques and Applications: CTAC-83, eds. J. Noye and C. Fletcher, Elsevier Science Publishers B. V. (North-Holland), pp. 375–393.

Venkatesh, S. and Murty, T. S. (1994), "Numerical simulation of the movement of the 1991 oil spills in the Arabian Gulf", Water, Air and Soil Pollution, **74**, pp. 211–234.

Verboom, G. K., De Ronde, J. G., and Van Dijk, R. P. (1992), "A fine grid tidal - flow and storm surge model of the north sea", Continental Shelf Research, **12**, No. 2/3, pp. 213–233.

Von Trepka, L. (1968), "Investigations of the tides in the Persian Gulf by means of a hydrodynamic numerical model", in Proceeding of the Symposium on Mathematical and Hydrodynamic Investigation of Physical Processes in the sea. Institut fur Meerskund der Universitat von Hamburg, **10**, pp. 59–63.

Weiyan, T. (1992). Shallow water hydrodynamics. Beijing- Amsterdam: Water and Power Press, Elsevier, 434 pp.

Zahel, W. (1973), "The diurnal K_1 tide in the world ocean - A numerical investigation", Pageoph, **109**, pp. 1819–1825.

Zhang, D. L., Chang, H. R., Seaman, N. L., Warner, T. T. and Fritsch, J. M. (1986), "A two-way interactive nesting procedure with variable terrain resolution", Monthly Weather Review, **114**, pp. 1330–1339.